A treatise on first-principles studies of ZnO as diluted magnetic semiconductor

Dissertation

zur Erlangung des Grades
Doktor der Naturwissenschaften

an der Fakultät für Physik
der Universität Duisburg-Essen

von
Sanjeev Kumar Nayak
aus Odisha, Indien

Referent: Prof. Dr. Peter Entel
Korreferent: Prof. Dr. Wolfram Hergert
Tag der mündlichen Prüfung: 24.04.2012

Abstract

Diluted magnetic semiconductors (DMS) are important functional materials that bring together two fundamental aspects of electron, namely the charge and the spin, to derive new properties in materials. Based on mean-field models it was shown that wide band gap diluted semiconductors (with ZnO and GaN) could lead to room temperature ferromagnetism. This triggered much interest in the subject. However, these results are still under intensive debate.

The scope of the present thesis is to study the properties of ZnO doped with transition metal elements by the density functional theory (DFT). The DFT is an accurate theory for modeling material properties, which describe the fundamental interactions of electrons with the nucleus and is in principle free from any parameterization. In this thesis, there is extensive study of the electronic structure of ZnO beyond the generalized gradient approximation (GGA) as exchange-correlation functional ($E_{\rm xc}$), which is well known to be associated with some drawback in predicting the semiconducting properties. One of the methods adopted for improvement is by adding extra correlation-energy to GGA (GGA+U) in line with the Hubbard model. We find that with adding U on Zn d-orbitals, the band gap improves with simultaneous shift of the Zn d-bands to lower energies. The band gap nevertheless is still far below the experimental value. Another approach to correct for the $E_{\rm xc}$ is by the treatment of screened hybrid-functionals proposed by Heyd-Scuseria-Ernzerhof (HSE), where the contribution to the exchange energy is through the blend of some percentage of screened Hartree-Fock exchange and rest from the GGA exchange. The correlation energy is derived from GGA. This method also has limitations in describing the electronic structure of ZnO. A simple proposition of mixing the GGA+U and the hybrid-functional treatment may be a solution, which has been investigated in this work. The band structure of ZnO has been compared for various level of theory for $E_{\rm xc}$, namely, LDA, GGA, GGA+U, and HSE functionals with different screening lengths (ω). A proposal for HSE+U functionals has been been put forward and supported.

Using some of the treatments for $E_{\rm xc}$ as stated above, the magnetic properties of TM (Cr, Mn, Fe, Co, and Ni) doped ZnO are studied. Firstly, the electronic structure calculations for TM doped ZnO are done with the Korringa-Kohn-Rostoker (KKR) method with the LDA and using the coherent potential approximation (CPA). The exchange integrals are then calculated using the Liechtenstein's formalism, which are then used in the Monte Carlo simulations to estimate the critical temperature. A case study for Co doped ZnO is discussed, where we have calculated the magnetic phase diagram of the system. Apart from this, supercell calculations with Vienna *ab-initio* simulation package (VASP) have been done to compare the role of various treatment to the $E_{\rm xc}$. In case of GGA+U, the U is separately

treated on Zn d-orbitals and TM d-orbitals, and then together. From the total energy differences in magnetic states, it is observed that with incorporation of U, all the TM favor antiferromagnetic interactions. This may partially explain why some experimental studies on TM doped ZnO do not show any ferromagnetic correlation. Similar conclusion is also reached for most cases in HSE and HSE+U approach.

One of the recent topics under discussion for polar semiconductor materials like ZnO is d^0 magnetism. There are several reports in experiments on magnetism due to intrinsic-defect and $2p$-block elements doped extrinsic ZnO, the source of magnetism is due to localization of holes and is a topic under active discussion. In present study based on GGA it is shown that Zn-vacancy (V_{Zn}) and C substitution on O site (C_O) lead to spin-polarized solution. The magnetic energy is mostly below the room-temperature. Related to this, some perspectives of experimental situations which could lead to quenching of such magnetization is also presented.

Furthermore, studies on pure ZnO clusters based on GGA and HSE functionals are presented. A general tendency which is observed is that the bond length predicted in HSE calculations are larger than those predicted by GGA. Characteristic arrangement of magnetization density in V_{Zn} and C_O in clusters as calculated from GGA is presented.

A direct comparison of the present results with experiments is difficult because there is wide variety of experimental results for TM doped ZnO which are mostly dependent on sample preparation techniques and for the case of d^0-magnetism there are very few element specific experimental characterization. However, the studies presented in the thesis has up-to-date theoretical footing and this is the strength of the work.

Zusammenfassung

Verdünnte magnetische Halbleiter (DMS) sind bedeutende funktionale Materialien, die die zwei fundamentalen Aspekte des Elektrons nämlich Ladung und Spin zusammen nutzen, um neue Materialeigenschaften zu generieren. Im Rahmen von *Mean-field* Modellen wurde gezeigt, dass für verdünnte Halbleiter mit großer Bandlücke (die auf ZnO und GaN basieren) Ferromagnetismus bei Raumtemperatur möglich ist.

Dies hat zu einem großen Interesse an diesen Systemen geführt. Allerdings sind diese Ergebnisse immer noch Gegenstand intensiver Diskussion. Das Ziel der vorliegenden Dissertation ist die Untersuchung von ZnO, das mit Übergangsmetallen dotiert wurde im Rahmen der Dichtefunktionaltheorie (DFT). Die DFT ist eine genaue, im Prinzip parameterfreie Methode zur Modellierung von Materialeigenschaften, die die fundamentalen Wechselwirkungen des Elektronensystems mit den Kernen beschreibt. In dieser Arbeit werden intensive Studien von ZnO durchgeführt, die über die verallgemeinerte Gradientenkorrektur (GGA) für das Austausch-Korrelationsfunktional (E_{xc}) hinausgehen, da die GGA den halbleitenden Charakter nicht hinreichend beschreiben kann. Eine Methode besteht darin der GGA im Rahmen des Hubbard-Modells eine extra Korrelationsenergie zuzufügen (GGA+U). Wir finden, dass U angewendet auf die Zn d-Orbitale zu einer besseren Beschreibung der Bandlücke führt und gleichzeitig die Zn d-Bänder zu tieferen Energien verschoben werden. Trotzdem ist die Bandücke nach wie vor deutlich kleiner als der experimentelle Wert. Eine andere Näherung, die verwendet wird, um E_{xc} zu korrigieren, ist das von Heyd-Scuseria-Ernzerhof (HSE) vorgeschlagene abgeschirmte (*screened*) Hybridfunktional. Dabei wird die Austauschenergie anteilig aus *screened* Hatree-Fock- und GGA-Austauschenergie zusammengesetzt. Die Korrelationsernergie wird mittels GGA bestimmt. Auch diese Methode hat ihre Grenzen hinlänglich der Beschreibung der elektronischen Struktur von ZnO. Eine Lösung scheint die Kombination von GGA+U und Hybridfunktional zu sein, was im Rahmen dieser Arbeit untersucht wurde. Es wurden die Bandstrukturen von ZnO verglichen, die sich im Rahmen verschiedener Näherungen für E_{xc} nämlich LDA, GGA, GGA+U und HSE mit unterschiedlichen Abschirmlängen (ω) ergaben. Die Untersuchungen lassen die Schlussfolgerung zu, dass die Verwendung von HSE+U die beste Beschreibung liefert.

Unter Verwendung der oben genannten Näherungen für E_{xc} wurden die magnetischen Eigenschaften von TM (Cr, Mn, Fe, Co und Ni) dotiertem ZnO untersucht. Zuerst wurde die elektronische Struktur des TM dotierten ZnO im Rahmen der Korringa-Kohn-Rostoker (KKR)-Methode unter Verwendung der LDA und der *Coherent Potential Approximation* (CPA) bestimmt. Zur Berechnung der Austauschintegrale wurde der Formalismus von Liechtenstein verwendet. In anschließenden Monte

Carlo Simulationen wurden die damit bestimmten Austauschintegrale zur Abschätzung der kritischen Temperatur benutzt. In einer Fallstudie wurde für Co dotiertes ZnO die Berechnung des magnetischen Phasendiagramms durchgeführt.
Weiterhin wurden Superzellenrechnungen unter Verwendung des Vienna *Ab Initio* Simulation Package (VASP) gemacht, um den Einfluss verschiedener Behandlungen von E_{xc} zu untersuchen. Im Fall der GGA+U Approximation wurde U separat auf die d-Orbitale von Zn und TM angewendet sowie auch auf beide d-Orbitale gleichzeitig. Aus den Differenzen der Gesamtenergien folgt, dass in Anwesenheit von U alle TM Atome paramagnetisch sind. Dies könnte teilweise erklären, warum in experientellen Untersuchungen TM dotiertes ZnO keine ferromagnetischen Korrelationen gefunden werden. Ähnliche Schlußfolgerungen ergeben sich in den meisten Fällen auch im Rahmen der HSE und HSE+U Näherung.
Ein aktuelles Thema bezüglich polarer Halbleiter wie ZnO ist der d^0-Magnetismus. Obwohl bereits einige experimentelle Arbeiten für ZnO vorliegen, die Magnetismus aufgrund von intrinsischen Defekten und extrinsischen Defekten aufgrund von Dotierung mit Hauptgruppenelementen diskutieren, ist der Ursprung des Magnetismus nicht geklärt und immer noch Gegenstand aktueller Forschung. In der vorliegenden auf der GGA basierenden Arbeit wird gezeigt, dass für Zn-Leerstellen (V_{Zn}) und C auf dem Sauerstoffplatz (C_O) eine endliche Spinpolarisation auftritt. The magnetische Energie liegt in den meisten Fällen unterhalb der Raumtemperatur. In diesem Zusammenhang wird auch diskutiert welche Bedingungen im Experiment zu einer Auslöschung der magnetischen Moments führen können.
Weiterhin wurden ZnO Cluster unter Verwendung von GGA und HSE Fuktionalen untersucht. Dabei zeigt sich, dass die in HSE-Rechnungen vorhergesagte Bindungslänge größer ist, als die mit GGA bestimmte Bindungslänge. Im Fall von GGA wurde auch die Magnetisierungsdichte aufgrund von V_{Zn} und C_O untersucht.
Ein direkter Vergleich der Ergebnisse mit experimentellen Daten ist schwierig, da zwar eine Vielzahl von Ergebnissen für TM dotiertes ZnO vorliegen, diese aber meist von der Probenpräparation abhängen und für den Fall von d^0-Magnetismus nur wenige elementspezifische Daten verfügbar sind. Die Stärke dieser Arbeit liegt daher in der Auffindung und Diskussion einer geeigneten theoretischen Beschreibung für magnetische Halbleiter wie ZnO.

Contents

List of Abbreviations

ASA	Atomic sphere approximation
CPA	Coherent potential approximation
CT	Charge transfer insulators
DFT	Density functional theory
DMS	Diluted magnetic semiconductors
DOS	Density of states
EPR	Electron paramagnetic resonance
FC	Field cooled
FPLO	Full-potential local-orbital minimum-basis code
FSM	Fixed spin moment
GGA	Generalized gradient approximation
GMR	Giant magneto resistance
HEG	Homogeneous electron gas
HF	Hartree-Fock method
HMF	Half-metallic ferromagnet
HOMO	Highest occupied molecular orbital
HSE03	Heyd-Scuseria-Ernzerhof hybrid-functional with screening parameter ω = 0.3 Å
HSE06	Heyd-Scuseria-Ernzerhof hybrid-functional with screening parameter ω = 0.2 Å
KKR	Korringa-Kohn-Rostoker method
LDA	Local density approximation
LSDA	local spin density approximation

LUMO	Lowest unoccupied molecular orbital
MC	Monte Carlo
MFA	Mean-field approximation
MH	Mott-Hubbard insulators
MT	Muffin-tin approximation
PAW	Projector-augmented wave
PBE	Perdew-Burke-Ernzerhof GGA parameterization
PBE0	Perdew-Ernzerhof-Burke hybrid-functional
PL	Photoluminescence
PLD	Pulsed laser deposition
PW91	Perdew-Wang ’91 GGA parameterization
RMS	Reactive magnetron sputtering
RT	Room temperature
SIC	Self-interaction correction method
SKKR	Screened Korringa-Kohn-Rostoker code
SPRKKR	Spin polarized relativistic Korringa-Kohn-Rostoker code
SQUID	Superconducting quantum interference device
TB	Tight-binding model
TM	Transition metal
TMR	Tunnel magneto resistance
VASP	Vienna *ab-initio* simulation package
VMW	Vosko-Wilk-Nusair LDA parameterization
XANES	X-ray absorption near edge spectroscopy
XLD	X-ray linear dichroism
XMCD	X-ray magnetic circular dichroism

XPS	X-ray photoelectron spectra
ZFC	Zero field cooled

List of Figures

List of Tables

1. Introduction

Zinc oxide (chemical formula ZnO) is a wide band gap semiconductor which has been in use from the ancient times. ZnO is widely used in variety of applications due to its unique physical and chemical properties [1]. One of the advanced usage include application in space and satellite technology due to its property of resistance against radiation exposure. The futuristic and ambitious prospect of ZnO lies in meeting the energy demands from nano devices made of ZnO. It has been possible to develop piezoelectric nanogenerator from ZnO nanowires taking advantage of its piezoelectric property to produce electricity [2]. This could possibly lead to generate clean electricity from non conventional sources like wind and ocean waves. Another potential future application of ZnO is anticipated in the field of spintronics which is in its infant stage. The theme of the thesis is closely related to the motivation of spintronics application and hence needs further elaboration.

1.1. Materials for spintronics application

Spintronics is a subject which refers to the study of the role played by electron spin (and also nuclear spin) in condensed matter physics and materials science. Naturally, this subject also bounds the research of devices that specifically exploit spin properties in addition to charge degrees of freedom. Spin properties have already been in use for important practical applications, i.e., in hard disk read-write devices. The underlying mechanism is that the device resistance changes from small to large depending on the relative orientation of magnetizations. This phenomena is called the giant magneto resistance (GMR) effect. More recently the tunnel magneto resistance (TMR) is achieved in magnetic tunnel junction devices where the tunneling current depends on spin orientations of the electrodes.
Materials for spintronics application can be broadly classified into two types, namely, metallic spintronic materials and semiconducting spintronic materials. In this regard, the GMR materials like the magnetic multilayers may be treated into the class of metallic spintronic materials. The success of GMR effect and its impact in computer technology has led to the Nobel prize in physics to its founders, Peter Grünberg and Albert Fert, in 2007.
There is lot of interest in finding novel ways of both generation and utilization of spin-polarized currents. These include investigation of spin transport in semiconductors and looking for ways in which semiconductors can function as spin filters and spin valves. The importance of using semiconductors based spintronic materials lies in the fact that the existing metal-based devices can not amplify signals, whereas semiconductor based spintronic devices could not only provide amplification but also

at the same time serve as multi-functional devices. More importantly, semiconductor-based devices is easier to be integrated with traditional semiconductor technology. In this regard, the diluted magnetic semiconductors (DMS) are a remarkable class of materials where magnetic ions are incorporated into semiconductor host lattices. These materials can exhibit a wide range of magnetic properties. Usually, the diluted magnetic semiconductors are substitutional alloys of either II-VI, III-V or IV-VI semiconductors with transition metal ions. DMS materials as a subject of research is rather old. It can be traced back to 1960s when research was being carried out on ferromagnetic spinel with Cr and Eu chalcogenide [3]. The physical concepts for understanding the physics of DMS like, magnetic polaron, spin molecules, spin-dependent scattering and indirect coupling via carriers, were developed. Rigorous research in this field have led to the discovery of pronounced magneto-optical activity in this class of materials, particularly the Faraday rotation whose origin was explained to be due to the giant Zeeman splitting [4].

The essential characteristic for a spintronics device is accomplishment of spin-polarization as ground state and the transport of spin-polarization. In case of semiconductor spintronic materials both the aspects immensely depend on the material properties. The first report of spin polarized electrons into a semiconductor at room temperature was reported by Zhou *et al.* [5]. Accomplishing spin-polarization in semiconductors means making semiconductor ferromagnetic and for practical applications the critical temperature of the ferromagnetic semiconductor must be above room temperature (RT). Most likely a semiconductor with intrinsic spin polarization achieved through transition metal dopant would be a starting material. Ferromagnetic semiconductor was first reported in EuO with a Curie temperature of 70 K [6]. Another semiconductor best known to have ferromagnetic properties is Mn doped GaAs where the critical temperature is shown to be 173 K [7, 8]. It is reported that diluted magnetic semiconductor where the dopant induces a carrier mediated long range magnetic order, can stabilize still higher critical temperature [9]. One of the observations in DMS is the anomalous magnetization curve as a function of temperature, M(T). While in insulating samples the magnetization curve is concave [10, 11], in metallic samples the magnetization curve is almost linear over a temperature range [12, 13]. The magnetization plots are in deviation from the Brillouin function behavior, which is known to be valid from the mean-field theory [14]. The origin of such anomaly is attributed to disorder in the lattice, since high quality samples show comparatively less deviation from Brillouin function behavior [15]. In case of GaMnAs based DMS systems, Mn contributes a hole, however, there are some debate over the band in which the hole resides. There are reports that the holes are doped into the GaAs valence band thus with increasing Mn doping the hole concentration increases [16–20], while other reports suggest in favor that with increase in the Mn doping from dilute limit to the heavily doped regime, the shallow Mn acceptor states broaden and form an impurity band [21–27]. Using several model studies and Monte Carlo simulations, Alvarez *et al.* have obtained the phase diagram of III-V DMS systems from a generic Monte Carlo study of lattice spin-fermion model. Detailed study can be found in Alvarez's dissertation [28]. The overall summary is represented as a phase diagram shown in Fig. 1.1 (left), where it is found that the Curie temperature increases with the

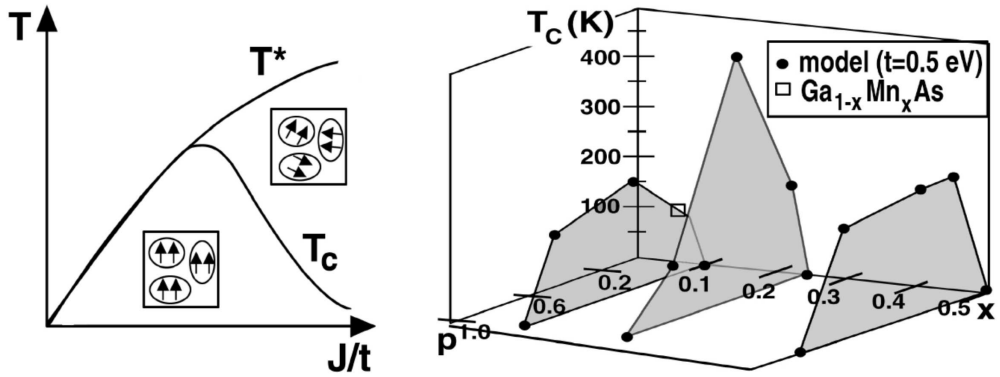

Figure 1.1.: (left) Phase diagram of typical III-V DMS system. Figure adopted from Ref. [23]

exchange coupling strength (measured in units of the hopping strength t in the model) upto a optimal value. Thereafter increase in J lead to formation of clusters of spins in the lattice. The transition temperature, T^*, at which the clusters have no correlation is higher but the true Curie temperature is smaller and has a decreasing tendency beyond the optimal J. The nature of Curie temperature for different concentration of impurity (x) as a function of hole concentration (p) is shown in the Fig. 1.1 (right).

1.2. ZnO based DMS

It must be mentioned here that out of several materials being studied, $Ga_{1-x}Mn_xAs$ has consistently shown ferromagnetic properties. The problem, however, is that the Curie temperature is much below the room temperature. Using a modified Zener's model, Dietl *et al.* predicted that ZnO based DMS could lead the transition temperature much higher than the room temperature [29]. This, together with the properties such as transparency in visual region and piezoelectricity have generated huge interest on ZnO based DMS. There are numerous literature and reviews regarding this problem and other issues related to ZnO [30–32]. There is a lot of debate about the predictions and the variety of results that are obtained from theoretical and experimental studies.

Although several reports of room temperature ferromagnetism in DMS based on ZnO and GaN exist, the degree of reproducibility is rather low. This is so because of difficulties in sample preparation and the magnetism is very sensitive to underlying defects and imperfections in the sample. So far there are no clear identification and quantification of the factors for ferromagnetism. In a recent study, Kammermeier *et al.* [33] have studied particular case of Co doped ZnO (also Gd doped ZnO) to look for possible intrinsic mechanism of magnetism in these materials. The materials had been investigated by superconducting quantum interference device (SQUID) and X-ray magnetic circular dichroism (XMCD). The X-ray absorption near edge spectroscopy (XANES) measurements with linear polarized light, exploiting the X-ray linear dichroism (XLD), gives information about the local

environment of the probed atoms. The samples were grown by reactive magnetron sputtering (RMS). In the 10% Co doped in the sample, 95% of the Co atoms were incorporated on substitutional Zn-sites as shown by XLD analysis. They have concluded that no RT ferromagnetism is found in their samples, instead paramagnetic behavior of dopant were proved [34–36]. In another set of experimental studies, Djenadic *et al.* have undertaken magnetic studies for Co doped ZnO nanoparticles [37]. They have synthesized the ZnO nanoparticles using the chemical vapor synthesis method and found single wurtzite phase in the nanoparticles. Using their synthesis method they could dope as large as 33% Co in ZnO. They have also tried some co-doping with Li. From magnetic characterization they find no ferromagnetism or any cooperative magnetism exist in their samples. On the other hand there are other reports of ferromagnetism from TM doped ZnO [38, 39]. Shi *et al.* have reported that they find different magnetic properties for different samples even if the procedure of sample preparation is same [40]. While some samples show paramagnetic tendencies, others are clearly ferromagnetic above the RT. They conclude that Zn-vacancy (V_{Zn}) is crucial for the observation of high temperature ferromagnetism in Co-doped ZnO. It will be shown in present work that intrinsic cation defect, V_{Zn}, leads to spin-polarized solution itself. A similar observation of ferromagnetism is observed in Na and Co co-doped ZnO, where the the magnetism is attributed to O-vacancy defects (V_O) [41]. Similar reports are enormous in literature, not only of Co, but for other TM elements like V, Cr, Mn, Fe, Ni, and Ca.

1.3. First-principles studies of DMS

There are two important characteristic physical properties of DMS, the semiconducting property and the magnetic property, both of which needs the discipline of quantum mechanics for proper description of the phenomena. In quantum mechanics the physics of materials are described by interacting electrons which obey the Schrödinger equation. However, it is practically impossible to solve the Schrödinger equation for a materials. For example, if we treat the nuclei as classical particles and ignore the relativistic-effects, for a N electron system this would require the solution of Schrödinger equation with 3N spatial variables and N spin variables. Since the number N is of the order of $10^{23}\mathrm{cm}^{-3}$, it is obvious that the solution cannot be obtained without the use of approximations. On another hand, density functional theory (DFT) has emerged as a powerful alterative. The conceptual basis of DFT is completely different and at the same time provides a parameter-free formalism for mapping the many-electron problem to a problem involving only three spatial coordinates of the charge density. The DFT formalism is covered in chapter 2. Hence it makes complete sense to study DMS properties from first-principles approach based on DFT.

In DFT the Kohn-Sham Hamiltonian is solved with an approximated form of exchange-correlation functional (V_{xc}). The usual route to construct the functionals is via a mapping of the interacting system onto a non-interacting system having the same ground state charge density. It is found that a simple matching to the homogeneous gas is accurate enough to describe the material properties.

This approximation is called the local density approximation (LDA). However, to deal with transition metal systems it is found that gradient corrections to the LDA, known as the generalized gradient approximation (GGA), lead to better results. DFT is an invaluable tool for understanding magnetism. It has contributed to the understanding of chemical bonding and are being used for first-principles molecular dynamics simulations to understand the the pathways of chemical reactions. DFT is used now a days in almost all subjects related to condensed matter and materials sciences, namely physics, chemistry, geology and more recent applications in bio-physics. As a result of the successes of DFT, Walter Kohn was awarded the 1998 Nobel Prize in Chemistry.

It is known that the exchange-correlation treatment with LDA and GGA are not sufficient to predict reasonable band gap for semiconductors. The underestimation of the band gap varies from 50% in Si to as large as 80% in ZnO [42]. This is of severe consequence for problems relating to doping, since the impurity state of the dopant is expected to lie within the band gap. A clear situation is presented by Zunger *et al.* [43]. Thus, it is important to attempt the “beyond-DFT" treatment to the problem. In this aspect the common methods that are adopted are the addition of Hubbard U correlation into the specific localized orbitals. Another approach is to improve the exchange potential by adding an effective contribution from GGA exchange and the Hartree-Fock exchange. Thus, the exchange potential can no longer be treated as a functional of density. Both the methods of correction for the exchange-correlation potentials nevertheless still have some drawback. A detailed description of which can be found in chapter 5.

The goal of the present thesis is to study the properties of doped ZnO with state-of-the-art *ab-initio* techniques of density functional theory (DFT) together with different exchange-correlation functionals. Variety of schemes have been used to understand the magnetic interaction of TM doped ZnO. Chapter 6 presents the results of the distance-dependent exchange interactions between impurity atoms estimated from the Korringa-Kohn-Rostoker (KKR) method applied to the alloy problem through the coherent potential approximation (CPA) approach. The resulting exchange integrals (J_{ij}) are be used in Monte Carlo simulations of the classical Heisenberg spin model to extract the phase diagram. Supercell calculations with the TM atoms occupying the nearest neighbor positions studied with various treatments of the V_{xc} are studied and the results are presented in chapter 7. Before that, however, the role of different treatment of V_{xc} in influencing the electronic structure of pure ZnO are discussed in chapter 5. Some of the aspect of defect-related magnetism obtained from the DFT calculations are summarized in chapter 8 through the studies of V_{Zn} and C_O defects. Finally, chapter 9 gives a brief summary of studies on defect-magnetism in ZnO clusters.

2. Electronic Structure Calculations

2.1. Introduction

Densify functional theory (DFT) is a conceptual improvement which leads to large simplification of the many body problem and allows practical computation of properties of real-materials. In principle, it is an exact theory except for few approximations used to treat the many body correlation effects. DFT leads as the most favored method for the materials simulations, most of the properties predicted by DFT finds direct experimental support. The predictive ability for materials properties allows us to study more complex materials, for which experiments are still lacking. However, the approximations adopted within DFT is sometimes too short for semiconductors and other oxide and nitride systems. Some of the tasks undertaken in this dissertation deals with such problems. In the following the outline of the DFT theory is presented, essentially collected from regular sources [44–50].

2.2. Density Functional Theory

The properties of materials can in principle be determined by solving the time-independent Schrödinger equation

$$\left(\sum_{i=1}^{N}\left[-\frac{\hbar^2}{2m}\nabla_i^2 + V_{\rm ext}(\mathbf{r}_i)\right] + \frac{1}{2}\sum_{i\neq j=1}^{N}\frac{e^2}{|\mathbf{r}_i-\mathbf{r}_j|}\right)\Psi(\mathbf{r}_1,\cdots,\mathbf{r}_N) = E\,\Psi(\mathbf{r}_1,\cdots,\mathbf{r}_N), \tag{2.1}$$

where, $\mathbf{r}_i$ is the position of the $i^{\rm th}$ electron, N is the total number of electrons in the system, $V_{\rm ext}$ is the external field in which the electrons move, and E is the total electronic energy. The above expression implicitly takes into account the Born-Oppenheimer approximation, which treats the electronic and the nuclear degrees of freedom as separable variables. The eigenfunction Ψ contains $3N$ degrees of freedom and thus it is not possible to solve Eq. (2.1) in general. The electron-electron interaction term prohibits Eq. (2.1) to be expressed with reduced degrees of freedom.

Since most physical observables can be expressed in terms of one-electron density matrix

$$\rho^{(1)}(\mathbf{r},\mathbf{r}') = N\int \Psi^*(\mathbf{r}_1,\mathbf{r}_2,\cdots,\mathbf{r}_N)\Psi(\mathbf{r'}_1,\mathbf{r}_2,\cdots,\mathbf{r}_N)d\mathbf{r}_2\cdots\mathbf{r}_N \tag{2.2}$$

or the two-electron density matrix

$$\rho^{(2)}(\mathbf{r}_1, \mathbf{r}_2, \mathbf{r'}_1, \mathbf{r'}_2) = \frac{N(N-1)}{2} \int \Psi^*(\mathbf{r}_1, \mathbf{r}_2, \mathbf{r}_3, \cdots, \mathbf{r}_N)\Psi(\mathbf{r}'_1, \mathbf{r}'_2, \mathbf{r}_3, \cdots, \mathbf{r}_N) d\mathbf{r}_3 \cdots \mathbf{r}_N$$

or the real space electron density,

$$\rho^{(1)}(\mathbf{r}) = \rho(\mathbf{r}, \mathbf{r}) \tag{2.3}$$

therefore if one can have a different formalism than the Schrödinger's picture, the complete knowledge of Ψ may be skipped which will also lead to practical computation of materials properties.

The early attempts in this direction was the Thomas-Fermi theory. Although approximate, this theory deals with calculating all the properties from knowledge of the charge density, Eq. (2.3).

2.2.1. The Hohenberg-Kohn Theorem

Hohenberg and Kohn proved that the ground state electron density uniquely determines the external potential $V_{\text{ext}}(\mathbf{r})$ [51]. This implies that the charge density in three-dimensional space is sufficient to construct the full Hamiltonian of Eq. (2.1), which can then be solved to obtain all the ground-state properties. One of the important point to note is that the Hohenberg-Kohn theorem proves the existence of functionals that would lead to the ground-state density, but it gives no information about how to obtain the functionals. Even then Hohenberg-Kohn theorem is a big leap forward in computational materials science because it shows one need not deal with the many-body wavefunctions $\Psi(\mathbf{r}_1, \cdots, \mathbf{r}_N)$ but only with the charge density $\rho(\mathbf{r})$ to obtain the ground-state properties.

2.2.2. The Kohn-Sham method

Kohn and Sham reformulated the problem of calculating the total energy E as a functional of electron density $\rho(\mathbf{r})$, $E = E[\rho]$, as that of solving a set of single-particle Schrödinger-like equations [52]. One of the main difference to that of the previously existing Thomas-Fermi model is the treatment of the the kinetic energy term. While Kohn-Sham theory uses the quantum-mechanical operator $(-\nabla^2/2)$ for kinetic energy, Thomas-Fermi theory replaces this with an effective local potential [53]. In practice, the kinetic energy of the interacting system is found from the projection on to the non-interacting system but with equal density as that of the interacting system. This can be described as follows:

The kinetic energy and the energy due to the external potential can be written as the functional of ground state charge density as;

$$T = T[\rho] \tag{2.4}$$

$$E_{\text{ext}} = \int \rho(\mathbf{r}) V_{\text{ext}}(\mathbf{r})\, d\mathbf{r}. \tag{2.5}$$

The electron-electron Coulomb repulsion term in terms of density functional is written as;

$$E_{\mathrm{C}} = \frac{e^2}{2} \iint \frac{\rho(\mathbf{r}_1)\rho(\mathbf{r}_2)}{|\mathbf{r}_1 - \mathbf{r}_2|} d\mathbf{r}_1 \mathbf{r}_2 = \frac{1}{2} V_{\mathrm{C}}(\mathbf{r})\rho(\mathbf{r}) d\mathbf{r}. \tag{2.6}$$

Thus the total energy functional can be written as

$$E[\rho] = T[\rho] + \int \left[V_{\mathrm{ext}}(\mathbf{r}) + \frac{1}{2} V_{\mathrm{C}}(\mathbf{r}) \right] \rho(\mathbf{r}) d\mathbf{r} + \xi_{\mathrm{xc}}[\rho] \tag{2.7}$$

where, $\xi_{\mathrm{xc}}[\rho]$ is called the exchange-correlation energy functional. This terms in principle must contain all the interactions (exchange term and many-body interaction terms) that are not described by the other terms.

Applying the variational principle, i.e., energy of the trial density ($\tilde{\rho}$) obeying the constraint

$$N = \int \rho(\mathbf{r}) d\mathbf{r} \tag{2.8}$$

is always higher than the energy of the ground-state density

$$E[\tilde{\rho}] \geq E[\rho] \tag{2.9}$$

together with the Lagrange multipliers, one gets

$$\frac{\delta}{\delta \rho} \left[E - \mu \left(\int \rho(\mathbf{r} d\mathbf{r} - N) \right) \right] = 0 \tag{2.10}$$

$$\Rightarrow \quad \mu = \frac{\delta T}{\delta \rho} + V_{\mathrm{ext}}(\mathbf{r}) + V_{\mathrm{C}}(\mathbf{r}) + \frac{\delta \xi_{\mathrm{xc}}}{\delta \rho} \tag{2.11}$$

where, μ is the Lagrange multiplier which is defined as the Fermi energy.

Consider the above equation with that for N non-interacting particles moving in another external potential V_{eff} such that the total density of the system is same as that of the real system. The equivalent equation can be written as

$$\frac{\delta \tilde{T}}{\delta \rho} + V_{\mathrm{eff}}(\mathbf{r}) = \mu. \tag{2.12}$$

Here $\tilde{T}[\rho]$ is the kinetic energy of non-interacting particles.

We can now solve the Schrödinger equation which can be separated into N single-particle equations of the form

$$\left[-\frac{\hbar^2}{2m} \nabla^2 + V_{\mathrm{eff}}(\mathbf{r}) \right] \psi_i(\mathbf{r}) = \varepsilon_i \psi_i(\mathbf{r}) \tag{2.13}$$

The ground state of this non-interacting system is the N occupied lowest energy single-particle states

and the ground state density is obtained from the occupied states as

$$\rho(\mathbf{r}) = \sum_{i=1}^{N} |\psi_i(\mathbf{r})|^2 . \tag{2.14}$$

The relation between the external potential $V_{\rm ext}$ of an interacting system to that of the external potential $V_{\rm eff}$ of the non-interacting system can this be determined as both of them have the same charge density. Comparing Eq. (2.11) and Eq. (2.12) we have,

$$\begin{aligned} V_{\rm eff}(\mathbf{r}) &= V_{\rm ext}(\mathbf{r}) + V_{\rm C}(\mathbf{r}) + \frac{\delta \xi_{\rm xc}}{\delta \rho} + \frac{\delta T}{\delta \rho} - \frac{\delta \tilde{T}}{\delta \rho} \\ &= V_{\rm ext}(\mathbf{r}) + V_{\rm C}(\mathbf{r}) + \frac{\delta E_{\rm xc}}{\delta \rho} \\ &= V_{\rm ext}(\mathbf{r}) + V_{\rm C}(\mathbf{r}) + V_{\rm xc}(\mathbf{r}) \end{aligned} \tag{2.15}$$

where, $V_{\rm xc}$ is the exchange-correlation potential.
As per the assumption, the electron density of the non-interacting system is same to that of the electron density of the real system. However, this is not true for the case of total energy and that of the single-particle orbitals. The total energy of the non-interacting system is the sum of the single particle energies ε_i of the occupied orbitals, but the total energy of the real system is given by

$$E[\rho] = \sum_{i=1}^{N} \left\langle \psi_i \left| -\frac{\hbar^2}{2m}\nabla^2 \right| \psi_i \right\rangle + \int \left(V_{\rm ext}(\mathbf{r}) + \frac{1}{2} V_{\rm C}(\mathbf{r}) \right) \rho(\mathbf{r}) d\mathbf{r} + E_{\rm xc}[\rho] \tag{2.16}$$

Using Eq. (2.15) and Eq. (2.13), Eq. (2.16) can be written as,

$$E[\rho] = \sum_{i=1}^{N} \varepsilon_i - \int \left(\frac{1}{2} V_{\rm C}(\mathbf{r}) + V_{\rm ext}(\mathbf{r}) \right) \rho(\mathbf{r}) d\mathbf{r} + E_{\rm xc}[\rho] \tag{2.17}$$

This shows how the total energy is modified due to various contributions from external and electron-electron interaction as compared to the non-interacting case.

2.3. Solutions of Kohn-Sham equations

The Kohn-Sham equations (2.13-2.15) can be solved by self-consistent calculations. The essence is; for a given electron density $\rho(\mathbf{r})$ the potential is calculated using Eq. (2.15), thereafter the single-particle wavefunctions are constructed using Eq. (2.13), from which new charge density is estimated via Eq. (2.14). When the input and the output density are identical within the allowed tolerance, the self-consistent solution is said to be reached. The flowchart shown in Fig. 2.1 summerizes the procedure adopted for self-consistent determination of solutions for the Kohn-Sham Hamiltonian of Eq. (2.13).

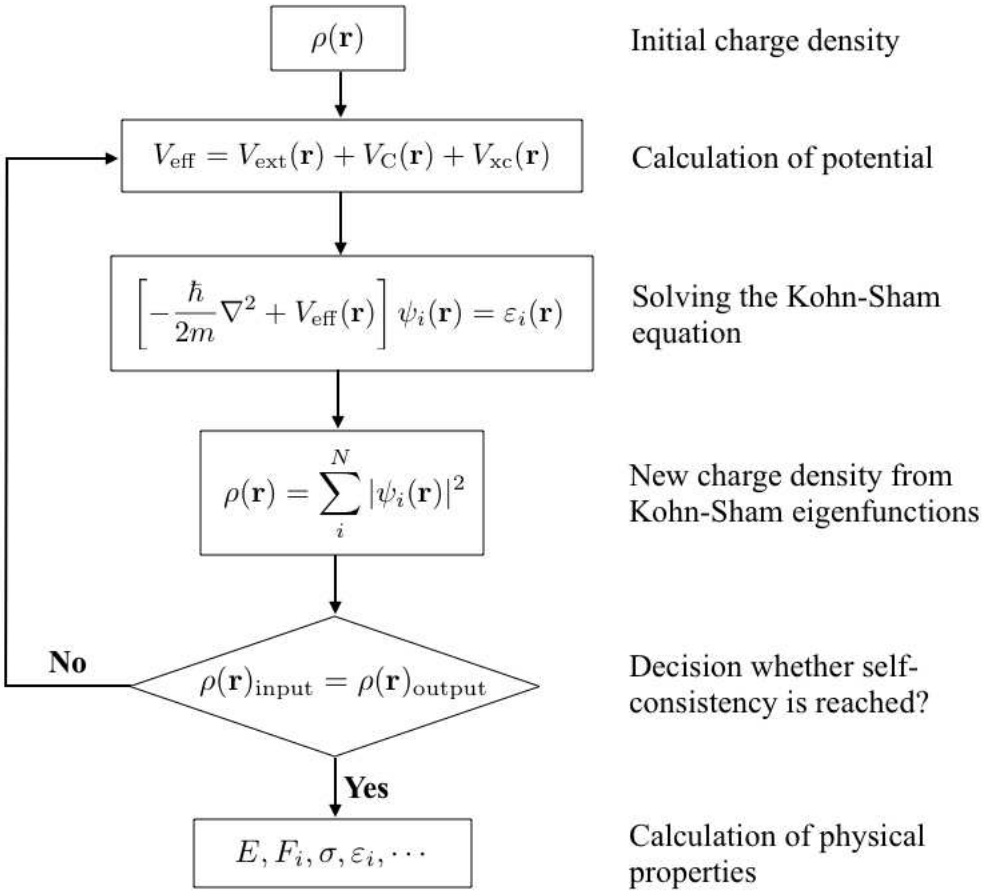

Figure 2.1.: Flowchart showing the steps used for solving the Kohn-Sham equations in self-consistent scheme.

The formalism of using the charge density as the central quantity to determine the electronic structure of solids greatly simplifies the task. This gives an advantage as compared to other wavefunction based methods, especially when heavier elements are considered. The essential idea is to “freeze" the densities of the core electrons and keep them as in isolated atoms. Although the frozen-core approximation can also be used in wavefunction based methods, but one would need the wavefunctions unlike the density as needed by the Kohn-Sham DFT.

In actual implementations of Kohn-Sham DFT, the eigen function ψ_i is expanded in some basis, where the potentials could be treated more accurately. Thus we have

$$\psi_i(\mathbf{r}) = \sum_{j=1}^{N_b} c_{ij}\phi_j(\mathbf{r}) \tag{2.18}$$

where, N_b is the maximum number of basis functions ϕ_j used for the calculation. The electron density

can now be written as,

$$\rho(\mathbf{r}) = \sum_{i=1}^{N} \sum_{j=1}^{N_b} c_{ij}^* c_{ik} \phi_j^*(\mathbf{r}) \phi_k(\mathbf{r}) \tag{2.19}$$

The Coulomb potential ($V_{\mathrm{C}}(\mathbf{r})$), also known as the Hartree potential can be obtained by solving the Poisson's equation with the required boundary conditions.

$$\nabla^2 V_{\mathrm{C}}(\mathbf{r}) = -4\pi e^2 \rho(\mathbf{r}) \tag{2.20}$$

It is found that the V_{C} and the V_{xc} cannot be written in analytical form in almost all types of basis sets as a result the evaluation of matrix elements are not possible. In practice, V_{C} and V_{xc} are evaluated using auxiliary basis functions. So, we have

$$\rho(\mathbf{r}) \simeq \tilde{\rho}(\mathbf{r}) = \sum_{i=1}^{N_\rho} c_i^\rho f_i^\rho(\mathbf{r}) \tag{2.21}$$

$$V_{\mathrm{xc}}(\mathbf{r}) \simeq \tilde{V}_{\mathrm{xc}}(\mathbf{r}) = \sum_{i=1}^{N_{\mathrm{xc}}} c_i^{\mathrm{xc}} f_i^{\mathrm{xc}}(\mathbf{r}) \tag{2.22}$$

The auxiliary functions are chosen such that Eq. (2.20) can be solved analytically

$$V_{\mathrm{C}}(\mathbf{r}) \simeq \tilde{V}_{\mathrm{C}}(\mathbf{r}) = \sum_{i=1}^{N_C} c_i^C f_i^C(\mathbf{r}) \tag{2.23}$$

and to get E_{xc} as

$$E_{\mathrm{xc}} = \int \varepsilon_{xc} \left[\rho, |\nabla\rho|, \nabla^2\rho, \cdots\right] d(\mathbf{r}) \tag{2.24}$$

one can make use of auxiliary functions to find the approximate value of $\varepsilon_{xc}(\mathbf{r})$

$$\varepsilon_{xc}(\mathbf{r}) \simeq \tilde{\varepsilon}_{\mathrm{xc}}(\mathbf{r}) = \sum_{i=1}^{N_\varepsilon} c_i^\varepsilon f_i^\varepsilon(\mathbf{r}) \tag{2.25}$$

Once the basis functions ϕ_j and the auxiliary functions f_i are selected, the calculations can be made using the following steps.

1. The nuclear positions are specified.

2. Appropriate guess for potentials V_{C} and V_{xc} are selected to start as initial potential

3. Using the initial potentials and the basis functions, the overlap matrix elements and the Hamil-

tonian is calculated.

$$S_{jk} = \langle \phi_j | \phi_k \rangle \tag{2.26}$$

$$H_{jk} = \left\langle \phi_j \left| -\frac{\hbar^2}{2m}\nabla^2 + V_{\rm C} + V_{\rm xc} \right| \phi_k \right\rangle \tag{2.27}$$

4. The secular equation

$$H \cdot c_i = \varepsilon_i \cdot S \cdot c_i \tag{2.28}$$

is diagonalized which gives the Kohn-Sham energies ε_i and the orbitals ψ_i.

5. New density is calculated using Eq. (2.19) from which new potentials $V_{\rm C}$ and $V_{\rm xc}$ are calculated and new iteration from step 3 is started.

6. After the convergence is reached, various physical quantities, like total energy, forces, charge density, etc., are calculated using the Kohn-Sham eigenvalues and the eigenfunctions.

The main difference in the various implementations of DFT is the choice of the basis set ϕ_j and those of the auxiliary functions f_i.

2.4. Kohn-Sham and Hartree-Fock equations

It has already been mentioned that the Kohn-Sham DFT relies on the Hohenberg-Kohn theorem where the central quantity is the charge density for determination of all the physical properties of the system. On the other hand, Hartree-Fock method which is one of the accurate methods developed for the electronic structure calculations of solids treat the wavefunction as the central quantity. It is essential to know the difference of the two approaches.
The single-particle restricted Hartree-Fock equation (where, the majority and the minority electrons are forced to occupy the same spatial orbital ψ_i) for a closed-shell system with even number of electrons (N) is given as,

$$\left[-\frac{\hbar^2}{2m}\nabla^2 + V_{\rm ext}(\mathbf{r}) + e^2 \sum_{j=1}^{N} \int \left|\psi_j(\mathbf{r}')\right|^2 \frac{1}{|\mathbf{r}-\mathbf{r}'|} d\mathbf{r}' \right.$$
$$\left. -\frac{e^2}{2} \sum_{j=1}^{N} \int \psi_j^*(\mathbf{r}) \frac{1}{|\mathbf{r}-\mathbf{r}'|} \hat{P}_{\mathbf{r}\mathbf{r}'} \psi_j(\mathbf{r}') \mathbf{r}' \right] \psi_i(\mathbf{r}) = \varepsilon_i^{\rm HF} \psi_i(\mathbf{r}) \tag{2.29}$$

Here, the first and the second terms are identical to the Kohn-Sham equations for non-interacting systems with potential $V_{\rm ext}$ as in Eq. (2.13). The third term is the classical electrostatic Coulomb potential times the eigenfunction $\psi_i(\mathbf{r})$ and hence is equivalent to the term $V_{\rm C}(\mathbf{r})$ in the Kohn-Sham

equations. The fourth term involves the permutation operator $\hat{P}_{\mathbf{rr'}}$ and does not have a direct analogue in the Kohn-Sham formalism. This is the exchange term which is non-local and cannot be written in terms of potential. Since the exchange-term is explicitly taken into consideration in the Hartree-Fock theory, the eigenfunctions are treated as orbitals and the eigenvalues as the orbital energies. They are certainly different form the eigenvalues and eigenfunctions obtained from Kohn-Sham equations. Thus it can be summarized that the the two important methods, namely the Kohn-Sham method and the Hartree-Fock method, differ in the way the exchange term is treated.

2.5. The plane wave basis sets

There are various ways to approach the Kohn-Sham solutions. As already mentioned different implementations of Kohn-Sham DFT differ in the way they treat the basis set and the auxiliary functions (refer section 2.3). The plane wave pseudopotential approach is one such approach which involves using a plane wave basis set. Alternatively one can use basis functions that are localized around individual atoms [54, 55]. Yet another method is the KKR-Green's method based on the multiple scattering approach which is briefly discussed in section 2.7.1.

A plane wave basis is always used together with description of the system with the periodic boundary conditions. This implies that the external potential and hence the ground state density is periodic in space, as essential condition to treat crystalline solids. Hence we have,

$$V_{\text{ext}}(\mathbf{r}+\mathbf{R}) = V_{\text{ext}}(\mathbf{r}), \tag{2.30}$$

and

$$\rho(\mathbf{r}+\mathbf{R}) = \rho(\mathbf{r}), \tag{2.31}$$

where $\mathbf{R}$ is arbitrary lattice vector, defined by

$$\mathbf{R} = l\mathbf{a} + m\mathbf{b} + n\mathbf{c}, \tag{2.32}$$

where l, m, and n can each take any integer value, and $\mathbf{a}$, $\mathbf{b}$, and $\mathbf{c}$ are vectors defining the the unit cell. and the volume of the cell Ω, given by

$$\Omega = |\mathbf{a}\cdot(\mathbf{b}\times\mathbf{c})|. \tag{2.33}$$

In order to produce the periodic density contribution, $|\phi(\mathbf{r})|$ must be periodic. In addition, in order to satisfy the Kohn-Sham equations for a periodic potential, we must have

$$\phi(\mathbf{r}+\mathbf{R}) = \phi(\mathbf{r})e^{i\mathbf{k}\cdot\mathbf{R}}, \tag{2.34}$$

where $\mathbf{k}$ is a reciprocal space vector. This leads to the condition satisfying the Kohn-Sham orbitals, namely,

$$\phi(\mathbf{r}) = u(\mathbf{r})e^{i\mathbf{k}\cdot\mathbf{r}}, \tag{2.35}$$

where u is a periodic function satisfying

$$u(\mathbf{r}+\mathbf{R}) = u(\mathbf{r}). \tag{2.36}$$

Since $\mathbf{k}$ is not uniquely defined, hence we restrict that $\mathbf{k}$ lies within the Brillouin zone. The normalization condition for the Kohn-Sham orbital is given as,

$$\int \phi^*(\mathbf{r})\phi(\mathbf{r})\, d\mathbf{r} = 1. \tag{2.37}$$

There are a set orbitals for every possible value of $\mathbf{k}$. In practice, we deal with a finite set of $\mathbf{k}$-points, usually distributed evenly in the Brillouin zone as given by the Monkhorst-Pack scheme [56]. Hence when the periodic boundary conditions are in use, the orbitals are indexed by $\mathbf{k}$, as well as i. If there are N orbitals per $\mathbf{k}$-point and supposing that there are N_k such $\mathbf{k}$-points, then each $\mathbf{k}$-point is given a "weight" of $1/N_k$. Thus we have the correct normalization with a complete set of orbitals for each $\mathbf{k}$-point. The density is now given by

$$\rho(\mathbf{r}) = \sum_{\mathbf{k}} \sum_{i} \phi^*_{i\mathbf{k}}(\mathbf{r})\phi_{i\mathbf{k}}(\mathbf{r}). \tag{2.38}$$

It was discussed before that the Kohn-Sham orbitals are defined as the N eigenstates of the Kohn-Sham equations with lowest eigenvalue, but now it must be defined as the eigenstates of lowest eigenvalue, the integration of density over which gives the value N within the unitcell (or supercell under consideration).

2.5.1. Pseudopotentials and plane waves

For a reasonable description of a system, the number of plane-waves required (for plane-wave basis) is in general much larger than the size of basis required for localized basis set. This is so because the orbitals tend to oscillate very rapidly in the vicinity of atomic nuclei, and are much more smoothly varying elsewhere. The rapid oscillation can only be accounted with large cut-off energy for plane-waves (or shorter wavelengths). The use of pseudopotentials is to replace the core potentials (nuclear or/and filled orbitals) with a general effective potential such that the problem can be easily numerically dealt with [57–59]. Pseudopotentials together with the plane waves basis can thus reduce the magnitude of this problem to practical solvable limit. Thus pseudopotential approach is useful by effectively removing core electrons from the calculation. As a result the number of Kohn-Sham or-

bitals is reduced. This reduces the time required to evaluate orbital-dependent quantities. Another advantage of using the pseudopotential formalism is that, since the pseudopotential is not uniquely defined for a particular element, there is scope for optimizing the potential.
To understand how pseudopotential works, let us consider a single isolated atom, with atomic number Z. So we gave Z electrons, moving in an external potential given by

$$V_{\rm ext}(r) = \frac{Z}{r}. \tag{2.39}$$

Developing the Kohn-Sham DFT for single atom will result in a set of N Kohn-Sham orbitals, $\psi_i(\mathbf{r})$, a corresponding density, $\rho(\mathbf{r})$, and the effective potential, $V_{\rm eff}(\mathbf{r})$ (given by Eq. 2.15). Before proceeding to generate the pseudopotential, we must classify the orbitals as core and valence. We also have to select the cut-off radius, r_c. In general, orbitals in "closed shells" configurations are considered as core, while the remainder are considered valence. The pseudopotentials, $\hat{V}_{\rm PS}$, are usually non-local. This is so because in an orbital, separate local potential, $V_{\rm PS}^{(l)}(r)$, act on each angular momentum component, l. If we now replace the external potential, $V_{\rm ext}(r)$, in the Kohn-Sham ansatz with the pseudopotential, $\hat{V}_{\rm PS}$, and treat the valence electrons, the resulting pseudo-orbitals, $\psi_{\rm PS}(\mathbf{r})$, must satisfy the following:

(a) Each pseudo-orbital, $\psi_{\rm PS}(\mathbf{r})$, must be equal to the corresponding orbital obtained from the all-electron calculation, $\psi_{\rm AE}(\mathbf{r})$, outside the cut-off radius.

(b) The eigenvalues of $\psi_{\rm PS}(\mathbf{r})$ must be equal to the eigenvalue of the corresponding $\psi_{\rm AE}(\mathbf{r})$

(c) The first and second derivatives of $\psi_{\rm PS}(\mathbf{r})$ must be equal to those of the corresponding $\psi_{\rm AE}(\mathbf{r})$ at the cut-off radius.

(d) Inside the cut-off radius, $\psi_{\rm PS}(\mathbf{r})$ should have no radial nodes.

Pseudopotentials for which the electronic charge within the cut-off radius is same as that of the charges obtained for all-electron within the cut-off radius is defined as the norm-conserving pseudopotentials. There are other class of pseudopotentials for which this condition is relaxed. They are called the ultrasoft pseudopotentials [55].
The non-local pseudopotential which has separate local potential for each angular momentum component may be written in terms of the orbitals as

$$\hat{V}_{\rm PS}\psi(\mathbf{r}) = \sum_{lm} V_{\rm PS}^{(l)}(r) Y_{lm}(\theta,\phi)\langle Y_{lm}|\psi(\mathbf{r})\rangle, \tag{2.40}$$

where, $Y_{lm}(\theta,\phi)$ are the spherical harmonics. In one of the formulation of pseudopotential, as suggested by Kleinman-Bylander pseudopotentials [60], the angular component of the pseudopotential is separated into a local (loc) and a non-local component as follows:

$$V_{\rm PS}^{(l)}(r) = V_{\rm PS}^{\rm loc}(r) + \delta V_{\rm PS}^{(l)}(r). \tag{2.41}$$

The non-local component, $\delta V_{\mathrm{PS}}^{(l)}$, is then approximated as

$$\delta V_{\mathrm{PS}}^{(l)}(r) = \frac{\left|\delta V_{\mathrm{PS}}^{(l)}(r)\psi_l^0(r)\right\rangle \left\langle\psi_l^0(r)\delta V_{\mathrm{PS}}^{(l)}(r)\right|}{\left\langle\psi_l^0(r)\left|\delta V_{\mathrm{PS}}^{l}(r)\psi_l^0(r)\right\rangle\right.}, \tag{2.42}$$

where, $\psi_l^0(r)$ are the pseudo-orbitals for the atomic system.
Pseudopotentials are of much importance in practical applications because it helps to reduce the computational demand of the problem at hand and scales linearly with the number of plane waves.

2.5.2. Spin-Dependent DFT

While an exact DFT calculation is guaranteed to return the correct ground state and energy of any system, it would not necessarily tell us anything about the spin of the electrons. In standard Kohn-Sham theory, because there is no spin component in the Kohn-Sham potential, the numbers of spin-up and spin-down orbitals never differ by more than one. Therefore, even if the system is highly spin-polarized, the Kohn-Sham orbitals do not reflect this fact. Spin-dependent DFT is a generalization of the standard Kohn-Sham formalism that allows us to deal more sensibly with systems that have collinear spin polarization. This involves adding a spin-index to both the density and the Kohn-Sham potential, one for spin-up electrons and one for spin-down electrons, i.e.

$$\rho(\mathbf{r}) \rightarrow \rho(\mathbf{r},\sigma), \text{and,} V_{\text{eff}}(\mathbf{r}) \rightarrow V_{\text{eff}}(\mathbf{r},\sigma), \tag{2.43}$$

with the density now related to the Kohn-Sham orbitals via

$$\rho(\mathbf{r},\sigma) = \sum_{i\mathbf{k}} f_{i\mathbf{k},\sigma}\phi_{i\mathbf{k}}^*(\mathbf{r})\phi_{i\mathbf{k}}(\mathbf{r}). \tag{2.44}$$

Here the factor $f_{i\mathbf{k},\sigma}$ allows for fractional occupancies of orbitals in the spin channel σ, and can have any value from 0 to 1. The spin polarization of a system emerges via the exchange-correlation functional, for example, the LDA can be extended to the local spin density approximation (LSDA) [52].

2.6. The local density approximation

As discussed in previous sections, the DFT theory based on Hohenberg-Kohn theorems is an exact theory. However, in practice we rely on the Kohn-Sham formalism, where an approximations has to be adopted for treating the exchange-correlation potential. One of the approximations which was proposed by Kohn and Sham is the local density approximation (LDA) [52]. The LDA is derived from

the homogeneous electron gas (HEG) and can be written as

$$E_{\rm xc}^{\rm LDA}[n^{\mathbf{n}}] = \int n(\mathbf{r}) V_{\rm xc}^{\rm LDA}(\mathbf{r}) d\mathbf{r} \tag{2.45}$$

where $V_{\rm xc}^{\rm LDA}$ is a function of density. The exchange part of the HEG is analytically given by

$$V_{\rm x}^{HEG} = -\frac{3}{4}\left(\frac{3}{\pi}\right)^{1/3} \int n(\mathbf{r})^{4/3} d\mathbf{r} \tag{2.46}$$

More accurate value for the correlation term have been obtained from quantum Monte Carlo methods for the HEG. In general the parametric form of correlation is given as,

$$V_{\rm c}^{\rm HSG} = \begin{cases} A\ln(r_s) + B + r_s(C\ln(r_s) + D) & \text{for high density limit} \\ \dfrac{1}{2}\left(\dfrac{g_0}{r_s} + \dfrac{g_1}{r_s^{3/2}} + \cdots\right) & \text{for low density limit} \end{cases} \tag{2.47}$$

where, the Wigner-Seitz radius r_s is related to the density as

$$\frac{4}{3}\pi r_s^3 = \frac{1}{\rho} \tag{2.48}$$

and A, B, C, D, g_0, g_1 are some parameters. The LDA exchange-correlation functionals have been used with much success, especially for metallic systems. This is because metals can be described by an effective free-electron model. Transition metals on the other hand need gradient corrections in the LDA, commonly known as the generalized gradient approximations (GGA), for better electronic structure description because of the participation of d-orbitals which are correlated.

2.7. KKR method

Unlike the previous method of solution by the plane wave pseudopotential approach, the calculation of ϕ can be avoided if one considers the singe-particle Green's function $G(\mathbf{r}, \mathbf{r}'; E)$ of the Schrödinger's equation. One of the advantage of this method is that the charge density and the local density of states can be directly calculated form the Green function. The description of the method is taken from Ref. [61, 62].

2.7.1. Green's Function Method

The solution of the Kohn-Sham equation for an energy E with a source at the position $\mathbf{r}'$ is given by (treating $\hbar$ = 1 and m_e = 1),

$$\left(\nabla^2 + V(\mathbf{r}) - E\right) G(\mathbf{r}, \mathbf{r}'; E) = -\delta(\mathbf{r} - \mathbf{r}'). \tag{2.49}$$

Using the spectral representation for the retarded Green function we have

$$G(\mathbf{r},\mathbf{r}';E+i\varepsilon)=\sum_{\sigma}\frac{\psi_{\sigma}(\mathbf{r})\psi_{\sigma}^{*}(\mathbf{r}')}{E+i\varepsilon-E_{\alpha}}, \tag{2.50}$$

it can be shown that the charge density $n(\mathbf{r})$ can be directly expressed by an energy integral over the imaginary part of the Green function, which can be treated as the local density of states at the position $\mathbf{r}$.

$$\begin{aligned} n(\mathbf{r}) &= 2\sum_{\substack{\alpha \\ E_{\alpha}<E_{\mathrm{F}}}}|\psi_{\alpha}(\mathbf{r})|^{2} \\ &= -\frac{2}{\pi}\int^{E_{\mathrm{F}}}dE\ \mathrm{Im}\,G(\mathbf{r},\mathbf{r};E) \end{aligned} \tag{2.51}$$

and the local density of states on particular atom within volume V is obtained by integrating the imaginary part of the Greens function over volume (Ω):

$$n_{V}(E)=-\frac{2}{\pi}\int_{V}d\mathbf{r}\ \mathrm{Im}\,G(\mathbf{r},\mathbf{r};E) \tag{2.52}$$

Thus, the evaluation of the wave functions $\psi_{\alpha}(\mathbf{r})$ are avoided. Note that the index i in section 2.2.2 has been replaced by α so as to avoid confusion with the imaginary number i. By using the analytical properties of the Green function $G(z)$, where z is a complex variable of energy, $z=E+i\Gamma$, the energy integral can be transformed into contour integral in the complex energy plane

$$n(\mathbf{r})=-\frac{2}{\pi}\,\mathrm{Im}\int_{E_{B}}^{E_{\mathrm{F}}}dz\ G(\mathbf{r},\mathbf{r};z) \tag{2.53}$$

where the energy bounds of the contour are from bottom of the valence band, E_B, to that of the Fermi energy, E_{F}.

An interacting system may be treated with Hamiltonian H such that,

$$H=H_{0}+V \tag{2.54}$$

where, H_0 is the Hamiltonian of the non-interacting system. The Green function for this Hamiltonian can be written as

$$\begin{aligned} G(E) &= \frac{1}{E+i\varepsilon-H} \\ &= \frac{1}{E+i\varepsilon-H_{0}-V} \end{aligned} \tag{2.55}$$

The Green function for non-interacting system is given by

$$G_0 = \frac{1}{E + i\varepsilon - H_0} \tag{2.56}$$

which is easy to calculate. The Green function $G(E)$ can be obtained using the Dyson's equation

$$\begin{aligned} G(E) &= G_0(E) + G_0(E)\, V\, G(E) \\ &= G_0(E) \frac{1}{1 - V\, G_0}. \end{aligned} \tag{2.57}$$

For a bulk calculation one starts with the free space Green function G_0 ($H_0 = -\nabla^2$), such that V is the sum of the potentials of all atoms. For an impurity in a crystal one starts with the bulk Green function G_0, such that V represents the change of impurity potential with respect to the bulk potential together with the potentials of the neighboring host atoms as perturbations.

2.7.2. KKR Green Function Method for Impurities

The use of the Green's function method for the electronic structure calculations is due to Korringa, Kohn and Rostoker (KKR), and thus the method is named after them [63–65]. In their approach the Schrödinger equation is solved by the multiple scattering theory which describes the propagation of wave in the solid as a repetition of single scattering events from different atoms. Let us consider that the whole space is divided into non-overlapping and space filling spheres with center at position $\mathbf{R}^n$. In each cell the electrons are scattered by potentials V^n, and for simplicity we assume V^n to be spherically symmetric and centered at $\mathbf{R}^n$. By introducing cell-centered coordinates, the Green function $G(\mathbf{r} + \mathbf{R}^n, \mathbf{r}' + \mathbf{R}^{n'}; E)$ can be expanded in each cell as a function of $\mathbf{r}$ and $\mathbf{r}'$ in terms of spherical harmonics:

$$\begin{aligned} G(\mathbf{r} + \mathbf{R}^n, \mathbf{r}' + \mathbf{R}^{n'}; E) = \delta_{nn'} \sqrt{E} \sum_L H_L^n(\mathbf{r}_>; E) R_L^n(\mathbf{r}_<; E) \\ + \sum_{LL'} R_L^n(\mathrm{r}; E) G_{LL'}^{nn'}(E) R_{L'}^{n'}(\mathbf{r}; E), \end{aligned} \tag{2.58}$$

where, $\mathbf{r}$ and $\mathbf{r}'$ are restricted to the cells n and n' and $\mathbf{r}_<$ and $\mathbf{r}_>$ denote the the two vectors $\mathbf{r}$ and $\mathbf{r}'$ with smaller and larger absolute value. The $R_L^n(\mathbf{r}; E)$ and $H_L^n(\mathbf{r}; E)$ represent the product of spherical harmonics and the radial eigenfunctions of the central potential $V^n(r)$.

$$R_L^n(\mathbf{r}; E) = R_l^n(r; E)\, Y_L(\mathbf{r}) \tag{2.59}$$

$$H_L^n(\mathbf{r}; E) = H_l^n(r; E)\, Y_L(\mathbf{r}) \tag{2.60}$$

Now, $R_L^n(\mathbf{r}; E)$ is the solution which varies at the origin as r^l which represents the solution for an incoming spherical Bessel function $j_j(\sqrt{E}\, r) Y_L(\mathbf{r})$. On other hand, H_l^n is the corresponding irregular

solution varying as $1/r^{l+1}$ at the origin which is identical with the spherical Hankel function $h_l(\sqrt{E}\,r)$ outside the range of the potential. Both the radial functions are connected by the Wronskian relation, which guarantees that the first term in Eq. (2.58) represents the exact Green function for the single potential $V^n(r)$ in free space. Since this term contains the source condition $-\delta(\mathbf{r}-\mathbf{r}')$ for the Green function of Eq. (2.49), the second term is source free and thus have the regular solutions R^n_L and $R^{n'}_{L'}$ with double angular momentum expansion.

Eq. (2.58) describes the Green's function which satisfy the of Schrödinger's equation (2.49) in each cell n. $G^{nn'}_{LL'}(E)$ is called the structural Green's function, which describes the connection of the solutions between different cells. Hence the structural Green's function contains all the information about the multiple scattering problem. So the main advantage of the KKR method is in separating between the single-site properties, which are described by the radial solutions $R^n_L(\mathbf{r})$ and $H^n_L(\mathbf{r})$ and the multiple scattering properties, which are described by the matrix $G^{nn'}_{LL'}(E)$.

The structural Green function matrix can be extracted by matching the solutions of the neighboring cells at the cell boundary, however, in the multiple-scattering theory it is calculated from the Green's function of the inner region of the cell. This poses additional advantage in achieving the convergence in l. The structural Green's function can also be obtained from the g matrix in free space by solving the Dyson equation [64]

$$G^{nn'}_{LL'}(E) = g^{nn'}_{LL'}(E) + \sum_{n''L''} g^{nn''}_{LL''}(E)\; t^{n''}_{l''}(E)\; G^{n''n'}_{L''L'}(E) \tag{2.61}$$

where the t-matrix t^n_l for the potential $V^n(r)$ is given by

$$t^n_l(E) = \int_0^R r^2\, dr\; j_l(\sqrt{E}\,r)\; v^n\; R^n_l(r;E) \tag{2.62}$$

Once the structural Green function $\overset{\circ}{G}{}^{nn'}_{LL'}(E)$ of the ideal crystal is known, the structural Green function $G^{nn'}_{LL'}(E)$ can be easily calculated for the crystal with impurity using the Dyson equation

$$G^{nn'}_{LL'}(E) = \overset{\circ}{G}{}^{nn'}_{LL'}(E) + \sum_{n''L''} \overset{\circ}{G}{}^{nn'}_{LL'}(E)\; \Delta t^{n''}_{l''}\, G^{n''n'}_{L''L'}(E) \tag{2.63}$$

where $\Delta t^n_l = t^n_l - \overset{\circ}{t}{}^n_l$ is the difference of the t-matrices in perturbed and in the ideal lattice. The perturbation of the potential is restricted to the vicinity of the impurity, as a result the Green function is determined by real space by matrix inversion. The matrix to be inverted has rank $n_d\,(l_{max}+1)^2$, where n_d is the number of perturbing potential and l_{max} is the maximum number of angular momentum.

The all-electron methods based on a spherical potential of muffin-tin type, as discussed above, or based on the atomic sphere approximation (ASA) have been successful for describing the electronic structures of solids. However, to deal with systems with lower symmetry one needs more accurate formalism beyond the spherical approximation. This is done by generalizing the above derivations

through a full potential description. A detailed description of which can be found in many review and lecture notes.

2.7.3. Coherent Potential Approximation (CPA)

The KKR Greens function approach gives a practical way to study the alloy system through the coherent potential approximation (CPA) approach. In must be remembered that alloy systems are disordered systems and hence the Bloch theorem cannot be applied to this system. CPA approach is developed to deal with such situation which has its origin in the multiple scattering description of disordered systems and was first proposed by Soven and Shiba [66–68]. The essential theme is that a substitutional disorder alloy is replaced by a periodic system of same coherent potentials representing an ensemble average over all possible configurations, thus defining an effective medium which is close to the real alloy. In other words, we replace the t-matrix with the coherent t-matrix at each site which represents the average scattering properties and which has to be determined self-consistently. Comprehensive description of the KKR and the KKR-CPA methods and their applications can be found in Ref. [69].

2.7.4. Exchange Interactions

In the context of present thesis it is intended to study the magnetic properties of diluted magnetic semiconductors. One of the most direct way for the studies would be to calculate the exchange integrals between localized spins in the semiconductor host. The formalism for calculating the exchange integrals in the KKR method has been derived by Lichtenstein *et al.* [70]. In simple words, the energy differences from infinitesimal rotation of localized spins obtained from the electronic structure calculation is mapped onto a classical Heisenberg Hamiltonian with the magnitude of spins as that of the local magnetic moment of the transition metal atom in the host.

$$H_{\mathrm{cl}} = -\frac{1}{2}\sum_{i\neq j} J_{ij}\mathbf{s}_i \cdot \mathbf{s}_j \tag{2.64}$$

From the above mapping it is possible to infer the type of interaction and the strength of the interactions between the TM atoms. One of the advantages of this approach is that one can use the exchange integrals and use the same classical Heisenberg model to perform Monte Carlo simulations and thereby simulate the magnetic properties at non-zero temperatures and can calculate the critical temperatures for magnetic phase transition.

3. Monte Carlo method

3.1. Introduction

The Monte Carlo simulation method was the technique used to perform the first computer simulation of a molecular system. Monte Carlo methods are a class of techniques that can be used to simulate the behavior of a physical or mathematical system. They are different from other materials simulation methods such as molecular dynamics, by being stochastic, i.e. of non-deterministic nature. This stochastic behavior in Monte Carlo methods generally results from the use of random number sequences. Monte Carlo methods are frequently applied in the study of systems with a large number of strongly coupled degrees of freedom. Examples include liquids, disordered materials, and strongly coupled solids. One of the main advantages of this methods is in evaluating high dimensional integrals [71].

3.2. Random Numbers and Statistical Analysis

A random number may be defined as a numerical value resulting from a process which cannot be predetermined by the initial conditions. Many natural processes display randomness – from the decay of subatomic particles to the trajectories of dust particles across the surface of a liquid in Brownian motion.

From previous discussions we understand that DFT is a method to determine the ground state properties of a system. In order to study the finite temperature properties of materials such as the DMS, we have to adopt statistical methods using model Hamiltonians. Our problem of estimating the critical temperatures of the magnetic phase in DMS can be modeled by a classical Heisenberg model, given by Eq. (2.64).

The thermal average of any observable $\mathcal{O}(\mathbf{x})$ at a particular temperature T in a canonical ensemble is given by,

$$\langle \mathcal{O}(\mathbf{x}) \rangle_T = \frac{1}{Z} \int d\mathbf{x}\, \mathcal{O}(\mathbf{x})\, \exp\left(\frac{-H_{\mathrm{cl}}(\mathbf{x})}{k_{\mathrm{B}} T} \right), \text{with}, \tag{3.1}$$

$$Z = \int d\mathbf{x}\, \exp\left(\frac{-H_{\mathrm{cl}}(\mathbf{x})}{k_{\mathrm{B}} T} \right). \tag{3.2}$$

The average energy, specific heat, average magnetization and magnetic susceptibility can thus be

given from above expectation values as,

$$E = \frac{\langle H_{\rm cl}\rangle_T}{N}, \tag{3.3}$$

$$C_V = \frac{\left(\langle E^2\rangle - \langle E\rangle^2\right)}{k_{\rm B}T^2} \tag{3.4}$$

$$M = \frac{\left\langle \sum_i^N S_i \right\rangle_T}{N}. \tag{3.5}$$

$$\chi = \frac{\left(\langle M^2\rangle - \langle M\rangle^2\right)}{k_{\rm B}T^2} \tag{3.6}$$

where, V is the volume under consideration.

3.2.1. The importance sampling approach

The points $\mathbf{x}$, as in Eq. (3.1), can be sampled on a regular grid. This is called the simple sampling method. This method has certain disadvantages. For example, in our problem we know that especially at low temperatures only few states are important. But within the simple sampling method many states are considered which do not influence the system. One way to make efficient phase space sampling is through what is called as the importance sampling method (also known as umbrella sampling). Importance sampling is a general technique for estimating properties of a particular distribution, while only having samples generated from a different distribution. Importance sampling refers to the principle of choosing a density function, $p(\mathbf{x})$, which is chosen to promote configurations that would otherwise be inaccessible to a Boltzmann-weighted Monte Carlo run. This would ensure that only points which contribute to the statistical quantities are selected with higher probability. Thus the thermal average of canonical ensemble of Eq. (3.1) now becomes,

$$\langle \mathcal{O}(\mathbf{x})\rangle_T = \frac{1}{Z}\int d\mathbf{x}\; \mathcal{O}(\mathbf{x})\; \exp\left(\frac{-H_{\rm cl}(\mathbf{x})}{k_{\rm B}T}\right)\; p(\mathbf{x}), \tag{3.7}$$

where,

$$Z = \int d\mathbf{x}\; \exp\left(\frac{-H_{\rm cl}(\mathbf{x})}{k_{\rm B}T}\right)\; p(\mathbf{x}). \tag{3.8}$$

3.2.2. Markov process and Metropolis algorithm

One of the important aspects of Monte Carlo simulation is the Markov process. In a common description, a stochastic process with the Markov property, or memorylessness, is one for which conditional on the present state of the system, its future and past are independent. Given a starting state μ from which we generate a state ν, for the Markov process to be valid, the transition probability of going to

ν from state μ, given by $P(\mu \to \nu)$ must satisfy,

(a) Ergodicity: Ergodic hypothesis states that, over long periods of time, the time spent by a particle in some region of the phase space of micro states with the same energy is proportional to the volume of this region, i.e., that all accessible micro states are equiprobable over a long period of time. In other words, the ergodic hypothesis means that the average of a process parameter over time and the average over the statistical ensemble are the same.

(b) Detailed balance: A Markov process is said to have detailed balance if the transition probability, P, between each pair of states μ and ν in the phase space obey

$$p_\mu P(\mu \to \nu) = p_\nu P(\nu \to \mu) \tag{3.9}$$

This condition can be applied to all physical phenomena obeying the time-reversal symmetry. So, in order to improve our sampling we select the sampling probability p($\mathbf{x}$) in Eq. (3.7) as the Boltzmann probability

$$\begin{aligned} \frac{P(\mu \to \nu)}{P(\nu \to \mu)} &= \frac{p_\nu}{p_\mu} \\ &= e^{-\delta H/k_{\mathrm{B}}T} = p(\mathbf{x}) \end{aligned} \tag{3.10}$$

The above selection of Boltzmann probability, where the configurations are generated from previous state using a transition probability which depend on the energy difference between the initial and the final states is called the Metropolis method, named after the inventor. Thus the Metropolis importance sampling Monte Carlo algorithm is

1. Choose an initial state
2. Choose a site i
3. Calculate the energy change ΔE which results if the spin at site i is overturned
4. Generate a random number r such that $0 < r < 1$
5. If $r < \exp(-\delta E/k_{\mathrm{B}})$, flip the spin
6. Go the next site and go to step 3

The algorithm stated above is sometimes called the single spin-flip method. Instead of allowing the change in energy to determine the 'new' spin configuration, one can simply randomly select a new spin direction and then compare a random number r with the Boltzmann probability of the trial configuration, i.e.,, accept the new configuration if $r < \exp(-E'/k_{\mathrm{B}}T)$ where E' is the energy of the trial state. This method is most useful if the single spin-flip method has a low acceptance state.

This algorithm is called the “Heat-bath algorithm". The Monte Carlo code developed in our group by Dr. Alfred Hucht makes use of the heat-bath algorithm, where there is provision to specify number of measurement M at each temperature. One measurement is channeled as output after K Monte Carlo sweeps. Thus the run time of the Monte Carlo code scales as $K \times M \times n_T \times N \times n_J$, where $n_T = (T_f - T_i)/dT$ is the number of temperature steps, N is the number of atoms and n_J is the number of couplings per atom. It is recommended to use for K a value between $1 - 10$ and for M a large value of $10^4 - 10^6$ for good statistics.

3.2.3. Determination of T_c

By analyzing the dependence of specific heat and magnetic susceptibility with respect to temperature one can determine the critical point of a phase transition. The analysis of specific heat can be more cumbersome because it incorporates the effect of all the terms contributing to the Hamiltonian (the Hamiltonian we considered is rather more simple with only magnetic contribution), susceptibility analysis would give informations about the magnetic phase transition. Thus to determine the magnetic critical temperature, the analysis of magnetic susceptibility is used. In the Hamiltonian considered here, both the specific heat and the magnetic susceptibility can be used.

Another useful and perhaps more accurate method of determining the critical temperature of especially a ferromagnetic system is based on the “universality" feature of the standard Hamiltonians. Already there are few model Hamiltonians whose physics falls under this universality class and there are accurate thermodynamical scaling laws defined for them. It is encouraging that the classical Heisenberg also falls under this class of Hamiltonians and thus we can directly make use of the universal feature of classical Heisenberg Hamiltonian to extract more accurate Curie temperature (remember that we are discussing about ferromagnetic systems here). From the scaling theory it is known that the magnetization of three-dimensional classical Heisenberg model evolve with respect to temperature with the relationship

$$M \propto \left(\frac{T - T_{\mathrm{C}}}{T_{\mathrm{C}}} \right)^{\beta}, \tag{3.11}$$

where T_{C} is the Curie temperature and β is the critical exponent, which for a 3-dimensional Heisenberg model has the value $\beta = 0.3646$ [72, 73]. Thus when we plot $M^{1/\beta}$ (here, M^3) with respect to temperature we obtain a straight line which is decreasing with increasing temperature. The point of intersection of this line with the horizontal (temperature) axis can be interpreted as the critical temperature. Thus, Curie temperature can be determined for ferromagnetic system through a linear regression of the function $f(M) = M^{1/\beta}$.

In particular for DMS problems, the concentration of magnetic ions can be low, i.e., from 1-5%. This poses a major problem in data analysis, especially when M is used to extract the information for the magnetic phase transition temperature. This makes more sense for models with additional degree

of freedom, for example like molecular movement included. In this case it is important to analyze the specific heat (C) and susceptibility (χ). Since C and χ are physical orbservables that involve second derivative, hence a better statistics has to be generated to extract the informations. While χ gives information about the magnetic phase transition (see Eq. (3.6)), C gives in general all the factors responsible for phase transition, refer Eq. (3.4). We have used these informations to extract informations about the magnetic phase transition in our Monte Carlo studies.

4. Theory of Exchange Interaction

4.1. Introduction

One of the important effects of the principle of identical particles is the exchange interaction. This is a quantum mechanical effect which contributes to the expectation value of the operators when the wave-functions of identical particles overlap. It is responsible for the interaction between spins. More general origin of magnetism is the interplay between the electronic spin degree of freedom, the repulsive Coulomb interaction between electrons and the fermionic quantum statistics. The essence of studying the magnetic properties for the diluted magnetic semiconductors is in identifying the mechanism responsible for interaction between localized spins. However a rigorous theoretical analysis of any particular mechanism cannot be made in terms of electronic structure calculations. Many mechanisms have been identified from model studies that can establish the correlation between localized spins, such as RKKY, Heisenberg direct exchange, Kramer's superexchange and Zener double exchange. So, it is useful to categorize the different mechanisms which is described below based on Ref. [74].

4.2. Exchange interaction

The Coulomb repulsion is the origin of exchange interactions between fermions. Let us consider two $3d$ electrons, 1 and 2. If the individual wavefunctions for these electrons with positions r_1 and r_2, are written as $\psi(r_1)$ and $\psi(r_2)$. The Coulomb interaction is given by,

$$H = \frac{1}{2}\iint \psi^*(r_1)\psi^*(r_2)\frac{e^2}{|r_1 - r_2|}\psi(r_2)\psi(r_1)d\tau_1 d\tau_2, \tag{4.1}$$

where the integrals are over the spatial coordinate and there is summation over two different spins. In terms of field-operators, $\psi(r)$ can be expressed as

$$\psi(r) = \sum_{n,m,\sigma} c_{nm\sigma}\phi_{nm}\theta_\sigma. \tag{4.2}$$

where, ϕ_{nm} is the spatial wave function and θ_σ is the spin wave functions. The indices n, m, and σ denote the ionic site, orbital and spin quantum numbers, respectively. Using, $S = 1/2$ for electrons,

we obtain after integrating over the spatial part of, Eq. (4.1),

$$H_{\text{ex}} = \frac{1}{2}\sum_{n,m,\sigma}\left\langle n_1 m_1, n_2 m_2 \left| \frac{e^2}{|r_1 - r_2|} \right| n_3 m_3, n_4 m_4 \right\rangle c^\dagger_{n_1 m_1 \sigma_1} c^\dagger_{n_2 m_2 \sigma_2} c_{n_4 m_4 \sigma_2} c_{n_3 m_3 \sigma_1}. \quad (4.3)$$

Equation (4.3) may be broken categorically into different processes which demonstrate different physics of the system.

4.2.1. Hund's coupling

Equation (4.3) with two electrons in different orbitals but on the same ion ($n_1 = n_2 = n_3 = n_4 = n$) can be written as,

$$\begin{aligned} H_H &= \frac{1}{2}\left\langle m_1, m_2 \left| \frac{e^2}{|r_1 - r_2|} \right| m_1, m_2 \right\rangle \sum_{\sigma_1,\sigma_2} c^\dagger_{m_1\sigma_1} c_{m_1\sigma_1} c^\dagger_{m_2\sigma_2} c_{m_2\sigma_2} \\ &\quad -\frac{1}{2}\left\langle m_1, m_2 \left| \frac{e^2}{|r_1 - r_2|} \right| m_2, m_1 \right\rangle \sum_{\sigma_1,\sigma_2} c^\dagger_{m_1\sigma_1} c_{m_1\sigma_2} c^\dagger_{m_2\sigma_2} c_{m_2\sigma_1} \\ &= K^0_{m_1,m_2} n_{m_1} n_{m_2} - 2J^0_{m_1 m_2}\left(\mathbf{S}_{m_1}\cdot\mathbf{S}_{m_2} + \frac{1}{4} n_{m_1} n_{m_2}\right). \end{aligned} \quad (4.4)$$

The first term is the Coulomb interaction with positive $K^0_{m_1 m_2}$ and the second term is the Hund's rule coupling with the value of $J^0_{m_1 m_2}$. The Hund's coupling favors parallel spin arrangement.

4.2.2. Direct exchange interaction

If two ions are assumed to have single orbital, we will have $n_1 = n_4$, $n_2 = n_3$ or $n_1 = n_3$, $n_2 = n_4$. Exchanging the indices n and m in (4.4) we have,

$$\begin{aligned} H_J &= \frac{1}{2}\left\langle n_1, n_2 \left| \frac{e^2}{|r_1 - r_2|} \right| n_1, n_2 \right\rangle \sum_{\sigma_1,\sigma_2} c^\dagger_{n_1\sigma_1} c_{n_1\sigma_1} c^\dagger_{n_2\sigma_2} c_{n_2\sigma_2} \\ &\quad -\frac{1}{2}\left\langle n_1, n_2 \left| \frac{e^2}{|r_1 - r_2|} \right| n_2, n_1 \right\rangle \sum_{\sigma_1,\sigma_2} c^\dagger_{n_1\sigma_1} c_{n_1\sigma_2} c^\dagger_{n_2\sigma_2} c_{n_2]\sigma_1} \\ &= K_{n_1,n_2} n_{n_1} n_{n_2} - 2J_{n_1 n_2}\left(\mathbf{S}_{n_1}\cdot\mathbf{S}_{n_2} + \frac{1}{4} n_{n_1} n_{n_2}\right). \end{aligned} \quad (4.5)$$

Here too we have $K_{n_1 n_2}$ and $J_{n_1 n_2}$ as the Coulomb and exchange integrals terms, respectively. Since this term reflects the exchange of electrons between ions, it is called the direct exchange interaction. In case of electronic structure of ZnO, the value of $J_{n_1 n_2}$ would depend on the overlap of $3d$ orbital from Zn and $2p$ orbital of neighboring oxygens.

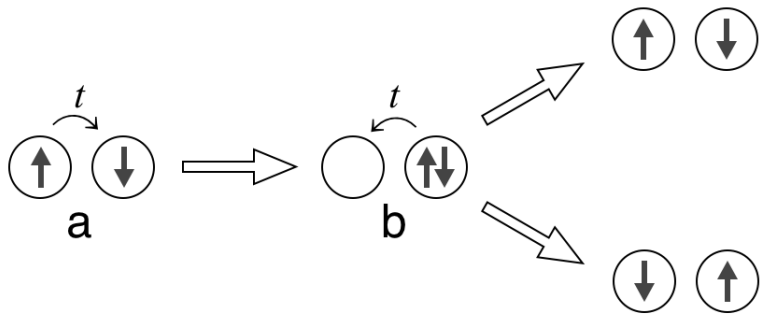

Figure 4.1.: Pictorial representation of superexchange mechanism.

4.2.3. Hubbard interaction.

If we set $n_1 = n_2 = n_3 = n_4 = n$ and $m_1 = m_2 = m_3 = m_4$ in Eq. (4.3), then this would correspond to the electron-electron interaction on the same orbital at the same site. It may be written as;

$$H_U = \frac{1}{2}\sum_{\sigma}\left\langle n,n\left|\frac{e^2}{|r_1-r_2|}\right|n,n\right\rangle c^{\dagger}_{n\sigma}c^{\dagger}_{n-\sigma}c_{n-\sigma}c_{n\sigma} = Un_{n\uparrow}n_{n\downarrow} \tag{4.6}$$

with $n_{n\sigma} = c^{\dagger}_{n\sigma}c_{n\sigma}$, which is the number operator of an electron occupying the site n and orbital σ. Irrespective of all such effects which reduce U, this remains the largest interaction between electrons [75, 76]. The Hubbard interaction causes the antiferromagnetic interactions between ions.

4.2.4. Superexchange interaction

The Hubbard Hamiltonian is given by [75, 76],

$$H = -t\sum_{\langle ij\rangle\sigma}\left(c^{\dagger}_{i\sigma}c_{j\sigma} + \mathrm{h.c}\right) + U\sum_{i} n_{i\uparrow}n_{i\downarrow}, \tag{4.7}$$

where, t is the hopping integral of electron between neighboring sites and $\langle i,j\rangle$ is the sum over sites i and j without double counting. It is assumed in Eq. (4.7) that U is much larger than t.

In the case of half-filling, the number of electrons is the same as the number of ions and the ground state is achieved when each electron is localized on each ion. If the electron moves to the neighboring site, the energy increases by U. As a result of this large energy change, electrons cannot move and the system is insulating. This is famously called the Mott insulators.

Starting with the Mott insulating state and treating t as a perturbation, the second order processes involving t are shown in Fig. 4.1. The intermediate state (Fig. 4.1(b)) has an energy larger by U than the ground state (Fig. 4.1(a)). In the intermediate state the parallel spin configuration is not allowed

because of the Pauli exclusion principle. The energy due to the second order process corresponds to

$$H' = -\sum_{\langle ij \rangle} \sum_{\sigma,\sigma'} \frac{2t^2}{U} c^{\dagger}_{i\sigma'} c_{j\sigma'} c^{\dagger}_{j\sigma} c_{i\sigma}. \tag{4.8}$$

Taking the summation over the spin in Eq. (4.8). Equation (4.8) can be written as,

$$H' = \sum_{\langle i,j \rangle} \frac{4t^2}{U} \left(\mathbf{S}_i \cdot \mathbf{S}_j - \frac{1}{4} \right). \tag{4.9}$$

When half-filled, i.e. $n_i = n_j = 1$, the energy goes to zero for the parallel spin configuration. Hence an electron cannot hop when their spins are parallel. Equation (4.9) favors antiferromagnetic interaction between spins caused by the motion of electrons [77, 78], hence this is called the kinetic exchange interaction. Although it is not easy to calculate the exchange interaction for a given ionic configuration, there exists a rule for the sign of the exchange interaction based on the orthogonality of wave functions. This is called the Kanamori-Goodenough rule [79, 80].

For TM ions on the right hand side of the periodic table e.g., Cu and Ni, the Hubbard model (4.7) is not sufficient and the oxygen $2p$ orbitals must be taken into account. The energy level scheme of cuprates is shown in Fig. 4.2. The $3d(x^2 - y^2)$ orbital of Cu^{2+} has one electron, in spite of the fact that the energy of $3d(x^2 - y^2)$ orbital is lower than the O^{2-} $2p$ orbital, due to the strong Coulomb interaction U. The excitation energy from oxygen to copper is defined as the charge-transfer energy (Δ). The value of Δ for cuprates is of the range of 2$\sim$ 3 eV, which is considerably smaller than U. Insulators where $\Delta < U$ are classified as charge-transfer (CT) insulators [81], and those where $\Delta > U$ is called the Mott-Hubbard (MH) insulators. It is found that for the cuprates CT insulators, the antiferromagnetic exchange interaction between Cu^{2+} is proportional to fourth order of the hopping integral and the effective exchange is of the form,

$$J = \frac{4t_{pd}^4}{\Delta^2} \left(\frac{1}{\Delta} + \frac{1}{U} \right). \tag{4.10}$$

4.2.5. Double-exchange interaction

Most of the transition metal oxides are in the mixed valence states and exhibit metallic properties. In 1950, Jonker and van Santen [82] prepared mixed crystals of $La_{1-x}Ca_x(Mn^{+3}_{1-x}, Mn^{4+}_x)O_3$ and studied the metallic ferromagnetic state which occurred in the range of $0.2 < x < 0.4$. It is known that $LaMnO_3$ and $CaMnO_3$ are antiferromagnetic insulators. There were several theoretical attempts to explain the properties, notable of them is are Zener [83], Anderson and Hasegawa [84, 85] and de Gennes [86], who examined the relation between ferromagnetism and their metallic behavior.

Let us consider as an example the complex $La_{1-x}Ca_x(Mn^{+3}_{1-x}Mn^{+4}_x)O_3$, where three $3d$ electrons are in the the t_{2g} states of the Mn^{4+} and Mn^{3+} each and one electron in the e_g state. The spins of these

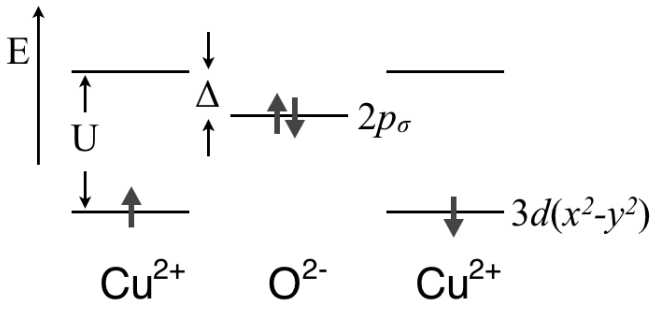

Figure 4.2.: The energy level scheme of Cu^{2+} and O^{2-} ions in cuprates. Arrows denotes electron spins.

electrons are parallel to each other because of the Hund's coupling. Supposing that Mn^{3+} and Mn^{4+} are neighboring ions, it is possible that an e_g electron on the Mn^{3+} can move to an empty e_g state of the Mn^{4+} ion and as a result the valence of the ions is exchanged. Since the electron hopping depends on the spin states, it can be understood that the motion of electrons is allowed only in the ferromagnetic state. In other words ferromagnetism often occurs in metals. This type of phenomena is called the double-exchange interaction Zener [83].

4.3. Exchange mechanism in DMS

Generally the magnetic interaction are outcome of complicated interplay of the spin-degrees of freedom, the Coulomb energy, and the kinetic energy. In most cases a phenomenological understanding sheds more light, although more realistic approach to study the material-specific properties is by studying the electronic structure of a system by incorporating interactions together. This can be done through the first-principles methods, like the DFT. It is a hard task to filter the phenomenological classification form the output of DFT calculations, some of them have been attempted and presented well for the TM doped III-V semiconductors by Dederichs *et al.* [87, 88].

5. Electronic properties of ZnO

5.1. Introduction

The first task to understand a material is to study its crystal structure. Zinc oxide is a wide band gap semiconductor which crystallizes in wurtzite crystal structure (B4) under ambient conditions where each ions of the other type. Due to the large electronegative difference between Zn and O, ZnO is treated as ionic semiconductor. There are other crystal structures found in ZnO, namely zinc blende (B3) and rock salt (B1), where B1, B3 and B4 are the nomenclature of the crystal lattice in the *strukturbericht* reports. The B1, B3 and B4 crystal lattices consist of one, one and two units of ZnO in their primitive cell, respectively. The zinc blende structure has been observed when ZnO is grown on cubic substrates. The rock salt phase is stable only at very high pressure. Both zinc blende and wurtzite structures are tetrahedrally coordinated with 4 nearest neighbors and 12 next-nearest neighbors, hence the electronic structure of both structures is similar with similar bond lengths. Quoting Wyckoff, *no clear distinction can be drawn between the types of compounds which crystallize with the ZnO (B4) and ZnS (B3) structures. The two arrangements are so much alike in their spatial distribution that one would not expect important energy difference between them. It is therefore not surprising to find that a number of compounds appear in both structures.* There is a pattern between these two close lying structures. The wurtzite structure consists of triangularly arranged alternating bi-atomic close-packed planes in the stacking sequence of AaBbAaBb... along the [0001] direction. On the other hand, the zinc blende structure consists of AaBbCcAaBbCc... stacking sequence along the [111] direction. In fact, there has been experimental observation of biphase crystal structure in GaN nanowire where the inner is wurtzite phase and outer is zinc blende phase with sharp transition of 1 – 3 atomic layers [89]. A similar situation can be expected for ZnO, although this has not been observed in experiments yet. Almost all the studies in the present thesis are done for the wurtzite structure of ZnO.

Wurtzite crystal structure is a derived name from the mineral wurtzite ((Zn,Fe)S) which is named after the chemist Charles-Adolphe Wurtz. The crystal structure is characterized by sublattice of two individual atom types in a hexagonal closed pack structure. The wurtzite structure is non-centrosymmetric (i.e., lacks inversion symmetry) and hence generally have properties such as piezoelectricity and py-

roelectricity. The atomic structure is given in terms of lattice vectors,

$$\begin{aligned} \mathbf{A}_1 &= \frac{1}{2}aX - \frac{\sqrt{3}}{2}aY \\ \mathbf{A}_2 &= \frac{1}{2}aX + \frac{\sqrt{3}}{2}aY \\ \mathbf{A}_3 &= cX \end{aligned} \tag{5.1}$$

and the basis vectors given in terms of lattice vectors (known as direct coordinates) is

$$\begin{aligned} \mathbf{B}_1 &= \frac{1}{3}\mathbf{A}_1 + \frac{2}{3}\mathbf{A}_2 \\ \mathbf{B}_2 &= \frac{2}{3}\mathbf{A}_1 + \frac{1}{3}\mathbf{A}_2 + \frac{1}{2}\mathbf{A}_3 \\ \mathbf{B}_3 &= \frac{1}{3}\mathbf{A}_1 + \frac{2}{3}\mathbf{A}_2 + u\mathbf{A}_3 \\ \mathbf{B}_4 &= \frac{2}{3}\mathbf{A}_1 + \frac{1}{3}\mathbf{A}_2 + \left(\frac{1}{2} + u\right)\mathbf{A}_3 \end{aligned} \tag{5.2}$$

Here, a and c are two independent lattice parameters, X, Y and Z are the components of the Cartesian coordinate system. The wurtzite crystal symmetry is identified with number 186 in the list of 230 Bravais lattices according to the nomenclature adopted by international standards. The basis atoms occupy the positions obeying the 2b point group symmetry with $\mathbf{B}_1, \mathbf{B}_2$ occupied by one type of atoms and $\mathbf{B}_3, \mathbf{B}_4$ occupied by the other type.

The electronic structure properties and the crystal structure of ZnO have been intensively studied - mostly within DFT methods, however, the studies presented in this thesis are more oriented towards the magnetic properties of ZnO based DMS. It is therefore quite necessary to understand the electronic properties of pure ZnO from various approximations and theoretical approaches. Most of the studies are based on the local density approximation (LDA). LDA is a traditional approximation in DFT, where the exchange correlation function is derived from the homogeneous electron gas (HEG) at that particular value of charge density. Including gradient corrections in addition to LDA lead to the generalized gradient approximation (GGA). Hitherto in all discussions the basic exchange-correlation treatment is GGA and it will be shown that additional improvements on GGA is necessary and has been studied. Since the wurtzite crystal structure contains three parameters, a, c/a and u, a straight forward energy minimization with respect to the lattice parameters cannot be realized. Thus we began by looking at the energy for various c/a for each a. For each such set of a and c/a, the lattice was relaxed with conjugate gradient algorithm to minimize the local strain and thus a suitable u parameter was achieved. The variation of a versus c/a is shown in Fig. 5.1 (left) and the value of u obtained corresponding to the c/a obtained for each a is shown in Fig. 5.1 (right). The calculations are done by Vienna *ab-initio* simulation package (VASP) [92, 93] using the PW91 parameterization for the GGA

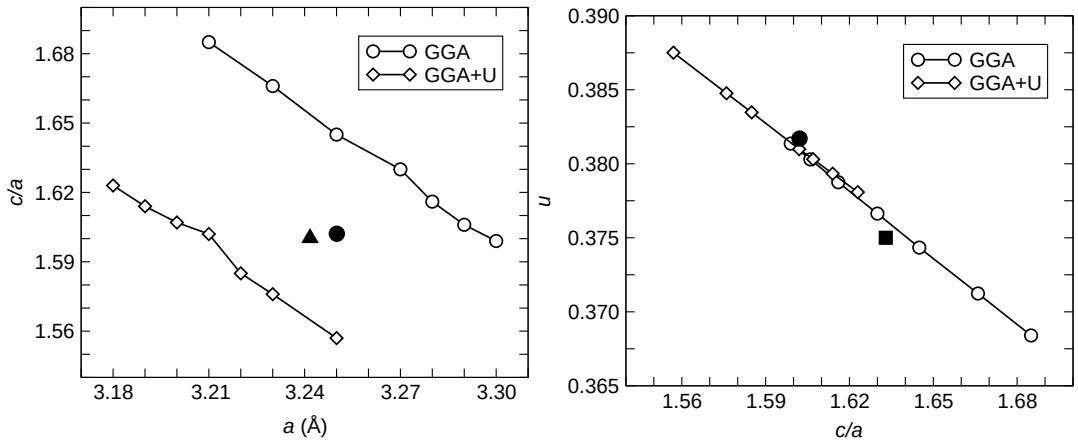

Figure 5.1.: (left) Comparison of minimum energy lattice parameters a and c/a of ZnO for GGA and GGA+U ($(U-J)$ on the Zn d-orbital with 7.5 eV). The experimental values are given by the filled circle [90] and filled up-triangle [91]. (right) The value of u obtained by relaxing the lattice for various c/a at optimized a optimized obtained from GGA and GGA+U. The filled circle shows the experimental value [90], while the filled square shows the perfect value of u= 0.375 and $c/a = \sqrt{8/3}$.

Table 5.1.: Lattice parameters of wurtzite ZnO from different sources. GGA-PW91 [94] and GGA-PBE [101] are two flavor of GGA, U is the on-site correlation term, HSE06 is the screened hybrid-functional [102] (post GGA treatment is discussed below).

a (Å)	c/a	u	Remark
3.2495	1.6024	0.345	Data book [103]
3.27	1.608	0.345	KKR-LDA [104]
3.290	1.606	0.380	GGA-PW91 (present calculation)
3.30	1.603	0.381	GGA-PBE (present calculation)
3.28	1.61	0.38	GGA-PBE [105]
3.190	1.614	0.379	GGA+U (present calculation, U_d = 7.5 eV)
3.23	1.622	0.38	HSE06, $\alpha = 0.36$ [105]
3.246	1.604	0.382	Neutron diffraction expt. [90]
3.253	1.603	0.382	X-ray diffraction expt. [106]

functional [94]. Some of the values of lattice parameters are tabulated in Table 5.1.

The band structure of ZnO obtained from GGA is shown in Fig. 5.2. The electronic description of ZnO within GGA has few drawbacks. They are;

1. The band gap values calculated from GGA is significantly lower than the band gap obtained from experiments. The band gap of ZnO is 3.44 eV in experiments, however in DFT-GGA cal-

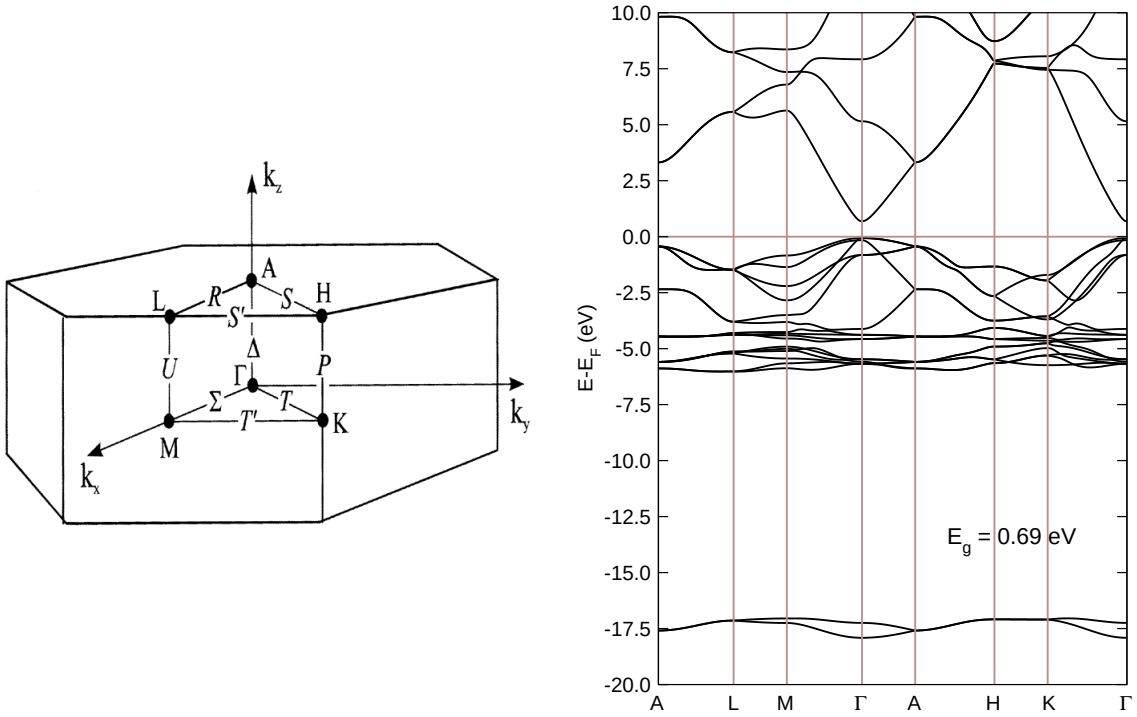

Figure 5.2.: (left) The Brillouin zone of wurtzite crystal structure. (right) The band structure obtained with GGA. The PW91 parameterization of GGA is used. There are several drawbacks in the calculated band structure as compared to the status in experiments, these are discussed in the text.

culation this amounts to be 0.69 eV. Due to variation of lattice parameters adopted in literature, slight variation in band gap are reported in literature.

2. The degree of charge transfer and hence the ionicity of ZnO is not accounted properly by GGA. Zn is a charge donor and O is a charge acceptor and analytic ZnO id written with expressions $Zn^{+(2-\delta)}O^{-(2-\delta)}$. Since ZnO is strongly ionic, hence the value of δ is small in real materials. However, from the Bader charge analysis [95] of the charge density obtained from GGA we find that δ = 0.75. This is a large value and this shows that GGA overestimates the covalency of the Zn–O chemical bond in ZnO.

3. The location of Zn d-bands below the Fermi energy is not correctly described by DFT-GGA. This is because there is spurious hybridization of Zn d-orbitals with O p-orbitals.

4. GGA also gives low estimations of the Bulk modulus for ZnO. The theoretical calculated value of bulk modulus is between 126.73 GPa [96] and 131.5 GPa [97], while the value reported from experiments lie between 142.6(2) GPa [98], 181 GPa and 183(7) GPa [99]. In the present calculation it was found to be 131.895 GPa in GGA and 132.078 GPa in GGA+U calculations. These values agree well with values reported by Jeffe *et al.* [100]. Since structural properties

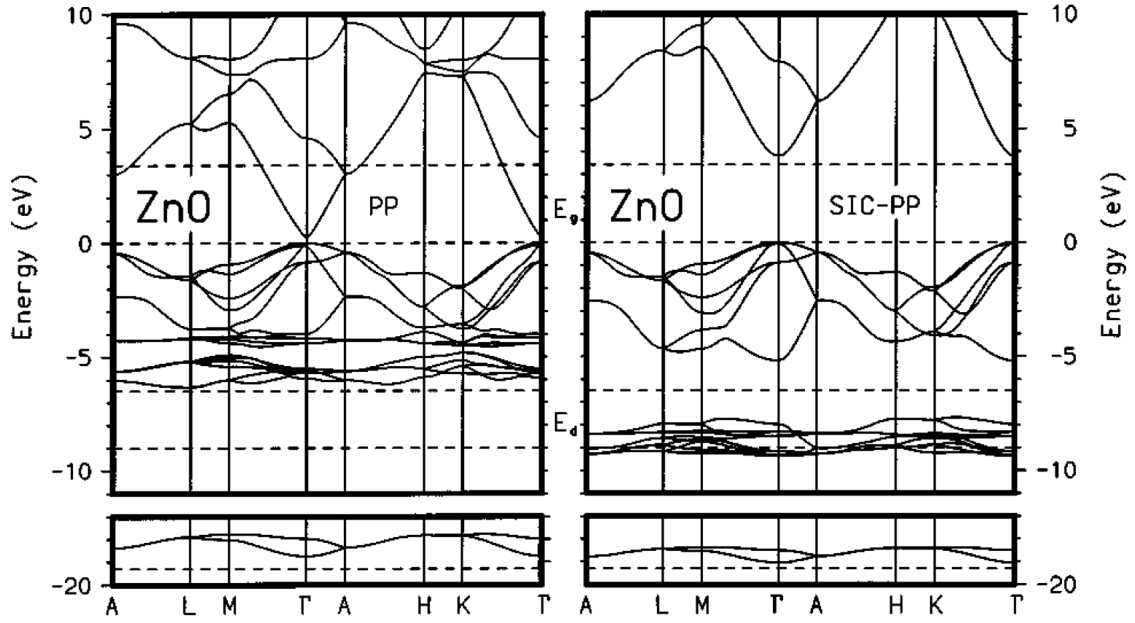

Figure 5.3.: Comparison of ZnO band structure calculated with LDA (left) and LDA+SIC (right) in DFT. The figure is adapted from Vogel *et al.* in Ref. [107].

like bond length and bulk modulus need accurate electronic structure description, hence the failure of GGA is directly reflected in the structural property.

5.2. Self-interaction correction in DFT

One of the early corrections used to circumvent the GGA failures is the self-interaction correction (SIC) method proposed by Perdew *et al.* [108].

The comparison of band structure of ZnO calculated with LDA and LDA+SIC is shown in Fig. (5.3). One finds a clear improvement in the band structure of LDA+SIC as compared to LDA. To summarize, the Zn d-band shifts to lower energy and is now placed at energy which is in good agreement with experiments (shown as dotted line). The band gap improves to almost the experimentally observed band gap (shown as dotted line). The valence band near the Fermi level consists mostly of O p-bands. The report on SIC correction by Vogel *et al.* predicts the Zn d-orbital to be placed averagely about 8.5 eV below the Fermi energy, while Maznichenko *et al.* [109] reports the location of the Zn d-orbital at around 11 eV below the Fermi energy, as shown in the DOS of Fig. 5.4. The experimental report on the location of Zn $3d$ states varies from 7.5 ± 0.2 eV to 8.8 eV below the valence band maxima [110–115].

Even after such improved electronic structure calculations by SIC, it has not been very popular because the practical implementation of the SIC-DFT is more complicated despite its apparent simplicity [116]. Moreover, SIC-DFT do not fit into the standard Kohn-Sham procedure because the SIC-DFT

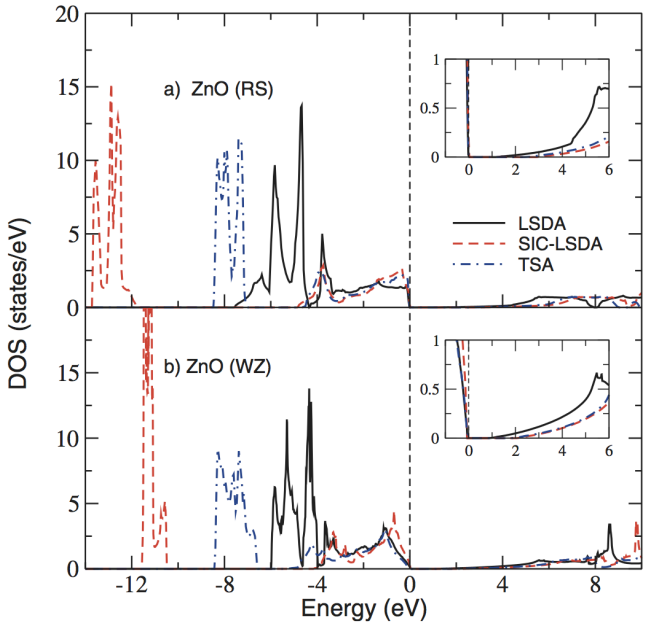

Figure 5.4.: Comparison of ZnO density of states as calculated with LDA and LDA+SIC in DFT for rock salt (top) and for wurtzite structure (bottom). The figure is adapted from Maznichenko *et al.* in Ref. [109]. One must compare the blue dashed dot and the red dashed lines of the wurtzite ZnO (bottom) with that of the band structure of Fig. 5.3.

potential is orbital-dependent and the energy functional is not invariant under unitary transformations in the orbitals.

5.3. Hubbard-U in electronic structure calculations

We now know that the exchange and correlation functionals like the LDA and GGA are built from a homogeneous electron gas and so the interactions are treated in a mean field fashion which is not accurate enough to properly describe the strong correlated phenomena. In analytical theory these systems (Mott insulators and strongly correlated materials in general) are treated with model Hamiltonians, like the Mott-Hubbard model or the Anderson impurity model, in which the bandwidth (related to the hopping) and the electronic correlations are explicitly considered. This allows us to take into account the behavior of the system in different regime in parametric form. A number of methods has been presented which attempt to link the model Hamiltonians into the frame work of *ab initio* electronic structure calculations. The main idea is to use effectively the physics from many body formalism and correct the defects of DFT.

One of the methods is the LDA (GGA) + U method. The LDA+U is used to account for the strong electronic correlation within the LDA through the addition of Hubbard-like Hamiltonian to describe the on-site interactions. The energy now depends on the site specific electron occupancy n. The

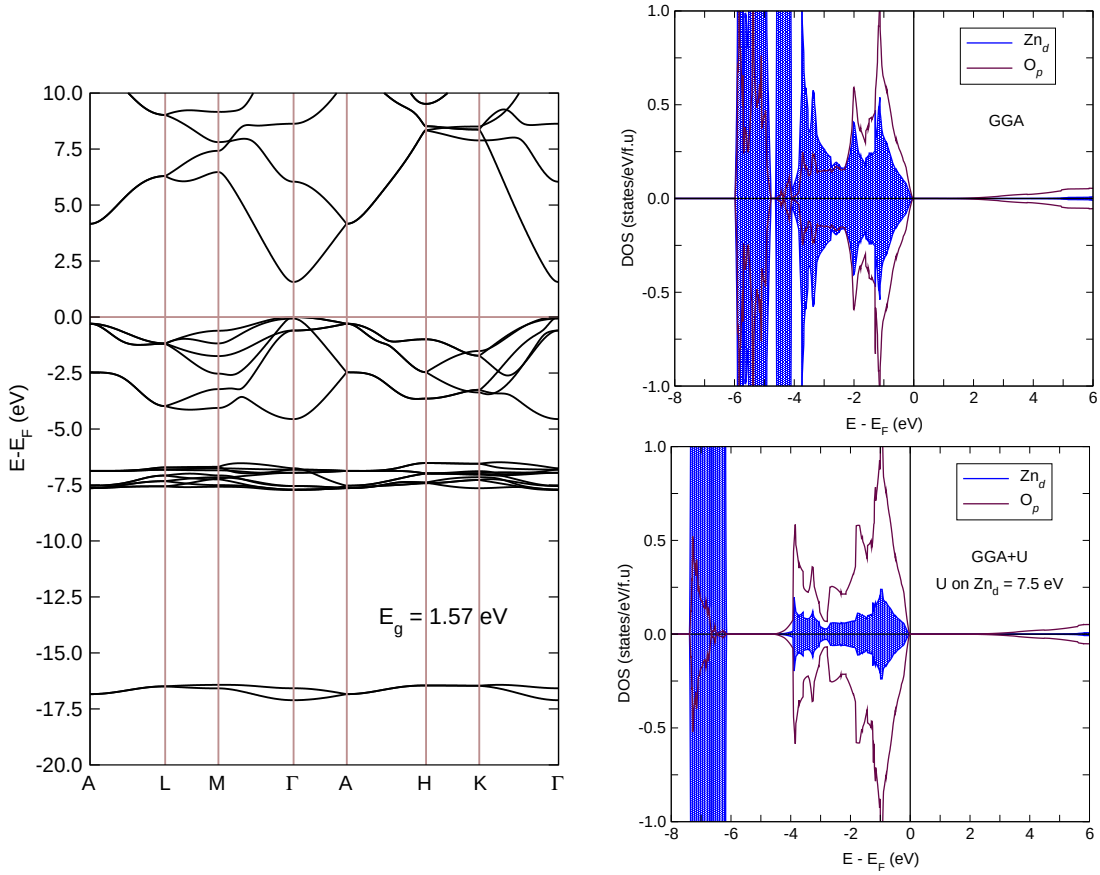

Figure 5.5.: (left) The band structure of ZnO in GGA+U with the value of U on Zn d-orbital with 7.5 eV. One observes an increase in band gap with 1.57 eV. The value is almost 50% to that of the experimental band gap. (right) Partial DOS with Zn d- and O p- orbital contribution as estimated in GGA (up) and GGA+U (down).

first expression of the LDA+U approach was formulated by Anisimov *et al.* [117–119] and was later developed by several groups [120–122]. The rotationally invariant form of LDA+U, which is more popular in use because of simplicity, was developed by Liechtenstein *et al.* [122] and Dudarev *et al.* [123]. The energy functional can be written as:

$$E_{LDA+U} = E_{LDA}[n^{\sigma}] + E_U\left[\{n^{\sigma}_{ii'}\}\right] \tag{5.3}$$

where, n^{σ} is the charge density associated with spin σ and $n^{\sigma}_{ii'}$ is the density matrix for the correlated electron with i and i' as the orbital indices on which the on-site correlation U is added. Following the rotationally invariant approach of Dudarev *et al.*, we can write the energy functionals as [123],

$$E_{DFT+U} = E_{DFT} + \frac{(U-J)}{2}\sum_{\sigma}\left[\left(\sum_{i} n^{\sigma}_{ii}\right) - \left(\sum_{ii'} n^{\sigma}_{ii'} n^{\sigma}_{i'i}\right)\right] \tag{5.4}$$

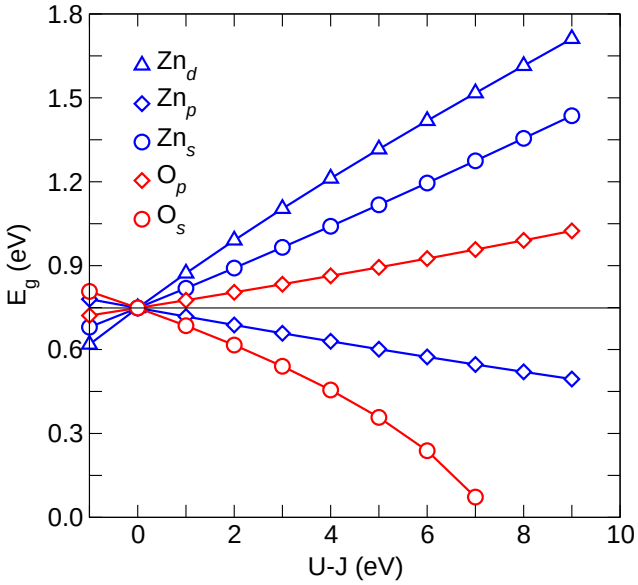

Figure 5.6.: The role of U on different orbitals on Zn and O atoms in ZnO and its influence on the band gap. One finds almost linear relationship with notable change in behavior for the case of O s and Zn p-orbitals as compared to other orbitals.

where U is the on-site correlation and J is the intra atomic exchange term. In the above form, however, the U and J are not treated individually and the effect of U is through effective $(U-J)$. One can also extract the potential from the energy expression above, as;

$$V_{ij}^{\sigma} = \frac{\partial E\left[\rho^{\sigma}\right]}{\partial n_{ij}} + (U-J)\left[\frac{1}{2} - {n_j}^{\sigma}\right] = V_{\mathrm{LDA}} + (U-J)\left[\frac{1}{2} - {n_j}^{\sigma}\right] \tag{5.5}$$

From the above expression it is clear that occupation of Hubbard-orbital with value more than 0.5 leads to attractive potential, while the occupation below 0.5 leads to repulsive potential. As a gap of width $\approx (U-J)$ opens between occupied ($n_j = 1$) and unoccupied ($n_j = 0$) orbitals.

The band structure of ZnO obtained from GGA+U formalism is shown in Fig. 5.5 (left) where a value of 7.5 eV U is applied on the Zn d-orbital. This is to be compared with the band structure obtained from GGA of Fig. 5.2. We find that as expected from the physics of the Hubbard model, the d-bands are shifted below the Fermi level. The location of Zn d-bands now match the experimental report [110]. However, the improvement of the band gap to 1.57 eV is still an underestimation of almost 50% of the experimental band gap. A more clear understanding of the hybridization scenario is depicted in the comparison of the DOS of GGA and GGA+U in the Fig. 5.5 (right) in top and bottom panel respectively. The DOS is plotted for O p-orbitals and Zn d-orbitals and compared with GGA and GGA+U with $U = U_{\mathrm{Zn}_d} = 7.5$ eV. We find that the Zn d-orbitals which hybridized with those of O p-orbitals resulting in delocalization in GGA has been recovered to more localized state with reduced band width.

The effect on the size of the band gap with U on different orbitals of ZnO is shown in the figure (5.6). We find that for all the orbitals the relationship of U and E_g is almost linear. While U on Zn d, Zn s and O s lead to positive slope, allowing for increasing the bandgap with increasing U, the Zn p and O s orbitals behave contrary. In fact O-s and Zn-p lie far away from the Fermi energy as bonding and anti-bonding levels with completely filled and completely empty states. Thus this should not influence the gap at all. The influence with U on these orbitals is only through an effective hybridization of orbitals.

We find that the adding Hubbard U correction can lead an improvement of the band gap for the strongly correlated materials, however there is no contribution to the exchange potential, which is still given by the LDA (GGA) functional. One could imagine two drawbacks in the formalism of LDA+U as presented above. First is that it neglects non-spherical contribution of U, which could be of importance for anisotropic hybridization. Since a thorough comparison with respect to wave-function based methods has not been attempted so for (as per my knowledge), hence it is difficult to conclude how serious this error could be. Second drawback of the method is that there is no attempt to improve the exchange potential, which is still expressed in relation to the HEG. There are other derivations leading to formulation independent of basis set where the expression of E_{Hubb} and E_{dc} are more general [121, 122], but these studies has not been taken up in present work.

5.4. Hybrid functionals in DFT

In order to obtain a better description of electronic structure, we have to go beyond the electron gas approximation used to model electron-electron interactions. One way to introduce such a correction is the Hartree-Fock (HF) approach which is based on the use of Slater determinants (built from atomic orbital) to represent the many body wave function. Although the Kohn-Sham DFT provides orbitals from which a Fock integral or “exact" exchange energy may be constructed, this method results in un-physically too large coupling due to the absence of screening.

Density functional approximations $E_{\rm xc}^{\rm GGA}$ (based on GGA) can be decomposed as,

$$E_{{\rm xc},\lambda}^{\rm GGA} = \langle \Psi_\lambda | \hat{V}_{ee} | \Psi_\lambda \rangle - \frac{e^2}{2} \int d^3r \int d^3r' \frac{\rho(\mathbf{r})\rho(\mathbf{r}')}{|\mathbf{r}-\mathbf{r}'|}, \tag{5.6}$$

such that,

$$E_{\rm xc}^{\rm GGA} = \int_0^1 d\lambda E_{{\rm xc},\lambda}^{\rm GGA}. \tag{5.7}$$

, Here, the λ^{-1} times the potential energy of exchange and correlation for electron-electron interaction is given by $\lambda e^2/|\mathbf{r}-\mathbf{r}'|$ and $v_\lambda(\mathbf{r})$ is adjusted to hold the electron density $\rho(\mathbf{r})$ fixed at its physical $\lambda = 1$ value. Ψ_λ is the ground state wave function of the system. At $\lambda = 0$ we recover the Kohn-Sham result for noninteracting system.

This allows us to define $E_{\mathrm{x}}^{\mathrm{GGA}} = E_{\mathrm{xc},\lambda=0}^{\mathrm{GGA}}$ and $E_{\mathrm{c}}^{\mathrm{GGA}} = E_{\mathrm{xc}}^{\mathrm{GGA}} - E_{\mathrm{x}}^{\mathrm{GGA}}$ and from them we can construct the hybrid coupling-constant dependence of exchange-correlation energy as,

$$E_{\mathrm{xc},\lambda}^{\mathrm{hyb}}(n) = E_{\mathrm{xc},\lambda}^{\mathrm{GGA}} + (E_{\mathrm{x}} - E_{\mathrm{x}}^{\mathrm{GGA}})(1-\lambda)^{n-1}. \tag{5.8}$$

Equation (5.8) reduces to the exact E_{x} at $\lambda = 0$ and to $E_{\mathrm{xc},\lambda}^{\mathrm{GGA}}$ at $\lambda = 1$. The integer n describes how rapidly the correction to GGA vanishes as $\lambda \to 1$. Thus we have

$$E_{\mathrm{xc}}^{\mathrm{hyb}} = \int_0^1 d\lambda E_{\mathrm{xc},\lambda}^{\mathrm{GGA}} + \frac{1}{n}\left(E_{\mathrm{x}} - E_{\mathrm{x}}^{\mathrm{GGA}}\right). \tag{5.9}$$

The optimum value of n is the lowest order of the perturbation theory which provides a realistic description of the λ-dependence of the exact $E_{\mathrm{xc},\lambda}$,

$$E_{\mathrm{xc},\lambda} \approx \int_0^1 e^2(c_0 + c_1\lambda + \cdots + c_{n-1}\lambda^{n-1}) \quad (0 \leqslant \lambda \leqslant 1). \tag{5.10}$$

This choice maximizes the similarity of $E_{\mathrm{xc},\lambda}^{\mathrm{hyb}}$ to $E_{\mathrm{xc},\lambda}^{\mathrm{GGA}}$ near $\lambda = 1$ at the same time ensuring that no unnecessary powers of λ are introduced into Eq. (5.8). In other words, it is assumed that $E_{\mathrm{xc},\lambda}^{\mathrm{hyb}}$ and $E_{\mathrm{xc},\lambda}^{\mathrm{GGA}}$ can be fitted accurately by the polynomial of Eq. (5.11) with an index n not higher than those needed for an accurate representation of the exact $E_{\mathrm{xc},\lambda}$

The hybrid potentials described above are named as PBE0 hybrid-functionals in credit to their developers, namely, J. P. Perdew, M. Ernzerhof and K. Burke [124]. The value of $n = 4$ has been shown to give reliable values for the atomization energies of typical molecules [124]. Thus PBE0 hybrid-functionals is constructed by mixing 25% Fock exchange with 75% of the PBE exchange [101] (one of the formulations for GGA). The electron correlation is represented by the correlation part of the PBE density functional. The resulting expression for exchange-correlation energy thus takes the form as:

$$E_{\mathrm{xc}}^{\mathrm{PBE0}} = \frac{1}{4}E_{\mathrm{x}} + \frac{3}{4}E_{\mathrm{x}}^{\mathrm{GGA}} + E_{\mathrm{c}}^{\mathrm{GGA}}. \tag{5.11}$$

A general expression can be written as

$$E_{\mathrm{xc}}^{\mathrm{PBE0}} = \alpha E_{\mathrm{x}} + (1-\alpha)E_{\mathrm{x}}^{\mathrm{GGA}} + E_{\mathrm{c}}^{\mathrm{GGA}}, \tag{5.12}$$

where, α is the fraction of exact-exchange used in the calculation.

PBE0 hybrid-functional has been in focus since its development and the description of finite systems have been mostly studied [125, 126]. The improvement with respect to traditional GGA calculations is attributed to the use of some portion of the Fock exchange which reduces the self-interaction error of the usual density functional. While for molecular systems the advantage of PBE0-functionals are apparent, however, under periodic boundary conditions for describing the bulk, its application within

real space formalism is prohibitive because of the slow convergence of the exchange interaction with distance.

5.5. Screened hybrid-functionals in DFT

To avoid the calculations of the integrals over the slowly decaying long-ranged part of the Fock exchange, Heyd *et al.* [102] have proposed to replace it by corresponding density functional. They have suggested to separate the exchange part of the electron-electron interaction into short range (sr) and long range (lr) part. The correlation part is still given by the correlation of the PBE density functional. The decomposition of Coulomb kernel can be obtained by using the following construction:

$$\begin{aligned} \frac{1}{r} &= S_\omega(r) + L_\omega(r) \\ &= \frac{\mathrm{erfc}(\omega r)}{r} + \frac{\mathrm{erf}(\omega r)}{r} \end{aligned} \tag{5.13}$$

where, $r = |\mathbf{r} - \mathbf{r}'|$ and ω is the parameter which defines the range of separation related to a characteristic distance $(2/\omega)$ at which the short-range interactions are treated as negligible. Here, $\mathrm{erf}(x)$ and $\mathrm{erfc}(x)$ are the error function and contemporary error function, respectively, given by;

$$\mathrm{erf}(x) = \frac{2}{\sqrt{\pi}} \int_0^x e^{-t^2} dt$$

and,

$$\begin{aligned} \mathrm{erfc}(x) &= 1 - \mathrm{erf}(x) \\ &= \frac{2}{\sqrt{\pi}} \int_x^\infty e^{-t^2} dt. \end{aligned}$$

It has been empirically established that the optimum value of range-separation parameter ω is approximately 0.3 Å^{-1} [102]. Paier *et al.* have reported the implementation of screened HSE03 hybrid-functionals in VASP [127]. Subsequent to their report, they have come up with an erratum [128] pointing out that the screened parameter ω had missed a conversion factor from Ångström to Bohr units. In addition Krukau *et al.* [129] have identified that the correct value of ω appearing in the correct implementation of the HSE functional is $\omega = 0.207$ Å instead of the earlier suggested value of $\omega = 0.3$ Å. To avoid any confusion, Krukau have proposed to maintain the name HSE03 to designate the earlier incoherent value of ω, while the correct implementation with $\omega = 0.207$ Å is called HSE06 functional. The bandgap of common insulators obtained from HSE03 hybrid-functional is shown in Fig. 5.10 (left). It has been shown that the lattice parameters, atomization energies and molecular thermochemistry vary only little when the screening parameter is changed from 0.3 to 0.207 Å, however, variation of the screening parameter influences solid band gaps the most. Although for ZnO the hybrid-functionals do give an improvement in bandgap, we find that the value of α = 0.25 as predicted

by the perturbation theory is not sufficient. One has to increase value of α to still higher values to obtain the bandgap of ZnO. The difference between ω of three hybrid-functionals, the default α from the perturbation theory, the estimation of the band gap with the default value and the the corrected α to obtain the experimental band gap of ZnO is tabulated in Table 5.2.

Table 5.2.: Table showing the hybrid-functional, the corresponding value of screening length (ω), the value of α as predicted, the estimate of band gap for ZnO and the value of α that is fit to obtain the experimental band gap for ZnO.

Functional	ω (Å^{-1})	α (theory [54])	E_g at α (theory)	α ($E_g^{\text{expt.}}$ of ZnO)
PBE0	0.00	0.25	3.135	0.276
HSE06	0.207	0.25	2.431	0.383
HSE03	0.30	0.25	2.179	0.449

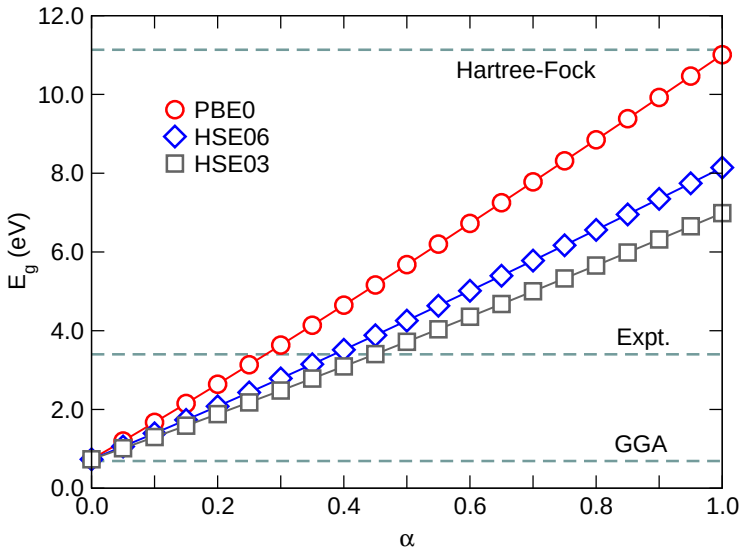

Figure 5.7.: The value of E_g obtained for different HF-exchange weight α in various hybrid-functionals. One finds a linear relation. The value of E_g obtained from GGA, the experimental value and that predicted by pure HF-exchange without and correlation effects are shown for comparison as the dashed horizontal lines.

Since α can be treated as a parameter, one is curious to see the change in bandgap with the change in α for the three hybrid-functionals. The plot in Fig. 5.7 shows the change in E_g with increase in α. We find that the change is linear with different slope (m) for the three functionals in the order $m_{\text{PBE0}} > m_{\text{HSE06}} > m_{\text{HSE03}}$. The experimental value of bandgap (3.4 eV) and the GGA value of the band gap (0.69 eV) is shown as horizontal dashed line. The bandgap obtained from pure Hartree-Fock exchange calculation, which includes no correlation effects, is observed to be too high at 11.13 eV. This gives an impression of the importance of correlation effects in calculations of bulk solids. The

band structure obtained by HSE06 at the default α (= 0.25) and at α fitted to the bandgap of ZnO (= 0.383) is shown in the left and the middle plots of Fig. (5.8), respectively. One finds that the Zn d-orbitals, although do not hybridize spuriously with the O p-orbital, but these energy location below the Fermi energy may be treated with caution.

5.6. Hybrid functional + U approach

It is clear by now that DFT is an exact theory and the only approximation used is in treating the exchange-correlation functionals. The traditional exchange-correlation functionals has drawbacks in describing the semiconductor properties and also cannot deal with the strong correlation effects. There has been attempts to add correlation corrections through Hubbard U with no exchange corrections at one end of the spectrum and treating with hybrid-functionals to correct the exchange functionals without any correction to the correlation part (above GGA correlation) at the other end of the spectrum. Both the corrections individually faced with limitations which has been discussed in previous section.

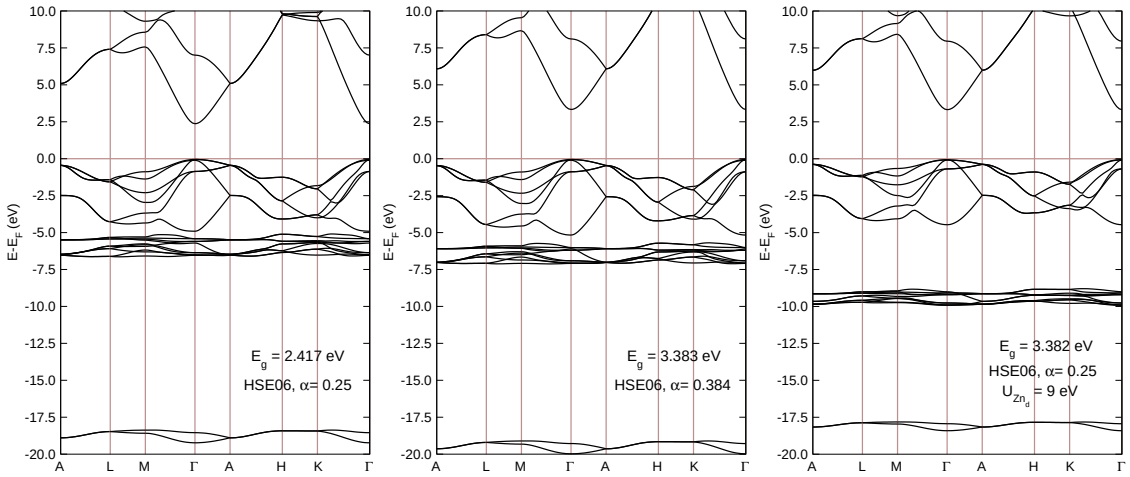

Figure 5.8.: A comparison of band structures obtained from HSE06 functional with different values of α and U. Left: α = 0.25. Center: α = 0.384 to fit the experimental E_g (center). Right: α = 0.25 with addition of U on Zn d-orbital. The band structure on the right can be corroborated to the DOS obtained from SIC-LDA as shown in Fig. 5.3 [109].

It is intriguing and also relatively straight forward at this stage to mix the two corrections i.e., the hybrid-functional correction plus Hubbard U to compensate for their individual drawbacks. Here we stick to the value of α = 0.25 which is predicted from the perturbation theory [54] and change the value of Hubbard U on the Zn d-orbitals. The resulting plot is shown in Fig. 5.9. We find that with no Hubbard U correction the band gap is below the experimental band gap. With addition of U the bandgap changes almost linearly for all the three hybrid-functionals. The slope of the change is almost similar resulting in parallel lines.

The band structure plot of HSE06 with α = 0.25 and U on Zn d-orbital with value of 10 eV is shown

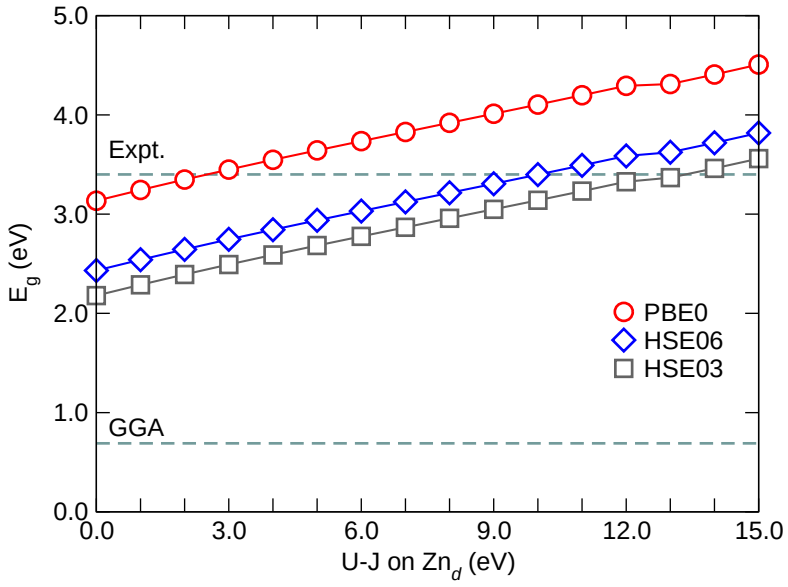

Figure 5.9.: The value of E_g obtained from various hybrid-functionals with default α = 0.25 together with changing the value of Hubbard U on the Zn d-orbital.

in the right plot of Fig. 5.8. The band structure is now quite satisfying. The band structure matches quite well with the SIC-corrected band structure of Vogel *et al.* as shown in Fig. 5.3. This can be the starting point is more careful selection of parameters for studying electronic structure of ZnO.

5.7. The GW method

There is no justification to interprete the unoccupied states from the DFT calculations as quasiparticle energies. Steiner *et al* have demonstrated including self-energy correction to the LDA gives significantly better quasiparticle properties, like the effective mass, exchange splitting and X-ray photoelectron spectra (XPS) without affecting the ground state properties for $3d$ TM ferromagnet [130]. A widely used approach to quasiparticle energies and the spectral function is the many-body perturbation theory, popularly called the GW method [131–134]. Since the GW method is a perturbative theory, the results often depend on the choice of exchange-correlation functionals used as the starting potential. Some of the results comparing different methods are presented in Ref. [135]. In this method the quasiparticle energies ($E^{\mathrm{QP}}_{n,\vec{k}}$) are extracted from the equations [136],

$$\left(T + V_{\mathrm{ne}} + V_{\mathrm{H}} - E^{\mathrm{QP}}_{n,\vec{k}}\right) \Psi_{n,\vec{k}}(\vec{r}) + \int d^3r' \Sigma \left(\vec{r}, \vec{r}', E^{\mathrm{QP}}_{n,\vec{k}}\right) \Psi_{n,\vec{k}}(\vec{r}') = 0 \tag{5.14}$$

where, T, V_{ne} and V_{H} is the kinetic energy operator, the potential of the nuclei and the Hartree potential, respectively. The self-energy operator Σ is given by,

$$\Sigma(\vec{r},\vec{r}',\omega) = \frac{i}{4\pi}\int_{\infty}^{\infty} e^{i\omega'\delta} G(\vec{r},\vec{r}',\omega+\omega')W(\vec{r},\vec{r}',\omega')d\omega' \tag{5.15}$$

where G is the Green's function, and W is the screened Coulomb interaction of the electrons. The GW method includes many-body effects in the electron-electron interaction through the dynamical screening of the exchange operator with the frequency dependent dielectric matrix of the system and thus goes beyond the mean-field approximation for independent particles. The GW method is computationally very demanding, hence often it is treated with approximations for the dynamical effects through the plasmon-pole model and/or replacing the quasi-particle eigenfunctions $\Psi^{\mathrm{QP}}_{n,\vec{k}}$ by LDA counterparts.

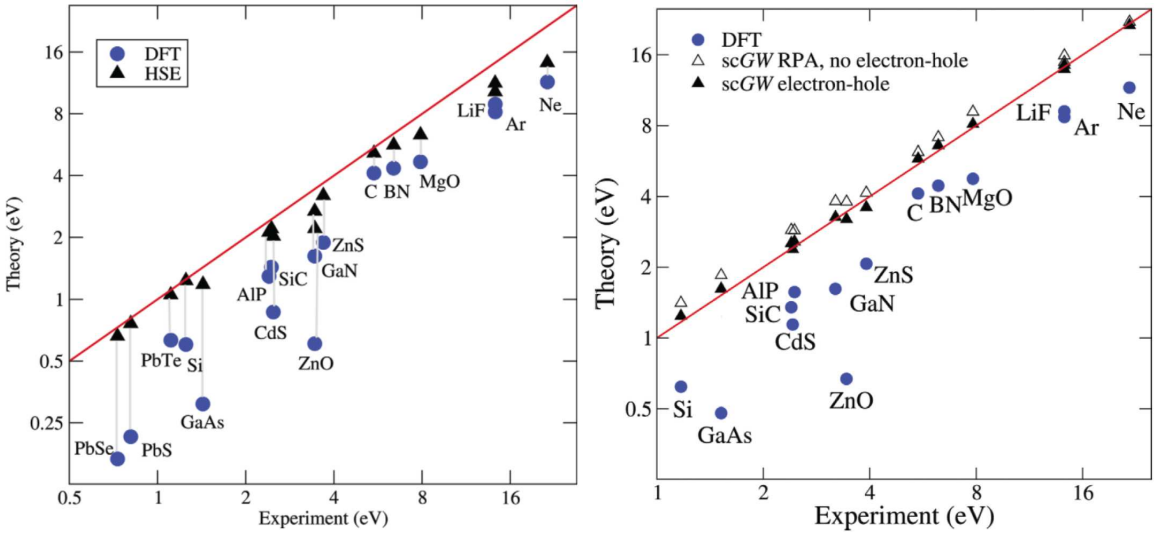

Figure 5.10.: Bandgap of common insulators obtained from HSE03 hybrid-functional (left figure) and GW method (right) and their comparison to GGA. The figure has been adopted from Ref. [136], and the original data can be found in Ref. [137–140].

At present there are three versions of GW-method implemented in VASP (version 5.2.11). The lowest level of sophistication is called the G_0W_0, where the GGA eigenvalues and eigenfunctions are used to calculate the Green's function G and the screened Coulomb interaction W using the random-phase approximation to the dielectric matrix. When the eigenvalues in the Green's function are updated while the screening still treated in RPA using the GGA eigenvalues and eigenfunctions, the approximation is called the GW_0. Updating the eigenvalues in Green's function G and in the screening matrix W leads to the self-consistent GW method. The G_0W_0 approximation underestimates the bandgap of most of the insulators [141, 142]. On the other hand the GW_0 approximation yields reasonable prediction of the band gaps, except for systems with shallow d-states like ZnO. This is because of the overestimation of the static dielectric constant in the RPA. The self-consistent GW approach gives too large

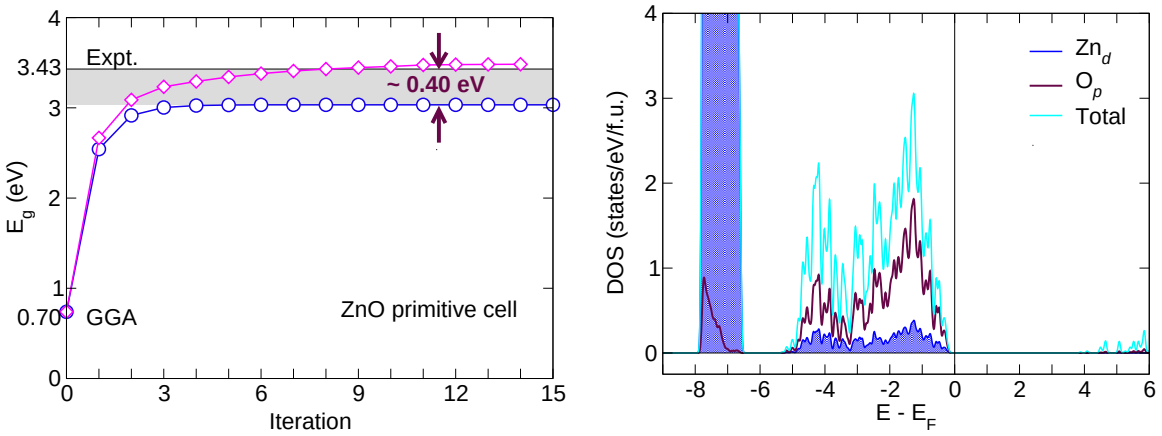

Figure 5.11.: Left: The evolution of band gap of ZnO with the iteration number in GW calculations. The circles denote the calculations with “ALGO=GW", while the diamond denote the calculations with “ALGO=scGW" (see text). Right: The orbital resolved DOS of ZnO as obtained from “ALGO=scGW".

bandgap for narrow-gap semiconductors. By treating the self-consistent GW method together with the electron-hole interaction correction which is included through vertex correction the overestimation of the bandgap can be corrected. The GW calculations with vertex correction is very demanding in time and memory requirement. Practically it has been not possible to go beyond the primitive cell of ZnO with reasonable of k-mesh (within the presently accessible computational infrastructure).
In the present studies, the selfconsistent GW within the quasi-particle picture are done as stated in the VASP manual release of March 2007. In the GW self-consistent cycle implementation the eigenvalues (and possibly the eigenfunctions) are updated, however the satellite peaks are not accounted. The two algorithms used in the calculation are “ALGO=GW" and “ALGO=scGW". The two algorithms differ in the way the non-diagonal terms of the quasi-particle (QP) Hamiltonion are treated. The “ALGO=scGW" takes into account the non-diagonal terms in calculations, while the “ALGO=GW" deals only with the diagonal term. The change of the ZnO band gap with the self-consistent iteration is shown in Fig. 5.11 (left). We find that the “ALGO=scGW" gives better results for the ZnO band structure and there is a constant underestimation of band gap by 0.40 eV when the non-diagonal part of the QP Hamiltonian are not taken into account (“ALGO=GW"). The partial DOS for “ALGO=GW" is shown in the Fig. 5.11 (right) compared to the total DOS.

5.8. Comparison of HSE+U and the GW results

In a recent experimental characterization results of pure ZnO done by reflection high-energy electron diffraction (RHEED) has been shown to agree very well with the GW calculations starting from the wavefunctions generated by HSE03 hybrid-functionals [143]. Motivated by this, the orbital resolved DOS of O p_{xy} are plotted and compared for various methods in Fig 5.12 (a). We find that the GGA and

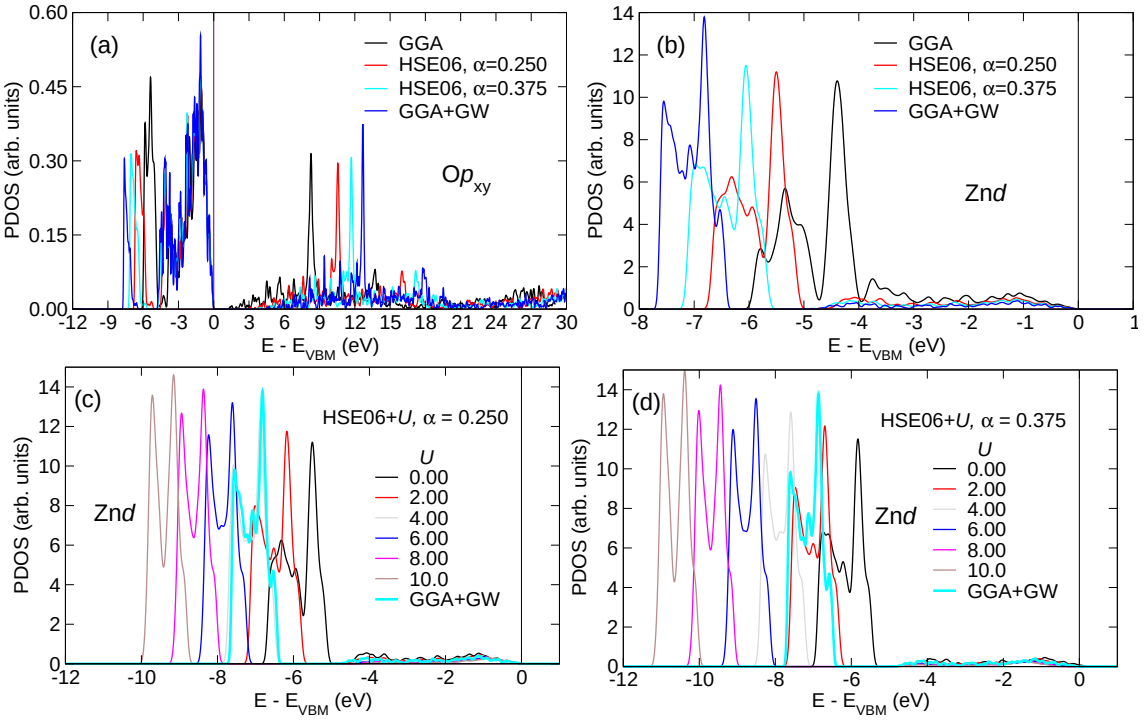

Figure 5.12.: Comparison of GGA and HSE06 DOS at two different α values with that of the GW calculations. (a): The orbital resolved DOS of O p_{xy} is compared for the functionals for both occupied and unoccupied states, as done in Ref. [143]. (b): The orbital resolved DOS of Zn d is compared for the functionals for the occupied states. Please note the center-of-weight location of the d-orbitals. (c) and (d): Comparison of orbital resolved DOS of Zn d for various U on Zn d-orbitals in the HSE06+U approach with α = 0.250 and α = 0.375, respectively, to that of the GW calculations.

and hybrid-functionals with two different values of α falls short in describing the electronic structure of the ZnO, both in the occupied region (notice the single peak occurring at the lowest energy) and also in the unoccupied region (large sharp peak above the valence band maxima). Note that the energy zero is the valence band maxima E_{VBM}. This is more clearly noticed in the location of Zn d-states in the occupied region. Although it seems that the increase in α in HSE06 can eventually fit the DOS as obtained by the GW calculations, but this would also mean that the band gap of the ZnO has been overestimated, as can be seen from Fig. 5.7.

It is observed that in HSE06+U method helps to fine tune the details of the DOS and hence can be very well compared with that of the DOS obtained from GW calculation. This is shown in Fig. 5.12 (c) and (d), where the Zn d-orbital DOS is plotted for various values of U on Zn d-orbitals at two different α values, 0.250 and 0.375, respectively. The value of $U = 6$ eV at $\alpha = 0.250$ is observed to reproduce the GW DOS reasonably well, on the other hand the value of U slightly larger than 2 eV at $\alpha = 0.375$ is observed to give well fitting DOS with that of the GW calculation. It may be noted from Fig. 5.9 that to describe the band gap reasonable well we need larger value of U than the value U = 6

eV at α = 0.250. Still one can be hopeful that a reasonable fit of U and α can eventually be reached.

5.9. Summary

The shortcomings of GGA (also LDA) exchange-correlation functionals in predicting the electronic structure for the strongly-correlated materials has been identified. Various methods of improvement like adding a site and orbital dependent correlation U, SIC-correction, adding extra exact-exchange (HF-exchange) has been discussed. It is observed that GGA+U method leads to partial improvement. Hybrid-functional treatment on other hand provides more reliable values of bandgap. However, from the ZnO band structure we observe that the Zn d-bands are not at the expected energy below the Fermi-level. There has been attempts to superimpose both methods to lead to HSE06+U corrections. With such type of correction one has two parameters, α and U, which can be used to fit the band structure to the experimental value and also to the GW calculations.

6. Transition metal doped ZnO - I: KKR-CPA and Monte Carlo methods

6.1. Introduction

In the present chapter the focus is on the magnetic interaction prevailing in ZnO when a transition metal impurity is added. The basic phenomenological idea is that the transition metal ions give rise to magnetic moments through localized spins. The magnetic moments can interact with each other to give rise to magnetic correlated effects. From technological aspect we are looking forward for correlations which could lead to room temperature ferromagnetism. Studies of the magnetic properties of ZnO as a diluted magnetic semiconductor (DMS) with Cr, Mn, Fe, Ni and Cu as TM dopant have been carried out.

The formalism of calculation of the exchange interactions is available through the Liechtenstein's formalism for the KKR-theory, where the basic assumption is that the exchange energy for weakly inhomogeneous spin-distribution can be described by the classical Heisenberg model as below;

$$H_{\mathrm{cl}} = -\frac{1}{2}\sum_{i\neq j} J_{ij}\mathbf{s}_i \cdot \mathbf{s}_j \tag{6.1}$$

where, $\mathbf{s}_i$ is the unit vector in the direction of magnetization at the i^{th} site and J_{ij} are the effective exchange parameters. This implies that in DFT calculations one can consider the total energy changes for the system under infinitesimal rotations of the magnetization of the sites. In the muffin-tin approximation the change in the direction of magnetization can be derived from the changes in the single-site scattering matrix (t), given by,

$$t_i = \frac{1}{2}(t_\uparrow + t_\downarrow) + \frac{1}{2}(t_\uparrow - t_\downarrow)\sigma \cdot \mathbf{s}_i \tag{6.2}$$

Using the scattering path operator T given by,

$$T^{-1} = t^{-1} - G \tag{6.3}$$

from the multiple scattering theory, where G is the structure Green function, one can derive the ex-

pression for J_{ij} (derived in Ref. [144]) as:

$$J_{ij} = \frac{1}{4\pi} \int_{-\infty}^{E_{\mathrm{F}}} dE \, \mathrm{Im} \Big[\, Tr_L (t_{\uparrow}^{-1} - t_{\downarrow}^{-1})^2 \, T_{\uparrow}^{ij} \, T_{\downarrow}^{ji} \Big] \tag{6.4}$$

Since both t and T are function of $\mathbf{R}$, the position of ions, hence J_{ij} is also a function of $\mathbf{R}$, written as $J_{ij}(\mathbf{R})$. The theory is a general one and is applicable to any complicated magnetic structure. For example, Liechtenstein *et al.* have calculated spin-wave stiffness in ferromagnetic metals using the J_{ij} from Eq. (6.4) which goes into the expression for calculation of the spin-wave stiffness tensor.
Using the above formalism the distance ($\mathbf{R}$) dependent and composition (x) dependent exchange integrals of TM doped wurtzite ZnO are calculated. The Machikaneyama-2002 [24] code is used to calculate the exchange integrals. The Machikaneyama-2002 code solves the scalar relativistic Hamiltonian in the muffin-tin (MT) approximation (named as A1). In the calculations the Green's function is expanded in angular momentum up to $l = 3$ and reasonably large k-points are used for accurate calculations. The calculations on J_{ij} using this code has been done by Dr. Masako Ogura from the group of Prof. Akai, at the Osaka university.
The Monte Carlo (MC) simulations were done using the *HeisenTools* code developed by Alfred Hucht for simulating the classical Heisenberg spin model using the Eq. (6.1). One of the main features of the *HeisenTools* code is that the three dimensional site-specific exchange integrals centered on particular ions obtained from the DFT calculations are directly mapped one-to-one on same lattice structure for the Monte Carlo simulations. As a result all the distant dependent and anisotropic features of J_{ij} from the DFT calculations are optimally used for the Monte Carlo calculations.
The main goal of the present chapter is to study the concentration dependent critical temperature for various TM doped ZnO systems by using the *ab-initio* J_{ij}s for the Monte Carlo simulations of the classical Heisenberg spin model, see Eq. (6.1).

6.2. Co doped ZnO: Case study

In order to understand the stability of magnetic properties of the system it is important to know the mechanism of exchange interaction prevailing in the system. The underlying exchange mechanism prevailing in DMS has been presented by Dederichs *et. al.* [87], which is already discussed in chapter 4.3. They have shown for (Ga,Mn)X (with X = N, P, As, Sb) DMS, that the exchange mechanism varies with X. At two extreme ends lies (Ga,Mn)Sb and (Ga,Mn)N. While (Ga,Mn)Sb favors the $p - d$ exchange mechanism, (Ga,Mn)N favors the double-exchange mechanism. The behavior of (Ga,Mn)As is in between the two extremes. A similar scenario is expected for II-VI semiconductors like ZnO.
The lattice constants used for calculation are taken from the first set of values presented in Table 5.1. The distance dependent exchange integrals for various concentration for Co doped ZnO obtained from approximation A1 (see 6.1) is shown in Fig. 6.1. It must be stressed that for all the calculations in this

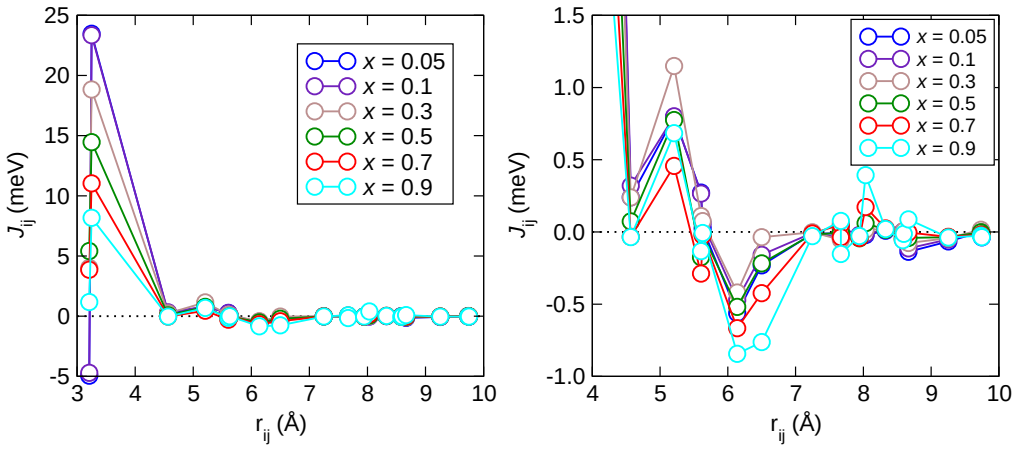

Figure 6.1.: The distance and concentration dependent J_{ij} calculated within A1 (left). One finds sharp fall of J_{ij} beyond the nearest neighbors. There is non vanishing and oscillatory long range J_{ij} seen in the zoomed in image (right)

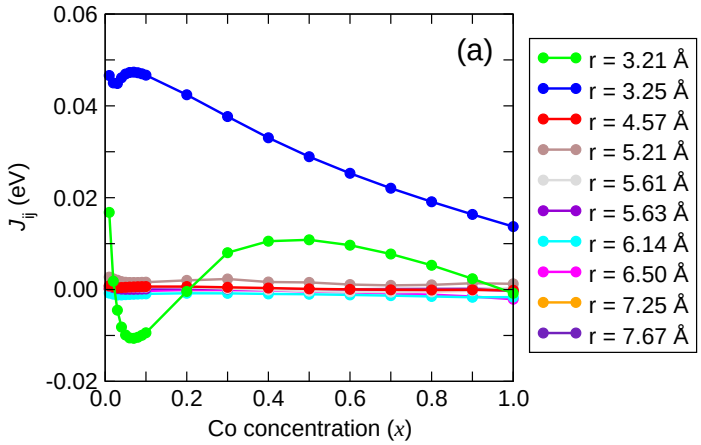

Figure 6.2.: Concentration dependent behavior of the exchange coupling J_{ij}s for various neighbors. One finds that the first two neighbors respond to the change more drastically than the others.

chapter we have only used the LDA exchange-correlation functional parameterized by Vosko-Wilk-Nusair (VMW) as stated in Ref. [145]. Although the band gap is not described well, however, LDA is sufficient to gain an impression of the exchange coupling behavior in the system.

The magnetic transition temperatures can be estimated by locating the peak in specific heat versus temperature plot or the peak in the susceptibility versus temperature plot. From the fluctuation theory we know that the specific heat is the fluctuation of energy while susceptibility is the fluctuation of the magnetization. The essential idea is that at the phase transition where the correlation length diverges, the fluctuation in respective quantities are maximum, hence we obtain a peak. The specific heat gives more general estimate of different types of phase transition occurring in the systems depending on the

model Hamiltonian. For example, if the Hamiltonian contains a term to model the structural and the magnetic changes, then the specific heat can be used to estimate both the structural and the magnetic phase transition, in principle, while magnetic susceptibility will give only the magnetic phase transition point. Since the present Hamiltonian is classical Heisenberg model, hence both specific heat and susceptibility would lead to similar results in estimation of transition point.

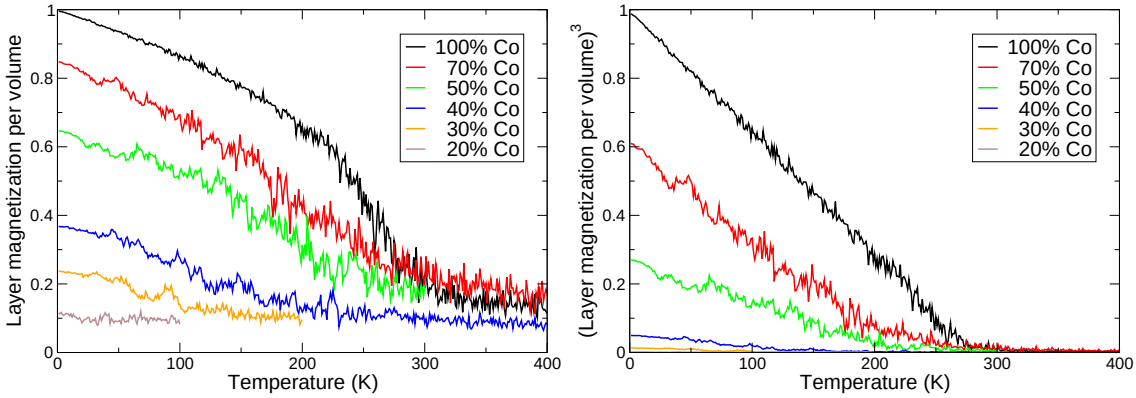

Figure 6.3.: The layered magnetization (magnetization obtained for the hexagonal layers) per volume for wurtzite $Zn_{1-x}Co_xO$ at various concentration of x expressed in percent (left). The estimation of critical temperature by fitting layered magnetization with Eq. 6.5.

A more refined way of computing phase transition point is by the application of the critical exponents [146], which describe the behavior of physical quantities near continuous phase transitions. They are sort of universal, i.e., they do not depend on the details of the physical system, but only on few quantities such as the dimension of the system, the interaction range, and the dimension of spin. Although there is no rigorous proof for it, critical exponents are supported for many exactly solvable models and also from experimental data [147]. Thus, the magnetization in 3D-Heisenberg model can be written as,

$$M \propto \left(\frac{T - T_{\mathrm{C}}}{T_{\mathrm{C}}}\right)^{\beta}, \tag{6.5}$$

where, β is the critical parameter which has a value of β = 0.3646 for 3D-Heisenberg spin model [72, 73].

In the Monte Carlo simulations the desired concentration of Co atoms is randomly distributed in a 14×14×14 supercell. Since the magnetic interaction is anisotropic with strong ferromagnetic coupling along the hexagonal plane, we characterized the system with layered arrangement of spins. The critical temperature at different composition is estimated by layered magnetization (Eq. 6.5). For simplicity, $1/\beta$ is approximated to 3. The phase diagram obtained by plotting the critical temperatures with respect to concentration is shown in Fig. 6.4. The phase diagram is easier discussed by breaking it into four regions in concentration, namely, $0 \leq x \leq 0.2$, $0.2 \leq x \leq 0.65$, $0.65 \leq x \leq 1.0$, and

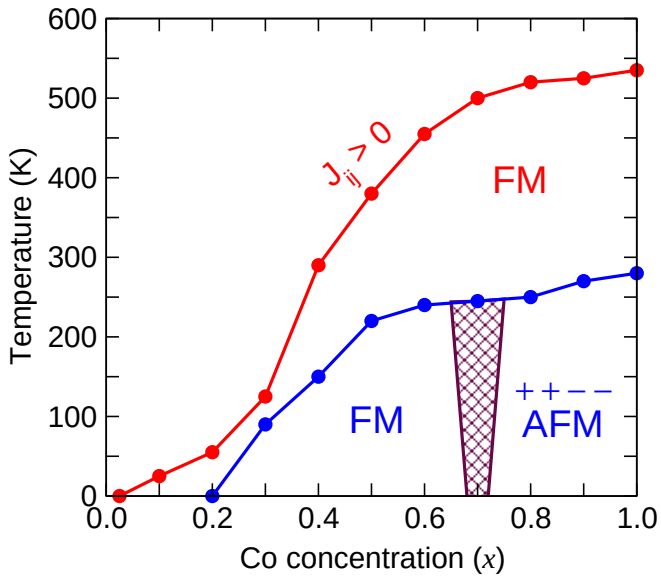

Figure 6.4.: The phase diagram of $Zn_{1-x}Co_xO$ obtained from Monte Carlo simulations of the DFT exchange parameters. Ferromagnetism appears from concentration of $x = 0.2$ onwards. This is above the percolation threshold of the wurtzite lattice (x = 0.17). The ferromagnetism only exists until concentrations of 60% Co, beyond that antiferromagnetic interactions become more dominant and the system aligns itself in a complicated magnetic phase.

$x = 1.0$.

1. Region I, $0 \leq x \leq 0.2$: This range of concentration fall below the percolation threshold for nearest-neighbor interactions in wurtzite crystal structure. Within this composition range, the J_{ij} for large distances are probabilistically more important. It is observed from Fig. 6.2 that the J_{ij} for small distances and at small concentrations seem to oscillate. J_{ij} for larger distant neighbors are flat. This suggests that the system is magnetically frustrated and thus unable to keep long range order. This is clearly observed in the simulation results, blue curve in Fig. 6.4, where the transition temperature is zero. The red curve is a reference curve simulated by taking $J'_{ij} = |J_{ij}|$. In the reference curve ferromagnetism develops from x = 0.025 onwards. Thus, no net magnetization in this composition range is explained to be a consequence of the oscillatory nature of J_{ij}.

   Incorporating the exchange interaction of the first and second nearest neighbor distances (since they are of higher magnitude than the rest) and using the mean-field approximation (MFA) expression from Eq. (6.6), we get Curie temperature of 43 K for $x = 0.05$. The Monte Carlo results, however, give no ferromagnetic correlation. One must note that role of the nearest and the next nearest neighbor interactions are negligible when the concentration range is below the percolation limit.

2. Region II, $0.2 < x \leq 0.65$: Cobalt concentration in this range stabilizes ferromagnetism. The Curie temperature is observed to rise with increase in Co concentration. As seen from Fig. 6.2, the magnetic interactions for both nearest and next nearest neighbors are ferromagnetic and they possess significant interaction strength. So, with respect to the overall negative J_{ij} contribution, the positive contribution wins, which leads to ferromagnetic phase.

3. Region III, $0.65 < x \leq 1.00$: From $x > 0.65$ onwards the system develops magnetic configuration where ferromagnetic coupling is observed in layers along the hexagonal plane. This is shown in the layered magnetization versus temperature plot of Fig. 6.3 (right). From the Fig. 6.2 we notice that the nearest neighbor J_{ij} (distance along the c-direction) is small in comparison with the other nearest neighbor J_{ij} (distance along the hexagonal plane), which are significantly positive. Hence layered ferromagnetic structures are possible in this range of composition. A detailed analysis shows that the system acquires a complicated magnetic phase of antiferromagnetically aligned ferromagnetic double-layers, represented as + + - -, where + and - gives the orientation of the average magnetic moment in the layers with respect to some reference layer. At $x \approx 0.65$, the system goes from ferromagnetism to layered antiferromagnetic phase, which is shown as shaded region in the phase diagram of Fig. 6.4. Thus in this range of concentration the blue curve essentially shows the order-disorder transition for the layered magnetic state.

4. Region IV, $x = 1.00$: This is the case of pure CoO in wurtzite structure. In nature, CoO occurs in the fcc crystal lattice structure, which is antiferromagnetic with a Néel temperature of 291 K [148]. For $x = 1$, the system prefers the layered $++--$ phase for majority of Co spins. This gives rise to a complicated magnetic ground state for wurtzite CoO. The transition temperature from this complicated ordered state to the disordered state is found to be 280 K. This transition temperature reasonably coincides with the experimental Néel temperature of CoO.

The phase diagram of Fig. 6.4 clearly suggests that no net magnetization exist for Co composition below $x = 0.2$. The ferromagnetic phase which is obtained for $0.2 < x \leq 0.65$ composition range has a Curie temperature below the room temperature. In real materials, however, a composition range of $x > 0.2$ is already too high to achieve homogeneous distribution of substituted Co in ZnO. This may support the presence of multiple phases as a possible explanation for room temperature ferromagnetism in ZnO DOS, which has been predicted recently [149, 150]. Our results can be matched with recent experimental results, where the author have studied the Co doped ZnO case systematically by changing the concentration of the Co ions upto 40% (x = 0.4) in ZnO. They find intrinsic magnetism in the system and the dose dependent saturation magnetic moment in their samples showed a clear rising tendency from 0.5×10^{17} to 1.5×10^{17} ion/cm^2, i.e., from x = 0.1 to x = 0.3 [151, 152]. Although the match seems to agree qualitatively, however, one must be very carefull in comparing the experimental results with that of the present theoretical results. This is because nature of sample preparation technique induces lot of defects in the system. Thus the atomistic origin of the dose de-

pendent magnetism in experiments may not be associated with mere Co addition unlike the outcome of theoretical results.

6.3. Comparison with ASA

The exchange-integrals as shown in the previous section were calculated by using the MT-approximation. Some improvement over this level of theory is still possible by treating with atomic sphere approximation (ASA) [153]. Noting that the shapes and the relative position of the energy bands do not vary much with the change in muffin-tin zero, V_{MTZ}, Andersen *et al.* approximated the KKR method by adjusting V_{MTZ} so that the structure constant became energy-independent [154]. In a nut-shell, the ASA consists of two parts. Firstly, the kinetic energy contribution of the electron in the interstitial region, given by $\kappa^2 = \varepsilon - V_{\mathrm{MTZ}}$, is taken as zero. In other words, the V_{MTZ} is set equal to the energy under study. Secondly, the muffin-tin radius r_{MT} is replaced by the Wigner-Seitz radius r_{WS}. The second step is supported by analyzing the errors introduced by the first step in which the propagation of electron in the interstitial space is neglected. For a complete derivation reader is referred to Ref. [153].

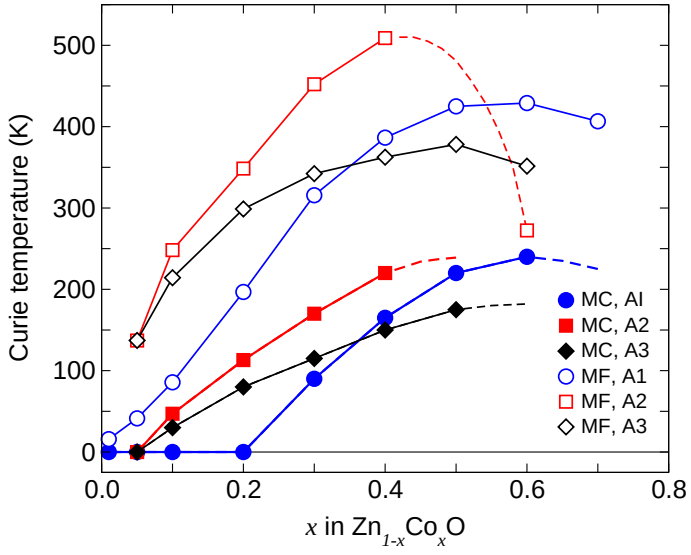

Figure 6.5.: The Curie temperature (T_{C}) calculated from the Monte Carlo simulations of the J_{ij} obtained from muffin-tin approximation (A1) and atomic sphere approximation with the scalar-relativistic (A2) and fully-relativistic (A3) treatment for DFT Hamiltonian (shown as solid symbols). Ferromagnetic correlations start from $x = 0.2$ in MT-approximation, while it start from $x = 0.05$ in ASA. Other than this, the tendency is similar for both approximations. The mean-field estimation of T_{C} calculated from Eq. 6.6 is shown as open symbols.

To check any improvement in the ASA calculation with respect to the MT calculations (A1), studies

have been done for ASA with scalar relativistic treatment (named as A2) using the Jülich SKKR - version 1.2 [155] and ASA with fully relativistic treatment (named as A3) using Munich SPRKKR - version 3.6 band structure program package [156, 157]. Similar to the A1 calculations, the Green's function is expanded in angular momentum up to $l = 3$ for the J_{ij} calculations.

$$k_{\mathrm{B}} T_x^{\mathrm{MFA}} = \frac{1}{3} x M^2 \sum_{j(\neq i)} J_{ij}, \tag{6.6}$$

Fig. 6.5 shows that different level of approximations give similar trend in results. The J_{ij} is oscillatory as a function of R and hence there is the competition between the ferromagnetic and the antiferromagnetic interactions in these systems. We find that that the onset of ferromagnetism in the ASA method is at $x = 0.05$. It is found that with increase in concentration of Co the T_C increases. Together with that the antiferromagnetic interactions also increase, which starts to dominate from $x > 0.4$ onwards. As a result the T_c approaches a maximum value and thereafter starts to reduce. For comparison the mean-field estimation of T_C calculated from Eq. 6.6 is also plotted as open symbols. It is well known that the mean-field results overestimate the T_C and the transition temperature obtained from Monte Carlo is lower than the mean-field predictions [42, 150]. We find that the mean-field calculations basically show similar trend as that of the Monte-Carlo in the estimation of transition temperature.

6.4. TM doped ZnO: LDA and LDA+SIC

From the previous section we realize that the three different approximations lead to similar results in the estimation of the Curie temperature for $Zn_{1-x}Co_xO$. So, the J_{ij} of other TM doped ZnO are calculated using the scalar relativistic Hamiltonian in the ASA only. The distance dependent J_{ij} for several compositions and the DOS at $x = 0.06$ are shown in Fig. 6.6 and 6.7, respectively.

As already mentioned in the previous chapter, the exchange-correlation functional in terms of LDA is not sufficient to describe the band structure of ZnO. In DMS, the underestimation of the band gap will lead to impurity states that ought to be within the band gap, to overlap with the valence band or the conduction band. Moreover, it is observed that the d-orbitals of the TMs lie at the Fermi level and this imparts ferromagnetic interaction due to the direct exchange which increases the electron hopping probability of the d-electrons. Hence it is essential to incorporate corrections in terms of LDA+U or the LDA+SIC. Toyoda *et al.* have studied the ZnO with all the transition metal atom by KKR-CPA and compared the LDA results with those of the LDA-SIC results [158]. The DOS of TM doped ZnO have been adopted from Ref. [158] in Fig. 6.8.

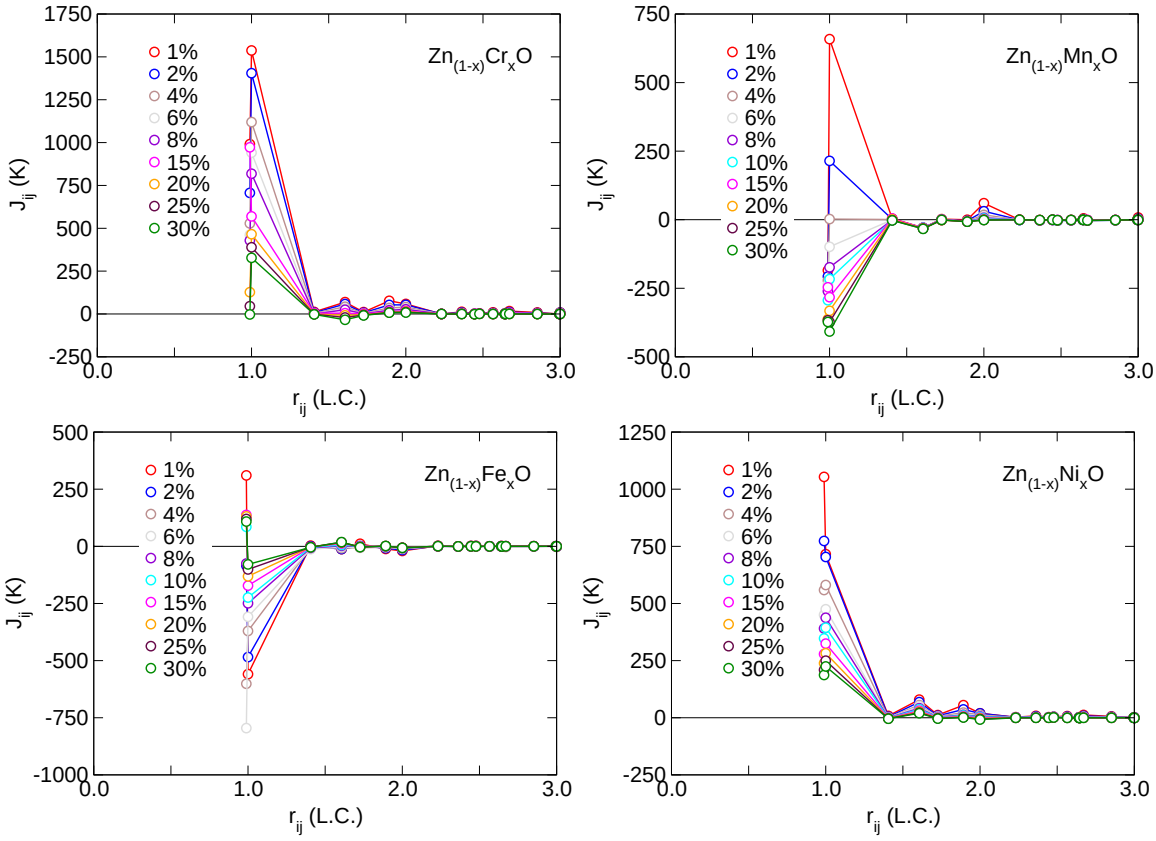

Figure 6.6.: Exchange integrals J_{ij} for $Zn_{1-x}TM_xO$, TM = Cr, Mn, Fe, and Ni. The exchange integrals are plotted in temperature scale. The magnitude of J_{ij} are in similar to the range obtained for $Ga_{1-x}Mn_xN$ in Ref. [150] (13 mRy $\sim$ 2050 K).

6.5. Incorporating the Vegard's law

The phase diagram studied in section (6.2) and section (6.3) was performed with fixed lattice constant for the wurtzite ZnO. When going from $x = 0$ to $x = 1$, we are actually going from pure ZnO towards pure TM oxide. While the crystal structure of ZnO is wurtzite, it is well known that most of the TM oxides, like MnO, CoO, NiO crystallize in rock salt structure. So it is reasonable to change the lattice parameters in such a manner that there is a crossover from wurtzite to rock salt structure. First the minimum energy lattice parameters of TM oxide (also ZnO) in wurtzite and rock salt crystal structures were calculated. The minimum energy lattice parameters of both the structures obtained from VASP calculations are tabulated in Table 6.1. Now, one set of data were generated with lattice constants changed linearly with x from wurtzite ZnO to wurtzite TM oxide. Similarly, another set of data were generated with lattice constants changed linearly with x from rock salt structure of TM oxide to the rock salt structure of ZnO. This type of linear approximation is called the Vegard's law, which is an approximate empirical rule. This approximation is often used in modeling the alloys. From the energy

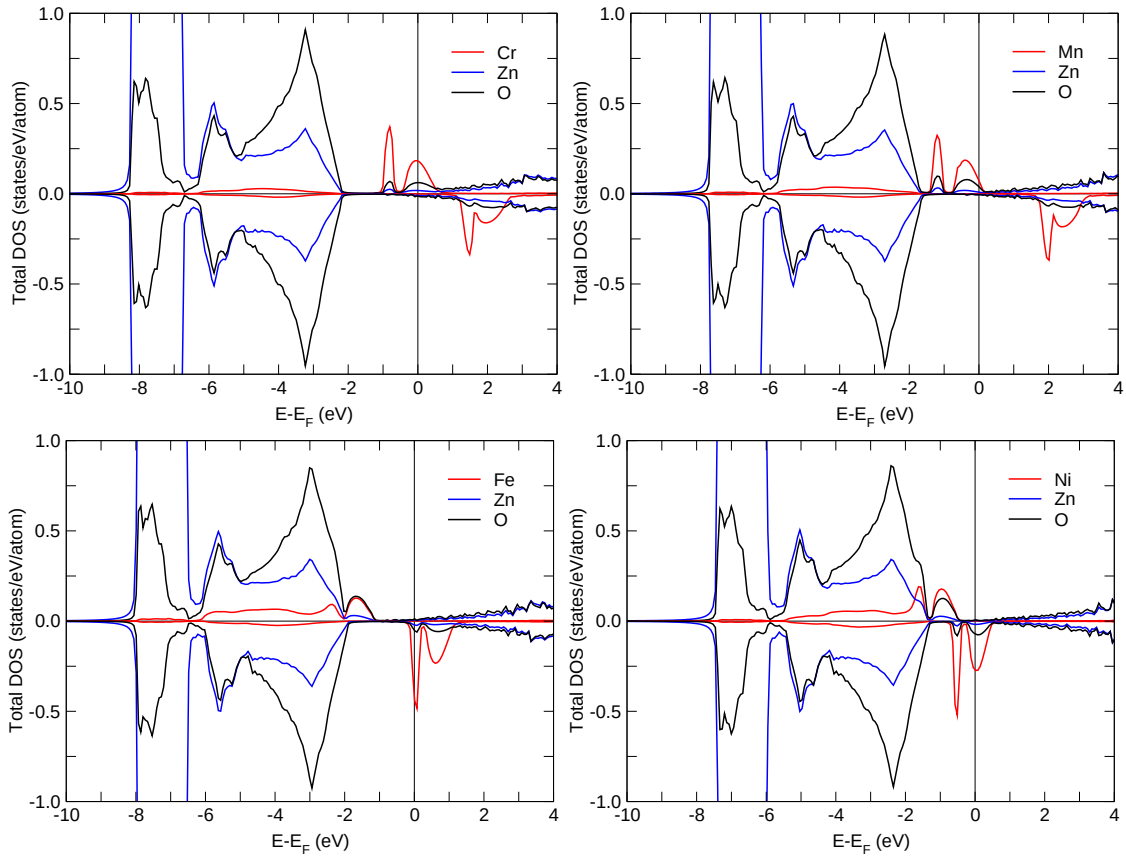

Figure 6.7.: Density of states for $Zn_{1-x}TM_xO$, TM = Cr, Mn, Fe, and Ni, at x = 0.06. The DOS agree quite well with the LDA DOS in Fig. 6.8.

difference obtained for the wurtzite to rock salt structure at each composition, one can get a first hand estimation of which structure is more favorable at that concentration.

Table 6.1.: Minimum energy lattice parameters of transition metal oxides for wurtzite and rock salt structure obtained from VASP. The Vegard's law of linear change in lattice parameters with concentration is taken for the doped chases with varying x.

TM oxide	wurtzite			rock salt
	a (Å)	c/a	u	a (Å)
MnO	3.40	1.560	0.372	4.44
FeO	3.00	1.930	0.320	4.31
CoO	3.13	1.698	0.358	4.24
NiO	3.00	1.860	0.339	4.19
ZnO	3.29	1.606	0.380	4.32

The difference in energy for the rock salt to that of the wurtzite structure ($E_{\mathrm{NaCl}} - E_{\mathrm{wurtzite}}$) at each composition is shown in Fig. 6.9. The positive value of the energy difference means that wurtzite

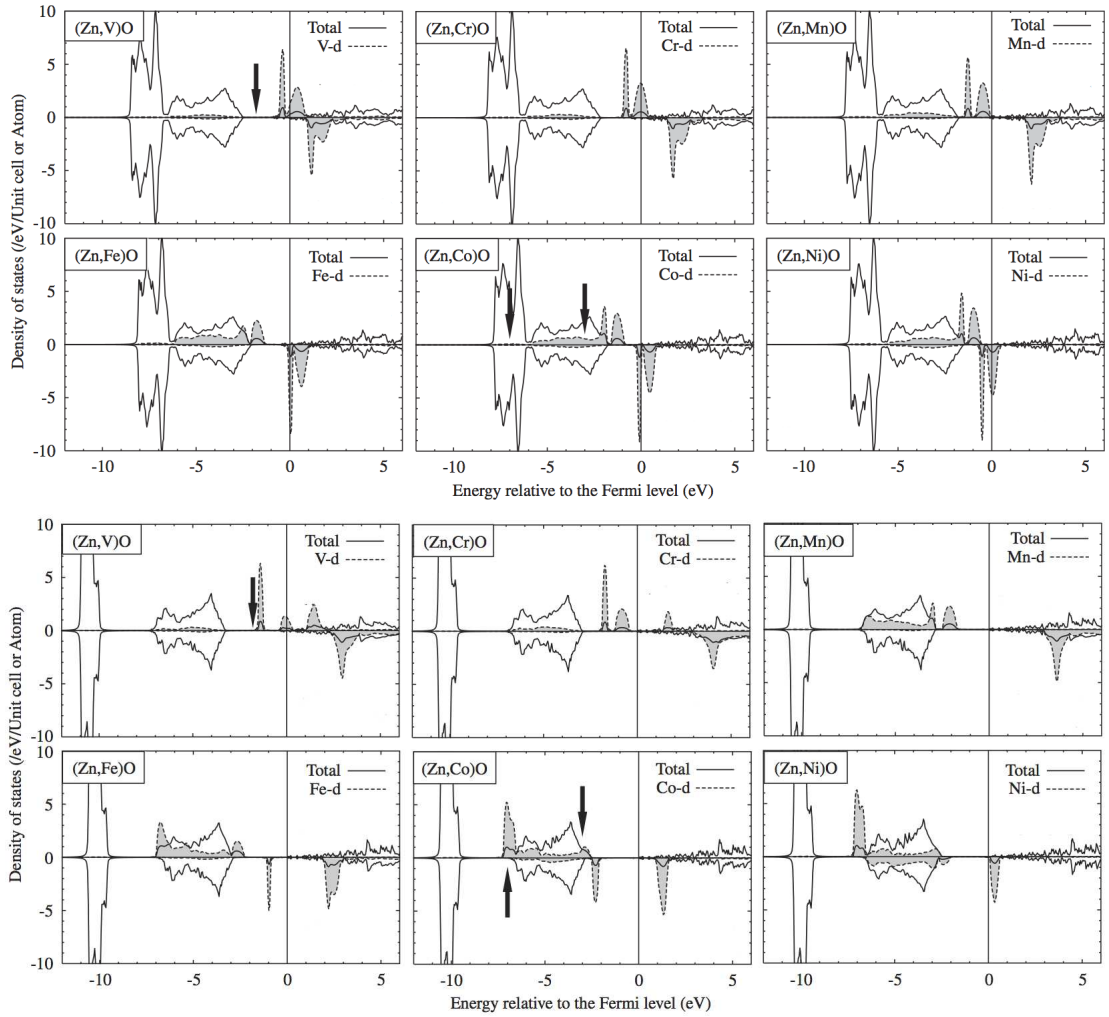

Figure 6.8.: $Zn_{1-x}TM_xO$ DOS obtained from LDA (top panel) and LDA+SIC (lower panel) for TM = V, Cr, Mn, Fe, Co and Ni. The figure is adopted from Ref. [158].

structure is stable, while a negative value indicate that the rock salt structure is stable at that composition. From the energy calculations done in KKR-CPA (using A2) we find a linear change in energy from wurtzite structure to rock salt structure as x increases, however the slope is different for different TM. For example, in case of Co, the wurtzite structure is preferable at all compositions except at $x = 1$. This is in line of recent reports where experimentalists were successful in synthesizing CoO with wurtzite structure [159]. This suggests that the wurtzite CoO is not too high in energy compared to its more stable rock salt structure. In case of $Zn_{1-x}Mn_xO$ and $Zn_{1-x}Ni_xO$, there is a smooth crossover from wurtzite to rock salt structure at $x = 0.4$ and $x = 0.65$, respectively. Although for $Zn_{1-x}Fe_xO$, a crossover occurs from wurtzite to rock salt structure at about $x = 0.5$, the energy is no more linear in rock salt structure. The convergency was a problem for composition close to the rock salt FeO. One explanation for this behavior is that different stoichiometry of oxide, namely Fe_2O_3, is

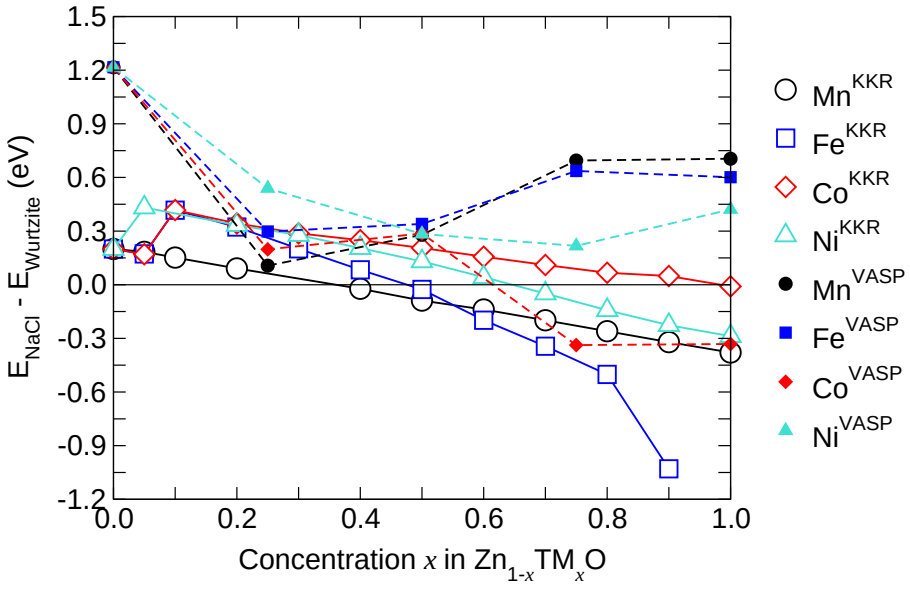

Figure 6.9.: The energy difference between the wurtzite and rock salt structure versus composition is plotted for $Zn_{1-x}O_xO$. Vegard's law of linear change in lattice parameters with concentration is taken into account for both the structure. The KKR-CPA gives smooth results which could be compared with supercell calculations with VASP only at low x.

energetically more stable.

The wurtzite to rock salt structural energies were compared at specific concentrations with supercell calculations within the VASP code, shown as solid symbols in Fig. 6.9. At low concentration the wurtzite crystal structure is predicted as the stable structure. However, for large values of x the results differ except for $Zn_{1-x}Co_xO$. The situation can be understood as following: For the case of $x = 0.5$, the supercell consists of equal number of Zn and TM atoms. In order to obtain the ground state lattice parameters, one must take into account the most favorable distribution of cations (TM and Zn) in the supercell. Since this was not done, hence the linear scaling of lattice parameters by Vegard's law may not be appropriate. For larger concentration of TM in ZnO, in addition to the above consideration, one must also consider the magnetic alignment of the TM atoms. For example, NiO and MnO are known to be antiferromagnetic along the [111] direction of the crystal lattice. Since CPA treats the configurational averages over all possible chemical environments as a mean field manner the KKR-CPA result is more reliable here.

From the *ab-initio* and Monte Carlo hybrid treatment the critical temperatures are calculated and are plotted in Fig. 6.10. The vertical lines of each color represent the concentration at which the corresponding $Zn_{1-x}TM_xO$ changes from wurtzite to rock salt structure. It must be mentioned that the critical temperatures are estimated by using the specific heat curves, since except for Co, other TM did not lead to ferromagnetic state, thus analyzing by fitting the magnetization with Eq. 6.5 was impossible. The magnetic feature of Co was more or less similar to that discussed above, except

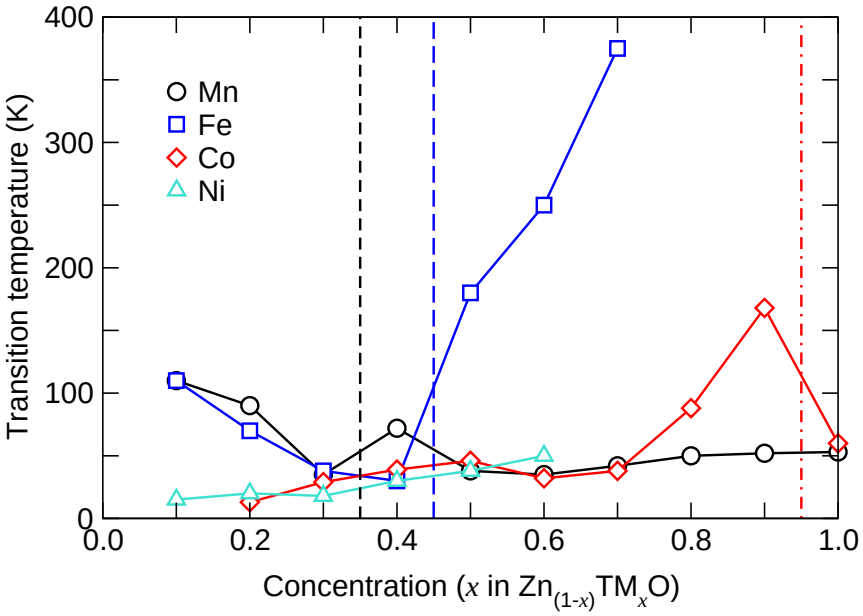

Figure 6.10.: Magnetic phase diagram obtained from *ab-initio* J_{ij} and Monte Carlo hybrid calculations. The structural change from wurtzite to the rock salt structure is taken into account through the Vegard's law. The vertical (colored) lines mark the concentration at which the respective (colored) element crosses over from wurtzite to rock salt structure. The plot gives little hope to find room temperature ferromagnetic DMS with ZnO.

that the magnitude of the critical temperature is reduced. From this general phase diagram we learn that there is no straightforward result for room-temperature ferromagnetic DMS in ZnO. Even though LDA as the exchange-correlation may have short comings in describing the band gap, treating the correlation effects will enhance the antiferromagnetic interaction can be understood in line with the Hubbard model.

6.6. Lloyd's correction in KKR-method

In multiple scattering theory the Greens's function is represented by sums over spherical Bessel's function, Henkel's functions and the radial function. In practical calculations the summation can only be allowed for a finite number of angular momentum $l_{\max}$. the sums must be truncated to a finite number of angular momentum $l_{\max}$. As a result the correct normalization of the multiple-scattering Green function is affected. Even a small error in the normalization can shift the calculated Fermi level to physically incorrect position, either in the valence or in the conduction band. This problem is more persistent in insulators and semiconductors and thus the position of the Fermi level cannot be determined accurately. One must take into account the Llyod's formula to treat the problem. The Llyod's correction can be understood as a replacement of the potential by a projection potential, which acts only on the lower angular momenta $l < l_{\max}$. This replacement modifies the position and the

size of the gap and also slightly affects the calculated number of states in the energy region of the valence and conduction bands, but does not change the exact integer number of states in the gap region. This implies that Lloyd's formula always leads to exact result for the number of states in the gap, independent of the chosen $l_{\max}$. The implementation of Lloyd's formula is as follows [160]:

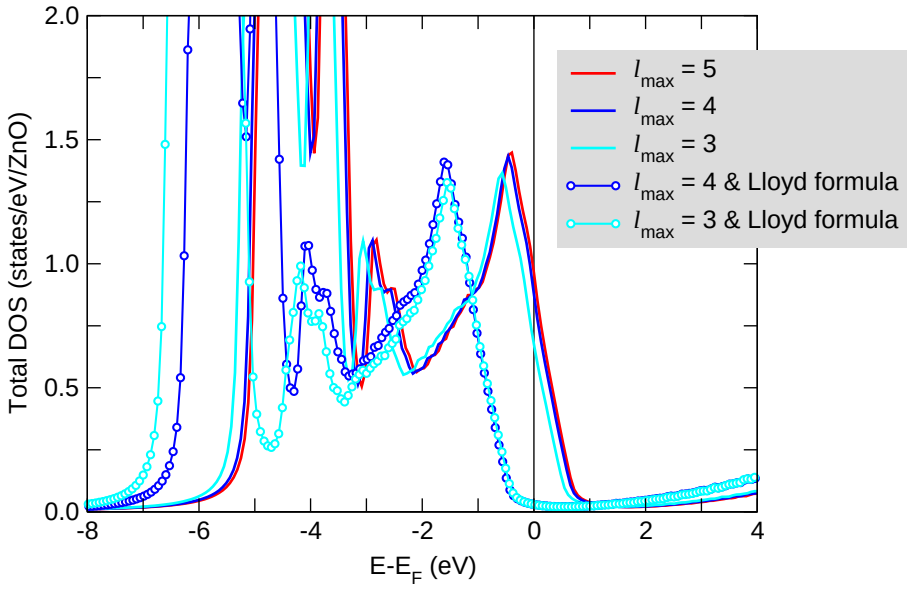

Figure 6.11.: Comparison of DOS obtained from Eq. 6.7 and with Lloyd's correction of Eq. 6.8. One clearly marks the difference in predicting the better location of Fermi energy although the DOS looks pretty similar. The DOS is convergent at l = 3 when Lloyd's correction is incorporated.

The calculation of the occupied electronic states is usually described by the equation below,

$$N(\mu,T) = -\frac{1}{\pi}\mathrm{Im}\int_{-\infty}^{\infty} dE\; f(E,\mu,T)\;\mathrm{Tr}\;G(E), \tag{6.7}$$

where, $f(E,\mu,T) = (1 + exp(\beta(E-\mu)))^{-1}$ is the Fermi-Dirac function with $\beta^{-1} = k_{\mathrm{B}}T$ and $\mathrm{Tr}G(E)$ is the trace of the single-particle Green function. Instead of above expression, we use the equation,

$$N(\mu,T) = -\mathrm{Im}\int_{-\infty}^{\infty} dE N(E)\frac{d}{dE}f(E,\mu,T), \tag{6.8}$$

where $N(E) = -1/\pi\int_{-\infty}^{E} dE'\mathrm{Tr}G(E')$ is the Lloyd's formula. Here, $N(E)$ is used as a complex quantity and that its imaginary part gives the integrated DOS.

A comparison of DOS for ZnO with $l_{\max}$ = 3, 4, 5 without the Lloyd's correction and for $l_{\max}$ = 3 and 4 with the Lloyd's correction is shown in Fig. 6.11. One clearly sees the error in the DOS when Lloyd's correction is not taken into account. In metals, however, the error is much less pronounced,

since due to the partial occupation of states the Fermi level is only slightly changed by an incorrect normalization and does not occur in a principally wrong position.

Table 6.2.: The magnitude of magnetic moment estimated without (no-L) and with Lloyd's correction (with-L). Underestimating the magnitude of moment is general trend without the Lloyd's correction. At low concentration, $Zn_{1-x}Cr_xO$ and $Zn_{1-x}Ni_xO$ lead to non-magnetic solution without the Lloyd's correction.

Conc. (x)	$Zn_{1-x}Cr_xO$		$Zn_{1-x}Mn_xO$		$Zn_{1-x}Fe_xO$		$Zn_{1-x}Co_xO$		$Zn_{1-x}Ni_xO$	
	no-L	with-L	no-L	with-L	no-L	with-L	no-L	with-L	no-L	with-L
0.01	0.00	2.70	2.28	4.01	2.93	3.72	2.48	2.56	0.00	1.56
0.02	0.00	2.85	2.34	4.07	2.98	3.71	2.52	2.55	0.00	1.54
0.04	0.00	2.97	2.44	4.11	3.07	3.66	2.58	2.53	0.00	1.52
0.06	0.00	3.04	2.53	4.13	3.16	3.63	2.64	2.51	0.00	1.51
0.08	0.28	3.08	2.60	4.15	3.24	3.59	2.69	2.49	0.64	1.51
0.10	1.29	3.11	2.67	4.16	3.32	3.58	2.74	2.48	0.91	1.50
0.15	1.98	3.17	3.02	4.18	3.50	3.56	2.84	2.48	1.27	1.50
0.20	2.37	3.21	3.32	4.20	3.67	3.54	2.88	2.48	1.47	1.49
0.25	2.61	3.24	3.52	4.22	3.82	3.53	2.90	2.48	1.59	1.49
0.30	2.76	3.26	3.66	4.23	3.94	3.52	2.90	2.48	1.65	1.49

The value of magnetic moments obtained for $Zn_{1-x}TM_xO$ (TM = Cr, Mn, Fe, Co and Ni) are tabulated in Table 6.2 without and with Lloyd's correction. One observes that without the Lloyd's correction the Fermi energy is not correctly placed thereby the exchange splitting is underestimated for all concentrations of $Zn_{1-x}TM_xO$. Extreme cases are the low concentration of $Zn_{1-x}Cr_xO$ and $Zn_{1-x}Ni_xO$, where without Lloyd's correction the calculation leads to non-magnetic solution.

A plot of the relative change of the magnetic moment with respect to the moment obtained at $x = 0.01$ versus the concentration x is shown in Fig. 6.12 for calculations without and with Lloyd's correction. One finds that without incorporating the Lloyd's correction, shown as solid symbol (no L), there is increase in relative magnetic moment for all TM with increase in x. The relative increase in magnetic moment is quite significantly high to almost 50% within $x = 0.3$ for Mn. However, with Lloyd's correction the trend is just opposite, i.e., the relative magnitude of magnetic moment decreases very slowly with increasing x. The change lies within 8%. As a last remark, it must be mentioned that in the derivation of exchange integrals by Liechtenstein *et al.* [70], Lloyd's correction in the electronic states is one of the starting equations and hence free from any related error. All the results discussed in this chapter incorporates the Lloyd's correction. This must be mentioned because in almost all the reports based on KKR-CPA this important point is explicitly not mentioned which might lead to confusion.

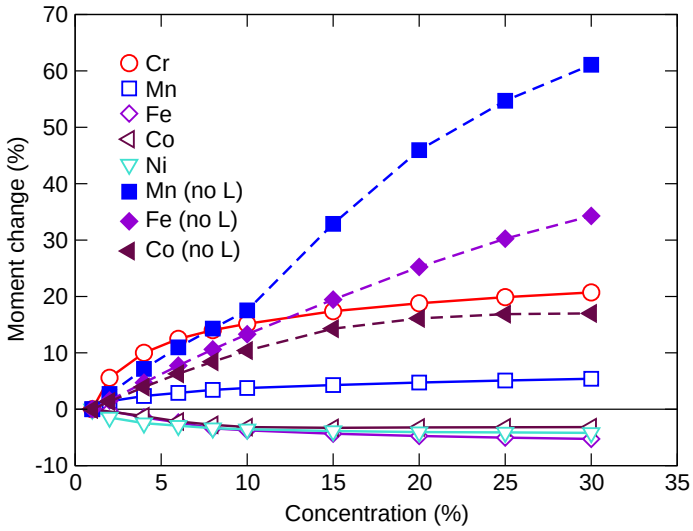

Figure 6.12.: Plot showing the relative change in magnetic moment (w.r.t. magnetic moment at $x = 0.01$) for $Zn_{1-x}TM_x$ with increasing x without and with Lloyd's correction. The error in the estimation of magnetic moment itself is quite high without the Lloyd's correction as seen from the data of magnetic moment in Table 6.2.

6.7. Summary

The magnetic properties of ZnO-based DMS were studied by using the CPA formalism in the KKR-method. KKR-CPA is a successful method for treating the alloy problems. The exchange-correlation functional is treated within LDA. The exchange integral calculated from the *ab-initio* calculation were fed into Monte Carlo simulations to get the magnetic phase and the transition temperature. Co doped ZnO has been used as a case study. It was found that ferromagnetic correlations develop from almost 5% to 20% concentration, depending on the approximations used in the calculations. At large concentrations, however, the anti-ferromagnetic correlations dominate. The structural change from wurtzite crystal structure for pure ZnO to that of the rock salt structure for pure TM oxide is taken into consideration by using linear relationship of lattice parameters through the Vegard's law and comparing the energy difference of structures. We find that the ferromagnetic correlations are suppressed and most of the critical temperatures are very low.

7. Transition metal doped ZnO - II: Supercell approach

7.1. Introduction

In the previous chapter the doping problem was dealt within the CPA formalism which, together with the KKR-Green's function method, has been successful in treating the alloy problems. One of the advantages of CPA is that the demand for computational resources is comparatively not very high because the primitive cell is enough to model the alloy problem by treating the potentials on the mixing-atoms in mean-field manner. Another approach to the problem from first principles is the supercell method. In this method a supercell, which is usually doped according to the problem at hand, is repeated infinitely by using the periodic boundary condition. In other words, the whole supercell is now the unit cell of the system under consideration [161, 162]. The suitable theory for supercell calculations is the plane-wave pseudopotential method as adopted in many of the DFT codes like VASP [92, 93]. The finite-cluster method is still another method to study defects [163, 164]. In this method the defect is incorporated in a finite atomic cluster with the surface of the cluster passivated to saturate any dangling bonds. Since this method is not used in the present work it is only mentioned for information. Apart form magnetic interaction, the defect studies in semiconductors itself is an important field of research. A detailed discussion on the current problems and state-of-the-art methods used for defect studies can be found in Ref. [165].
In supercell calculations, the size of the supercell is an integer translation of primitive unit cells along the desired lattice directions. In the following work, we will refer to the size of supercell by an integer triplet, $n_a n_b n_c$, suggesting the periodic repetition of n_a times along lattice vector $\mathbf{a}$, n_b times along lattice vector $\mathbf{b}$ and n_c times along lattice vector $\mathbf{c}$, respectively. For example, a supercell 345 would imply a supercell consisting of primitive vectors translated three times along $\mathbf{a}$, four times along $\mathbf{b}$ and five times along $\mathbf{c}$ directions.

7.2. LDA and GGA results

One of the first theoretical studies on TM doped ZnO in the wurtzite crystal structure was done by Sato *et al.* [104, 166]. They have studied the total energy differences of antiferromagnetic orientation of local moments to that of the ferromagnetic orientation of local moments for a variety of TMs like

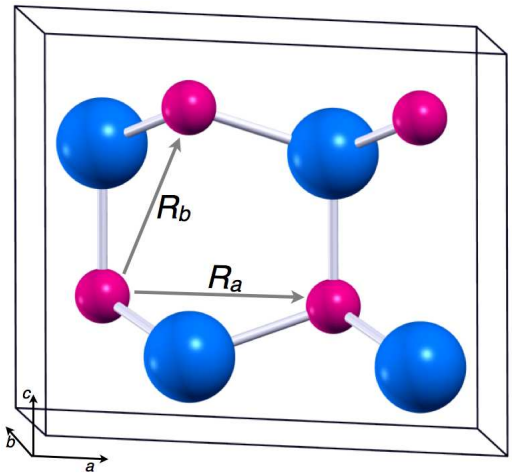

Figure 7.1.: The two nearest neighbor separations R_a and R_b are shown in the supercell 211. The two separations are almost nearly same with $R_b = 0.98R_a$, but owing to different surrounding environment, they are expected to give rise to difference in calculated properties.

Ti, V, Cr, Mn, Fe, Co Ni and Cu. Their results are shown in Fig. 7.2, where they have shown that the ferromagnetic state is stable for V, Cr, Fe, Co and Ni. Mn is the only element which favors antiferromagnetic interaction. Ti and Cu on the other hand do not have any spin polarization which is observed from the zero magnetic moment in the magnetic moment per impurity atom plot in the upper panel of Fig. 7.2. The magnetic moment of other elements rise and fall systematically with increasing number of d-electrons with its maximum moment occurring for Mn with 5 μ_B/atom. Regardless of the exact value of the magnetic moment, one can easily identify that the pattern of magnetic moment change matches with that of the change in the number of d-electrons for respective atomic cases. Their calculations have been performed using the KKR-method with LDA as exchange-correlation potential in the parameterization of Morruzi, Janak and Williams [167]. In their work they have reported that there are eight Zn sites in the supercell. ZnO in wurtzite crystal structure has two units of ZnO in the primitive cell, i.e., they must have used either supercell 122 (supercell 212 is equivalent since in wurtzite lattice the lattice directions a and b are equivalent) or supercell 221. Another important point is that the wurtzite crystal structure is anisotropic thus the two nearest neighbor (n.n.) cation (or anion) distances are not exactly same. The n.n. distance along the $\mathbf{c}$ direction (position vector strictly not parallel to $\mathbf{c}$) denoted by R_b is slightly smaller than R_a, the n.n. distance along $\mathbf{a}$. This is depicted in Fig. 7.1. With the lattice parameters used in calculations (third data in table 5.1), the length of the two n.n. are related as, $R_b = 0.98R_a$. Although almost similar in the separation, the crystal environment of the two types of n.n. atoms are different and hence they are expected to lead to noticeable different results.

The calculations for TM located at the two nearest neighbor cation sites have been studied. In order to compare with the results of Sato *et al.*, the system was modeled by supercell 221 for R_a and

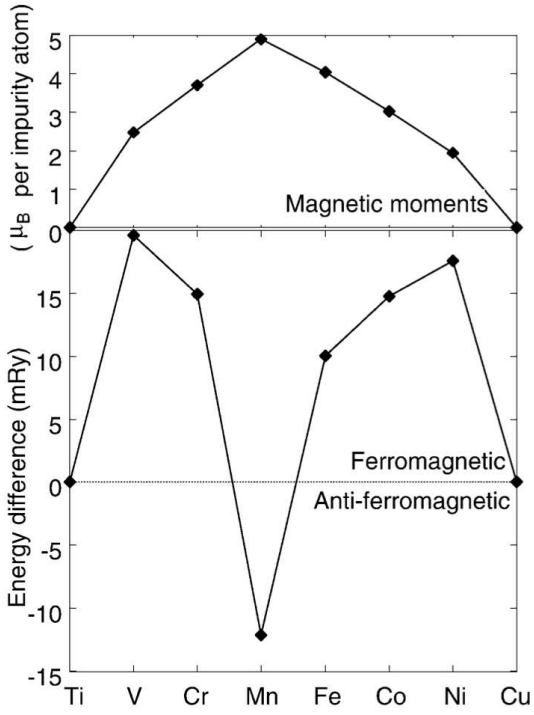

Figure 7.2.: The energy difference ($E_{\mathrm{AFM}} - E_{\mathrm{FM}}$) and the corresponding magnetic moment per TM atom for TM doped ZnO for the supercell 222 shown in lower and upper panel, respectively, as predicted from KKR calculations. Figure is adopted from Sato *et al.* [104, 166]

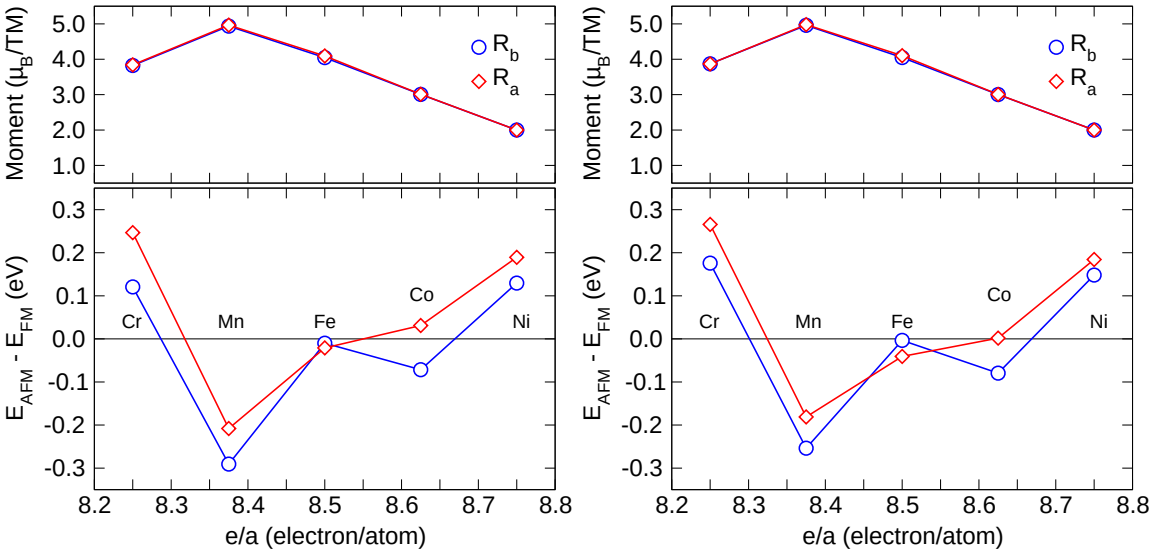

Figure 7.3.: Energy difference ($E_{\mathrm{AFM}} - E_{\mathrm{FM}}$) and the corresponding magnetic moment per TM atom for TM doped ZnO as calculated by VASP. The left and the right plots are the LDA and GGA results, respectively.

by supercell 122 for R_b. The calculations were done with LDA and GGA taking the same lattice constant as used by Sato *et al.* [104]. It must be noted that they have used 0.345 as the value of lattice parameter u. It is now known that this value corresponds to the high-temperature phase of ZnO. The present calculations are done by VASP using the LDA given by Ceperley and Alder [168] and parameterized by Perdew and Zunger [108] and for the GGA exchange-correlation potential the form of GGA-PW91 [94] is used. The plots used a scale electron/atom, which is the total number of valence electrons in the system divided by the total number of atoms. In the present supercell the value of e/a for various TM is tabulated in Table 7.1. Due to problems in achieving convergence for the supercells with V and Cu for the antiferromagnetic configurations, they are dropped in the discussions.

Table 7.1.: The value of e/a, where e is the total valency electrons and a is the total number of atoms in the supercell, respectively, obtained for various TM in $Zn_{1-x}TM_xO$ for the supercells 122 and 221. The value of a here is 16.

TM	Cr	Mn	Fe	Co	Ni
e/a	8.250	8.375	8.500	8.625	8.750

The LDA calculations are shown in Fig. 7.3 (left) and the GGA in Fig. 7.3 (right). One finds that there is disagreement for Fe, Co and Ni as compared to previous predictions [104, 166]. We also find that the magnetic interaction is slightly different for different n.n. distances. It must be mentioned that the lattice is not relaxed in our calculations for a ready comparison.

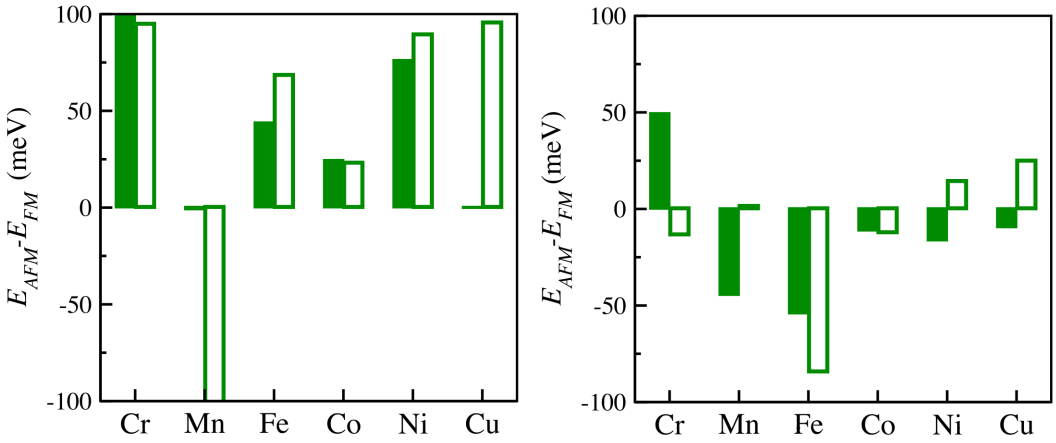

Figure 7.4.: The energy difference ($E_{AFM} - E_{FM}$) for TM doped ZnO for the n.n. interaction along the c-direction. The left and the right plots are those of LDA and LDA+U calculations. Figure is adopted from Gopal *et al.* [169]

Gopal *et al.* have used a supercell of 222 to calculate the magnetic energy differences between a “near" and a “far" configurations of TM dopant within LDA and LDA+U. Their “near” configuration is same as that of R_b in the present case and represented by the blue curve in Fig. 7.3 (left). The “far"

configuration is the n.n.n. separation (apart from two n.n. distances) with a separation distance of c. They find that the calculated magnetic orderings without ionic relaxations vary considerably both with the TM type and with the spatial arrangement. The strength and the sign of the magnetic interaction depends on the ionic relaxation. The results of Gopal *et al.* show that the “near" configurations are energetically more favorable than the “far" configurations and from the Fig. 7.4 (left) one concludes that TM like Cr, Fe, Co, Ni and Cu lead to ferromagnetic ground state.

The doping concentration in the calculations of Sato *et al.* and those of Gopal *et al.* are 25% and 12.5%, respectively. These are relatively large concentrations for the system of DMS. In DMS materials the doping is expected to be restricted to very small concentrations in the range of 5%. In order to stick to such low concentrations, larger supercells were taken into account. In the present calculations supercell 322 and supercell 223 are used to study the interactions at R_a and R_b. The supercells now consist of 24 ZnO units. Substitutional doping of two TM atoms in cation site results in doping concentration of 8.33 %. The lattice parameters used in these calculations are the minimum energy lattice parameters obtained in DFT-GGA, namely $a = 3.29$ Å, $c/a = 1.606$ and $u = 0.380$. For the LDA and GGA calculations (also for the GGA+U calculations) the k-point mesh is spanned by Γ-centered Monkhorst-Pack grid of $3\times5\times5$ and $5\times5\times3$ for supercells 322 and 223, respectively. With the increase in size of the supercell the concentration of TM decreases and the e/a ratio for various TM in ZnO is increased. This is because of the large supercell, where the percent of Zn atom which contributes more valency electrons (12 electrons) also increases. The relevant values of e/a for the present supercell are shown in Table 7.2. The value of e/a for pure ZnO is 9.

Table 7.2.: The value of e/a, where e is the total valence electrons and a is the total number of atoms in the supercell, respectively, obtained for various TM in $Zn_{1-x}TM_xO$ for the supercells 322 and 223. The value of a here is 48.

TM	Cr	Mn	Fe	Co	Ni
e/a	8.750	8.792	8.833	8.875	8.917

The results are presented in Fig. 7.5 (left) for LDA and Fig. 7.5 (right) for GGA, respectively. The results agree very well with the studies of Gopal *et al.* for the case of relaxed lattice coordinates (the blue curve in Fig. 7.5 must be compared to the unfilled histogram bars of the left plot of Fig. 7.4. The red curve in Fig. 7.5 which represents the interaction along the hexagonal plane (R_a), shows slightly different behavior to that of R_b (blue), especially for Fe and Co. Thus we find that for Fe and Co the n.n. interaction along the c-direction (R_b) is ferromagnetic while the n.n. interaction along the hexagonal plane (R_a) is antiferromagnetic. Comparing Fig. 7.3 and Fig. 7.5 we find that when the lattice parameter u = 0.345, then the interaction for R_a is ferromagnetic and interaction for R_b is antiferromagnetic, while with more appropriate value of u parameter (u = 0.380, or relaxing the supercell) it leads to just the opposite tendency. The studies presented by Chanier *et al.* [170] with supercells 331 and 222 within LDA by using the FPLO code also agree very well to the present results.

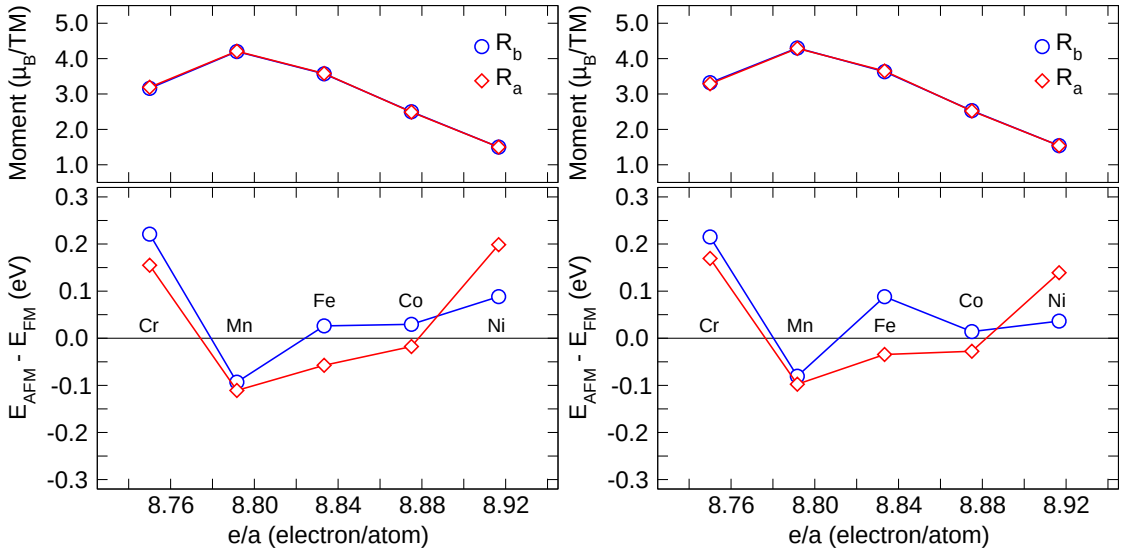

Figure 7.5.: The energy difference ($E_{\mathrm{AFM}} - E_{\mathrm{FM}}$) and the corresponding magnetic moment per TM atom for TM doped ZnO shown in lower and upper panel, respectively, for two n.n. interactions R_a and R_b. The LDA results are shown in left and that of the GGA is shown in right. The internal parameter u = 0.380.

Both LDA and GGA give similar tendencies across the TM-series.

7.3. GGA+U to treat strong correlations

In dealing with TM doped in ZnO, one is very likely to touch the feature of the TM oxide compounds, which is an important area of research in itself because of the correlated nature of the d-electrons. It is accepted by now that simple independent electron approaches fail to describe basic properties of TM-complexes, like whether they will behave as metals or as insulators [171]. One of the important step toward a satisfactory explanation has been through the introduction of the Mott-Hubbard model [75, 76]. In this model, the correlation gap is linked to the large effective on-site Coulomb interaction U. This model is quite successful for the early TM metals. Later it was recognized that the gap could also be of the charge transfer type, which is described by the the energy needed to transfer an electron from the ligand ion to a distant TM ion (Δ). Roughly the early TM monoxide, TiO and VO can be categorized into Mott-Hubbard regime, MnO, FeO, CoO, and NiO are antiferromagnetic insulators which fall in the intermediate regime, and CuO is an antiferromagnetic charge transfer semiconductor. The important difference between a band insulator and a Mott-Hubbard or charge transfer insulator is the highly localized nature of the valence orbitals, which brings forth variety of subtle forms of charge, spin, and orbital ordering. For a proper description of the magnetic properties it is often sufficient to consider only the d-orbitals of a TM ion and the p-orbitals of the oxygen-ligand ions. Some common TM-complexes categorized as MH and CT (intermediate in general) in terms of Δ and U are shown

in Fig 7.6.

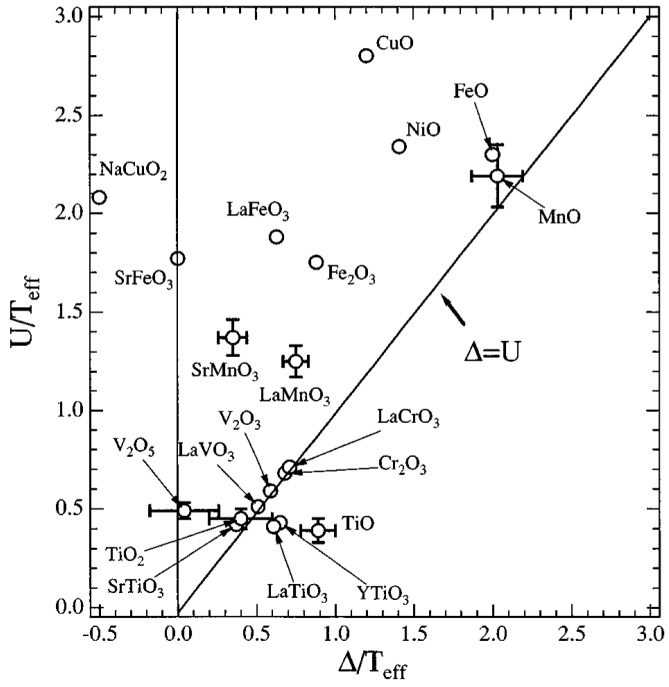

Figure 7.6.: Classification of some TM-complexes into charge transfer (CT) and Mott-Hubbard (MH) type in terms of Δ and U. Herr T_{eff} is the hybridization strength [181]. Δ and U are normalized by effective hybridization strength T_{eff}. The region above the $\Delta = U$ line is the CT region, while the region below it is the MH region. Figure is adopted from Bocquet *et al.* [181].

Table 7.3.: Table showing the value of U (eV) used in the present calculations for the d-orbitals of various TM atoms and values used in other references.

TM	U (eV) present calculation	U (eV) reported in literature
Cr	3.5	3.5[a], 3.0[b,c,d]
Mn	4.0	4.0[a], 2.0[e]
Fe	4.0	4.0[a], 3.0[e]
Co	3.3	3.3[a], 3.0[e], 4.1[f], 5.0[g]
Ni	6.4	6.4[a], 3.0[e]
Zn	9.0	9.0[h], 4.7[i], 7.5[j]

[a] Reference [172], [b] Reference [173], [c] Reference [174], [d] Reference [175], [e] Reference [176], [f] Reference [177], [g] Reference [178], [h] Reference [179], [i] Reference [180], [j] Reference [42]

Because of the strongly correlated nature of the d-electrons in TM, one needs to go beyond LDA (or GGA) in DFT. The two most common treatments are the hybrid-functionals (to be discussed in a

later section) and the DFT+U method [119]. In the DFT+U method one tries to describe the electron correlation effects by adding Hubbard-U term in the functional representing the on-site Coulomb repulsion among selected orbitals associated with the given atomic sites. The motivation for doing so is to correct the self-interaction error (refer to chapter 5) and the resulting bias toward noninteger orbital occupations in DFT [182]. The effect of U depends on the details of the implementation and hence a direct comparison of the value of the Hubbard-U across DFT codes is not straightforward. However, the systematic change in the results can be compared.

To account for the Hubbard-U parameter, the LSDA+U approach following Dudarev *et al.* was employed [123]. This method adds a penalty functional to the LSDA total energy expression which forces the on-site occupancy matrix in the direction of idempotency, i.e, either towards complete filling or towards zero filling. In this approach the U-parameter acts only on partially filled states. The value of effective U (($U - J$) in Dudarev formalism), also casually called the U used for the d-orbital of various TM are tabulated in Table 7.3.

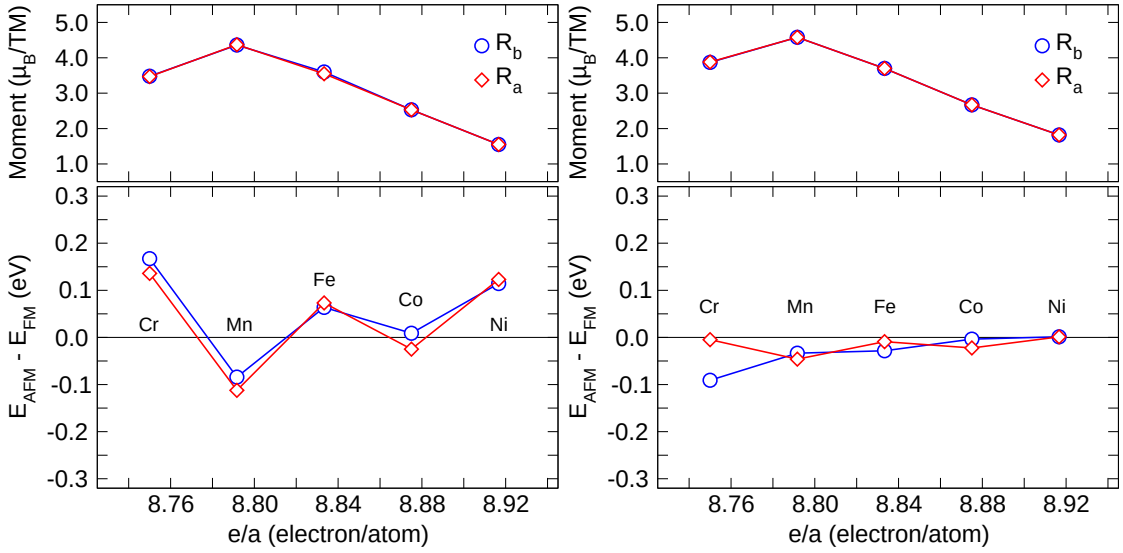

Figure 7.7.: The energy difference ($E_{\mathrm{AFM}} - E_{\mathrm{FM}}$) and the corresponding magnetic moment per TM atom for TM doped ZnO shown in lower and upper panel, respectively, for two n.n. interactions R_a and R_b. The GGA+U with U only on the Zn d-orbital are shown in left and those of U only of TM d-orbital (not on Zn d-orbital) is shown in right. The value of U used in the calculations are given in Table 7.3.

The calculations were done in three phases. First the U was applied on Zn d-orbitals alone, then on the TM d-orbitals alone and finally U was applied on both Zn d-orbitals and TM d-orbitals. The results for the energy difference ($E_{\mathrm{AFM}-E_{FM}}$) for the case where U was applied on Zn d-orbitals alone are shown in Fig 7.7 (left). Although in the earlier work of chapter 5 the value of U = 7.5 eV have been used, presently U = 9.0 eV is considered. The qualitative feature in the electronic structure is still the same except for some minute details, which is expected not to play a major role. The ($E_{\mathrm{AFM}-E_{FM}}$)

for the case where U is applied on the d-orbitals of TM atoms while no U was applied on Zn is shown in Fig. 7.7 (right). The results are in good agreement with those of Gopal *et al.* where they have used U = 4.0 eV (as already mentioned it should be read as $(U - J)$ for Dudarev method) for all the TM atoms including Zn. Comparing the left and the right plots of Fig. (7.7) one can see the drastic change in the prediction of magnetic state in treating U on different atoms.

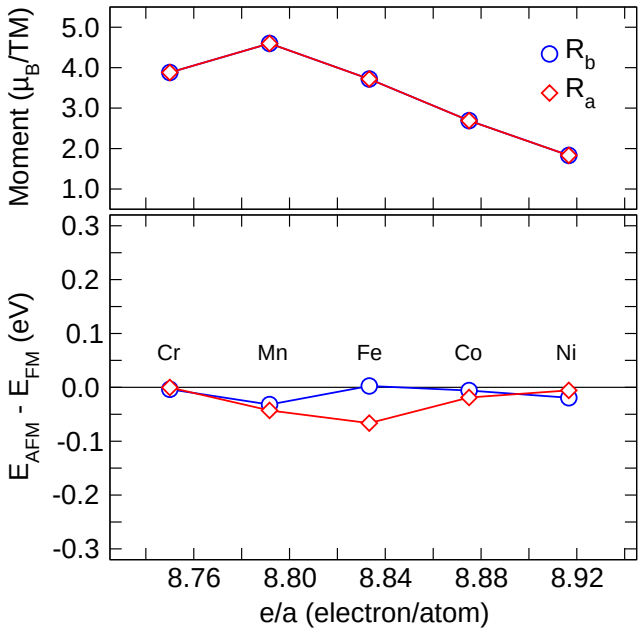

Figure 7.8.: The energy difference ($E_{\mathrm{AFM}} - E_{\mathrm{FM}}$) and the corresponding magnetic moment per TM atom for TM doped ZnO shown in lower and upper panel, respectively, for two n.n. interactions R_a and R_b. The U is applied on both Zn d-orbital and on the TM d-orbital together.

In order to compare the DOS obtained for the various exchange-correlation functional they are plotted from Fig. 7.10 to Fig. 7.14 for various TM atoms separately. The exchange-correlation functionals are identified with the Roman letters in the figures, namely, I for LDA, II for GGA, III for GGA+U_{Zn}, IV for GGA+U_{TM}, V for GGA+U_{Zn}+U_{TM}, VI for HSE06 and VII for HSE06+U_{Zn}, respectively. The LDA DOS for Co doped ZnO matched very well with Ref. [183]. Obviously, the correlation corrections is essential for both Zn d-orbitals as well as that for the doped TM under study. This can be seen from the DOS of Figs. (7.10-7.14), where the addition of U on Zn d-orbitals and TM d-orbitals are applied separately (cases III and IV in Figs. (7.10-7.14)) may be compared to that of the U applied on both Zn and TM d-orbitals (case V in Figs. (7.10-7.14)). The U values that have been used for different TMs and their corresponding references are summarized in Table 7.3 and the results of the energy difference between the magnetic configurations when U is applied on both Zn and TM d-orbitals are shown in Fig. 7.8. We recapitulate that the location of the Zn d-bands are shifted to lower energies with respect to the Fermi energy and the spurious hybridization between Zn d-states

and the O p-states are corrected to some extent as a result the band gap of ZnO also increases when U is added to Zn d-orbitals. It is observed from the cases III and IV of the Figs. (7.10-7.14) that the U on Zn and TM d-orbital change the on-site electronic properties rather independent of each other. This is actually a second order effect, for example if U is applied on Zn d-orbitals alone, it changes the hybridization of Zn d with that of O p, this results in the change of hybridization of TM d-states because it hybridizes with the O p states.

One of the important results is that the application of U on both the Zn and the TM d-orbitals completely change the hybridization picture (case IV in Figs. (7.10-7.14)). The impurity states appear to shift below the Fermi level and the antibonding d-state which were lying above the Fermi energy are now pushed to still higher energies with respect to the Fermi energy. The situation is similar for both R_a and R_b and energy differences ($E_{\mathrm{AFM}} - E_{\mathrm{FM}}$) are now lower in magnitude and mostly negative as seen in Fig. (7.8).

7.4. Hybrid functional treatment: Without and with U

In the present calculations the screened hybrid-functional of the HSE06 is used with the screening length 0.2 Å (refer Section 5.5). Due to the expensive computational demand of the method, the k-point grid is reduced to 2×2×2. With HSE06 hybrid-functional alone, one can perform calculations with HSE06 and GGA+U together. This makes sense because the GGA correlations are used as correlation functional in the HSE06 functional. The motivation and improvement of this type of calculations has been presented in chapter 5.

The results obtained for the HSE06 and HSE06+U are shown in Fig. 7.9 (left) and Fig. 7.9 (right), respectively. The studies for HSE06 show that the magnetic interaction for both the type on n.n in case of all TM in ZnO is antiferromagnetic. After adding U above the HSE06 hybrid-functional, the energy difference ($\mathrm{E}_{\mathrm{AFM}} - E_{\mathrm{FM}}$) is found to be negative and close to zero, suggesting the system would behave as antiferromagnetic or paramagnetic. These calculations can be improved with additional k-point grid. As shown by Gopal *et al.* taking large k-point grid lead to a different magnetic ground state than those predicted by sparse k-point grid. However, treating large k-points grid although attempted, could not be successfully run because of the large memory requirement.

One of the important aspects that can be revealed within the total energy calculations as done for R_a and R_b nearest neighbors it to check for the tendency of the TM atoms to prefer one of the neighboring position. This analysis is important to justify whether a random substitutional doping in TM doped ZnO can be expected. Using the GGA+U calculations Iuşan *et al.* have shown that Co has a tendency to cluster in ZnO [184]. With the availale data one can only compare the preferential positions for R_a or R_b. This is done by comparing the energy difference ($E_{R_b} - E_{R_a}$) for the same magnetic configuration (either FM or AFM). So, negative value of ($E_{R_b} - E_{R_a}$) suggest that R_b is the preferred nearest neighbor, while the positive values of ($E_{R_b} - E_{R_a}$) suggest that R_a is the preferred nearest neighbor. The data for the energy difference ($E_{R_b} - E_{R_a}$) are listed in Table for FM and

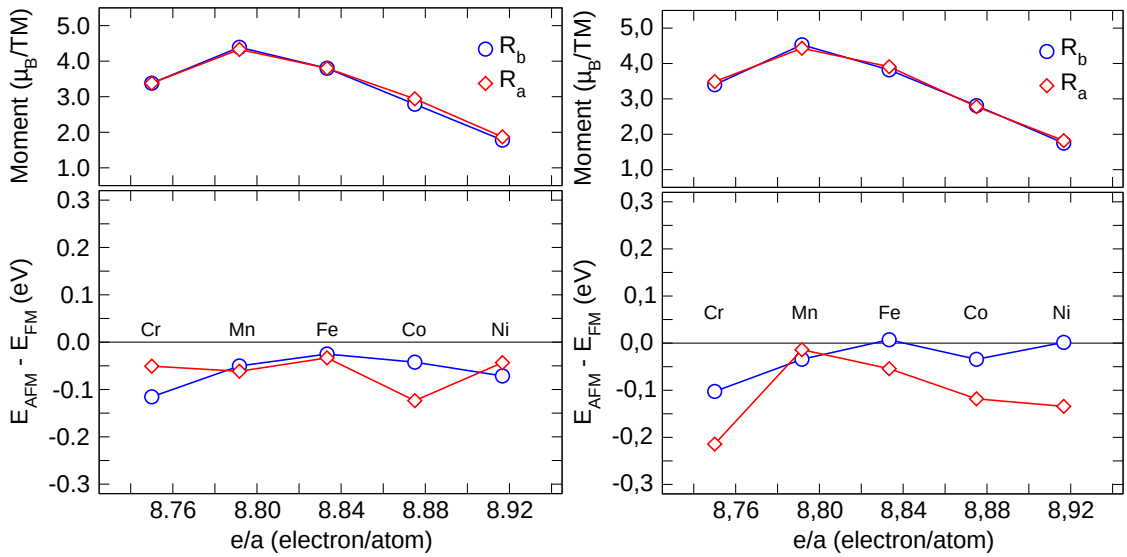

Figure 7.9.: The energy difference ($E_{\mathrm{AFM}} - E_{\mathrm{FM}}$) and the corresponding magnetic moment per TM atom for TM doped ZnO shown in lower and upper panel, respectively, for two n.n. interactions R_a and R_b. The HSE06 result is shown in left and those of HSE06+U is shown in right. In the latter case U is applied on Zn d-orbital with 9 eV.

AFM magnetic configurations for different treatment to the exchange-correlation functional. A clear contrasting tendency is observed for GGA and GGA+U methods to that of the HSE06 and HSE06+U methods. While the TM atoms in both R_a and R_b are found to be probabilistic (details varies with TM) in GGA and GGA+U methods, on the other hand the energy difference ($E_{R_b} - E_{R_a}$) in HSE06 and HSE06+U methods are clearly negative. This suggests that the R_b neighbor configuration is energetically more favorable than R_a for the TM atoms. Although other locations are still not studied, since the separation length of R_b is smaller than R_a, it may be possible to make a general remark that the TM atoms prefer to lie at close proximity.

7.5. Summary

The studies on magnetic interactions of TM (Cr, Mn, Fe, Co, and Ni) as the two n.n. cation positions in wurtzite ZnO are explored by various approximations of exchange-correlation functionals. In all calculations the atomic positions in the lattice are relaxed to avoid any forces acting on atoms. Ferromagnetic solutions are obtained in LDA, GGA and GGA+U with U on Zn d-orbitals. Using GGA+U with U on TM d-orbitals and U on TM and Zn d-orbitals clearly favors antiferromagnetic interactions. The energy differences ($E_{\mathrm{AFM}} - E_{\mathrm{FM}}$) obtained by using the HSE06 hybrid-functional with $\alpha = 0.375$ gives only one n.n. interactions, namely, R_a of Co as ferromagnetic. However, using the HSE06+U with U on Zn d-orbital the energy differences ($E_{\mathrm{AFM}} - E_{\mathrm{FM}}$) suggest that antiferromagntic correlations or paramagnetic behavior is more expected in these systems. The most favorable

location of TM among the two n.n. locations are judged by comparing the energy difference (E_{R_b}-E_{R_a}) obtained from two supercells 223 and 322 for ferromagnetic and antiferromagnetic alignment of spins, respectively. The data is summarized in Table 7.4. The negative value of ($E_{R_b} - E_{R_a}$) in the HSE06 and HSE06+U treatment suggests that n.n. configuration R_b is preferred. This suggests more in favor of finding TM clusters in ZnO. The methodologies adopted to study the DMS problem, namely the HSE06 and the HSE06+U are still under active discussion. The results need to be verified with more rigorous comparison with experiments.

Table 7.4.: Table showing the energy difference ($E_{R_b} - E_{R_a}$) (in eV) obtained from different treatment of exchange-correlation functional when TM is located at R_a and R_b sites modeled by supercells 322 and 223, respectively.

TM	magnetic configuration	LDA	GGA	U on Zn_d	U on TM_d	U on Zn_d and TM_d	HSE06 ($\alpha = 0.38$)	HSE06 ($\alpha = 0.25$) and U (Zn_d)
Cr	FM	0.130	0.139	0.110	0.102	0.004	-1.936	-1.002
	AFM	0.196	0.185	0.142	0.016	0.001	-1.943	-0.890
Mn	FM	0.001	0.004	-0.011	-0.002	0.000	-1.810	-1.329
	AFM	0.019	0.021	0.017	0.010	0.011	-1.638	-1.349
Fe	FM	-0.047	-0.040	0.030	-0.002	0.030	-2.090	-1.386
	AFM	0.036	0.083	0.020	-0.021	0.099	-2.082	-1.433
Co	FM	-0.024	-0.010	-0.022	-0.003	-0.016	-1.309	-0.778
	AFM	0.023	0.032	0.011	0.016	-0.003	-1.725	-1.239
Ni	FM	0.0509	0.097	0.069	0.016	0.013	-1.189	-0.993
	AFM	-0.0595	-0.006	0.060	0.016	-0.001	-1.217	-0.857

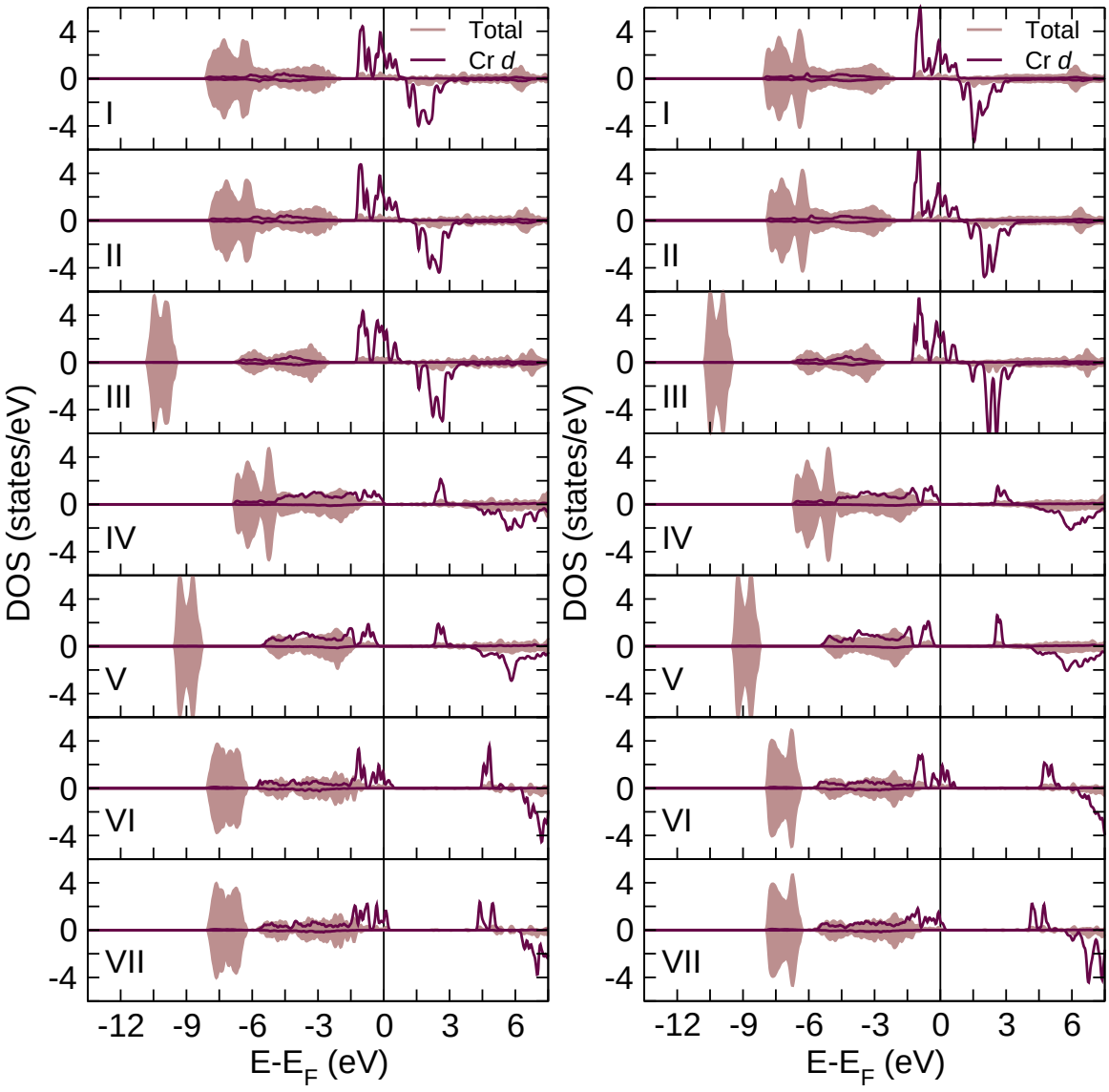

Figure 7.10.: Ferromagnetic DOS of Cr occupying two nearest neighbor R_b (left) and R_a (right) in $Zn_{46}Cr_2O_{48}$. Various types of exchange-correlation functionals, namely LDA (I), GGA (II), GGA+U_{Zn} (III), GGA+U_{Cr} (IV), GGA+U_{Zn}+U_{Cr} (V), HSE06 (VI) and HSE06+U_{Zn} (VII) are treated to study their electronic structure. The brown shaded region is the total density of states plotted per ZnO functional units, while the maroon solid lines represent the Cr d-states per atom.

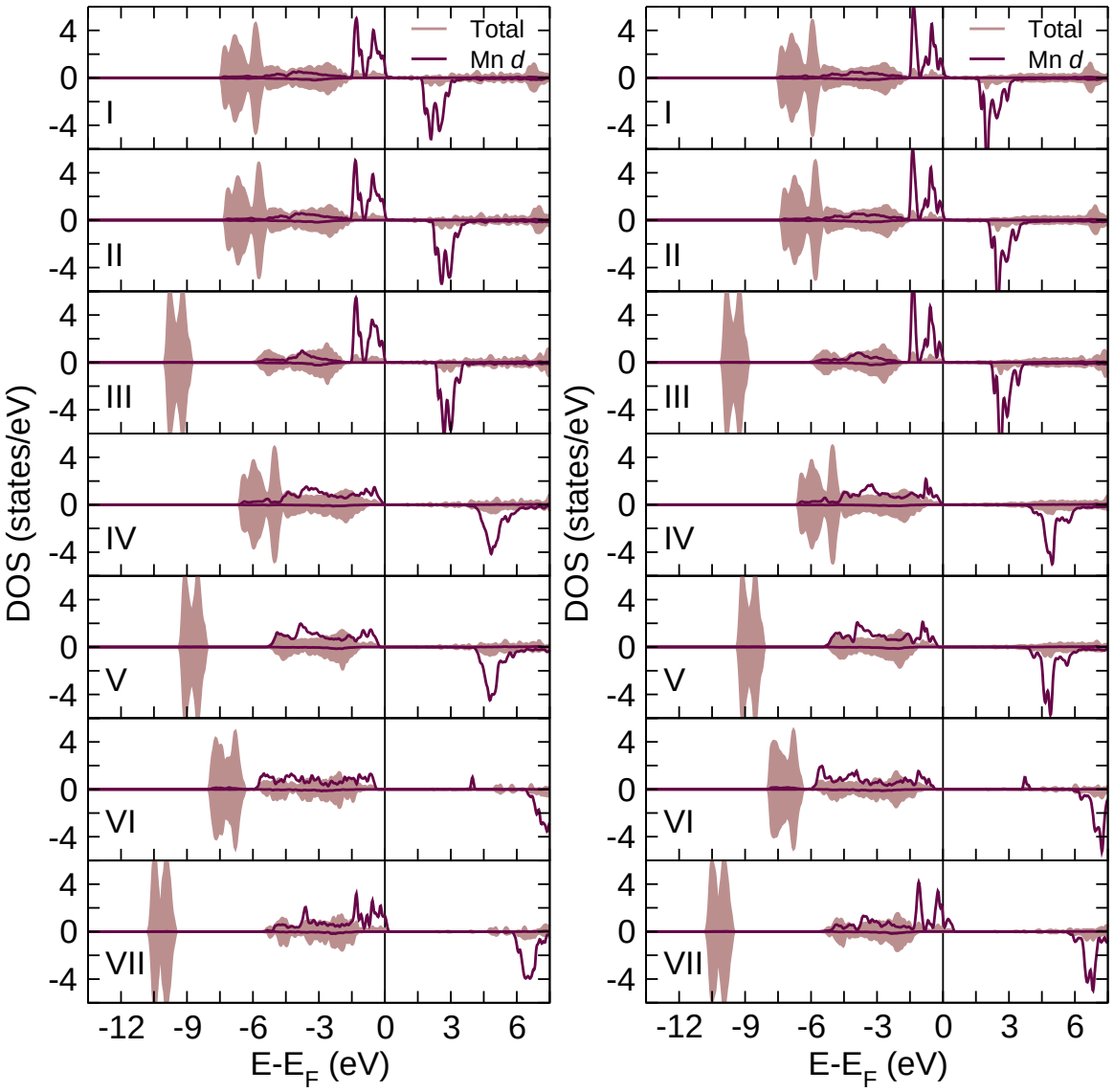

Figure 7.11.: Ferromagnetic DOS of Mn occupying two nearest neighbor R_b (left) and R_a (right) in $Zn_{46}Mn_2O_{48}$. Various types of exchange-correlation functionals, namely LDA (I), GGA (II), GGA+U_{Zn} (III), GGA+U_{Mn} (IV), GGA+U_{Zn}+U_{Mn} (V), HSE06 (VI) and HSE06+U_{Zn} (VII) are treated to study their electronic structure. The brown shaded region is the total density of states plotted per ZnO functional units, while the maroon solid lines represent the Mn d-states per atom.

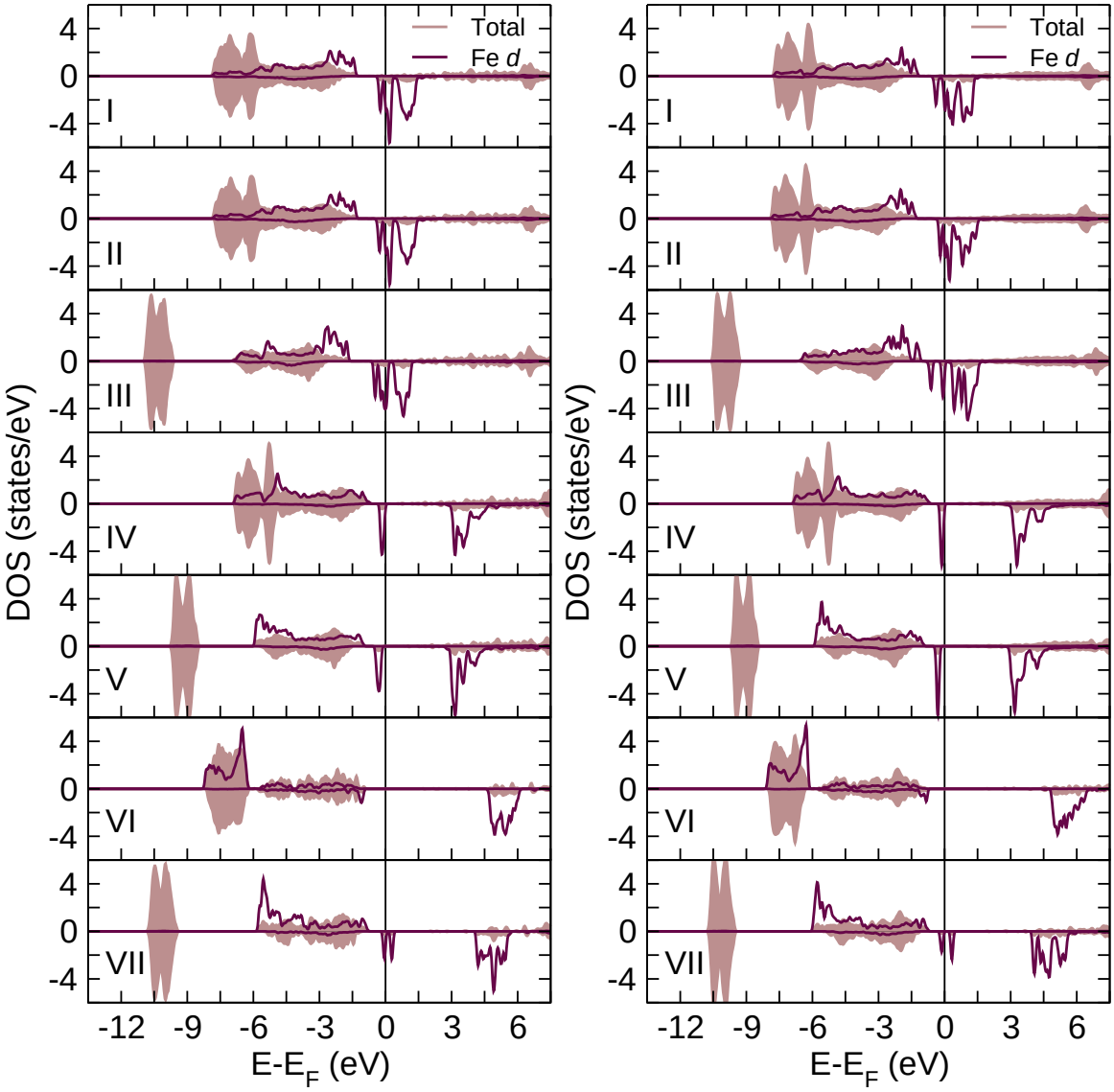

Figure 7.12.: Ferromagnetic DOS of Fe occupying two nearest neighbor R_b (left) and R_a (right) in $Zn_{46}Fe_2O_{48}$. Various types of exchange-correlation functionals, namely LDA (I), GGA (II), GGA+U_{Zn} (III), GGA+U_{Fe} (IV), GGA+U_{Zn}+U_{Fe} (V), HSE06 (VI) and HSE06+U_{Fe} (VII) are treated to study their electronic structure. The brown shaded region is the total density of states plotted per ZnO functional units, while the maroon solid lines represent the Fe d-states per atom.

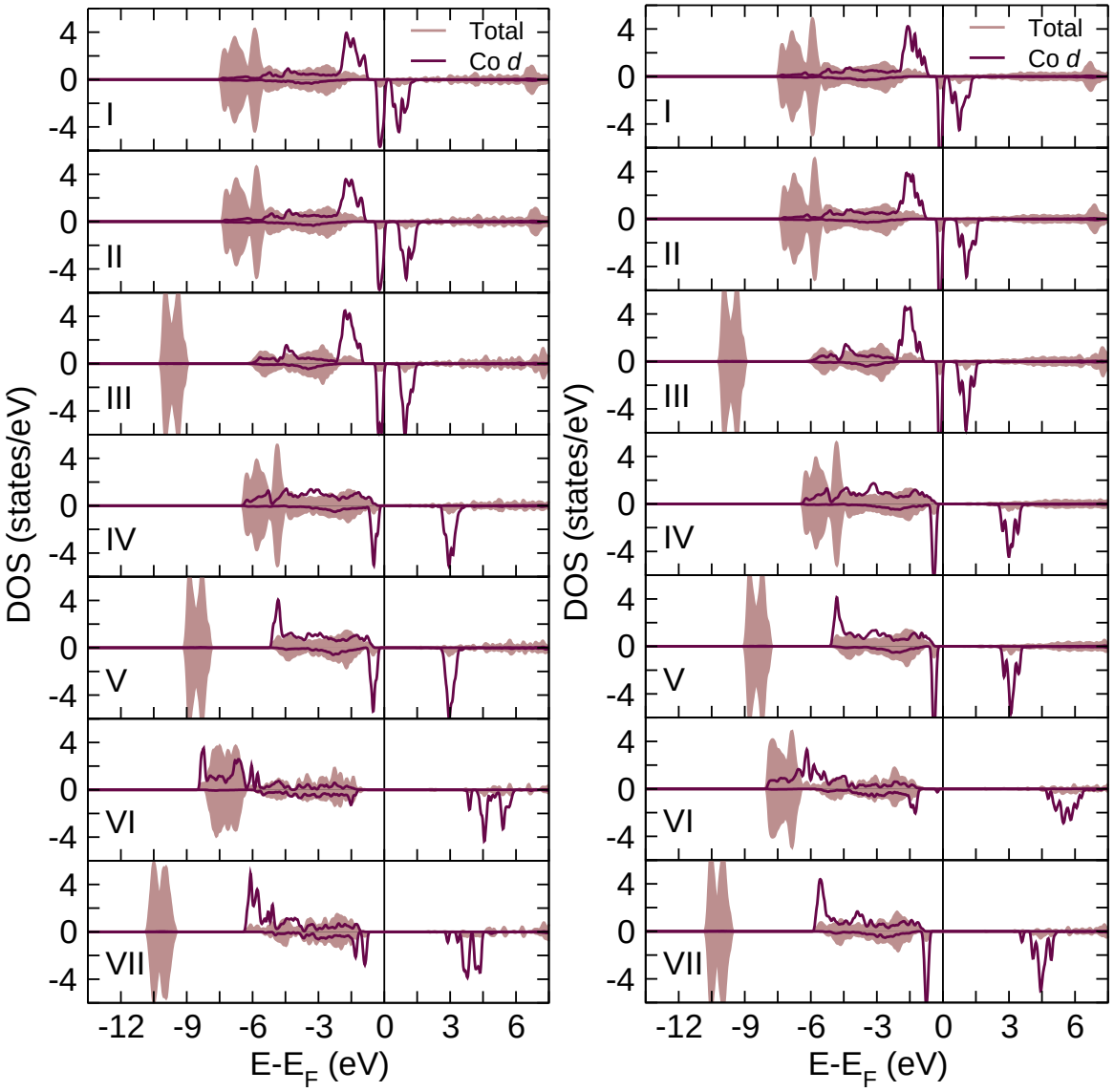

Figure 7.13.: Ferromagnetic DOS of Co occupying two nearest neighbor R_b (left) and R_a (right) in $Zn_{46}Co_2O_{48}$. Various types of exchange-correlation functionals, namely LDA (I), GGA (II), GGA+U_{Zn} (III), GGA+U_{Co} (IV), GGA+U_{Zn}+U_{Co} (V), HSE06 (VI) and HSE06+U_{Zn} (VII) are treated to study their electronic structure. The brown shaded region is the total density of states plotted per ZnO functional units, while the maroon solid lines represent the Co d-states per atom.

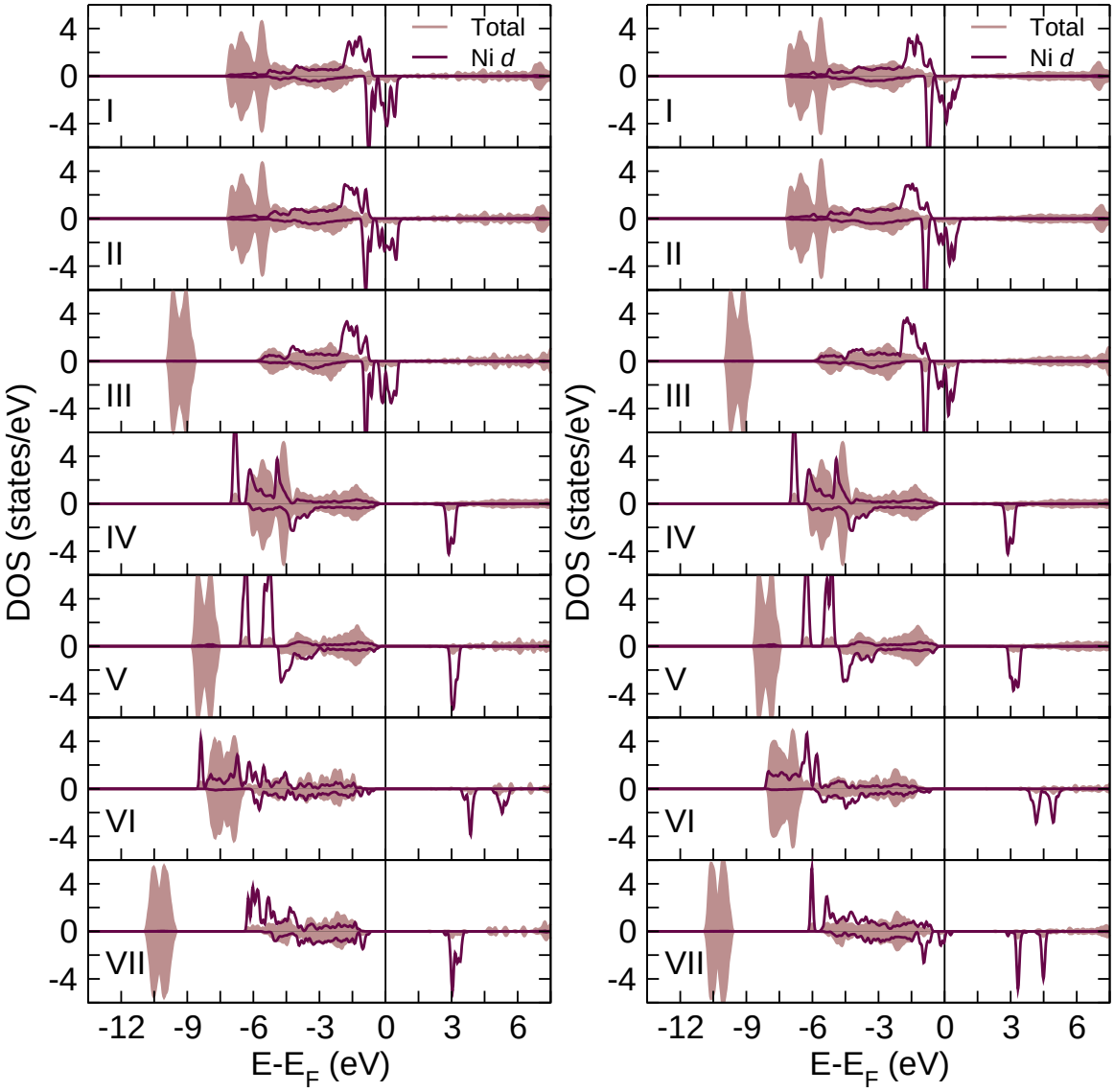

Figure 7.14.: Ferromagnetic DOS of Ni occupying two nearest neighbor R_b (left) and R_a (right) in $Zn_{46}Ni_2O_{48}$. Various types of exchange-correlation functionals, namely LDA (I), GGA (II), GGA+U_{Zn} (III), GGA+U_{Ni} (IV), GGA+U_{Zn}+U_{Ni} (V), HSE06 (VI) and HSE06+U_{Zn} (VII) are treated to study their electronic structure. The brown shaded region is the total density of states plotted per ZnO functional units, while the maroon solid lines represent the Ni d-states per atom.

8. d^0 magnetism in ZnO

8.1. Introduction

Magnetism is a quantum phenomena which arises due to localization of wavefunction and unfilled orbitals. It is well known that the d- and f-orbitals best fulfill these conditions and thus gives rise to magnetic properties. A short review of early models and their drawback have been discussed by Stearns in Ref. [185]. She proposes that the magnetism in pure Fe is an outcome of two contributions. Firstly the localized d-orbitals provides the magnetic moment and secondly there is some percentage of itinerant character of d-orbitals which help to correlate the local magnetic moments [185]. The competition between localization and the kinetic energy is discussed by Jelitto *et al.* [186]

Recently there are reports on magnetism in semiconducting materials without any d- or f- elements [187–190]. Most of the reports are on ionic semiconductors. It can be said for certainty that the picture of local moment positioned on an atom fails in these materials as there are no partially filled d-orbitals. So the argument naturally point towards spin-polarized sp-orbitals. This is commonly known as d^0-magnetism and discussed for different class of materials starting from pure carbon based materials like graphite, graphene, and non-metallic nanoparticles [191, 192]. We know that magnetism can develop in molecules due to overlap of orbitals which may give rise to multiplets (or triplet states) due to Hund's rules. Interestingly, magnetic properties have been reported for almost all ionic semiconductors in presence of intrinsic defects like cation vacancies or in presence of extrinsic defects like anion substitution. Since the early reports on d^0-ferromagnetic semiconductors [187, 189], there has been several reports on defect related magnetism. Cation vacancy defects are shown to develop ferromagnetism in MoO_2 [193], GaN [194, 195], TiO_2 [196], ZnO [197, 198], BN [195, 199], In_2O_3 [200], HfO_2 [201, 202], CaO [203, 204]. Understanding of cation vacancy as a candidate for magnetism has been inspired from the theoretical prediction by Elfimov *et al.* [204]. Defects such as cation substituted with non-magnetic elements have been shown to develop magnetic properties, as in, Mg-doped SnO_2 [205], alkali metals doped in In_2O_3 [200], Ca-doped GaN [194], Li-doped ZnO [206], K-doped SnO_2 [207]. Zhang *et al.* [208] conclude that interstitial Zn is responsible for ferromagnetism observed in ZnO granular samples. Anion substitution defects also are shown to be magnetic, for instance, MgO/MgN complex [209], N-doped MgO [210], N-doped In_2O_3 [211], N-doped TiO_2 [212], C-doped TiO_2 [213], C-doped CdS [214]. N-doped TiO_2 are shown to possess antiferromagnetic interactions for specific structure [215, 216].

From technological aspect this type of magnetism is important. There is active interest in search

for new magnetic materials for various applications like spin light-emitting diodes, spin field-effect transistors, spin valves, magnetic field sensors etc, the operation of which is based on the fundamental properties such as the spin injection, spin transport, optical spin orientation etc. These properties can be achieved in half-metallic ferromagnets (HMF), which are characterized by nonzero DOS at the Fermi level for one spin channel and with a forbidden gap for the other spin channel. The majority of the HMFs are the DMS, where the semiconducting host is doped by TM elements with incompletely filled d-orbitals. In this regard, the observation of d^0-magnetism, due to the non-magnetic doping in ionic semiconductors or due to lack of stoichiometry, also has tremendous prospects if the magnetic correlation between local magnetic moment can be controlled according to our needs. One of the important aspect of this problem is, however, in understanding the phenomena for which there is no unified microscopic theory.

The general aspect of defects in ZnO is very wide [217, 218] and various types of magnetic defects in ZnO have also been reported [180]. In the present chapter the magnetic properties of ZnO from intrinsic and extrinsic defects are discussed, where the intrinsic defects is modeled by vacancies (like zinc vacancy V_{Zn} or oxygen vacancy V_O) and the extrinsic defect is modeled by carbon substituting an ion at the lattice site (on zinc site C_{Zn} and on oxygen site C_O).

8.2. Computational Details

Electronic structure calculations are performed using the plane wave pseudopotential DFT method as implemented is the VASP [92, 93]. The system is modeled as a supercell of wurtzite lattice. While the case of single impurities were studied with relatively smaller supercell, in order to study impurity pairs large supercells namely supercell 622 and 226 have been used (see Fig. 8.1). The need for two type of supercells is justified owing to the fact that wurtzite lattice is a non-centrosymmetric and the bonds are anisotropic along the hexagonal plane and along the c-direction. This has been already discussed in chapter 7. Essentially, supercell 622 scans the interactions along the hexagonal plane of the lattice and the supercell 226 scans the interaction along c-axis of the lattice in a zigzag pattern (see Fig. 8.1).

The lattice constants of the primitive lattice is taken to be a = 3.29 Å, c/a = 1.606 and the relative shift of Zn and O planes, u = 0.380, which were found to be the minimum energy lattice parameters in GGA calculations [219] (see Table 5.1). The doped supercell configuration was relaxed to avoid any strain until the structural energy converged to 10^{-6} eV. At this level of tolerance, the forces in the system is found to be below 3×10^{-4} eV/Å. The relaxation was performed with a Γ-centered Monkhost-Pack k-points grid of $3\times5\times5$ and $5\times5\times3$ for supercells Cell622 and Cell226, respectively. The calculations have been performed using the plane wave energy energy-cutoff of 400 eV. The generalized gradient approximations (GGA) with the PW91 parameterization [94] are used and the ion-electron interactions are treated with the projector-augmented wave (PAW) method [220].

Some of the hybrid-functional (HSE06) studies on the electronic structure of single impurity are

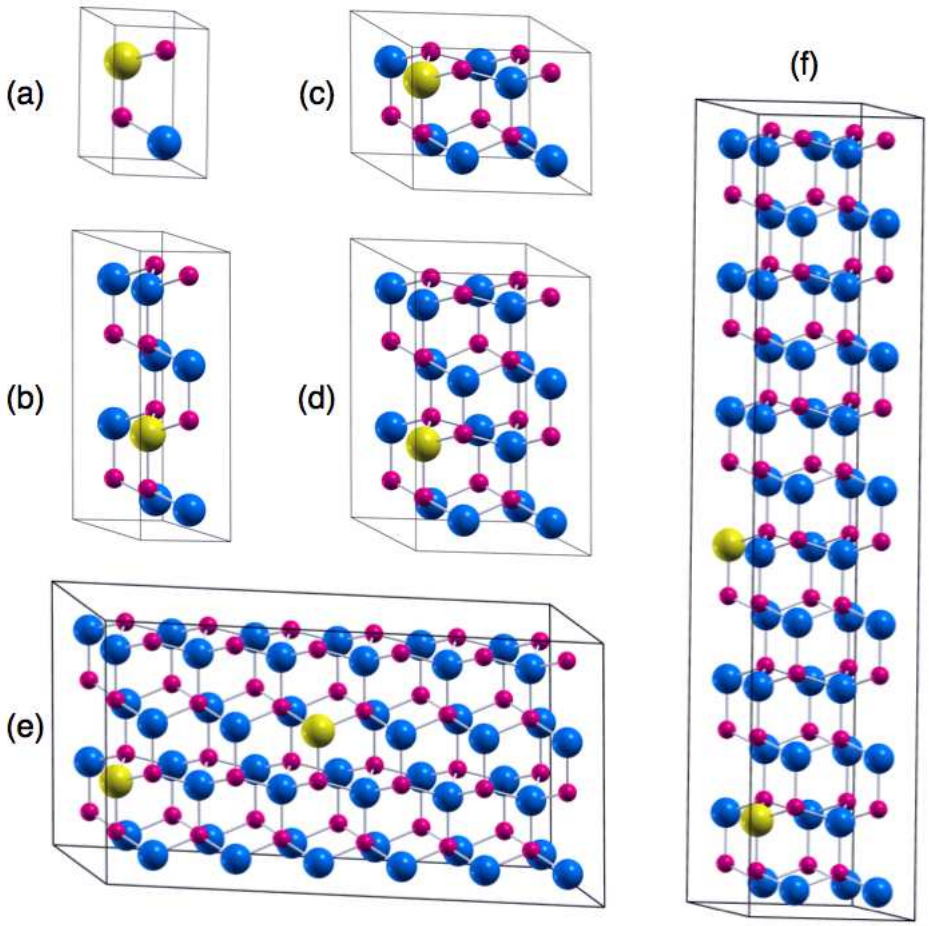

Figure 8.1.: Different supercell size containing one carbon substituted at O site in ZnO. The supercells 111 (a), 122 (b), 221 (c), 222 (d), 622 (e) and 226 (f) that are used in the study are shown. The blue, magenta and yellow spheres represent O, Zn and C, respectively. The concentration of carbon in the supercells vary as 50% for supercell 111, 12.5% for supercells 122 and 221, 6.25% for supercell 222 and two carbon atoms in supercell 226 and 622 represent 4.17% carbon doping.

presented. Some results are cross-checked with the full-potential local-orbital (FPLO) minimum-basis code which is a DFT code with localized basis sets [221].

8.3. Results and discussion

In a recent report Peng *et al.* showed the presence of spontaneous magnetization in ZnO in presence of holes [222]. Their observation was based on DFT calculations with GGA as the exchange-correlation functional and they attributed the spin-polarization to the localization $2p$ states of O. They have generalized their theory to nitride and oxide systems of first-row d^0 semiconductors.

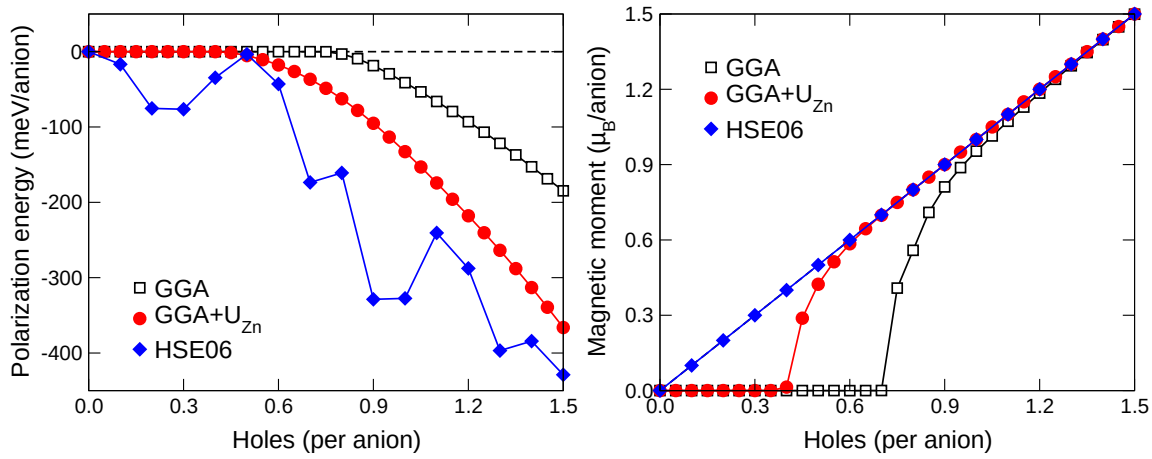

Figure 8.2.: Polarization energy ($E_{\text{spin polarized}}$-$E_{\text{non-spin polarized}}$) versus hole concentration (left) and corresponding magnetic moment (right) obtained for pure ZnO in GGA (black square), GGA+U with U on Zn d-orbital (red circle) and with hybrid-functional (blue square).

8.3.1. Spin-polarization in presence of holes

As a starting point, the calculation of Peng *et al.* are repeated for wurtzite ZnO (their calculation is for zinc blende structure). Studies of the same system is extended by treating the improved exchange-correlation functionals through GGA+U and hybrid-functional treatment. The polarization energy, which is the energy difference of the spin-polarized solution and the non-spin polarized solution ($E_{\text{spin polarized}}$-$E_{\text{non-spin polarized}}$), is plotted against the hole concentration in Fig. 8.2 (left) together with corresponding magnetic moment (right) for studies based on GGA, GGA+U with 7.5 eV U on Zn d-orbital and HSE06 functional with α = 0.375 (α defines the fraction of HF-exchange used in the calculation, refer section 5.4 and 5.5). The calculations are done with 8×8×8 k-point grid of primitive wurtzite ZnO. Some of the prominent observations are;

- In GGA the spin-polarization starts only after some critical concentration of holes added to ZnO. In GGA+U the estimation of critical hole concentration is lower than that of GGA. HSE06 functional, however, leads to spin polarized solution for any value of the hole concentration.

- The polarization energy in HSE06 is not smooth, but following one of its the extremum values we find a fit to the overall polarization energy obtained from GGA+U. The most probable source of oscillation in polarization energy in HSE06 is in the computation of $E_{\text{non-spin polarized}}$. Since $E_{\text{non-spin polarized}}$ achieved through fixed spin moment (FSM) method by fixing the spin to zero, it is expected that self-consistent solution may have been trapped in local-minima leading to non-monotonous behavior of total energy with respect to hole concentration.

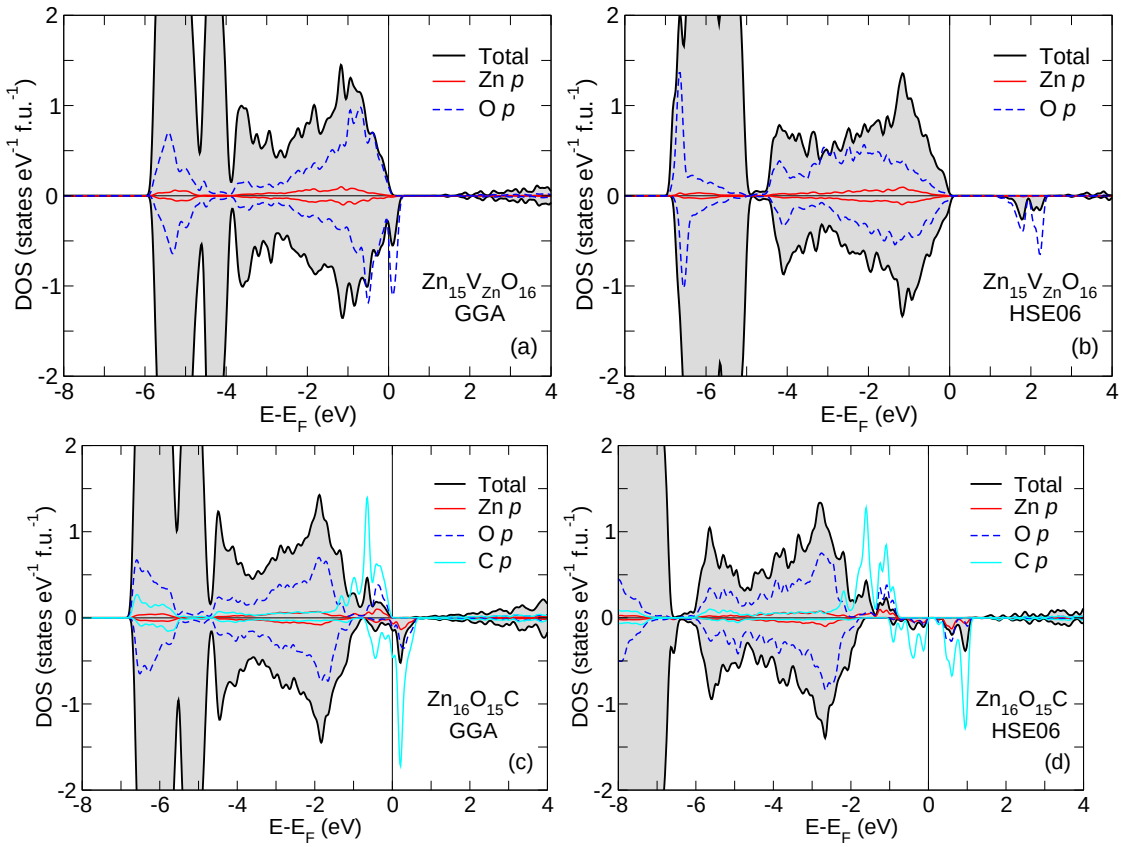

Figure 8.3.: DOS of V_{Zn} in ZnO calculated within GGA (a) and HSE06 (b) and C_O in ZnO calculated within GGA (c) and HSE06 (d). The majority-spin DOS and the minority-spin DOS is plotted as positive and negative y-axis. The total DOS is plotted in the scale states/eV/ZnO. The atomic contribution of nearest neighbor atoms of Zn, O and C are shown according to the system under context for V_{Zn} and C_O.

8.3.2. Intrinsic defects, V_{Zn} and V_O

Out of the many types of defects in ZnO, mainly the intrinsic defects like V_{Zn} and V_O and the substitutional extrinsic defects like C_{Zn} and C_O are studied.

The formation energy is the physical quantity which decides whether a defect configuration is thermodynamically stable or not. Accurate formation energy calculations require right reference of chemical potentials and the chemical potentials are selected depending on the experimental environmental conditions for a particular reaction. The essential idea is to scan through a set of chemical potentials with Fermi energy as a parameter. In semiconductors like ZnO it is recommended to add correction terms in the formation energy calculation to account for the charge defects which add unphysical Coulomb interactions between defect and its periodic images [232–234]. Since only charge neutral defects are discussed here, these correction terms do not contribute to the formation energy. The formation energy calculation is done from Eq. (8.1) as,

Table 8.1.: Formation energies of V_{Zn} and V_O and their comparison to literature. The numbers in parenthesis are the formation energies obtained after applying corrections like GGA+U *etc.* in the corresponding reference.

Defect	Present work	Data from literature
V_{Zn}	5.377 (Zn-rich)	5.8 (10.6)[a], 5.35 (5.60)[b], 6.0[c], 5.47[d], 5.94 (7.38)[e]
	2.364 (O-rich)	1.46[d], (3.8)[e]
V_O	0.873 (Zn-rich)	-0.8[f], 1.5 (2.4)[a], 0.85[g], 1.00 (1.71)[b], 0.9[c], 0.02[d], 0.1[h], 0.69 (3.72)[e], 1.00[i]
	3.886 (O-rich)	2.9[f], 2 (5.4)[a], 4.02[d], 3.2[h], (7.3)[e]

[a] Reference [223], [b] Reference [224], [c] Reference [225], [d] Reference [226], [e] Reference [227], [f] Reference [228], [g] Reference [229], [h] Reference [230], [i] Reference [231]

$$E_f = E_{\mathrm{Tot}} - E_{\mathrm{ZnO}} - \sum_i n_i \mu_i, \tag{8.1}$$

where E_f is the formation energy of the system under study, E_{Tot} is the total energy of the supercell with defect, E_{ZnO} is the energy of pure ZnO with the number of stoichiometric ZnO units, μ_i is the chemical potential and n_i is the number of defects in the supercell.

For ZnO, it is sufficient to treat the environment as O-rich, Zn-rich or something in between. The chemical potential for O-rich condition is taken from the total energy of oxygen molecule, $\mu_{\mathrm{O}} = \frac{1}{2}E_{\mathrm{O}_2}$, and that for Zn-rich condition μ_{O} is obtained as $\mu_{\mathrm{O}} = E_{\mathrm{Zn}^{\mathrm{bulk}}}$. The other corresponding extreme of chemical potentials, i.e. for Zn-poor and O-poor conditions, is taken as $\mu_{\mathrm{Zn}} = \mu_{\mathrm{ZnO}} - \frac{1}{2}E_{\mathrm{O}_2}$ and $\mu_{\mathrm{O}} = \mu_{\mathrm{ZnO}} - E_{\mathrm{Zn}^{\mathrm{bulk}}}$, respectively. The trend in formation energies obtained are in line with reported values, some of which are tabulated in Table 8.1. The formation energy of V_O in Zn-rich condition obtained from GGA and hybrid-functional (HSE) calculations [231] are in remarkable agreement with each other.

Cation vacancy is observed to give a spin polarized solution. The magnetic moment of a cation vacancy in supercell 222 is 1.8 μ_{B}/supercell in GGA. In HSE06 calculation, however, we find integral magnetic moment of 2 μ_{B}/supercell. From the DOS plot of GGA for V_{Zn}, Fig. 8.3 (a), the spin split is clearly observed and the minority-spin DOS crosses the Fermi level suggesting the presence of spin-polarized holes. This is in accordance with Dev *et al.* [235] who get an integral moment of 2 μ_{B}/cell through GGA+U calculations. On the other hand in the DOS with HSE06 functional we find a different picture, as seen in Fig. 8.3 (b). The impurity state is shifted higher in energy into the band gap. The energy gap from valence band maxima to the impurity state is found to be 1.2 eV.

The cation vacancy contributes holes at the cation site and the spatial distribution of surrounding p-orbitals are modified to face the hole site, in order to have as much compensation for the hole charge as

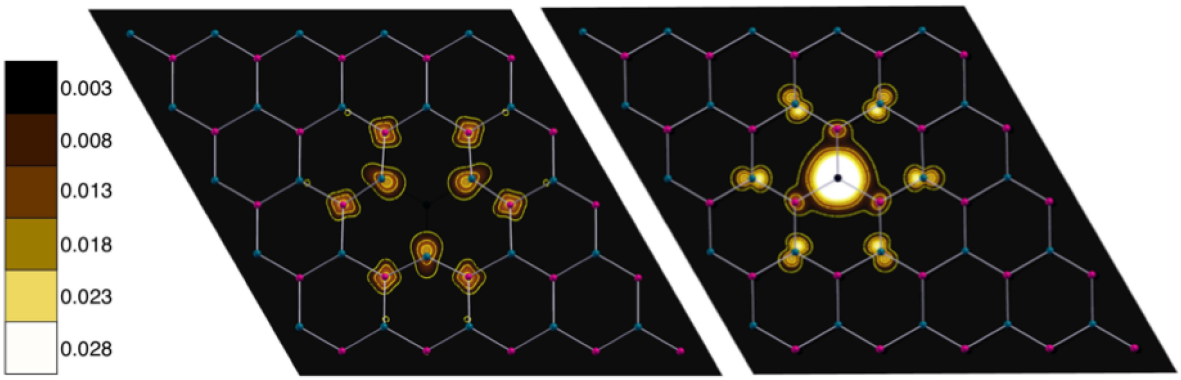

Figure 8.4.: Effective charge density ($\Delta\rho = \rho_\uparrow - \rho_\downarrow$) plotted along the plane perpendicular to c-axis and passing through V_{Zn} (left) and through C_O (right). The magenta, turquoise and black colored balls are used to represent Zn, O and C atoms [236]. The isoline (and also the color gradient) are plotted from 0.003 eÅ^{-3} to 0.028 eÅ^{-3} at intervals of 0.005 eÅ^{-3}. One can clearly observe that the spin-polarization arising from V_{Zn} and C_O extends to more than one nearest neighbor in space.

possible. This is clearly noticeable from the isoline of the effective spin density ($\Delta\rho = \rho_\uparrow - \rho_\downarrow$) plotted in Fig. 8.4 (left). The cation vacancy induces spin polarization in the charge density to distances more than nearest neighbor through the p-orbitals. This is clearly observed in the effective charge density plot of V_{Zn} in Fig. 8.4 (left).

8.3.3. Extrinsic defects, C_{Zn} and C_O

Table 8.2.: Formation energy of C_O and C_{Zn} calculated from Eq. (8.1) and their comparison to literature.

Environment	Defect	carbon rich	carbon poor
Zn-rich	C_O	-3.472	5.181
	C_{Zn}	-3.456	5.197 (4.0[a])
O-rich	C_O	-0.458 (0.4[b])	8.195 (9.4[b])
	C_{Zn}	-6.470 (-6.2[b])	2.183 (2.8[b], 2.2[a])

[a] Reference [237], [a] Reference [179]

The formation energy of carbon substitutionally doped at the Zn and the O site in ZnO is calculated from Eq. (8.1). The chemical potential used for Zn and O are already mentioned in section 8.3.2, the chemical potential of C-rich and for C-poor case is taken as $\mu_C = E_C$ and $\mu_C = E_{CO} - \frac{1}{2}E_{O_2}$, respectively, as stated in Ref. [179]. The values of the formation energy of carbon in ZnO are tabulated in Table 8.2. We observe slight disagreement in the values of the formation energies obtained here as compared to those in Ref. [179] because the calculations in Ref. [179]. The difference being the

calculation with GGA+U (in Ref. [179]) and GGA (present calculation). In Ref. [238] the total energy of single atom of O is used as the chemical potential (μ_O). This may not be appropriate because in reality nascent [O] is an highly unstable entity. It is found that the formation energy of carbon substituting oxygen site (C_O) in ZnO is more favorable in zinc-rich and carbon-rich environmental conditions. On the other hand, the formation energy of C_{Zn} shows that C_{Zn} is either competing (in Zn-rich and C-rich condition) or more stable (in O-rich and C-rich condition) than that of C_O. This is not true in general for other oxide semiconductors: For example, Varley *et al.* have shown that N prefers to substitute the O site in SnO_2 Ref. [239].
We find that single C_O in a ZnO supercell leads to a spin-polarized solution with an integral magnetic moment of $2\mu_B$/C. This has been already discussed in literature [240–242]. The spin polarized solution is lower than the non-spin polarized solution by an energy difference of 3.35 meV/ZnO. The DOS of C_O as single impurity is shown in Fig. 8.3 (c) for GGA. Magnetic solution for C_O is also obtained in HSE06 calculation with an magnetic moment of $2\mu_B$/C. The DOS obtained from HSE06 functional is shown in Fig. 8.3 (d). It can be seen that the impurity states which mainly consists of carbon states are pushed higher into the band gap as compared to the DOS obtained in GGA. The energy gap from Fermi energy to the impurity state is 0.18 eV. More detailed experimental results are required to validate the results shown from the present calculations. Other defects like V_O and C_{Zn} do not lead to any spin polarization and is in good agreement with results of Ref. [243].

8.3.4. Origin of spin polarization

The d^0-magnetic properties of semiconductors are dependent on the relative strength of electronegativity between the dopant element and the anion of the semiconductor. If the bond between the dopant and the cation is weaker then this leads to localized atomic-like $2p$ orbitals of the dopant and a stable magnetic ground state. On the other hand, if the strength of the bond is large this will lead to delocalization of dopant $2p$ orbitals due to strong hybridization with the cations and thus there is reduced or no magnetic state in the system [242]. The observation of spin-polarization and ferromagnetic behavior is not restricted to V_{Zn} or C_O in ZnO. Mavropoulos *et al.* have discussed that substituting the anion site by an element with smaller valence can introduce shallow spin-polarized states in the gap which can then mediate the magnetic interaction through direct exchange mechanism [244]. The electronegativity of the dopants play a crucial role because the strength of the bonds is proportional to the electronegativity of elements involved. It has been shown by Peng *et al.* [245] that many elements in the second row of the periodic table except fluorine, (X = B, N, C as X_O), develop spin polarization. However, the conclusion of Ref. [245] is different for B_O and N_O, namely that they find antiferromagnetic correlations while others find ferromagnetic correlation [222, 246, 247]. The defect states due to N doping (N_O) in ZnO are actively under discussion. Adeagbo *et al.* points out that [180] both N_O and N_{Zn} develops spin-polarization with almost 1 μ_B/N in ZnO. Lyons *et al.* [105] have studied N_O in ZnO by hybrid-functional calculations and observed that N_O defect creates a deep lying impurity state, a situation which is unlikely to give rise to holes. Nevertheless, the deep lying impurity states if

Table 8.3.: Table showing the nearest neighbor distance (n.n) and next-nearest neighbor distance (n.n.n) of C with its periodic boundary image in Å units. The total magnetic moment of the supercell is tabulated in column M_{Total}. The values in parenthesis are the corresponding quantities obtained using FPLO code and those without parenthesis are computed from VASP.

Supercell	$r_{n.n}$ (Å)	$r_{n.n.n}$ (Å)	M_{Total} (μ_B)
111	3.290	5.284	0.291 (0.499)
122	3.290	6.580	0.953 (1.194)
221	5.284	6.580	2.000 (2.000)
222	6.580	10.57	2.000 (2.000)

partially filled can be spin-polarized due to the Hund's rules.

With respect to magnetic properties, a wide variety of conclusions are drawn in literature. Like ZnO, carbon substitution on sulphur site in ZnS have been shown to develop magnetic moment of $2\mu_B$/C and the interaction is projected to be ferromagnetic [248]. ZnS also acquires spin-polarization when doped with second row elements like Be, B, and C impurities, while N-doped ZnS does not display magnetic behavior [249]. Carbon codoped with transition metal atom in ZnO has been shown to lead to ferromagnetism [240]. In a recent study, Rahman *et al.* concluded that carbon substituting the oxygen site in SnO_2 in a deep layer does not develop spin-polarization, rather it induces magnetism on the (001) surface layer and the magnetic moment is localized on surface atoms [250]. It was suggested by Jin *et al.* that room-temperature ferromagnetism of undoped GaN nanoparticles arises from N-dangling bonds generated by Ga-vacancies on the surface [251].

Chan *et al.* demonstrate that important correlation effects due to open p-shells exist not only for elements in the second row of periodic table but also for much heavier anions like Te. This dramatically changes the structural, electronic and magnetic properties along the series of Zn compounds (ZnO, ZnS, ZnSe, and ZnTe) and impedes ferromagnetism [252]. Using the self-interaction correction (SIC) scheme Droghetti *et al.* conclude that the resulting ferromagnetism may vanish [253]. Thus it is apparent that different corrections to the electronic structure calculations result in different conclusions.

8.3.5. Supercell dependent magnetic properties

One of the main difficulties in studying DMS by supercell method is that one has to construct very large supercell to mimic practical limit of doping concentrations. With smaller supercell the doping concentration is more and as a result the impurity atoms feel the periodic image and hybridize with itself to form impurity bands. A systematic study by changing the supercell has been done to see the effect of carbon states with change in the supercell size. In this context, four supercells as shown in Fig. 8.1 are discussed. For all the supercells only one carbon atom is substituted in place of oxygen resulting in carbon concentration of 50% (supercell 111), 12.5% (both supercell 122 and 221) and

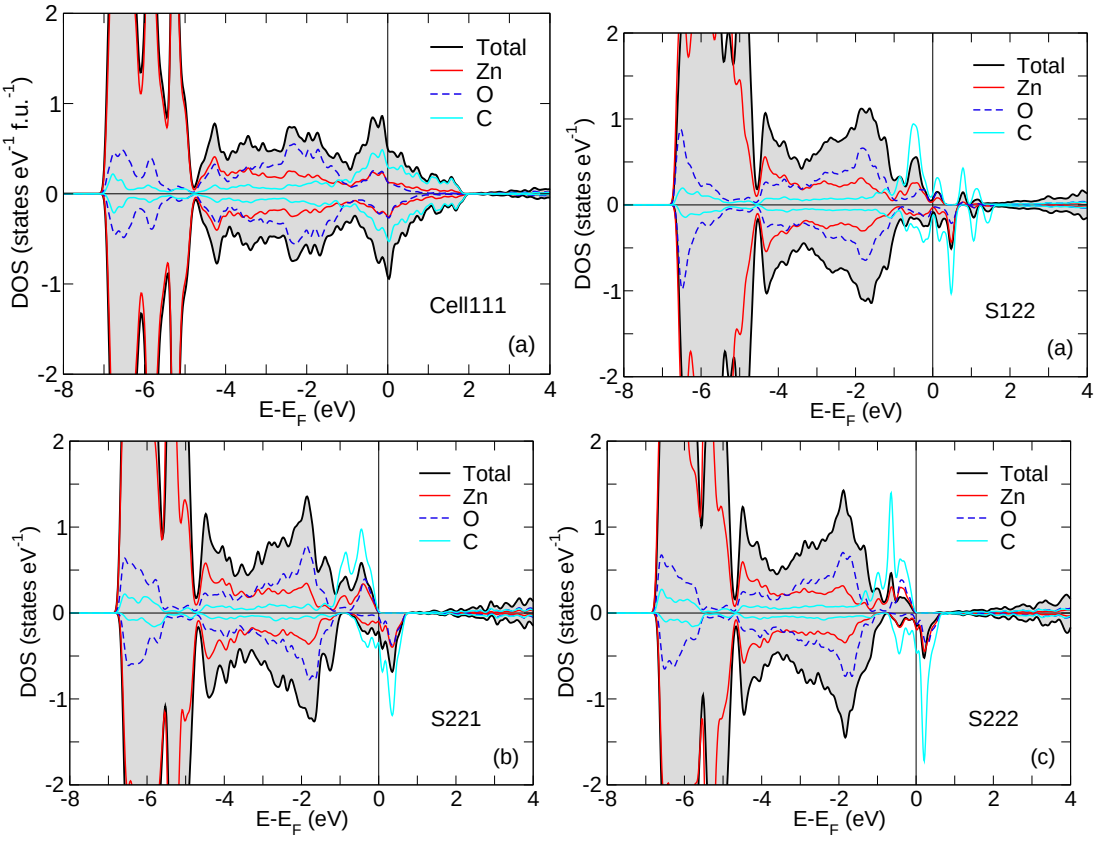

Figure 8.5.: DOS of C_O for supercells 111, 122, 221 and 222 shown in upper left, upper right, lower left and lower right panel, respectively. The total DOS is plotted as states/eV/ZnO and the atomic DOS are plotted as states/eV/atom. Only the nearest Zn and O atoms shown in the DOS plots. The impurity carbon peak changes from metallic DOS for smaller supercell to localized impurity like peaks with increase in supercell.

6.25% (supercell 222), respectively. From the DOS of supercell 111, Fig. 8.5 (a) it is inferred that the system is metallic and the magnetic moment is significantly quenched (see Table 8.3). Although the supercells 221 and 122 are equivalent in the doping concentration, they do not give the equivalent electronic properties, as shown by the DOS in Fig. 8.5 (b) and (c). The volume versus energy and the volume versus magnetic moment for both the supercells are plotted in Fig. 8.6. One observes from the volume versus energy curve that supercell 122 has slightly lower total energy than that of supercell 221. The magnetic moment of supercell 122 is lower than that of the supercell 221 at all volumes. Above differences between supercell 221 and 122 are explained by considering the separation of carbon and its periodic image. The nearest neighbor separation and next nearest neighbor anion site separation are tabulated together with the magnetic moment information in Table 8.3 for different supercells. It is observed that the nearest neighbor separation of C in supercells 111 and 122 are small which lead to the mixing of carbon orbitals with that of its periodic image, thus forming band states. The resulting band states quench magnetic moment in the supercell. In comparison to supercell 122,

supercell 221 has slightly larger nearest neighbor distance, this does not lead to sufficient hybridization of carbon with its image and thus the magnetic moment is larger. This is also reflected in the total energy, which is lower for the supercell 122 than that of supercell 221. Thus the change in total energy difference difference ($\Delta E = E(\mathrm{Cell221}) - E(\mathrm{Cell122})$) with respect to volume in the inset of Fig. 8.6 can be explained by similar argument. The site-projected density of states for corresponding supercells are plotted in Fig. 8.5 (a)-(d), which shows the evolution of carbon impurity states from metallic behavior towards more localized impurity states.

In order to check whether the spin-polarization observed is a consequence of the states trapped in some local minima, some fixed spin moment (FSM) calculations were carried out. The plot in Fig. 8.7 (a) shows the polarization energy with respect to the fixed spin moment. The polarization energy is defined as the energy difference of the system at a given fixed spin to that of the energy at zero spin moment. The plot shows the polarization energy of relaxed and unrelaxed lattice calculated by VASP and compared to that of the unrelaxed lattice calculated by FPLO for the four supercells shown in Fig 8.1 (a)-(d). It can be observed that the effect of relaxation on the polarization energy is not much as found in Fig. 8.7 (a) (compare the square and the circle symbols). The details of the trends of polarization energy can be corroborated one-to-one with that of the density of states of the supercells in Fig. 8.5 (a)-(d). For metallic system (supercell 111) the magnetic moment obtained is small (as tabulated in Table 8.3), as a result the minimum polarization energy is obtained at smaller value for FSM. The agreement of the polarization energy calculations obtained from two different implementation of DFT is encouraging. The total magnetic moment also show similar trends in both the codes, tabulated in Table. (8.3).

In order to study the magnetic interaction between the carbon atoms as a function of C_O-C_O separation in the lattice large supercells (supercell 226 and 622) are used. The concentration of carbon in these supercells turns out to be 4.2% which is within the experimental range of impurity concentration. When the carbon atoms are separated far from each other, each carbon contributes a total of 2 μ_B (together with induced magnetic moment on neighboring Zn and O atoms) and thereby the total moment in the supercell is 4 μ_B.

One can deduce the nature of exchange interaction between C_O-C_O from the distance dependent behavior. Maximum carbon-carbon separation of around 16 Å and 11 Å in Cell226 and Cell622, respectively, is achieved. Special attention is paid to check that no periodic image is smaller than the C_O-C_O separation in consideration. This may be a cumbersome at first glance, but some mathematical trick simplifies the task. It can be shown that the difference between the components of the position vector must be less than half of the corresponding component of lattice vectors. The difference between the total energy of antiferromagnetic orientation of carbon spins to that of the the ferromagnetic orientation of carbon spins ($E_{\mathrm{AFM}} - E_{\mathrm{FM}}$) is plotted in Fig. 8.8. The upper panel and the lower panel of Fig. 8.8 are the energy difference for supercells 226 and 622, respectively. Several observations can be made from the graphs of Fig. 8.8.

1. Atomic relaxation in the lattice has no major effect in the supercell 226. On the other hand

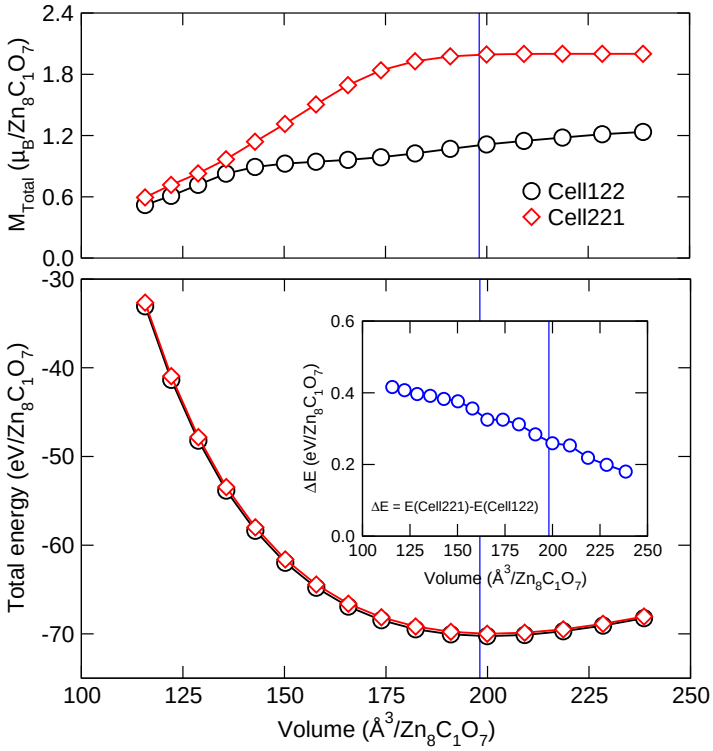

Figure 8.6.: Total magnetic moment in the supercell versus volume (upper panel) and the total energy versus volume (lower panel) of C_O in ZnO for the supercells 122 and 221 shown in dark (black) circles and light (red) circles. Even though the concentration of carbon is same in two supercells, the electronic structure is different owing to the difference between separation of carbon atom with its image. The supercell with low value of the separation has lower total energy and reduced carbon moment due to metallic states. The difference in total energy, shown as inset in lower panel, falls with increasing volume in line with the conjecture that carbon-carbon separation influences the electronic structure.

in supercell 622 lattice relaxation reduces the magnetic energy to almost half of the unrelaxed values.

2. The system favors ferromagnetic interaction whose magnitude goes down with larger separation. This is more clear in supercell 226. Since the magnetic interaction in strongly anisotropic, hence the total energy difference leads to different values depending on the orientation of two carbon atoms with respect to the wurtzite crystal lattice. As a result we do not find a systematic dependence of the energy difference on the carbon separation. This is more prominent in the supercell 622.

3. The nearest neighbor separation relaxation leads to carbon-dimer and favors non-magnetic solution. The C_O-C_O bond length is reduced from initial lattice separations (3.26 Å along hexagonal plane and 3.25 Å in the next stacking plane along the c-axis) to 1.26 Å and 1.35 Å, respec-

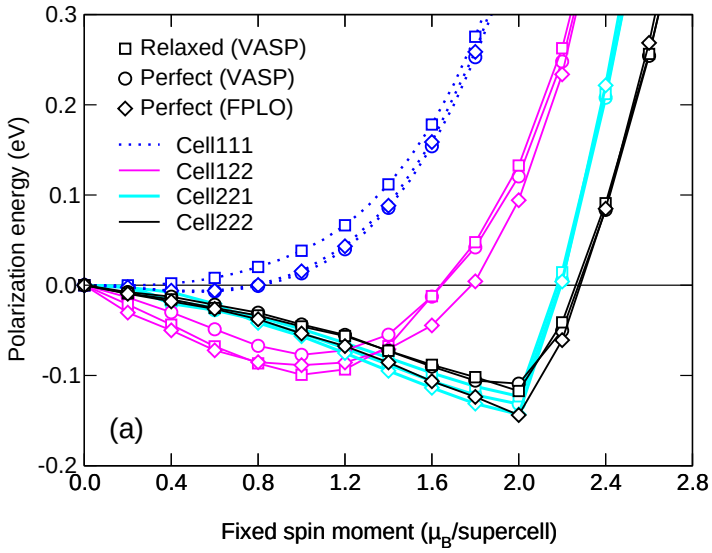

Figure 8.7.: Polarization energy as a function of magnetic moment (upper panel) for different supercells calculated from fixed spin moment (FSM) calculations. The minima in polarization energy gives the most stable magnetic moment in the supercell. Polarization energy as a function of FSM obtained from VASP and that of FPLO are in clear agreement with each other. Lattice relaxation only has only minor effect in the polarization energy.

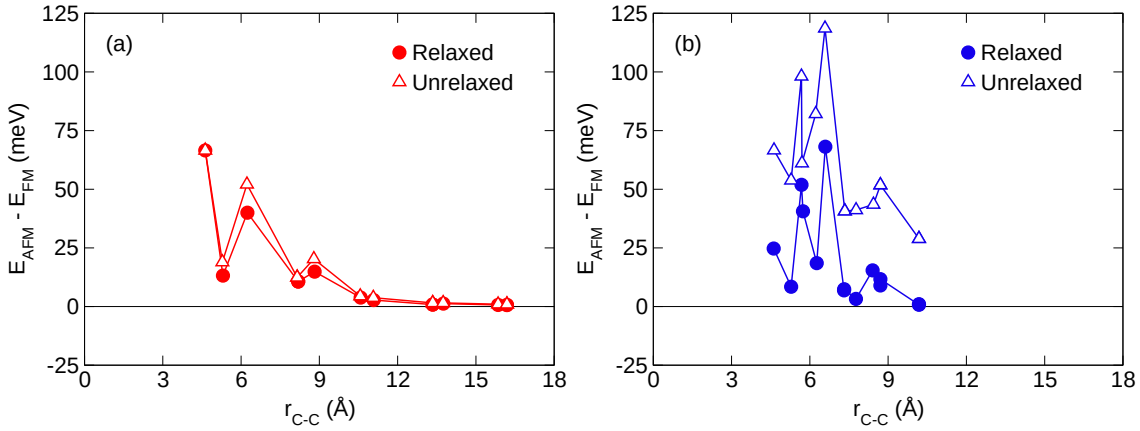

Figure 8.8.: Final separation of C_O vs. energy difference between anti-ferromagnetic and ferromagnetic orientation of carbon spins for supercells 226 (left) and 622 (right). The open symbols are the magnetic energy for unrelaxed supercells and the filled symbols are the relaxed supercell.

tively. The dimer does not contribute to any magnetic moment in GGA. Treating the exchange-correlation potential through the screened hybrid functional, Wu *et al.* have found a triplet ground state for the C_2 dimer in ZnO [254]. The idea of such type of elemental dimers from the second row of periodic table has been projected as a strong contender for ferromagnetism other

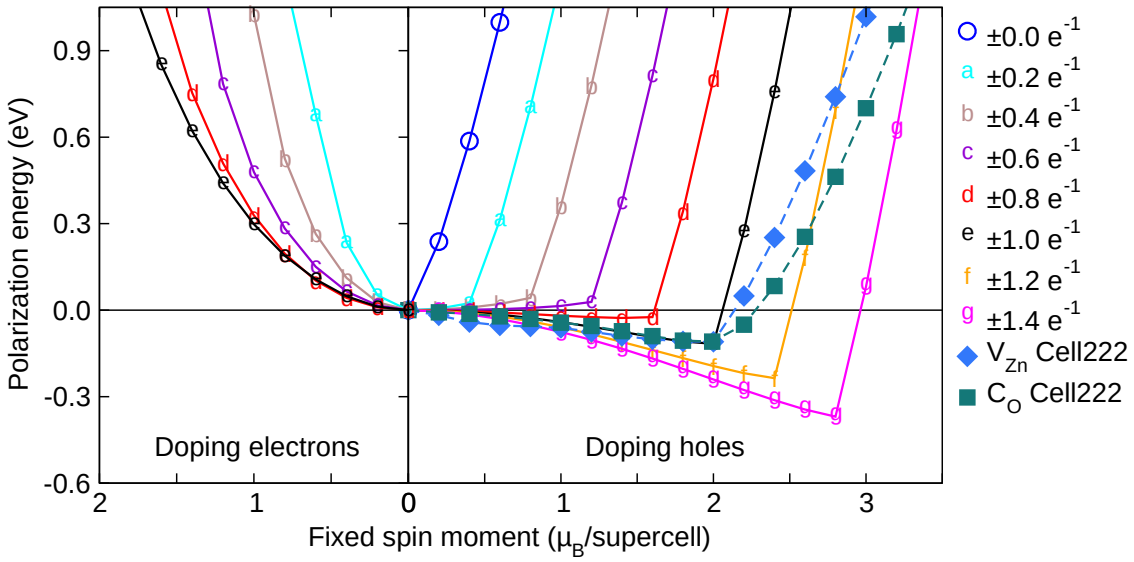

Figure 8.9.: Polarization energy in ZnO for excess electrons concentration, hole concentration, V_{Zn} defect in ZnO and C_O defect in ZnO plotted against the fixed spin moment. Please notice that the y-scale is positive at both sides of origin of axis. Excess electrons do not favor magnetic solutions at any concentrations. Hole concentration develops magnetic solution only from certain concentration onwards. The hole concentration per O is denoted as -e. Holes at concentration of one hole per oxygen, V_{Zn} and C_O develop magnetic moment of 2 μ_B per supercell. We find that for all the three cases the value of the polarization energy at minima are similar.

ionic semiconductors [255, 256].

8.3.6. Analogy between different kinds of defect magnetism

It is shown that magnetic solution for ZnO are stabilized with intrinsic and extrinsic defects like V_{Zn} and C_O, respectively. Magnetic solution in ZnO at sufficient hole concentration has also been reported through DFT studies [222], which were verified here by taking the exchange-correlation functional beyond GGA. It must be noted that all the three mechanism involve holes as the carrier. To clarify the similarity of different mechanisms the plot in Fig. 8.9 shows the polarization energy with respect to fixed spin moment. Please note that the abscissa of the plot is positive both to the right of zero and to the left of zero. With electron doping in pure ZnO it is found that the total energy increases parabolically with increase in fixed spin moment suggesting that non-spin polarized solution is the lowest energy. On the other hand, with holes the total energy with respect to FSM shows a point of inflation. The corresponding value of the FSM at the inflation point is dependent on the concentration of holes in the system which slowly goes to negative polarization energy and becomes a minima. ZnO acquires magnetic moment of 2 μ_B at hole concentration of 2 hole per primitive cell (also represented as 1 hole/O).

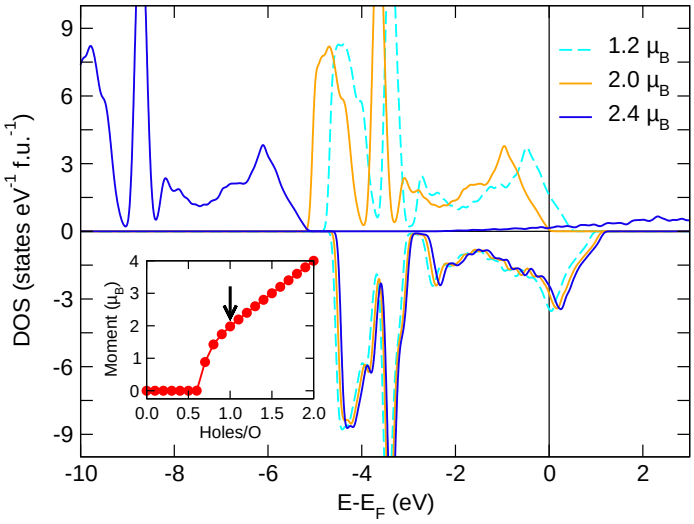

Figure 8.10.: DOS at different fixed spin moment for 1 hole/O in ZnO. It is observed that at FSM value of 2 μ_B, the majority channel is completely filled. Any further increase in magnetic moment would mean accommodating electrons in the conduction band of the majority spin. This would cost large energy. Hence we find a steep rise of polarization energy just after the minima in Fig. 8.9 with the increase in FSM.

The polarization energy versus fixed spin moment for V_{Zn} and C_O are shown as filled blue diamond and filled green square in Fig. 8.9, respectively. It is found that the polarization energy of V_{Zn}, C_O and hole concentration of one hole per oxygen in ZnO supercell are similar in magnitude suggesting that the polarization energy depends on the electronic structure of the host and not on the type of impurity involved.

In order to understand the steep rise of the polarization energies beyond the minima with increase in magnetic moment, the DOS at the hole concentration of 1 hole/O for various fixed moments is shown in Fig. 8.10. In the presence of a large hole concentration the valence band, consisting mainly of O p states, is split and the Fermi level passes through the DOS of both, the majority and the minority spin channel. As the magnetic moment is increased, the DOS of the majority spin channel is shifted such that the band edge approaches the Fermi level. The DOS of the minority spin channel moves opposite to the DOS of the maority spin channel because of the increasing in magnetic moment. At the magnetic moment corresponding to minimum polarization energy the DOS of majority spin channel is completely filled. Since there are no states available to accommodate additional electrons in the majority spin channel, any further increase in the magnetic moment must add electrons to the conduction band states at the majority spin-channel. This is reflected in the large shift of the majority spin DOS with M = 2.4 μ_B. Moving electrons to states above gap costs energy and hence the polarization energy rises sharply after the minimum is obtained. On the other hand, impurities, like V_{Zn} and C_O, contribute acceptor states which lie within the band gap, but more towards the conduction band. The energy needed to populate the impurity acceptor states is comparatively small

resulting in softer increase of the polarization energy beyond the minimum.

8.3.7. Experimental perspective

It is important at this stage to understand why observation of magnetic phenomena in ZnO may be difficult to obtain from an experimental stand point.

1. It is observed that formation energy of V_{Zn} as a magnetic defect is positive and hence it is thermodynamically not a stable defect in many common environment. The formation energy of C_O although is negative at some selective environment, C_{Zn} which is non-magnetic defect has equivalent or still lower formation energy. Thus the the probability of C_O in ZnO is low as compared to C_{Zn} (see Table (8.1) and Table (8.2)).

2. It is shown that defect mechanism arise for p-type ZnO (with V_{Zn}, C_O or with holes). It is a common knowledge however that under normal conditions n-type defects are favorable which is non magnetic.

3. It is known that H is a common impurity in ZnO and it is an electron-donor. Reference calculations with H codoped in the ZnO supercell with single V_{Zn} and C_O defects show each electron from H compensates one Bohr magneton of magnetic moment. Upon addition of two H in the supercell, the magnetic moment was completely quenched to zero. In experiments the hydrogen concentration during ZnO synthesis is difficult to control. It has been shown that the energy barrier for escape of H through ZnO surface can be as large as 0.58 eV [257]. Hence it may be safely assumed that most of the hydrogen available are trapped in the ZnO host and presuming that the concentration of V_{Zn} or that of C_O is less than half of hydrogen concentration, one can justify why some of the successful C_O doping may still have no magnetic properties.

8.4. Summary

The magnetic properties arising from non-TM doped ZnO has been studied in this chapter. Mainly three cases were discussed, namely, magnetism due to hole doped, magnetism due to V_{Zn} defects and magnetic properties of C_O defects. Typical similarity of all the three situations are that they all lead to p-type carriers (based on valency electron counting). This leads to the conjecture that p-type environment is essential to make ZnO magnetic. The practical verification of this conjecture is rather difficult due to the fact that commonly ZnO is found to possess n-type carriers. Comparing the polarization energy we find that the V_{Zn}, C_O and hole doped at a concentration of one hole per oxygen lead to similar value of polarization energy. Relatively large supercells are used to study the distance dependent magnetic interaction for C_O-C_O defects. Some of the difficulties in realizing magnetic ZnO in experiments have been discussed through fundamental aspect of material properties like defect formation energy and unwanted hydrogen diffusion.

9. ZnO cluster

9.1. Introduction

Zinc oxide clusters attract much of attention because of their potential applications in technology. ZnO clusters find application in opto-electronic devices and also as catalyst. There have been several attempts to study ZnO nanoparticles by theoretical methods. For instance, the stable configurations of $(ZnO)_n$, $n < 16$, have been studied by molecular dynamics using pair-potentials [258]. The authors have shown that stable spheroid molecules of ZnO may exist and it is likely that $(ZnO)_n$ fullerene structures are most stable around some particular magic numbers. From symmetry arguments the value of n for stable fullerene structure is predicted to be 12 and 16. There are studies of the ground state structure of ZnO clusters with $n \leq 6$ based on DFT with GGA as the exchange correlation energy functional [259] and with hybrid-functionals [260, 261]. From the above theoretical studies the ring structure were predicted as the global minima for cluster size $n \leq 7$. Clusters with $n = 7$ and 8 preferred three-dimensional spheroidal structure. Matxain *et al.* have studied the excitation energies of small ZnO clusters ($n \leq 15$) with ring-like and bubble-like configurations using the time-dependent DFT. It is shown that the electronic excitation energy strongly depends on the geometrical structure of the cluster. In a recent report, Zhao *et al.* have studied structure, formation energy and electronic structures of ZnO with $9 \leq n \leq 64$ [262]. They have considered bubble-like and wurtzite-like clusters and have concluded that the bubble-like clusters are more stable than the wurtzite-like clusters for $n < 26$. For $n \geq 26$ formation of a core with four-fold coordination of atoms is more favorable. Using an evolutionary algorithm some stable structures have been reported in Ref. [263].

Bulgakov *et al.* have used laser ablation technique for cluster synthesis and reported on both stoichiometric and non-stoichiometric Zn_mO_n clusters [264]. They find that magic number clusters at $n =$ 9, 15 and 16 are more probable in occurence and have hollow spheroid structures related to fullerene. They also find local abundance minimum at $n = 13$ is concluded from the time-of-flight mass spectrometry [264]. Wu *et al.* have prepared small $(ZnO)_n$, n = 1-15, clusters using the electroporation of unilamellar vesicles [265]. They have compared their results with the DFT for the structure and TDDFT for the optical-transitions to match the maxima and the minima in the absorption bands at n = 2,5 and 12. The literature survey of experimental reports are not exhaustive. The cluster studies presented in this chapter includes some interesting features regarding magnetism.

9.2. Pure ZnO clusters

In the *bottom-up* approach, clusters may be treated as building block for bulk. Hence it is reasonable to start cluster studies with configurations cut from bulk structures. Several important cases like clusters with one ZnO unit, tetrahedral unit with Zn tetrahedral embedding oxygen atom and its mirror constituent of O tetrahedra embedding zinc atom is considered. One must note that the last two cases are the tetrahedral bonding units in bulk ZnO. Some clusters are considered which consist of tetrahedral interstitial, octahedral interstitial region or both due to the cation and anion atoms. The clusters are relaxed using the conjugate gradient algorithm as implemented in VASP to search for its structural optimized geometry. Both GGA and HSE06 with α = 0.375 have been used to make comparative studies.

Figure 9.1 and 9.2 shows the schematic diagram of initial positions, final positions obtained in GGA and the final positions obtained in HSE06 functional (α = 0.375). Several cases have been considered. Case (a) is the simplest unit of one ZnO, cases (b) and (c) are those of the tetrahedral bonding units with one atom surrounded with four atoms of the other type. Case (b) is zinc centered, while case (c) is O centered. Case (d) signifies the penetrating tetrahedron made up of opposite types of atoms. This type of structure when cut from bulk has six atoms with dangling bonds, three of each kind. Case (e) is similar to case (d) except that the penetrating tetrahedron of each type of atoms are now aligned oppositely. This type of arrangement leads to closed structure. Case (f) signifies the penetration of two structures constituting the octahedral interstitial formed for each type of clusters. Special cases of penetrating tetrahedron interstitial and octahedral interstitial structures are depicted as cases (g) and (h) in Fig. 9.2.

Some of the interesting observations are as follows: Case (a) shows that the bond length of single Zn and O bond is estimated a little higher in HSE06 calculations than that of GGA. It must be noted that the bulk lattice constant obtained from HSE06 functional (Ref. [105]), is smaller than those obtained from the GGA (see Table 5.1). For the case of (b) and (c), which are non-stoichiometric, the prediction of final structure is completely different.

It is observed that the structures (b) and (c) relaxes to a planar structure in GGA while in HSE06 the relaxed structure is symmetric three-dimensional structure with the O-O bonds and the Zn$--$Zn bonds lying perpendicular to each other. Both the relaxed structures posses a total magnetic moment of 2 μ_{B} and the average magnetic moment per element is tabulated in Table 9.1. The spin-polarization is shared by all atoms for case (c), however, for case (b) the spin polarization is mostly on O atoms.

In spite of different starting geometries, the relaxation in both GGA and HSE06 leads to similar final structures.The final structure is of characteristic geometry where the Zn atoms form an inner tetrahedron and O constitute the outer tetrahedron which is reverse with respect to the orientation of the inner Zn tetrahedron. The relaxed geometries for the structure with initial geometry constructed from inter-penetrating octahedral interstitial boundary atoms are shown in Fig. 9.1 (f) and Fig. 9.2 (h) and that of inter-penetrating octahedron and tetrahedron together is shown in Fig. 9.2 (g). Comparing

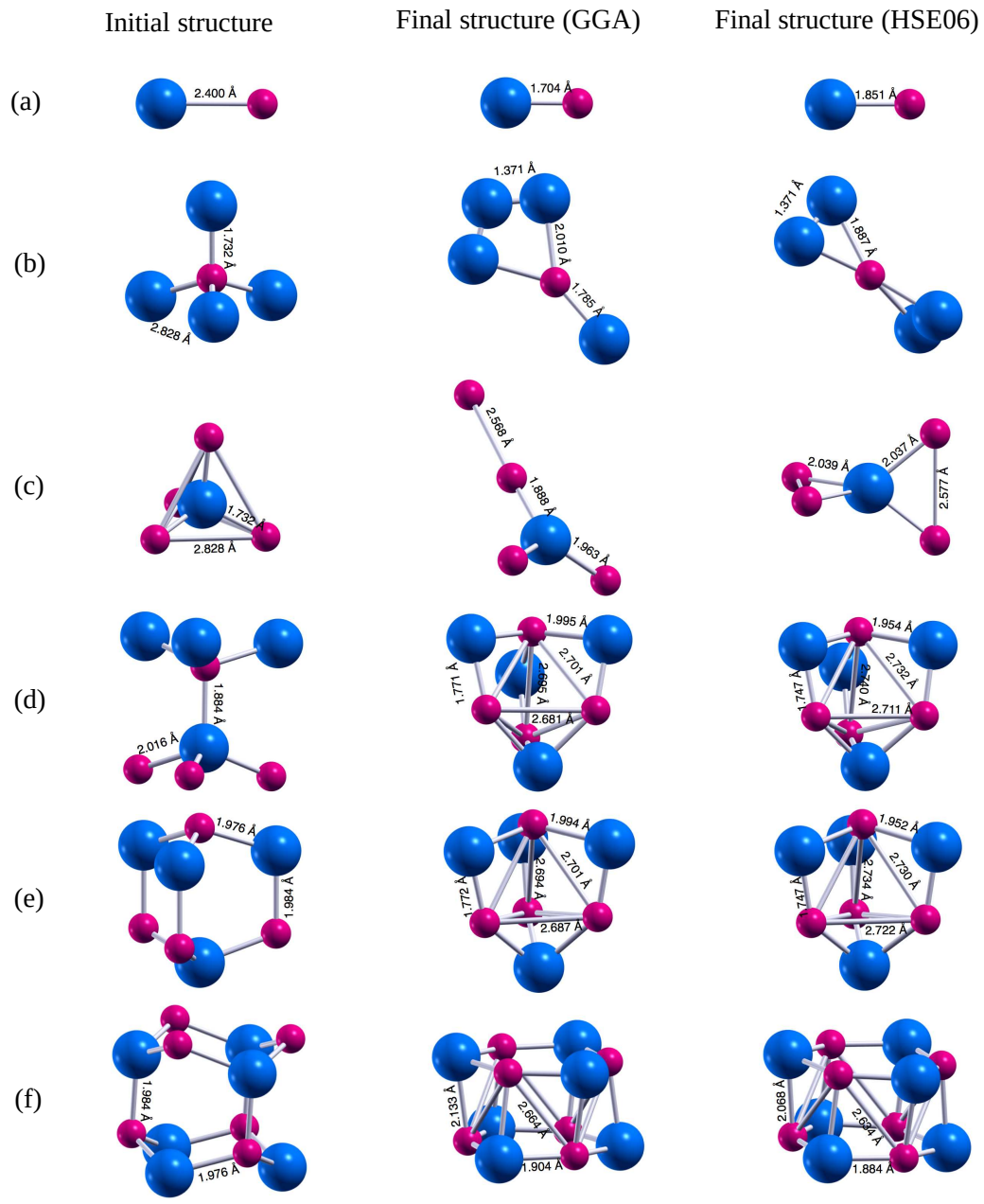

Figure 9.1.: The initial configuration of some ZnO clusters studied in this work are shown in the left column. The relaxed clusters configurations obtained within GGA and HSE06 functionals are given in the middle column and the right column, respectively

to the global minima (GM) structures suggested by Cheng *et al.* [266], it is observed that final-relaxed structures of case (f) and case (g) (plotted in Fig. 9.1 and 9.2, respectively) are similar to their respective global minima. It may be contemplated that the final structure of case (f) may act as nucleation center for the growth of wurtzite ZnO clusters by regular addition of ZnO units. Such type of mechanism has to be proved from more rigorous calculations, which has not been done. The

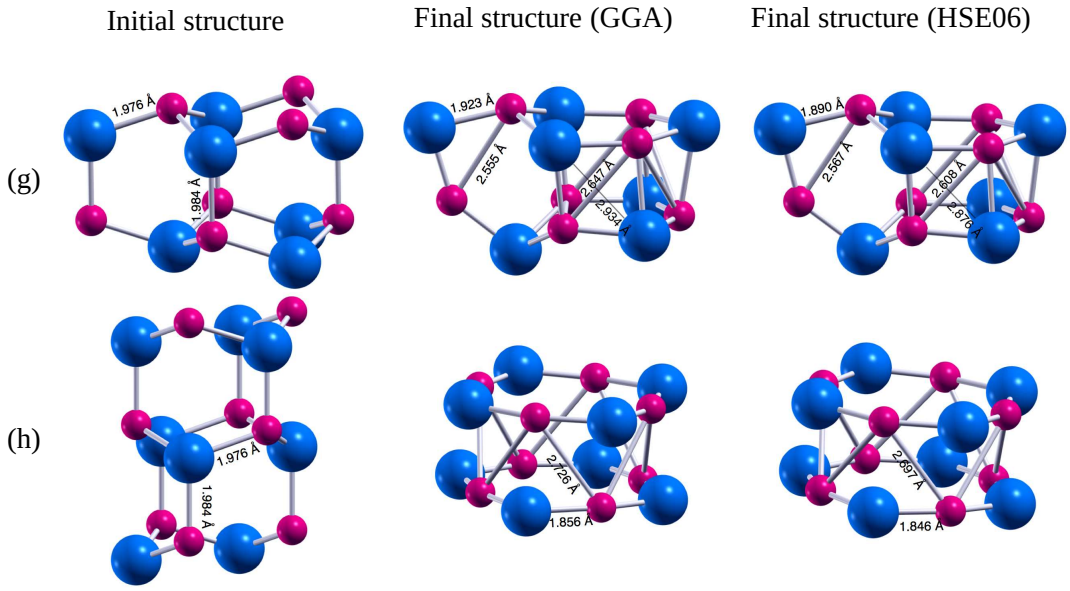

Figure 9.2.: Similar to Fig. 9.1, the initial configuration (left) and the relaxed configuration obtained from GGA (middle column) and the HSE06 functional (right column) are shown. The initial clusters typically consists of both tetrahedral and octahedral defects.

Table 9.1.: The magnetic moment (μ_{B}) on individual atoms in the clusters for the structures (b) and (c) as shown in Fig. 9.1.

E_{xc}	case (b)		case (c)	
	Zn	O	Zn	O
GGA	0.039	0.395	0.168	0.264
HSE06	-0.032	0.438	0.181	0.186

relaxed structure for the case (d) is however not the GM structure. For this case the GM is predicted as a planer ring structure [266].

The binding energy calculated for various cluster sizes for GGA and HSE06 is shown in Fig. 9.4. The binding energy is calculated according to

$$E_{\mathrm{B.E}} = E_{(\mathrm{ZnO})_n} - (nE_{\mathrm{Zn}} + nE_{\mathrm{O}}), \tag{9.1}$$

where E_{Zn} is the energy of individual Zn atom and $E_{\mathrm{O}} = E_{\mathrm{O}_2}/2$ is compared with the O_2 molecule. The binding energy is plotted with respect to the number of functional units n in Fig. 9.3. The difference between the binding energy obtained from GGA and HSE06 functionals ($\mathrm{E_{B.E}}$(HSE06)-$\mathrm{E_{B.E}}$ (GGA)) is plotted in the inset of Fig. 9.3. The binding energy decreases continuously with increasing functional units of ZnO. The difference between the binding energies is reducing with increasing n as shown in the inset of Fig. 9.3. We find that the binding energy obtained from HSE06

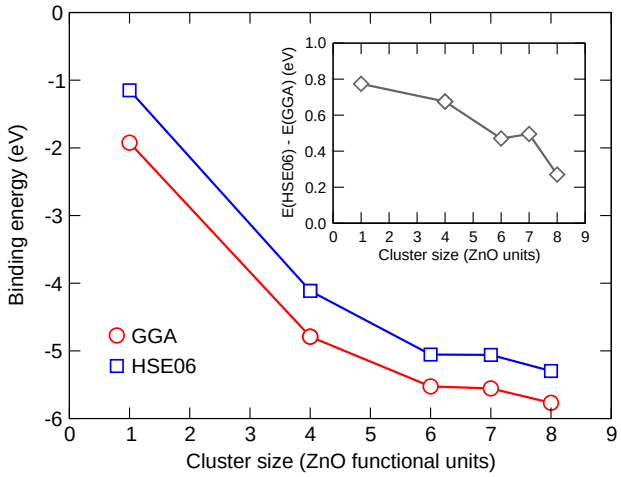

Figure 9.3.: The binding energy (calculated according to Eq. 9.1) of the $(ZnO)_n$ cluster with respect to the number of functional units n.

is than that of the binding energy calculated from GGA by almost a constant factor.

9.3. Magnetism due to defects in ZnO nanoclusters

In order to understand the role of V_{Zn} and C_O in nanoclusters and how they compare with the bulk behavior, we have constructed a cluster by cutting the bulk along the crystallographic planes $\{10\bar{1}0\}$ and $\{10\bar{1}1\}$ to get a stoichiometric ZnO cluster. It is known that atoms with dangling bonds in cluster modeling pose a major problem because the surface atoms reconstruct to achieve most favorable bonding and as result the bulk symmetry and orientation is lost. One of the ways to circumvent this problem is to passivate the surface using suitable atoms (sometimes pseudo-atoms) which take care of the surface reconstruction and thereby avoid any appearance of surface states within the forbidden gap of the semiconductor. Since the present study is essentially about the role of surfaces in changing the magnetic properties, we do not passivate the dangling atoms. It must be noted that stoichiometry is preserved in the input structure as a starting point, otherwise the system may be comparable to a cluster with defects, which is a problem we want to focus on. The present studies are done only within GGA.

The cluster consists of 216 atoms in total where the separation between the planes between extreme ends (and parallel to three hexagonal directions) is 15 Å and the separation of planes parallel to the direction along c-axis is 8.5 Å. After relaxation the bond lengths in hexagonal planes is observed to contract by 1.5%, which is smaller than that reported by Wang *et al.* [267], (who reported 12%) because of the large size of the cluster. Owing to the polar nature of O-terminating and Zn-terminating surfaces, the surfaces are unstable and the charge neutralization is achieved by flattening Zn−−O the double-planes. It must be noted that the surface layers relax inwards to flatten the double-planes,

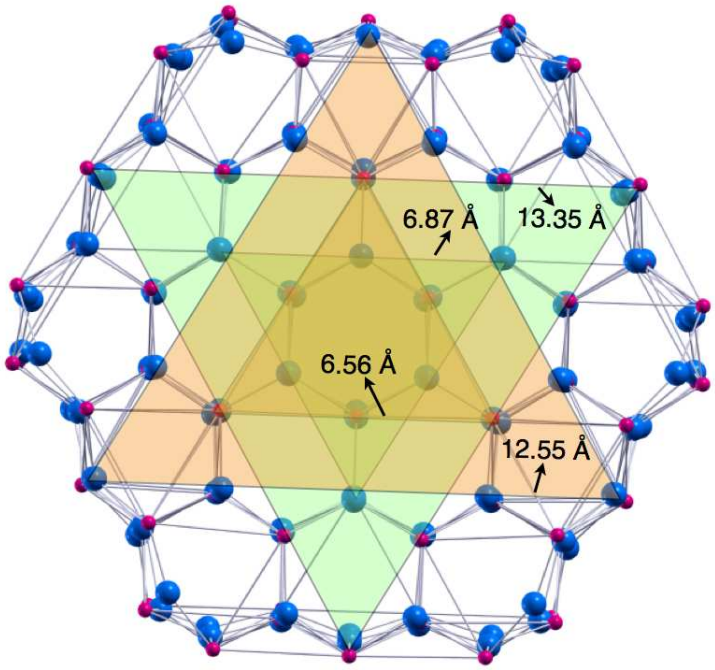

Figure 9.4.: Relaxed ZnO cluster consisting of 216 atoms ($(ZnO)_{108}$). One can see the two types of triangular reconstructions (shown as solid and dashed lines) alternating between the double layers along the c-axis.

called graphitic structure, which may persist for almost 10 monolayers [268]. As a comparison we note that the present cluster has only four double-layers and hence all the layers tend to flatten the double planes. In addition to the flattening, we observe that the flattened double layers (0001) and $(000\overline{1})$ surfaces develop curvature which is hyperbolic with respect axis parallel to the c-axis. Viewing from the c-axis direction, we notice triangular surface reconstruction along the hexagonal plane. This is shown in Fig. 9.5 where the atoms within the triangle have minimum relaxation compared to the atoms exterior to the drawn triangle. The solid and the dashed triangles represent alternating triangular constructions for consecutive double-layers. There are observations of triangular reconstruction also in bulk, which has been discussed both in theory [269, 270] and in experiment [271]. It has been shown that surface energy of Zn-terminated (0001) surface is larger than that of the O-terminated $(000\overline{1})$ surface in bulk ZnO, and thus the Zn-terminated surface is more active for surface reconstruction [272]. These type of surface reconstruction discussed for clusters are only qualitative and are do not follow the same physical mechanism as obtained in bulk.

The formation energies of various defects in the ZnO cluster, the magnetic moment per cluster and the polarization energy are tabulated in Table 9.2. We observe that the formation energy of V_O is comparable to the bulk case, while the formation energy of V_{Zn} in the cluster is reduced significantly (still positive), suggesting that the probability to find V_{Zn} is higher than in bulk. This is in agreement with the trend in change in formation energy for GaN nanowires with V_{Ga} [273]. The magnetic

Table 9.2.: Formation energy, magnetic moment in ferromagnetic mode, and ΔE (= $E^{\text{spin polarized}} - E^{\text{non-spin polarized}}$) for various defects and morphology of ZnO clusters.

Defect type	# defects	location	E_f (eV)	Moment (μ_B)	ΔE (eV)
V_O	1	interior	3.896	0.00	0.0000
V_{Zn}	1	interior	0.103	2.00	-0.1361
V_{Zn}	1	surface	0.562	1.76	-0.0989
V_{Zn}	2	both interior	2.252	4.00	-0.2766
V_{Zn}	2	both outer	1.087	1.00	-0.2413
C_{Zn}	1	interior	-7.232	0.00	0.0000
C_O	1	interior	-0.727	2.00	-0.3148
C_O	1	surface	-1.390	2.00	-0.6019
C_O	2	both interior	-2.122	2.00	-0.1306
C_O	2	both outer	-1.620	4.00	-0.5282

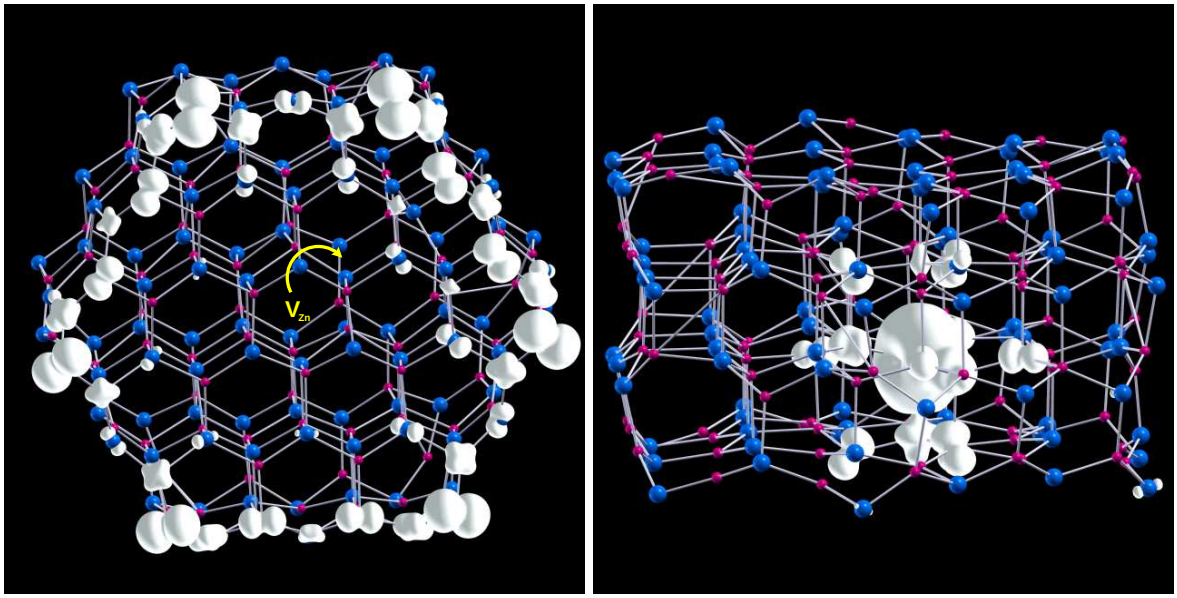

Figure 9.5.: Effective charge density ($\Delta\rho = \rho_\uparrow - \rho_\downarrow$) plotted for the cluster defects V_{Zn} (left) and C_O (right) in ZnO cluster. The spin polarization for V_{Zn} in the cluster is spread away from the V_{Zn} and observed on the dangling oxygen atoms on the surface along at the edge of the O-terminating surface, while the spin-polarization of C_O in the cluster is localized on the carbon atom similar to the bulk case. The isosurface is plotted at a value of 0.02 e/Å^3. The color of the balls is consistent with Fig. 8.4.

moment of V_{Zn} is comparable to that obtained in bulk (also in agreement with [273]).

Detailed effective charge density ($\Delta\rho = \rho_\uparrow - \rho_\downarrow$) analysis of Fig. 9.5 shows that for a V_{Zn} the spin-density is more localized on the dangling O atoms at the O-terminated surface, while for C_O the spin-density is localized mostly on the C site and the neighboring O sites. This type of differences on

the spread of spin-density in clusters can have profound implications, especially, for the interaction of cluster with its surrounding. For example, Wang *et al.* have shown ligand induced ferromagnetism in ZnO clusters [267]. Since they have considered only anionic ligands, they concluded that the ligands bind to surface Zn sites. Without loss of generality, one can consider that cationic ligands bind to the surface O-atoms and in this case the spin-polarization residing on the surface O-atoms (due to an interior V_{Zn}) will rearrange due to hybridization and may give rise to magnetic property specific to the type of ligands used.
Similar to bulk, V_{Zn} and C_O develop a magnetic moment of 1.8 and 2 μ_B/C, respectively, and multiple defects in ZnO cluster couple ferromagnetically in agreement with previous reports [274, 275]. The formation energy of single C_O reduces from an interior position in the cluster to surface suggesting that C_O may be more likely to be found on the surface. This is in accordance with the reports, Ref. [275], where they have found that the C impurities are more probable to be found on the surface than in the interior of clusters. The magnetic moment is however unchanged and is the same as in bulk. The polarization energy (ΔE) is enhanced compared to bulk. Comparing the energy of two C_O located on the surface and in the interior of the cluster we find that the formation energy is lower for the latter. This shows that carbon tries to find itself in a complete bonded environment and is least stable on the surface. Both locations of carbon still stabilize a ferromagnetic interaction.

9.4. Summary

Small clusters are studied with different functionals like the GGA and the HSE06 functional. Apart from the non-stoichiometric tetrahedral units of Zn_4O_1 and Zn_1O_4, most stoichiometric clusters relax to similar structure. We have studied the magnetic properties of V_{Zn} and C_O defects in ZnO. We observe that both type of defects, V_{Zn} and C_O, develop magnetic moment by localizing holes and electrons, respectively. We find that for the case of V_{Zn} the effective charge density resides on the O atoms located at the bounding edges of the cluster, while for C_O the effective charge is centered on the C_O atom. This type of spread of effective charge could have important consequences, especially for the cluster while interacting with its surrounding.

10. Outlook

10.1. TM clusters in ZnO matrix

One of the important questions for understanding the experimental reports claiming ferromagnetism in TM doped ZnO is identifying the role of magnetic clusters in the semiconducting host. It must be noted that a good DMS is considered as those where the dopant atoms are substitutional and lie at random sites. Clustering of dopant or of any intrinsic defects in DMS materials is treated as a drawback because clusters tend to act as scattering centers thereby influencing the transport properties undesirably. There are reports that nanosized metallic inclusions are often present in the experimentally developed samples [276–280] and they can also result in room temperature magnetic response [281, 282].

Using the DFT approach there have been some studies on the nature of Co clustering in ZnO [184]. In their studies the authors have considered the substitution of Co at the zinc site. From formation energies as a function of clusters size they find that there is a strong tendency for Co atoms to preferentially lie close to each other at the cation site in ZnO matrix. The magnetic interaction however is not always ferromagnetic. Although LDA calculations predicted that two and three atom Co clusters could align in ferromagnetic orientation, but LDA+U gives a tendency for dominant antiferromagnetic interactions. The value of U for Co d-orbital in the LDA+U calculations was taken to be 5 eV.

As suggested in experiments, we actually see Co clusters in ZnO matrix which are metallic. Moreover the crystal structure of the cluster is shown to be of hcp type [280]. This brings us to propose that such case is possible if doped Co takes the nearest neighbor Zn positions and also an O position in-between the doped Zn sites. To study the role of such type of clusters, a large supercell with 144 units of ZnO consisting of nine double layers (each consisting of Zn and O layers) along the c-direction and applying periodic boundary conditions along the a- and the b-directions to create a semi-infinite boundary condition has been modeled. Essentially this model is close to the situation of thin-film where one of the surfaces is exposed while the interior surfaces have bulk structural parameters. The surface of the Zn-terminated and the O-terminated surfaces has been passivated by fictitious hydrogen with partial valency charges [283–285]. In case of ZnO, the Zn-terminating surface is passivated by hydrogen with valence 1.5 and that of the O-terminating surface is passivated by hydrogen with valence 0.5. A representation of the passivated ZnO film obtained after relaxation is shown in Fig. 10.1 (left). One clearly finds that the wurtzite structure is stabilized.

Now, a deliberate surface is created (passivation removed) and five TM atoms (TM = Co, Ni) are

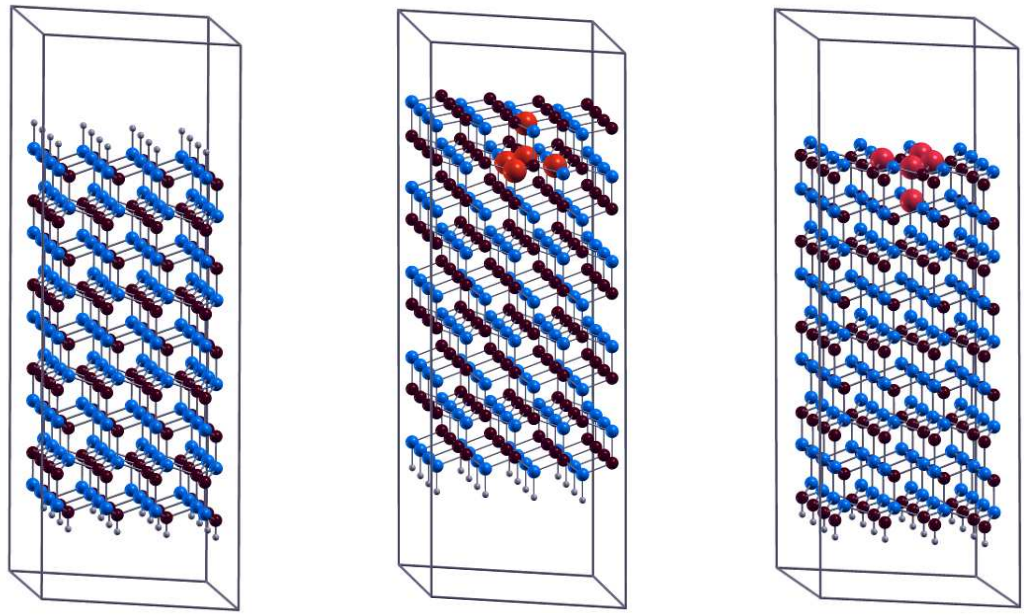

Figure 10.1.: The Zn- and O-terminating surfaces along the [0001] and [000$\bar{1}$] directions are passivated by pseudo hydrogen having valency charge of 1.50 e and 0.50 e, respectively. The relaxed structure without doping (left) show the stability of the wurtzite structure. The relaxed position of O-terminated and Zn-terminated surfaces together with the embedded five atom tetrahedral TM (here TM = Co) cluster (embedded in special positions; see text) is shown in the center and the right figure, respectively.

substituted in such a manner that four TM atom replaces nearest neighbor Zn and the fifth TM atom occupies the central oxygen position. So, a tetrahedral structure is enforced on the clusters. Relaxation of the whole system is done until the change total energy is below 10^{-6} eV. At this tolerance in energy the forces in the supercell is below 0.001 eV/Å. After relaxation we find that the cluster maintains tetrahedral structure (distorted from regular geometry) for all the embedded depths. We estimate the embedding energy of the system (from Eq. 10.1) and the total magnetic moment of TM cluster for the case of O-terminated surface, Fig. 10.2 (left) and that of the Zn-terminated surface, Fig. 10.2 (right) as the TM cluster is moved from bulk to surface. Reference calculation with Mg clusters is shown in order to contemplate the role of cluster magnetization.

The embedding energy is defined as

$$E_{\mathrm{Embed}} = E_{\mathrm{Zn}_a\mathrm{Co}_b\mathrm{O}_c\mathrm{H}_d} - aE_{\mathrm{Zn}} - bE_{\mathrm{Co}} - E_{\mathrm{O}} - E_{\mathrm{H}}, \tag{10.1}$$

where $E_{\mathrm{Zn}_a\mathrm{Co}_b\mathrm{O}_c\mathrm{H}_d}$ is the total energy of the system under consideration, E_{Zn} and like wise are the energies of respective atomic species calculated in the same supercell. It must be noted that E_{H} depends on the valency of the pseudo hydrogen that is under discussion.

Some important conclusions from the above studies are;

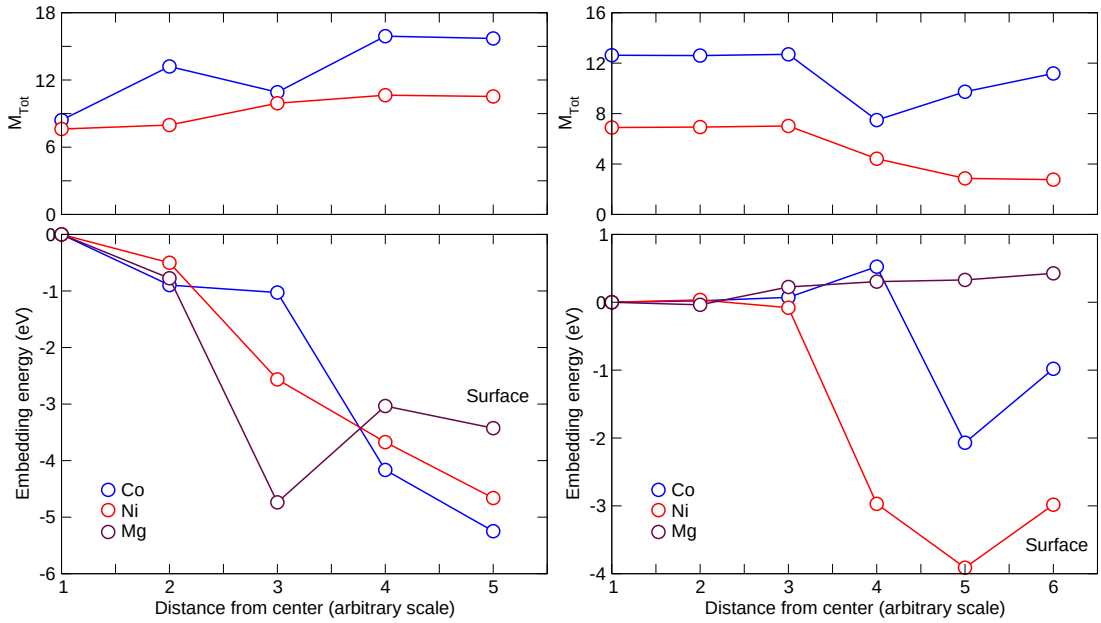

Figure 10.2.: The total magnetic moment (upper panel) and the embedding energy (lower panel) calculated for five-atom clusters in ZnO for the O-terminating surface (left) and Zn-terminating surface (right). Mg cluster is taken for reference calculations.

- The embedding energy of O-terminated surface reduces as the cluster is moved towards the surface. This suggest that the most probable site of metallic-phase clusters are on the surface or near the interface regions. This is supported from experimental studies. In case of Zn-terminating surface, the embedding energy shows that the surface is felt by the cluster to only few layers deep, however for O-terminating surface the clusters can feel the surface from five layers deep.

- In case of Mg cluster, the embedding energy shows that Zn-terminating surface is unfavorable to hold the Mg cluster on surface.

- The magnetic moment of TM clusters are aligned parallel for most cases so the individual spins collectively together constitute a macro-spin.

- The magnitude of the magnetic moment is reduced as the cluster approaches the surface.

While the preliminary results show some patterns that can be correlated to experiments, more detailed analysis has been hindered because of the awful amount of computational resources required in dealing with such large supercells.

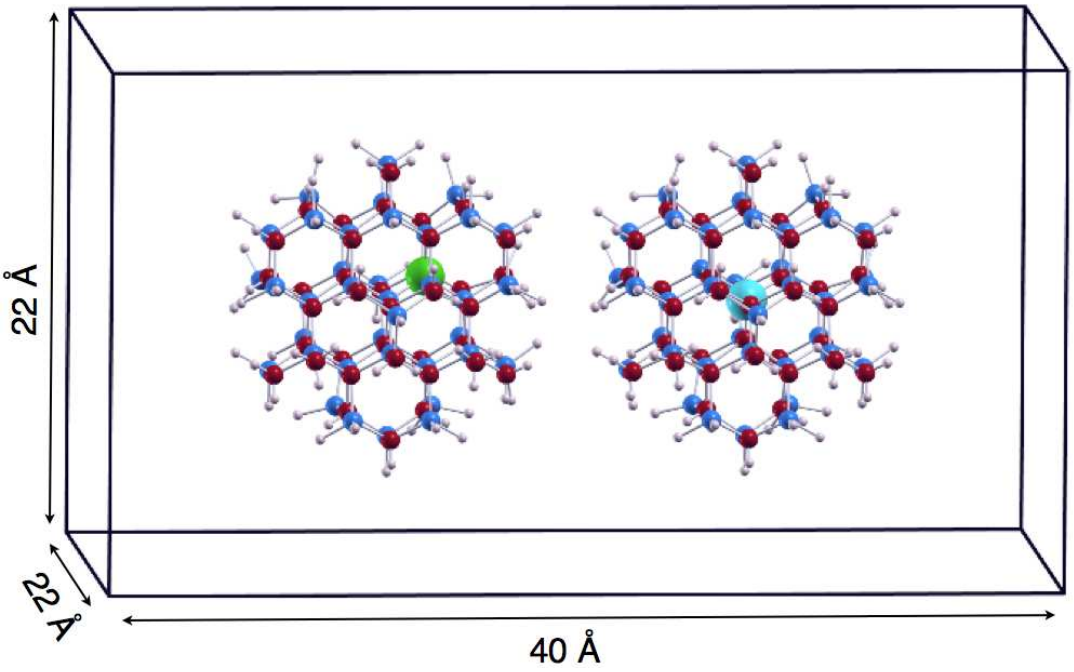

Figure 10.3.: Schematic representation of pn-junction in nanoparticles of ZnO in a supercell. The p-type cluster is created by doping N_O (shown as large green ball on the left nanoparticle) and the n-type cluster is created by doping In_{Zn} (shown as large cyan ball on the right nanoparticle). The particles are passivated with fictitious hydrogen to preserve the wurtzite structure.

10.2. ZnO cluster based nano pn-junctions

There exist some experimental studies on the rectification property of pn-junction based on ZnO nanoparticles [286–288]. In the experiments, the p-type and n-type ZnO nanoparticles were synthesized independently by chemical treatment using selected polymers as stabilizing agents. Thereafter the pn-junctions were created essentially by sequential adsorption of p-type and n-type ZnO nanoparticles. The junction exhibited rectification demonstrating the formation of a depletion layer between the nanoparticles.

One of the important points for the understanding of the pn-junctions in bulk semiconductors is that the diffusion of charges at the interface lead to a negative voltage which stops further diffusion of charges and thus forms a depletion layer. In clusters, however, some important questions must be taken into account. Firstly, the charge transfer due to diffusion will face potentials arising due to the nanoparticle surface. Secondly, due to the quantization of electronic states, the charge transfer will be affected. An even more important aspect is the phenomena of band bending at the depletion region needs some reconsideration when applied for the nanoparticles, because the range of particle size is smaller than the depletion layer itself. The depletion layer in bulk is in the range of 10^{-6} m (10^3nm)

[289]. This brings to a straightforward question: Can two nanoparticles, one of p-type and another of n-type, when brought together behave as a pn-junction device? This question is important from the point-of-view of single nanoparticle devices.

To study the problems stated above, the system may be modeled for ZnO by doping indium at the Zn site for the n-type cluster and nitrogen at the O site for the p-type cluster. The cluster may be passivated with fictitious hydrogen (hydrogen with partial valency) to stabilize the structure of the cluster. A schematic representation of the p- and n- cluster together in the simulation box is shown in Fig. 10.3. After relaxing the system to minimize the forces the charge transfer can be studied through the Mulliken population analysis or the Bader charge analysis. These studies will give more understanding about the nature of charge transfer in nano devices and shed more light on the transport properties in multiply-doped ZnO nanoparticle ensemble.

A. Experimental status of Co doped ZnO

At present the magnetic properties of TM doped ZnO is under serious consideration in research. Although some theoretical models have predicted ferromagnetism above the room-temperature, and some experimental report in favor of ferromagnetic signal in samples, the details is far from being understood. The essence of the experimental results found by Ney *et al.* is presented in this appendix. The reason for discussing their results are two-folded. Firstly the present theoretical studies went hand-in-hand with the experimental studies due to the similar nature of the research topics and secondly, interestingly enough their experimental results of absence of room-temperature ferromagnetism in Co doped ZnO corroborates well with the present studies. Below is a brief outline of the experimental status, details can be found in [33–36, 290–303].

A.1. Experimental characterization of Co doped ZnO

A.1.1. Sample preparation

The Co-doped samples were prepared by mainly three different techniques, namely, pulsed laser deposition (PLD) at finite oxygen partial pressure (oPLD), PLD at an inert gas atmosphere (iPLD), by reactive magnetron sputtering (RMS) from metallic Zn/Co targets at various oxygen partial pressure and by molecular beam epitaxy (MBE) in c-plane sapphire [36, 298].

A.1.2. Estimation of lattice constant

Analysis of X-ray diffraction and from fitting the XANES and the XLD spectra by the FDMNES code it was ascertained that all sample methods result in Co doped ZnO films with wurtzite structure and the lattice parameters were determined as, a = 3.2459 Å, c = 5.2069 Å and u = 0.382. Slight increase in c parameter was observed which depended on the film thickness and the Co concentration. A comparison of XLD signals of all samples showed excellent structural quality.

A.1.3. XANES/XLD measurements

The XANES was performed at the Co K-edge for Co doped ZnO to study the local structural environment [36, 297, 298]. The XANES allows to distinguish between the metallic Co, Co substitution in ZnO lattice or any other complexes of Co, like CoO or Co_3O_4. All samples showed identical XANES

and XLD of similar size suggesting that all the samples have high degree of substitutional Co incorporated on Zn lattice sites. The valley between the pre-edge peak and the main peak in XANES give the valence state of Co, which was analyzed to be in Co^{+2} which would be true for Co substituting Zn lattice sites.

A.1.4. SQUID measurements

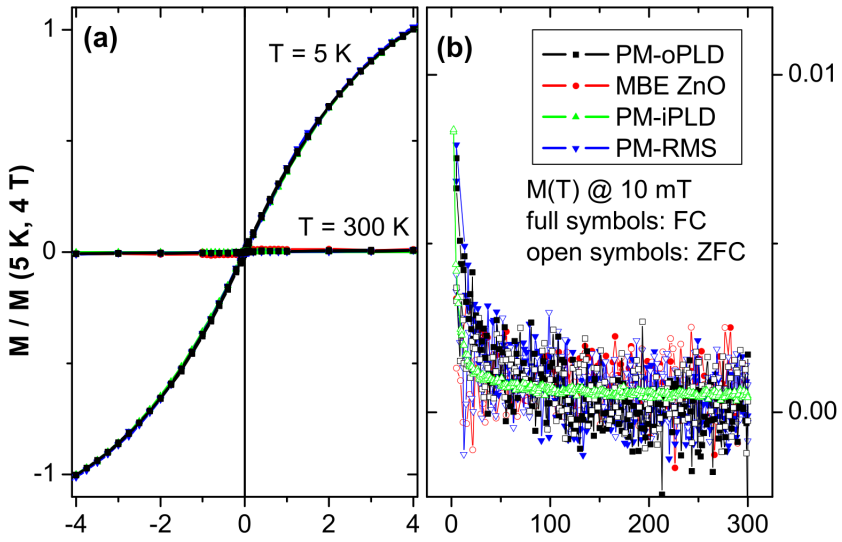

Figure A.1.: M(H) plot at 300 K and 5 K (a) and M(T) plot at magnetic field of 10 mT (b) showing paramagnetic behavior of the samples. Figure taken from “Habiltationschrift" of Dr. Andreas Ney, University of Duisburg-Essen [290].

The M(H)-curves were measured at 300 K and at 5 K and the M(T) measurements were performed under field cooled (FC) and zero-field cooled (ZFC) conditions with the superconducting quantum interference device (SQUID) [34, 290]. All the three samples exhibited identical M(H) behavior without any opening in the M(H)-curves at 5 K or any considerable magnetization 300 K. Moreover, the M(T)-curves of the three samples overlapped showing no separation between the FC and ZFC data. Thus it was concluded that doping 5-10% Co in ZnO induces only paramagnetic behavior without leading to phase segregation.

A.1.5. XMCD measurements

The functional dependence of the dichroic signal recorded at the pre-edge peak as a function of external magnetic field is identical to the functional dependence of M(H)-curve recorded for main peak, but with opposite sign. All the samples exhibited maximum XMCD signal of 0.3pre-edge which is interpreted as due to the paramagnetic response of the Co sublattice [36, 298]. So the element specific XMCD measurement corroborates with the paramagnetic nature of Co doped ZnO samples deduced

from SQUID measurements.

A.1.6. EPR measurements

From EPR measurements also any relevance of exchange pairs were discarded. This highlights the fact that there is no other interaction beyond the weak dipolar coupling.

A.2. Conclusion

A series of $Zn_{1-x}Co_xO$ films ($0<x\leq10\%$) have been studied to understand the role of magnetic dopant and its consequence to the magnetic properties by adopting advanced characterization techniques. It was observed that the samples are mostly ferromagnetic. Some instances of ferromagnetic-like behavior has been interpreted as due to the due to the formation of the magnetic nanoparticles (mean diameter $1\tilde{2}$ nm). The phase segregation is also supported through the transport and magnetic investigations. It was demonstrated that even slight changes in the preparation conditions of Co:ZnO can promote the onset of phase separation.

B. Theoretical modeling photoluminescence

Photoluminescence characterization is one of the important techniques adopted to characterize nanoparticles. This is primarily possible because of the quantization of states and the HOMO-LUMO (highest occupied molecular orbital - lowest unoccupied molecular orbital) gap depends on the size of the nanoparticle. In addition, the oscillator strength on nanoparticles is increased because of the localization of electron and hole wavefunctions [304, 305]. There have been some theoretical studies on photoluminescence recently on quantum dots and quantum well [306–311]. Studies are also reported for optical absorption on spherical and ellipsoidal silicon nanocrystals [312]. The role of phonons in the photoluminescence (PL) process and the PL spectra of self-assembled helical super-molecular assemblies have been reported [313–315]. Experimental studies have shown that the photoluminescence of quantum dots is quenched when the quantum dots are capped with hydro-carbon polymers [316]. Experimental verification of photoluminescence of TM doped wide band semiconductor or information regarding magnetism is not at hand. Here, we simply outline our preliminary investigation on PL of semiconductors based on a tight-binding (TB) model. Extension to include magnetism still needs to be undertaken.

B.1. Photoluminescence in tight-binding model

In the Coulomb gauge, Maxwell's equations can be written as,

$$\nabla^2 \mathbf{A} = -\mu_0 \mathbf{J}$$

where,

$$\mathbf{A}(\mathbf{r},\omega) \quad = \quad \frac{\mu_0}{4\pi} \int d^3r' \frac{J(r',\omega)}{|r-r'|} e^{\frac{i\omega|r-r'|}{c_0}}$$

$$\mathbf{J}(\mathbf{r},\omega) \quad = \quad i\omega \mathbf{A}(\mathbf{r},\omega) = i\omega\mu_0 \int d^3r' \frac{J^{\mathrm{T}}(r',\omega)}{4\pi|r-r'|} e^{\frac{i\omega|r-r'|}{c_0}}.$$

Here J^{T} is the transverse current. From the Poynting's theorem we have,

$$\frac{\partial u}{\partial t} + \nabla \cdot \mathbf{S} = -\mathbf{J} \cdot \mathbf{E},$$

where, u is the time derivative of the energy density, $\mathbf{S} = \mathbf{E} \times \mathbf{H} = \frac{1}{\mu}\mathbf{E} \times \mathbf{B}$ ($\mathbf{E} \Rightarrow$ electric field, $\mathbf{B} \Rightarrow$ magnetic field) is the Poynting vector representing the energy, $\mathbf{J}$ is the current density.
In the integral form,

$$\int d\nu\, \mathbf{J} \cdot \mathbf{E}$$

is the power consumed by the Lorentz force acting on the charge carriers. The emitted light of frequency ω per sample volume Ω is equal to,

$$\begin{aligned} P(\omega) &= -\frac{1}{2\pi}\frac{1}{\Omega}\int d^3r \langle TJ(r,\omega)E(r,\omega)\rangle \\ &= \frac{\omega^2\mu_0}{4\pi^2 c_0}\frac{1}{\Omega}\iint d\mathbf{r}d\mathbf{r}'\langle TJ(r,\omega)E(r,\omega)\rangle \\ &= \frac{\mathfrak{Z}}{\Omega}\iint d\mathbf{r}d\mathbf{r}'dt e^{i\omega(t-t')}\langle TJ(r,t)J(r',t')\rangle, \quad \text{where } \mathfrak{Z} = \frac{\omega^2\mu_0}{4\pi^2 c_0} \\ &= \frac{\mathfrak{Z}}{\Omega}\iint d\mathbf{r}d\mathbf{r}'dt e^{i\omega(t-t')}\langle TJ(r,t)J(r',t')\rangle \end{aligned}$$

In order to calculate the above expression we have expanded $\mathbf{E}(\mathbf{r},\omega)$ as a function of $\frac{\omega}{c_0}$ and kept the term up to the order of $\frac{\omega_0}{c_0}$ because in the optical limit $\frac{\omega_0}{c_0}$ is small.
Now,

$$J = \sum_i J_i = ie\left[H, \sum_{i,\alpha} R_i C^\dagger_{i\alpha} C_{i\alpha}\right]$$

where, H is the Hamiltonian of the system, α is the orbital index, $C^\dagger_{i\alpha}$ and $C_{i\alpha}$ are the creation and annihilation operators operating on the particle state state $|i\alpha\rangle$ and R_i is the position vector of the ions.
After solving the commutation operator it can be shown that,

$$J = ie\sum_i \sum_{m_1,m_2} \sum_{\alpha,\beta} (\varepsilon_{m_1} - \varepsilon_{m_2})\, R_i |m_1\rangle\langle m_1|i\beta\rangle \Delta^{\alpha\beta} \langle i\alpha|m_2\rangle\langle m_2|$$

where, the selection rule $\Delta^{\alpha\beta}$ is such that

$$\Delta^{\alpha\beta}\begin{cases} = 1 & \text{for allowed transitions,} \\ = 0 & \text{if transitions are not allowed.} \end{cases} \tag{B.1}$$

Using the expressions, $R_i\Delta^{\alpha\beta} = R_i^{\alpha\beta}$ and $|m_i\rangle = \sum_{i,\alpha} a_{i\alpha}^{m_1}|i\alpha$, where $a_{i\alpha}^m = \langle i\alpha|m\rangle$, we can write

$$\vec{J} = ie \sum_{\substack{i \\ m_1,m_2 \\ \alpha,\beta}} (\varepsilon_{m_1} - \varepsilon_{m_2})\, a_{i\beta}^{*m_1} \vec{R}_i^{\alpha\beta} a_{i\alpha}^{m_2} C^\dagger_{m_1} C_{m_2}$$

We now define the power function

$$P(\omega) = -\frac{\Im e^2}{\Omega} \sum_{\substack{i,j \\ \alpha,\alpha';\beta,\beta' \\ m_1,m_2;m_3,m_4}} \int_{-\infty}^{\infty} dt e^{i\omega(t-t')} R_i^{\alpha\beta} R_j^{\alpha',\beta'} a_{i\beta}^{*m_1} a_{i\alpha}^{m_2} a_{j\beta'}^{*m_3} a_{j\alpha'}^{m_4} (\varepsilon_{m_1} - \varepsilon_{m_2})$$
$$(\epsilon_{m_3} - \varepsilon_{m_4}) \left\langle TC_{m_1^\dagger}(t) C_{m_2}(t) C_{m_3}(t')^\dagger C_{m_4}(t') \right\rangle$$

For photoluminescence $|m_2\rangle$ should be occupied and $|m_1\rangle$ state is empty so there is a transition $|m_2\rangle \longrightarrow |m_1\rangle$ with $\varepsilon_{m_2} > \varepsilon_{m_1}$. So the time ordered product can be written in terms of the Fermi function $f_F(x)$ and $1 - f_F(x)$. The expression thus leads to, we have

$$P(\omega) = \frac{\Im e^2}{\Omega} \sum_{\substack{i,j \\ m_1,m_2 \\ \alpha,\beta}} \int_{-\infty}^{\infty} dt e^{i\omega(t-t')} \Delta^{\alpha\beta} \Delta^{\alpha'\beta'} a_{i\beta}^{*m_1} a_{i\alpha}^{m_2} a_{j\beta'}^{*m_2} a_{j\alpha'}^{m_1} (\varepsilon_{m_1} - \varepsilon_{m_2})^2$$
$$f_F(\varepsilon_{m_2}) (1 - f_F(\varepsilon_{m_1}))$$
$$= \frac{\omega^2 \mu_0 e^2}{4\pi^2 c_0} \frac{1}{N_\Omega} \sum_{m_1,m_2} \partial(\omega + \varepsilon_{m_1} - \varepsilon_{m_2}) \left| \sum_{i,\alpha,\beta} \Delta^{\alpha\beta} a_{i\beta}^{*m_1} a_{i\alpha}^{m_2} \right|^2$$
$$f_F(\varepsilon_{m_1+\omega}) (1 - f_F(\varepsilon_{m_1})) .$$

When the system is excited with photon of energy ν, then the occupation of the states is modified within the energy window $\varepsilon_F - \nu$ to $\varepsilon_F + \nu$. In fact, the occupation of the electrons reduces in the energy regime $\varepsilon_V - \nu$ to ε_V, where ε_V is the valence states energy, and the occupation of electron increases in the energy regime ε_C to $\varepsilon_C + \nu$. We assume that the change of occupation in these energies is f_0. Therefore the Fermi functions can be modified as,

$$f(\varepsilon) \to f'(\varepsilon) = f(\varepsilon) + f_0, \text{ for } \varepsilon_C < \varepsilon < \varepsilon_C + \nu$$
$$f(\varepsilon) \to f'(\varepsilon) = f(\varepsilon) - f_0, \text{ for } \varepsilon_V < \varepsilon < \varepsilon_V + \nu$$

Thus, the power function can be written as,

$$P(\omega) = \frac{\omega^2 \mu_0 e^2}{4\pi^2 c_0} \frac{1}{N_\Omega} \sum_{m_1,m_2} \partial(\omega + \varepsilon_{m_1} - \varepsilon_{m_2}) f'(\varepsilon_{m_1} + \omega) \left(1 - f'(\varepsilon_{m_1})\right) \left| \Delta^{\alpha\beta} a_{i\beta}^{*m_1} a_{i\alpha}^{m_2} \right|^2$$

B.2. Application to Si clusters

The silicon clusters were cut as spheres of bulk silicon with diamond crystal structure. The clusters were relaxed to minimize the interatomic forces by using the VASP package. The position of the relaxed clusters were used in the tight-binding model for description of the electronic structure. It

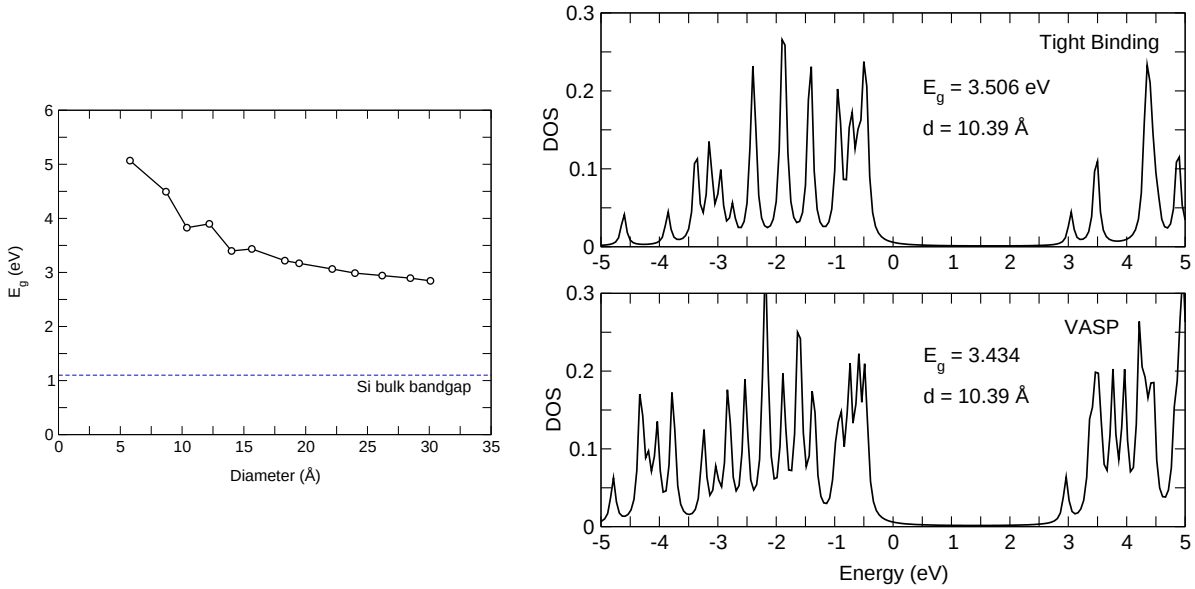

Figure B.1.: Cluster diameter versus bandgap of Si clusters obtained from the tight-binding method (left plot) using parameters from literature. The DOS of Si_{29} cluster (unrelaxed) as obtained from TB method (upper panel on right) is compared to that of the DOS obtained from VASP (lower panel on right).

must be noted that the band dispersion of bulk Si (indirect nature of band gap) can described well by introducing excited states like in sp^3s^* or in sp^3d^5 as considered in literature [317, 318]. On the other hand Tserbak *et al.* could achieve reliable band structure parameters with sp^3 orbital basis by including interactions up to third nearest neighbors [319]. In the present calculations the tight-binding model for silicon clusters were constructed using parameters available in literature[319, 320]. The Slater-Koster interpolation scheme [321] has been used and distance dependent scaling of the TB matrix elements are used as suggested by Kwon *et al.* [322]. The bandgap versus size of Si clusters obtained from the tight-binding formalism is shown in Fig B.1 (left). The DOS obtained from tight-binding model and that from VASP or the Si_{29} cluster is shown in Fig B.1 (right). The DOS obtained from TB-formalism and DFT matched quite reasonably.

The DOS and the corresponding PL intensity obtained from Eq. (B.2) is shown for two different particle sizes namely Si_{29} and Si_{705}, respectively, in Fig. B.2. The PL-intensity is plotted for excitation energy ω = 5 eV and for comparison the PL-intensity is plotted for no excitation, which in zero. We find that the PL-emission frequency is proportional to the bandgap of the clusters. The patterns in the PL-spectra is a result of various parameters like the product of electron and hole DOS with respect to the mid-point of the bandgap and also on the electronic states available which satisfy the dipole selection rules. We find that there is a small PL-peak at energy below the bandgap emission energy. This is attributed to the intra-band transition. In experimental conditions the intra-band emission in silicon clusters may not contribute because of the presence of phonons which absorbs and thereby

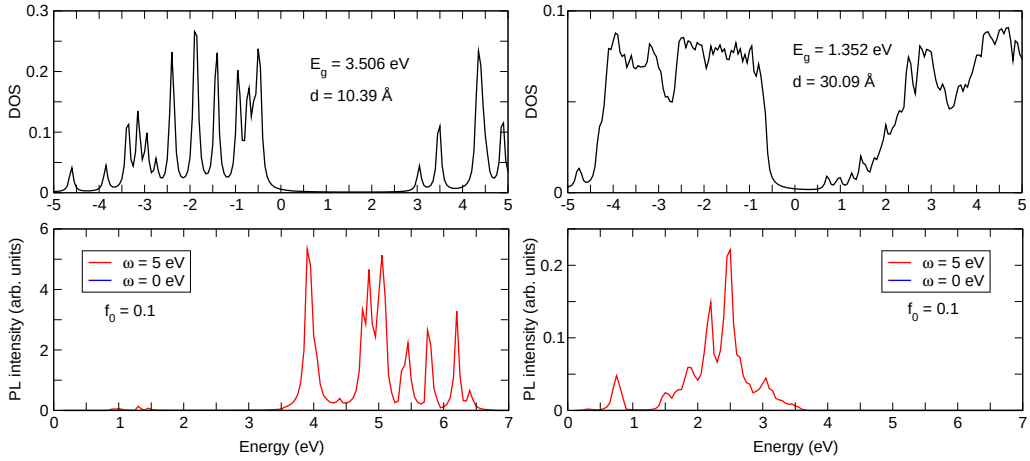

Figure B.2.: DOS and PL intensity (arbitrary units) plotted for Si_{29} cluster (left) and Si_{705} cluster (right). Peak patterns are observed when the clusters are excited with photon. The red-shift (low energy) of PL peak with increase in size can be observed.

allows for non-radiative recombination. The present formalism does not include any role of phonon. It has been demonstrated by Gupta *et al.* that functionalization of Si nanoparticle by simple polymer molecules alters the surface properties while maintaining the size of the nanoparticle intact (similar to the size of non-functionalized Si nanoparticles). Since the surface property of the nanoparticle changes, the PL peak changes its energy position [316]. One of the possible explanation for this could be the steric hindrance of the polymer molecules. For a better understanding this phenomenological behavior can be studied from the theory discussed here by incorporating TB-parameters for C and H (C-C, H-H, C-H and C-Si bonds), data of which can be easily found from literature. An extension of the theory to include magnetism is left for future work.

So far, the photoluminescence calculations (using TB formalism) has been applied by us to small Si clusters. Application to ZnO doped with magnetic and non-magnetic impurities was the final goal but these calculations could not be finished in time. Due aim of this calculation is to further discriminate between the DOS of various dopants in ZnO. Work along these lines is in progress.

Bibliography

[1] *ZnO rediscovered - once again!?*, Advances in Spectroscopy for Lasers and Sensing, Ed. B. D. Bartolo and O. Forte, 2006 (Springer, Netherlands).

[2] *http://www.energyharvestingjournal.com/articles/energy-harvesting-from-zinc-oxide-nanowires-00001431.asp*

[3] IBM J. Res. Develop. **14**, Issue 3 (1970).

[4] J. A. Gaj, R. R. Gatzzka and M. Nawrocki, *Giant exciton Faraday rotation in* $Cd_{1-x}Mn_xTe$ *mixed crystals*, Solid State Commun. **25**, 193 (1978).

[5] H. J. Zhu, M. Ramsteiner, H. Kostial, M. Wassermeier, H. P. Schönherr and K. H. Ploog, *Room-temperature spin injection from Fe into GaAs*, Phys. Rev. Lett. **87**, 016601 (2001).

[6] B. T. Matthias, R. M. Bozorth and J. H. Van Vleck, *Ferromagnetic interaction in EuO*, Phys. Rev. Lett. **7**, 160 (1961).

[7] H. Ohno, A. Shen, F. Matsukura, A. Oiwa, A. Endo, S. Katsumoto and Y. Iye, *(Ga,Mn)As: A new diluted magnetic semiconductor based on GaAs*, Appl. Phys. Lett. **69**, 363 (1996).

[8] K. Y. Wang, R. P. Campion, K. W. Edmonds, M. Sawicki, T. Dietl, C. T. Foxon and B. L. Gallagher, *Magnetism in (Ga,Mn)As Thin Films With* T_C *Up To 173K*, AIP Conf. Proc. **772**, 333 (2005).

[9] A. H. MacDonald, P. Schiffer and N. T. Samarth, *Ferromagnetic semiconductors: Moving beyond (Ga,Mn)As*, Nature Materials **4**, 195 (2005).

[10] Y. D. Park, A. T. Hanbicki, S. C. Erwin, C. S. Hellberg, J. M. Sullivan, J. E. Mattson, T. F. Ambrose, A. Wilson, G. Spanos and B. T. Jonker, *A group-IV ferromagnetic semiconductor:* Mn_xGe_{1-x}, Science **295**, 651 (2002).

[11] S. J. Potashnik, K. C. Ku, S. H. Chun, J. J. Berry, N. Samarth, and P. Schiffer, *Effects of annealing time on defect-controlled ferromagnetism in* $Ga_{1-x}Mn_xAs$, Appl. Phys. Lett. **79**, 1495 (2001).

[12] B. Beschoten, P. A. Crowell, I. Malajovich, D. D. Awschalom, F. Matsukura, A. Shen and H. Ohno, *Magnetic circular dichroism studies of carrier-induced ferromagnetism in $(Ga_{1-x}Mn_x)As$*, Phys. Rev. Lett. **83**, 3073 (1999).

[13] H. Ohno and F. Matsukura, *A ferromagnetic III-V semiconductor: (Ga,Mn)As*, Solid State Commun. **117**, 179 (2001).

[14] R. K. Patheria, *Statistical Mechanics*, Butterworth-Heinemann, Oxford (1996).

[15] K. C. Ku, S. J. Potashnik, R. F. Wang, S. H. Chun, P. Schiffer, N. Samarth, M. J. Seong, A. Mascarenhas, E. Johnston-Halperin, R. C. Myers, A. C. Gossard and D. D. Awschalom, *Highly enhanced Curie temperature in low-temperature annealed [Ga,Mn]As epilayers*, Appl. Phys. Lett. **82**, 2302 (2003)

[16] J. Sinova, T. Jungwirth, S. R. Eric Yang, J. Kucera, and A. H. MacDonald, *Infrared conductivity of metallic (III,Mn)V ferromagnets*, Phys. Rev. B **66**, 041202 (2002).

[17] G. Zarand and B. Janko, *$Ga_{1-x}Mn_xAs$: A frustrated ferromagnet*, Phys. Rev. Lett. **89**, 047201, 2002.

[18] T. Dietl, *Ferromagnetic semiconductors*, Semicond. Sci. Technol. **17**, 377 (2002).

[19] J. König, H. H. Lin and A. H. MacDonald. *Theory of diluted magnetic semiconductor ferromagnetism*, Phys. Rev. Lett. **84**, 5628 (2000).

[20] S. R. Eric Yang, J. Sinova, T. Jungwirth, Y.P. Shim and A.H. MacDonald, *Non-drude optical conductivity of (III,Mn)V ferromagnetic semiconductors*, Phys. Rev. B **67**, 045205 (2003).

[21] M. Berciu and R. N. Bhatt, *Effects of disorder on ferromagnetism in diluted magnetic semiconductors*, Phys. Rev. Lett. **87**, 107203 (2001).

[22] A. Chattopadhyay, S. Das Sarma, and A. J. Millis, *Transition temperature of ferromagnetic semiconductors: A dynamical mean field study*, Phys. Rev. Lett. **87**, 227202 (2001).

[23] G. Alvarez, M. Mayr and E. Dagotto, *Phase diagram of a model for diluted magnetic semiconductors beyond mean-field approximations*, Phys. Rev. Lett., **89**, 277202, (2002).

[24] H. Akai, *Ferromagnetism and its stability in the diluted magnetic semiconductor (In, Mn)As*, Phys. Rev. Lett. **81**, 3002 (1998).

[25] M. Mayr, G. Alvarez and E. Dagotto, *Global versus local ferromagnetism in a model for diluted magnetic semiconductors studied with Monte Carlo techniques* Phys. Rev. B, **65**, 241202, 2002.

[26] G. Alvarez and E. Dagotto, *Single-band model for diluted magnetic semiconductors: Dynamical and transport properties and relevance of clustered states*, Phys. Rev. B **68**, 045202, (2003).

[27] A. Kaminski and S. Das Sarma, *Polaron percolation in diluted magnetic semiconductors*, Phys. Rev. Lett. **88**, 247202 (2002).

[28] G. Alvarez, *Numerical study of the relevance of clustered states in diluted magnetic semiconductors and high temperature superconductors* Doctoral Thesis, Florida State University (2004)

[29] T. Dietl, H. Ohno, F. Matsukura, J. Cibert and D. Ferrand, *Zener model description of ferromagnetism in zinc-blende magnetic semiconductors*, Science **287**, 1019 (2000).

[30] C. Liu, F. Yun and H. Morkoç, *Ferromagnetism of ZnO and GaN: A Review*, J. Mater. Sci. - Mater. Electron. **16**, 555 (2005).

[31] C. Jagadish and S. Pearton, *Zinc Oxide Bulk, Thin Films and Nanostructures: Processing, Properties and Applications*, Elsevier, Oxford (2007).

[32] Hadis Morkoç and Ümit Özgür, *Zinc Oxide: Fundamentals, Materials and Device Technology*, WILEY-VCH verlag GmbH, Weinheim (2009).

[33] T. Kammermeier, *Structural and magnetic investigation of dilute magnetic semiconductors based on GaN and ZnO*, Doctoral Thesis, University of Duisburg-Essen (2008).

[34] A. Ney, *Element specific versus integral structural and magnetic properties of Co:ZnO and Gd:Gan probed with hard X-ray absorption spectroscopy*, Materials **3**, 3565 (2010).

[35] T. Kammermeier, V. Ney, S. Ye, K. Ollefs, T. C. Kaspar, S. A. Chambers, F. Wilhelm, A. Rogalev, and A. Ney, *Element specific measurements of the structural properties and magnetism of* $Co_xZn_{1-x}O$, J. Magn. Magn. Mater. **321**, 699 (2009).

[36] A. Ney, K. Ollefs, S. Ye, T. Kammermeier, V. Ney, T. C. Kaspar, S. A. Chambers, F. Wilheilm, and A. Rogalev, *Absence of intrinsic ferromagnetic interactions of isolated and paired Co dopant atoms in* $Zn_{1-x}Co_xO$ *with high structural perfection*, Phys. Rev. Lett. **100**, 157201 (2008).

[37] R. Djenadic, *Optimization of chemical vapor synthesis of oxide nanoparticles*, Doctoral Thesis, University of Duisburg-Essen (2011).

[38] H-J. Lee, S-Y. Jeong, C. R. Cho, and C. H. Park, *Study of diluted magnetic semiconductor: Co-doped ZnO*, Appl. Phys. Lett. **81**, 4020 (2008).

[39] M. Snure, D. Kumar, and A. Tiwari, *Progress in ZnO-based diluted magnetic semiconductors*, JOM-J. Min. Met. Mat. S. **61**, 72 (2009).

[40] T. Shi, Z. Xiao, Z. Yin, X. Li, Y. wang, H. He, J. Wang, W. Yan, and S. Wei, *The role of Zn interstitials in cobalt-doped ZnO diluted magnetic semiconductors,* Appl. Phys. Lett. **96**, 211905 (2010).

[41] H. Gu, Y. Jiang, Y. Xu, and M. Yan, *Evidence of the defect-induced ferromagnetism in Na and Co codoped ZnO*, Appl. Phys. Lett. **98**, 012502 (2011).

[42] S. K. Nayak, M. Ogura, A. Hucht, S. Buschmann, H. Akai and P. Entel, *Ab-initio simulations of diluted magnetic semiconductors: cobalt-doped zinc oxide*, Phys. Stat. Sol. (a) **205**, 1839 (2008).

[43] A. Zunger, S. Lany, and H. Raebiger, *The quest for dilute ferromagnetism in semiconductors: Guides and misguides by theory*, Physics **3**, 53 (2010).

[44] M. Springborg (ed), *Density-functional Methods in Chemistry and Materials Science*, (Wiley Research Series in Theoretical Chemistry), John Wiley and Sons Ltd., England (1997).

[45] R. M. Martin, *Electronic structure: basic theory and practical methods*, Cambridge, 2004

[46] R. M. Dreizler and E. K. U. Gross, *Density Functional Theory: An Advanced Course*, Springer, 2010

[47] S. J. Clarke, *Complex Structure in Tetrahedral Semiconductors*, Doctoral thesis, University of Edinburgh (1994). (Available online at $http$: $//cmt.dur.ac.uk/sjc/thesis/thesis/thesis.html$.)

[48] M. C. Gibson, *Implementation and Application of Advanced Density Functionals*, Doctoral thesis, University of Durham (2006). (Available online at $http$: $//portellen.phycmt.dur.ac.uk/sjc/thesis_mcg/$.)

[49] R. G. Parr and W. Yang *Density-Functional Theory of Atoms and Molecules*, Oxford University Press, New York (1989)

[50] G. Kotliar, S. Y. Savrasov, K. Haule, V. S. Oudovenko, O. Parcollet, and C. A. Marianetti, *Electronic structure calculations with dynamical mean-field theory*, Rev. Mod. Phys. **78**, 865 (2006).

[51] P. Hohenberg and W. Kohn, *Inhomogeneous electron gas*, Phys. Rev. **136**, B864 (1964).

[52] W. Kohn and L. J. Sham, *Self-consistent equations including exchange and correlation effects*, Phys. Rev. **140**, A1133 (1965).

[53] R. K. Nesbet, *Kinetic energy in density-functional theory*, Phys. Rev. A **58**, R12 (1998).

[54] R. Orlando, R. Dovesi, C. Roetti, and V. R. Saunders, *Ab initio Hartree-Fock calculations for periodic compounds: Application to semiconductors,* J. Phys.: Condens. Matter, **2**, 7769 (1990).

[55] J. M. Soler, E. Artacho, J. D. Gale, A. Garcia, J. Junquera, P. Ordejon, and D. Sanchez-Portal, *The SIESTA method for ab initio order-N materials simulation,* J. Phys.: Condens. Matter, **14**, 2745 (2002).

[56] H. J. Monkhorst and J. D. Pack, *Special points for Brillouin-zone integrations,* Phys. Rev. B **13**, 5188 (1976).

[57] J. C. Phillips, *Energy-Band Interpolation Scheme Based on a Pseudopotential,* Phys. Rev. **112**, 685 (1958).

[58] J. C. Phillips and L. Kleinman, *New Method for Calculating Wave Functions in Crystals and Molecules,* Phys. Rev. **116**, 287 (1959).

[59] M. L. Cohen and V. Heine, *The Fitting of Pseudopotentials to Experimental Data and Their Subsequent Application,* Solid State Physics **24**, eds. H. Ehrenreich, F. Seitz, and D. Turnbull (Academic Press, New York, 1970), p.37.

[60] L. Kleinman and D. M. Bylander, *Efficacious form for model pseudopotentials,* Phys. Rev. Lett. **48**, 1425 (1982).

[61] P. Mavropoulos and N. Papanikolaou, *The Korringa-Kohn-Rostoker (KKR) Green function method I. Electronic structure of periodic systems,* in Computational Nanoscience: Do It Yourself!, edited by J. Grotendorst, S. Blügel and D. Marx, NIC Series **31**, NIC-Directors Jülich 2006.

[62] P. H. Dederichs, S. Lounis, and R. Zeller, *The Korringa-Kohn-Rostoker (KKR) Green function method II. Impurities and clusters in the bulk and on surfaces,* in Computational Nanoscience: Do It Yourself!, edited by J. Grotendorst, S. Blügel and D. Marx, NIC Series **31**, NIC-Directors Jülich 2006.

[63] T. H. Dupree, *Electron scattering in a crystal lattice,* Ann. Phys. **15**, 63 (1961).

[64] J. L. Beeby, *The Density of Electrons in a Perfect or Imperfect Lattice,* Proc. Roy. Soc. London Ser. A **302**, 113 (1967).

[65] G. J. Morgan, *Bloch waves and scattering by impurities,* Proc. Phys. Soc. **89**, 365 (1966).

[66] P. Soven, *Coherent-potential model of substitutional disordered alloys,* Phys. Rev. **156**, 809 (1967).

[67] P. Soven, *Contribution to the Theory of disordered alloys*, Phys. Rev. **178**, 1136 (1969).

[68] H. Shiba, *A reformulation of the coherent potential approximation and its applications*, Prog. Theo. Phys. **46**, 77 (1971).

[69] A. Gonis, *Theoretical materials science*, Materials Research Society (2000).

[70] A. I. Liechtenstein, M. I. Katsnelson, V. P. Antropov and V. A. Gubanov, *Local spin density functional approach to the theory of exchange interactions in ferromagnetic metals and alloys*, J. Magn. Magn. Mater. **67**, 65 (1987).

[71] D. P. Landau and K. Binder, *A Guide to Monte Carlo Simulations in Statistical Physics*, Cambridge University Press, Cambridge (2000).

[72] P. Peczak, A. M. Ferrenberg, and D. P. Landau, *High-accuracy Monte Carlo study of the three-dimensional classical Heisenberg ferromagnet*, Phys. Rev. B **43**, 6087 (1991).

[73] C. Holm and W. Janke, *Critical exponents of the classical three-dimensional Heisenberg model: A single-cluster Monte Carlo study*, Phys. Rev. B **48**, 936 (1993).

[74] S. Maekawa, T. Tohyama, S. E. Barnes, S. Ishihara, W. Koshibae, and G. Khaliullin, *Physis of Transition Metal Oxides*, Springer-Verlag Berlin, 2004.

[75] J. Hubbard, *Electron correlations in narrow energy bands*, Proc. Roy. Soc. A**276**, 238 (1963).

[76] J. Hubbard, *Electron correlations in narrow energy bands. II. The degenerate band case*, Proc. Roy. Soc. A**277**, 237 (1964).

[77] P. W. Anderson, *New approach to the theory of superexchange interactions*, Phys. Rev. **115**, 2 (1959).

[78] P. W. Anderson, *A re-examination of concepts in magnetic metals: The 'nearly antiferromagnetic Fermi liquid'*, Adv. in Phys. **46**, 3 (1997).

[79] J. Kanamori, *Superexchange interaction and symmetry properties of electron orbitals*, J. Phys. Chem. Solids **10**, 87 (1959).

[80] J. B. Goodenough, *Theory of the role of covalence in the perovskite-type manganites [La, M(II)]MnO_3*, Phys. Rev. **100**, 564 (1955).

[81] J. Zaanen, G, Sawatzky and J. W. Allen, *Band gaps and electronic structure of transition-metal compounds*, Phys. Rev. Lett. **55**, 418 (1985).

[82] G. H. Jonkar and J. H. Santen, *Ferromagnetic compounds of manganese with perovskite structure*, Physica **16**, 337 (1950).

[83] C. Zener, *Interaction between the d-Shells in the transition metals. II. Ferromagnetic compounds of manganese with perovskite structure*, Phys. Rev. **82**, 403 (1951).

[84] P. W. Anderson and H. Hasegawa, *Considerations on double exchange*, Phys. Rev. **100**, 675 (1955).

[85] P. W. Anderson, *Antiferromagnetism. Theory of superexchange interaction*, Phys. Rev. **79**, 350 (1950).

[86] P. G. de Gennes, *Effects of souble exchange in magnetic crystals*, Phys. Rev. **118**, 141 (1960).

[87] P. H. Dederichs, K. Sato and H. Katayama-Yoshida, *Dilute magnetic semiconductors*, Phase Transitions **78**, 851 (2005).

[88] B. Belhadji, *Ab-initio calculations for diluted magnetic semiconductors*, Doctoral thesis, RWTH-Aachen (2008).

[89] B. W. Jacobs, V. M. Ayers, M. P. Petkov, J. B. Halpern, M. He, A. D. Baczewski, K. AcElroy, M. A. Crimp, J. Zhang, and H. C. Shaw, *Electronic and structural characteristics of zinc-blende wurtzite biphasic homostructure GaN nanowires*, Nano Lett. **7**, 1435 (2007).

[90] E. H. Kisi and M. M. Elcombe, *u parameters for the wurtzite structure of ZnS and ZnO using powder neutron diffraction*, Acta Crystallogr. C **45**, 1867 (1989).

[91] J. Albertsson, S. C. Abrahams and Å. Kvick, *Atomic displacement, anharmonic thermal vibration, expansivity and pyroelectric coefficient thermal dependences in ZnO*, Acta Crystallogr. B **45**, 34 (1989).

[92] G. Kresse and J. Furthmüller, *Efficiency of ab-initio total energy calculations for metals and semiconductors using a plane-wave basis set*, Comput. Mater. Sci. **6**, 15 (1996).

[93] G. Kresse and J. Furthmüller, *Efficient iterative schemes for ab initio total-energy calculations using a plane-wave basis set*, Phys. Rev. B **54**, 11169 (1996).

[94] J. P. Perdew, in *Electronic Structure of Solids'91*, edited by P. Ziesche and H. Eschrig (Akademie Verlag, Berlin 1991), pp.11-20.

[95] *Atoms in Molecules - A Quantum Theory*, R. F. W. Bader, Oxford University Press, Oxford, 1990

[96] S. Saib and N. Bouarissa, *Structural parameters and transition pressures of ZnO: Ab-initio calculations*, Phys. Stat. Sol. (b) **244** 1063 (2007).

[97] A. Schleife, F. Fuchs, J. Furthmüller, and F. Bechstedt, *First-principles study of ground- and excited-state properties of MgO, ZnO and CdO polymorphs*, Phys. Rev. B **73** 245212 (2006).

[98] S. Desgreniers, *High-density phases of ZnO: Structural and compressive parameters*, Phys. Rev. B **58** 14102 (1998).

[99] H. Karzel, W. Potzel, M. Köfferlein, W. Schiessl, M. Steiner, U. Hiller, G. M. Kalvius, D. W. Mitchell, T. P. Das, P. Blaha, K. Schwarz, and M. P. Pasternak, *Lattice dynamics and hyperfine interactions in ZnO and ZnSe at high external pressures*, Phys. Rev. B **53** 11425 (1996).

[100] J. E. Jeffe, J. A. Snyder, Z. Lin, and A. C. Hess, *LDA and GGA calculations for high-pressure phase transitions in ZnO and MgO*, Phys. Rev. B **62** 1660 (2000).

[101] J. P. Perdew, K. Bruke and M. Ernzerhof, *Generalized gradient approximation made simple*, Phys. Rev. Lett. **77**, 3865 (1996).

[102] J. Heyd, G. E. Scuseria and M. Ernzerhof, *Hybrid functionals based on a screened Coulomb potential*, J. Chem. Phys. **118**, 8207 (2003).

[103] R. W. G. Wyckoff, Crystal Structures, Vol 1, 2nd Edition, Wiley, New York, 1986, p. 112.

[104] K. Sato and H. Katayama-Yoshida, *Ferromagnetism in a transition metal atom doped ZnO*, Physica E **10**, 251 (2001).

[105] J. L. Lyons, A. Janotti, and C. G. Van de Walle, *Why nitrogen cannot lead to p-type conductivity in ZnO*, Appl. Phys. Lett. **95**, 252105 (2009).

[106] H. Schulz and K. H. Thiemann, *Structure parameters and polarity of the wurtzite type compounds SiC-2H and ZnO*, Solid State Commun. **32**, 783 (1979).

[107] D. Vogel, P. Krüger and J. Pollmann, *Self-interaction and relaxation-corrected pseudopotentials for II-VI semiconductors*, Phys. Rev. B **54**, 5495 (1996).

[108] J. P. Perdew and A. Zunger, *Self-interaction correction to density-functional approximations for many-electron systems*, Phys. Rev. B **23**, 5048 (1981).

[109] I. V. Maznichenko, A. Ernst, M. Bouhassoune, J. Henk, M. Däne, M. Lüders, P. Bruno, W. Hergert, I Mertig, Z. Szotek and W. M. Temmerman, *Structural phase transitions and fundamentals band gaps of $Mg_xZn_{1-x}O$ alloys from first principles*, Phys. Rev. B **80**, 144101 (2009).

[110] R. A. Powell, W. E. Spicer, and J. C. McMenamin, *Location of the Zn 3d states in ZnO*, Phys. Rev. Lett. **27**, 97 (1971).

[111] C. J. Vesely, R. L. Hengehold, and D. W. Langer, *uv photoemission measurements of the upper d levels in the IIB-VIA compounds*, Phys. Rev. B **5**, 2296 (1972).

[112] L. Ley, R. A. Pollak, F. R. McFeely, S. P. Kowalczyk, and D. A. Shirley, *Total valence-band densities of states of III-V and II-VI compounds from x-ray photoem ission spectroscopy*, Phys. Rev. B **9**, 600 (1974).

[113] W. Göpel, J. Pollmann, I. Ivanov, and B. Reihl, *Angle-resolved photoemission from polar and nonpolar zinc oxide surfaces* Phys. Rev. B **26**, 3144 (1982).

[114] Ü. Özgür, Y. I. Alivov, C. Liu, A. Teke, M. A. Reshchikov, S. Doğan, V. Avrutin, S. -J. Cho, and H. Morkoç, *A comprehensive review of ZnO materials and devices* J. Appl. Phys. **98**, 041301 (2005).

[115] K. Ozawa, K. Sawada, Y. Shirotori, and K. Edamoto, *Angle-resolved photoemission study of the valence band structure of ZnO(10$\bar{1}$0)*, J. Phys.: Condens. Matter **17**, 1271 (2005).

[116] O. A. Vydrov and G. E. Scuseria, *Effect of the Perdew-Zunger self-interaction correction on the thermochemical performance of approximate density functionals*, J. Chem. Phys, **121**, 8187 (2004), Erratum at http://www.mit.edu/ vydrov/erratum-2.htm.

[117] V. I. Anisimov, J. Zaanen and O. K. Andersen, *Band theory and Mott insulators: Hubbard U instead of Stoner I*, Phys. Rev. B **44**, 943 (1991).

[118] I. V. Solovyev, P. H. Dederichs and V. I. Anisimov, *Corrected atomic limit in the local-density approximation and the electronic structure of d impurities in Rb*, Phys. Rev. B, **50**, 16861 (1994).

[119] V. I. Anisimov, I. V. Solovyev, M. A. Korotin, M. T. Czyżyk and G. A. Sawatzky, *Density-functional theory and NiO photoemission spectra*, Phys. Rev. B **48**, 16929 (1993).

[120] W. E. Pickett, S. C. Erwin and E. C. Ethridge, *Reformulation of the LDA+U method for a local-orbital basis*, Phys. Rev. B **58**, 1201 (1998).

[121] V. I. Anisimov, F. Ayyasetiawan and A. I. Lichtenstein, *First-principles calculations of the electronic structure and spectra of strongly correlated systems: the LDA + U method*, J. Phys.: Condens. Matter **9**, 767 (1997).

[122] A. I. Liechtenstein, V. I. Anisimov and J. Zaanen, *Density-functional theory and strong interactions: Orbital ordering in Mott-Hubbard insulators*, Phys. Rev. B **52**, R5467 (1995).

[123] S. L. Dudarev, G. A. Button, S. Y. Savrasov, C. J. Humphreys, and A. P. Sutton, *Electron-energy-loss spectra and the structural stability of nickel oxide: An LSDA+U study* Phys. Rev. B **57**, 1505 (1998).

[124] J. P. Perdew, M. Ernzerhof and K. Bruke, *Rationale for mixing exact exchange with density functional approximations*, J. Chem. Phys. **105**, 9982 (1996).

[125] C. Adamo and V. Barone, *Toward reliable density functional methods without adjustable parameters: The PBE0 model*, J. Chem. Phys. **110**, 6158 (1999).

[126] V. N. Straroverov, G. E. Scuseria, J. Tao and J. P. Perdew, *Comparative assessment of a new nonempirical density functional: Molecules and hydrogen-bonded complexes*, J. Chem. Phys. **119**, 12129 (2003).

[127] J. Paier, M. Marsman, K. Hummer, G. Kresse, I. C. Ferber and J. G. Ángyán, *Screened hybrid density functionals applied to solids*, J. Chem. Phys. **124**, 154709 (2006).

[128] J. Paier, M. Marsman, K. Hummer, G. Kresse, I. C. Ferber and J. G. Ángyán, *Erratum: "Screened hybrid density functionals applied to solids"* , J. Chem. Phys. **125**, 249901 (2006).

[129] A. V. Krukau, O. A. Vydrov, A. F. Izmaylov and G. E. Scuseria, *Influence of the exchange screening parameter on the performance of screened hybrid functionals*, J. Chem. Phys. **125**, 224106 (2006).

[130] M. M. Steiner, R. C. Albers, and L. J. Sham, *Quasiparticle properties of Fe, Co and Ni*, Phys. Rev. **45**, 13272 (1992).

[131] L. Hedin, *Electron correlation in semiconductors and insulators: Band gaps and quasiparticle energies*, Phys. Rev. **139**, A796 (1965).

[132] L. Hedin and S. Lundqvist, *Effects of electron-electron and electron-phonon interactions on the one-electron states of solids*, Solid State Physics - Vol. 23, edited by H. Ehrenreich, F. Seitz, D. Turnbull (Academic Press, New York, 1969).

[133] M. S. Hybertsen and S. G. Louie, *Electron correlation in semiconductors and insulators: Band gaps and quasiparticle energies*, Phys. Rev. B **34**, 5390 (1986).

[134] F. Aryasetiawan and O. Gunnarsson, *Electron correlation in semiconductors and insulators: Band gaps and quasiparticle energies*, Rep. Prog. Phys. **61**, 237 (1998).

[135] F. Fuchs, J. Furthmüller, F. Bechstedt, M. Shishkin and G. Kresse, *Quasiparticle band structure based on a generalized Kohn-Sham scheme*, Phys. Rev. B **76**, 115109 (2007).

[136] J. Hafner, *Ab-initio simulations of materials using VASP*, J. Comput. Chem. **29**, 2044 (2008).

[137] J. Paier, R. Hirschl, M. Marsman, and G. Kresse, *The Perdew-Burke-Ernzerhof exchange-correlation functional applied to the G2-1 test set using a plane-wave basis set*, J. Chem. Phys. **122**, 234102 (2005).

[138] J. Paier, M. Marsman, and G. Kresse, *Why does the B3LYP hybrid functional fail for metals?*, J. Chem. Phys. **127**, 024103 (2007).

[139] M. Shishkin, M. Marsman, and G. Kresse, *Accurate quasiparticle spectra from self-consistent GW calcualtions with vertes corrections*, Phys. Rev. Lett. **99**, 246403 (2007).

[140] M. Shishkin and G. Kresse, *Self-consistent GW calculations for semiconductors and insulators*, Phys. Rev. B **75**, 235102 (2007).

[141] M. van Schilfgaarde, T. Kotani, and S. Faleev, *Quasiparticle self-consistent GW theory*, Phys. Rev. Lett. **96**, 226402 (2006).

[142] C. Friedrich, A. Schindlmayr, S. Blügel, and T. Kotani, *Elimination of the linearization error in GW calculations based on the linearized augmented-plane-wave method*, Phys. Rev. B **74**, 045104 (2006).

[143] A. R. H. Preston, B. J. Ruck, L. F. J. Piper, A. DeMasi, K. E. Smith, A. Schleife, F. Fuchs, F. Bechstedt, J. Chai, and S. M. Durbin, *Band structure of ZnO from resonant x-ray emission spectroscopy*, Phys. Rev. B **78**, 155114 (2008).

[144] A. I. Liechtenstein, M. I. Katsnelson and V. A. Gubanov, *Exchange interactions and spin-wave stiffness in ferromagnertic metals*, J. Phys. F: Met. Phys. **14**, L125 (1984).

[145] S. H. Vosko, L. Wilk, and M. Nusair, *Accurate spin-dependent electron liquid correlation energies for local spin density calculations: A critical analysis*, Can. J. Phys. **58**, 1200 (1980).

[146] M. E. Fisher, *Renormalization Group in theory of critical behavior*, Rev. Mod. Phys. **46**, 579 (1974).

[147] H. E. Stanley, *Introduction to Phase Transitions and Critical Phenomena*, Oxford University Press, 1971.

[148] K. Tomiyasu, T. Inami and N. Ikeda, *Magnetic structure of CoO studied by neutron and synchrotron x-ray diffraction*, Phys. Rev. B **70**, 184411 (2004).

[149] K. Sato, H. Katayama-Yoshida, and P. H. Dederichs, *High Curie temperature and nano-scale spinodal decomposition phase in dilute magnetic semiconductors*, Jpn. J. Appl. Phys. **44**, L948 (2005).

[150] H. Katayama-Yoshida, K. Sato, T. Fukushima, M. Toyoda, H. Kizali, V. A. Dinh and P. H. Dederichs, *Theory of ferromagnetic semiconductors*, Phys. Stat. Sol. **204**, 15 (2007).

[151] N. Akdogan, A. Nefedov, K. Westerholt, H. Zabel, H. Becker, C. Somsen, E. Khaibullin, and L. Tagirov, *Intrinsic room temperature ferromagnetism in Co-implanted ZnO*, J. Phys. D: Appl. Phys. **41**, 165001 (2008).

[152] N. Akdogan, H. Zabel, A. Nefedov, K. Westerholt, H. Becker, S. Gök, R. Khaibullin, and L. Tagirov, *Dose dependence of ferromagneism in Co-implanted ZnO*, J. Appl. Phys. **105**, 043907 (2009).

[153] W. M. Temmerman, B. L. Gyorffy, and G. M. Stocks, *The atomic sphere approximation to the KKR-CPA: Electronic structure of paramagnetic Cu_cNi_{1-c} alloys*, J. Phys. F: Metal Phys. **8**, 2461 (1978).

[154] O.K. Andersen and O. Jepsen, *Advances in the theory of one-electron energy states*, Physica B+C **91**, 317 (1977).

[155] KKR code developed in Research Center Jülich by R. Zeller *et. al.*

[156] H. Ebert, *Fully relativistic band structure calculations for magnetic solids - formalism and application in electronic structure and physical properties of Solids*, Lecture Notes in Physics, edited by H. Dreysse, vol. 50, p. 191, Springer Berlin (2000).

[157] http://olymp.cup.uni-muenchen.de/ak/ebert/SPRKKR

[158] M. Toyoda, H. Akai, K. Sato, and H. Katayama-Yoshida, *Electronic structures of (Zn, TM)O (TM: V, Cr, Mn, Fe, Co, and Ni) in the self-interaction-corrected calculations*, Physica B **376-377**, 647 (2006).

[159] A. S. Risbud, L. P. Snedeker, M. M. Elcombe, A. K. Cheetham, and R. Seshadri, *Wurtzite CoO*, Chem. Mater. **17**, 834 (2005).

[160] R. Zeller, *Lloyd's formula in multiple-scattering calculations with finite temperature*, J. Phys.: Condens. Matter **17**, 5367 (2005).

[161] M. C. Payne, M. P. Teter, D. C. Allan, T. A. Arias and J. D. Joannopoulos, *Iterative minimization techniques for ab initio total-energy calculations: Molecular dynamics and conjugate gradients*, Rev. Mod. Phys. **64**, 1045 (1992).

[162] *Theory of Defects in Semiconductors*, Eds. D. A. Drabold and S. K. Estreicher, Springer-Verlag Berlin Heidelberg, (2007).

[163] R. P. Messmer and G. D. Watkins, *Linear Combination of Atomic Orbital-Molecular Orbital Treatment of the Deep Defect Level in a Semiconductor: Nitrogen in Diamond*, Phys. Rev. Lett. **25**, 656 (1970).

[164] S. Öğüt, and H. Kim, and J. R. Chelikowsky, *Ab initio cluster calculations for vacancies in bulk Si*, Phys. Rev. B **56**, R11353 (1997).

[165] *Advanced Calculations for Defects in Materials: Electronic Structure Methods*, A. Alkauskas, O. Deák, J. Neugebauer, A. Pasquarello, and C. G. Van de Walle (Eds.), Wiley-VCH Verlag & Co. KGaA, Weinheim (2011).

[166] K. Sato and H. Katayama-Yoshida, *Electronic structure and ferromagnetism of transition-metal-impurity-doped zinc oxide*, Physica B **308**, 904 (2001).

[167] V. L. Moruzzi, J. F. Janak, and A. R. Williams, *Calculated electronic properties of metals*, Pergamon, U.S.A., 1978, p. 11.

[168] D. M. Ceperley and B. J. Alder, *Ground State of the Electron Gas by a Stochastic Method*, Phys. Rev. Lett., **45**, 566 (1980).

[169] P. Gopal and N. A. Spaldin, *Magnetic interactions in transition-metal-doped ZnO: An an-initio study*, Phys. Rev. B. **74**, 094418 (2006).

[170] T. Chanier, M. Sargolzaei, I. Opahle, R. Hayn, and K. Koepernik, *LSDA+U versus LSDA: Towards a better description of the magnetic nearest-neighbor exchange coupling in Co- and Mn-doped ZnO*, Phys. Rev. **73**, 134418 (2006).

[171] *Magnetic Properties of Antiferromagnetic Oxide Materials: Surfaces, Interfaces, and Thin Films*, edited by L. Duò, M. Finazzi, and F. Ciccacci (WILEY-VCH Verlag GmbH & Co. KGaA, Weinheim, 2010).

[172] L. Wang, T. Maxisch, and G. Ceder, *Oxidation energies of transition metal oxides within the GGA+U framework*, Phys. Rev. B **73**, 195107 (2006).

[173] T. Tsujioka, T. Mizokawa, J. Okamoto, A. Fujimori, M. Nohara, H. Takagi, K. Yamaura, and M. Takano, *Hubbard splitting and electron correlation in the ferromagneic metal CrO_2*, Phys. Rev. B **56**, R15509 (1997).

[174] M. A. Korotin, V. I. Anisimov, D. I. Khomskii, and G. A. Sawatzky, *CrO_2: A self-doped double exchange ferromagnet*, Phys. Rev. Lett. **80**, 4305 (1998).

[175] H.-T Jeng, G. Y. Guo, *First-principles investigations of the orbital magnetic moments is CrO_2*, J. Appl. Phys. **92**, 951 (2002).

[176] C, Rödl, F. Fuchs, J. Furthmüller, and F. Bechstedt, *Quasiparticle band structures of the antiferromagnetic transition-metal oxides MnO, FeO, CoO, and NiO*, Phys. Rev. B **79**, 235114 (2009).

[177] R. Hanafin, T. Archer, and S. Sanvito, *Magnetism of wurtzite CoO nanoclusters*, Phys. Rev. B **81**, 054441 (2010).

[178] H.-X Deng, J. Li, S.-S. Li, J.-B. Xia, A. Walsh, and S.-H. Wei, *Origin of antiferromagnetism in CoO: A density functional theory strudy*, Appl. Phys. Lett. **96**, 162508 (2010).

[179] S. Sakong and P. Kratzer, *Density functional study of carbon doping in ZnO* , Semicond. Sci. Technol. **26**, 014038 (2011).

[180] W. A. Adeagbo, G. Fischer, A. Ernst, and W. Hergert, *Magnetic effects of defect pair formation in ZnO*, J. Phys.: Condens. Matter **22**, 436002 (2010).

[181] A. E. Bocquet, T. Mizokawa, K. Morikawa, A. Fujimori, S. R. Barman, K. Maiti, D. D. Sarma, Y. Tokura, and M. Onoda, *Electronic structure of early $3d$-transition-metal oxide by analysis of the $2p$ core-level photoemission spectra*, Phys. Rev. B **53**, 1161 (2001).

[182] S. Kümmel and L. Kronik, *Orbital-dependent density functionals: Theory and applications*, Rev. Mod. Phys. **80**, 3 (2008).

[183] E. Lee and K. J. Chang, *Ferromagnetic versus antiferromagnetic interaction in Co-doped ZnO* Phys. Rev. B **69**, 085205 (2004).

[184] D. Iuşan, M. Kabir, O. Grånäs, O. Eriksson, and B. Sanyal, *Microscopic picture of Co clustering in ZnO*, Phys. Rev. B **79**, 125202 (2009).

[185] M. B. Stearns, *Why is iron magnetic?*, Physics Today **38**, 34 (1978).

[186] R. J. Jelitto and A. Ziegler, *Ferromagnetismus bei Übergangsmetallen*, Phys. Bl. **39**, 95 (1983).

[187] K. Kenmochi, M. Seike, K. Sato, A. Yanase, and H. Katayama-Yoshida, *New Class of Diluted Ferromagnetic Semiconductors based on CaO without Transition Metal Elements*, Jpn. J. Appl. Phys. **43**, L934 (2004).

[188] A. L. Ivanovskii, *Magnetic effects induced by sp impurities and defects in nonmagnetic sp materials*, Physics-Uspekhi **50**, 1031 (2007).

[189] M. Venkatesan, C. B. Fitzgerald and J. M. D. Coey, *Thin films: Unexpected magnetism in a dielectric oxide*, Nature **430**, 630 (2004).

[190] O. Volnianska and P. Boguslawshi, *Magnetism of solids resulting from spin polarization of p orbitals*, J. Phys.: Condens. Matter **22**, 073202 (2010).

[191] P. Esquinazi, D. Spemann, R. Höhne, A. Setzer, K-H. Han and T. Butz, *Induced Magnetic Ordering by Proton Irradiation in Graphite*, Phys. Rev. Lett. **91**, 227201 (2003).

[192] T. Makarova and F. Palacio (eds.), Carbon-based magnetism: An overview of metal free carbon-based compounds and materials (Elsevier, Amsterdam, 2006).

[193] L. Wang, Z. Pang, L. Lin, S. Fang, Y. Dai, and S. Han, *Origin of magnetism in undoped MoO_2 studied by first-principles calculations*, Phys. Rev. B **81**, 134407 (2010).

[194] S. W. Fan, K. L. Yao, Z. L. Liu, G. Y. Gao, Y. Min, and H. G. Cheng, *Ferromagnetic properties, electronic structure, and formation energy of $Ga_{0.9375}M_{0.0625}N$ (M = vacancy, Ca) by first principles study*, J. Appl. Phys. **104**, 043912 (2008).

[195] P. Dev, Y. Xue, and P. Zhang, *Defect-Induced Intrinsic Magnetism in Wide-Gap III Nitrides*, Phys. Rev. Lett. **100**, 117204 (2008).

[196] H. Peng, J. Li, S-S. Li, and J-B. Xia, *Possible origin of ferromagnetism in undoped anatase TiO_2*, Phys. Rev. B **79**, 092411 (2009).

[197] Q. Wang, Q. Sun, G. Chen, Y. Kawazoe and P. Jena, *Vacancy-induced magnetism in ZnO thin films and nanowires*, Phys. Rev. B **77**, 205411 (2008).

[198] X. Zuo, S-D. Yoon, A. Yang, W-H. Duan, C. Vittoria, and V. G. Harris, *Ferromagnetism in pure wurtzite zinc oxide*, J. Appl. Phys. **105**, 07C508 (2009).

[199] B. Song, J. C. Han, J. K. Jian, H. Li, Y. C. Wang, H. Q. Bao, W. Y. Wang, H. B. Zuo, X. H. Zhang, S. H. Meng, and X. L. Chen, *Experimental observation of defect-induced intrinsic ferromagnetism in III-V nitrides: The case of BN*, Phys. Rev. B **80**, 153203 (2009).

[200] L. X. Guan, J. G. Tao, C. H. Huan, J. L. Kuo and L. Wang, *Nonconventional magnetism in pristine and alkali doped In_2O_3: Density functional study*, J. Appl. Phys. **108**, 093911 (2010).

[201] J. Osorio-Guillén, S. Lany, S. V. Barabash and A. Zunger, *Nonstoichiometry as a source of magnetism in otherwise nonmagnetic oxides: Magnetically interacting cation vacancies and their percolation*, Phys. Rev. B **75**, 184421 (2007).

[202] C. D. Pemmaraju and S. Sanvito, *Ferromagnetism Driven by Intrinsic Point Defects in HfO_2*, Phys. Rev. Lett. **94**, 217205 (2005).

[203] J. Osorio-Guillén, S. Lany, S. V. Barabash and A. Zunger, *Magnetism without Magnetic Ions: Percolation, Exchange, and Formation Energies of Magnetism-Promoting Intrinsic Defects in CaO*, Phys. Rev. Lett. **96**, 107203 (2006).

[204] I. S. Elfimov, S. Yunoki and G. A. Sawatzky, *Dynamical Structure Factor of the Homogeneous Electron Liquid: Its Accurate Shape and the Interpretation of Experiments on Aluminum*, Phys. Rev. Lett. **89**, 216403 (2002).

[205] C-W. Zhang and S-S. Yan, *First-principles study on ferromagnetism in Mg-doped SnO_2*, Appl. Phys. Lett. **95**, 232108 (2009).

[206] J. B. Yi, C. C. Lim, G. Z. Xing, H. M. Fan, L. H. Van, S. L. Huang, K. S. Yang, X. L. Huang, X. B, Qin, B. Y. Wang, T. Wu, L. Wang, H. T. Zhang, X. Y. Gao, T. Liu, A. T. S. Wee, Y. P. Feng, and J. Ding, *Ferromagnetism in Dilute Magnetic Semiconductors through Defect Engineering: Li-Doped ZnO*, Phys. Rev. Lett. **104**, 137201 (2010).

[207] W. Zhou, L. Liu, and P. Wu, *Nonmagnetic impurities induced magnetism in SnO_2*, J. Magn. Magn. Mater. **321**, 3356 (2009).

[208] X. Zhang, Y. H. Cheng, L. Y. Li, H. Liu, X. Zuo, G. H. Wen, L. Li, R. K. Zheng, and S. P. Ringer, *Evidence for high-T_c ferromagnetism in $Zn_x(ZnO)_{1-x}$ granular films mediated by native point defects*, Phys. Rev. B **80**, 174427 (2009).

[209] A. Droghetti, N. Baadji, and S. Sanvito, *MgN: A possible material for spintronic applications*, Phys. Rev. B **80** 235310 (2009).

[210] B. Gu, N. Bulut, T. Ziman, and S. Maekawa, *Possible d^0 ferromagnetism in MgO doped with nitrogen*, Phys. Rev. B **79**, 024407 (2009).

[211] L. X. Guan, J. G. Tao, C. H. Huan, J. L. Kuo and L. Wang, *First-principles study on ferromagnetism in nitrogen-doped In_2O_3*, Appl. Phys. Lett. **95**, 012509 (2009).

[212] J. G. Tao, L. X. Guan, J. S. Pan, C. H. A. Huan, L. Wang, J. L. Kuo, Z. Zhang, J. W. Chai, and S. J. Wang, *Density functional study on ferromagnetism in nitrogen-doped anatase TiO_2*, Appl. Phys. Lett. **95**, 062505 (2009).

[213] K. Yang, Y. Dai, B. Huang, and M.-H Whangbo, *On the possibility of ferromagnetism in carbon-doped anatase TiO_2*, Appl. Phys. Lett. **93**, 132507 (2008).

[214] H. Pan, Y. P. Feng, Q. Y. Wu, Z. G. Huang, and J. Lin, *Surface characterization of Mn_xGe_{1-x} and $Cr_yMn_xGe_{1-x-y}$ dilute magnetic semiconductors*, Phys. Rev. B **77**, 125211 (2008).

[215] Y. Bai and Q. Chen, *N dopant induced antiferromagnetism in anatase TiO2 : First principle study*, Solid State Communications **147**, 169 (2008).

[216] K. Yang, Y. Dai, B. Huang, and M.-H. Whangbo, *Density functional studies of the magnetic properties in nitrogen doped TiO_2*, Chem. Phys. Lett. **481**, 99 (2009).

[217] M. D. McCluskey and S. J. Jokela, *Defects in ZnO*, J. Appl. Phys. **106**, 071101 (2009).

[218] S. B. Ogale, *Dilute Doping, Defects, and Ferromagnetism in Metal Oxide Systems*, Adv. Mater. **22**, 3125 (2010).

[219] S. K. Nayak, M. Ogura, A. Hucht, H. Akai and P. Entel, *Monte Carlo simulations of diluted magnetic semicondutors using ab-initio exchange parameters*, J. Phys.: Condens. Matter **21**, 064238 (2009).

[220] G. Kresse and D. Joubert, *From ultrasoft pseudopotentials to the projector augmented-wave method*, Phys. Rev. B **59**, 1758 (1999).

[221] K. Koepernik and H. Eschrig, *Full-potential nonorthogonal local-orbital minimum-basis band-structure scheme*, Phys. Rev. B **59**, 1743 (1999).

[222] H. Peng, H. J. Xiang, S-H Wei, S-S Li, J-B Xia, and J. Li, *Origin and Enhancement of Hole-Induced Ferromagnetism in First-Row d^0 Semiconductors*, Phys. Rev. Lett **102**, 017201 (2009).

[223] S. B. Zhang, S.-H. Wei, and A. Zunger, *Intrinsic n-type versus p-type doping asymmetry and the defect physics of ZnO*, Phys. Rev. B **63**, 075205 (2001).

[224] P. Erhart, K. Albe, and A. Klein, *First-principles study of intrinsic point defects in ZnO: Role of band structure, volume relaxation, and finite-size effects*, Phys. Rev. B **73**, 205203 (2006).

[225] P. Erhart, A. Klein and K. Albe, *First-principles study of the structure and stability of oxygen defects in zinc oxide*, Phys. Rev. B **72**, 085213 (2005).

[226] A. F. Kohan, G. Ceder, D. Morgan, and C. G. Van de Walle, *First-principles study of native point defects in ZnO*, Phys. Rev. B **61**, 15019 (2000).

[227] A. Janotti and C. G. Van de Walle, *Native point defects in ZnO*, Phys. Rev. B **76**, 165202 (2007).

[228] E.-C. Lee, Y.-S. Kim, Y.-G. Jin, and K. J. Chang, *Compensation mechanism for N acceptors in ZnO*, Phys. Rev. B **64**, 085120 (2001).

[229] A. Janotti and C. G. Van de Walle, *New insights into the role of native point defects in ZnO*, J. Cryst. Growth **287**, 58 (2006).

[230] F. Oba, S. R. Nishitani, S. Isotani, H. Adachi, and I. Tanaka, *Energetics of native defects in ZnO*, J. Appl. Phys. **90**, 824 (2001).

[231] F. Oba, M. Choi, A. Togo, A. Seko, and I. Tanaka, *Native defects in oxide semiconductors: A density functional approach*, J. Phys.: Condens. Matter **22**, 384211 (2010).

[232] C. G. Van de Walle and J. Neugebauer, *First-principles calculations for defects and impurities: Applications to III-nitrides*, J. Appl. Phys. **95**, 3851 (2004).

[233] S. Lany and A. Zunger, *Assessment of correction methods for the band-gap problem and for finite-size effects in supercell defect calculations: Case studies for ZnO and GaAs*, Phys. Rev. B **78**, 235104 (2008).

[234] C. Freysoldt, J. Neugebauer, and C. G. Van de Walle, *Fully Ab Initio Finite-Size Corrections for Charged-Defect Supercell Calculations*, Phys. Rev. Lett. **102**, 016402 (2009).

[235] P. Dev and P. Zhang, *Unconventional magnetism in semiconductors: Role of localized acceptor states*, Phys. Rev. B **81**, 085207 (2010).

[236] A. Kokalj, Comp. Mater. Sci. **28**, 155 (2003). Code available at http://www.xcrysden.org/.

[237] S. T. Tan, X. W. Sun, Z. G. Yu, P. Wu, G. Q. Lo, and D. L. Kwong, *p-type conduction in unintentional carbon-doped ZnO thin films* , Appl. Phys. Lett. **91**, 072101 (2007).

[238] Z. G. Yu, H. Gong, and P. Wu, *Study on anomalous n-type conduction of P-doped ZnO using P_2O_5 dopant source*, Appl. Phys. Lett. **86**, 212105 (2005).

[239] J. B. Varley, A. Janotti, and C. G. Van de Walle, *Group-V impurities in SnO_2 from first-principles calculations*, Phys. Rev. B **81**, 245216 (2010).

[240] X-L. Lin, S-S. Yan, M-W. Thao, S-J. Hu, X-X. Yao, C. Han, Y-X. Chen, G-L. Liu, Y-Y. Dai, and L-M. Mei, *Long-ranged and high temperature ferromagnetism in (Mn,C)-codoped ZnO studied by first-principles calculations*, J. Appl. Phys. **107**, 033903 (2010).

[241] H. Pan, J. B. Yi, L. Shen, R. Q. Wu, J. H. Yang, J. Y. Lin, Y. P. Feng, J. Ding, L. H. Van, and J. H. Yin, *Room-Temperature Ferromagnetism in Carbon-Doped ZnO*, Phys. Rev. Lett. **99**, 127201 (2007).

[242] K. Yang, R. Wu, L. Shen, Y. P. Feng, Y. Dai, and B. Huang, *Origin of d^0 magnetism in II-VI and III-V semiconductors by substitutional doping at anion site*, Phys. Rev. B **81**, 125211 (2010).

[243] S. Papan, S. Xiyu, H. Qinying, L. Yodong, and C. Wei, *First-principles calculation of the electronic band of ZnO doped with C*, J. Semicond. **30**, 052001 (2009).

[244] P. Mavropoulos, M. Ležaić, and S. Blügel, *Ferromagnetism in nitrogen-doped MgO: Density-functional calculations*, Phys. Rev. B **80**, 184403 (2009).

[245] X. Peng and R. Ahuja, *Non-transition-metal doped diluted magnetic semiconductors*, Appl. Phys. Lett. **94**, 102504 (2009).

[246] I. S. Elfimov, A. Rusydi, S. I. Csiszar, Z. Hu, H. H. Hsieh, H.-J. Lin, C. T. Chen, R. Liang and G. A. Sawatzky, *Magnetizing Oxides by Substituting Nitrogen for Oxygen* , Phys. Rev. Lett. **98**, 137202 (2007).

[247] L. Shen, R. Q. Wu, H. Pan, G. W. Peng, M. Yang, Z. D. Sha, and Y. P. Feng, *Mechanism of ferromagnetism in nitrogen-doped ZnO: First-principle calculations*, Phys. Rev. B **78**, 073306 (2008).

[248] S. W. Fan, K. L. Yao, and Z. L. Liu, *Half-metallic ferromagnetism in C-doped ZnS: Density functional calculations* , Appl. Phys. Lett. **94**, 152506 (2009).

[249] R. Long and N. J. English, *Magnetic properties of first-row element-doped ZnS semiconductors: A density functional theory investigation*, Phys. Rev. B **80**, 115212 (2009).

[250] G. Rahman and V. M. García-Suáez, *Surface-induced magnetism in C-doped SnO_2*, Appl. Phys. Lett. **96**, 052508 (2010).

[251] H. Jin, Y. Dai, B. Huang, and M. -H. Whangbo, *Ferromagnetism of undoped GaN mediated by through-bond spin polarization between nitrogen dangling bonds*, Appl. Rev. Lett. **94**, 162505 (2009).

[252] J. A. Chan, S. lany, and A. Zunger, *Electronic Correlation in Anion p Orbitals Impedes Ferromagnetism due to Cation Vacancies in Zn Chalcogenides*, Phys. Rev. Lett. **103**, 016404 (2009).

[253] A. Droghetti, C. D. Pemmaraju, and S. Sanvito, *Predicting d^0 magnetism: Self-interaction correction scheme*, Phys. Rev. B **78**, 140404 (2008).

[254] H. Wu, A. Stroppa, S. Sakong, S. Picozzi, M. Scheffler, and P. Kratzer, *Magnetism in C- or N-doped MgO and ZnO: A Density-Functional Study of Impurity Pairs*, Phys. Rev. Lett. **105**, 267203 (2011).

[255] D. M. Edwards and M. I. Katsnelson, *High-temperature ferromagnetism of sp electrons in narrow impurity bands: application to CaB_6*, J. Phys.: Condens. matter **18**, 7209 (2006).

[256] O. Volnianska and P. Boguslawshi, *Molecular magnetism of monoclinic SrN: A first-principles study*, Phys. Rev. B **77**, 220403 (2008).

[257] J. J. Lander, *Concentration of Hydrogen and semi-conductivity in ZnO under hydrogen-ion bombardment*, J. Phys. Chem. Solids **3**, 87 (1957).

[258] E. C. Behrman, R. K. Foehrweiser, J. R. Myers, and B. R. French, *Possibility of stable spheroid molecules of ZnO*, Phys. Rev. A **49**, R1543 (1994).

[259] A. Jain, V. Kumar, and Y. Kawazoe, *Ring structures of small ZnO clusters*, Comp. Mat. Sci. **36**, 258 (2006).

[260] J. M. Matxain, J. E. Fowler, and J. M. Ugalde, *Small clusters of II-VI materials: Zn_iO_i, i = 1-9*, Phys. Rev. A **62**, 053201 (2000).

[261] J. M. Matxain, J. E. Mercero, J. E. Fowler, and J. M. Ugalde, *Electronic excitation energies of Zn_iO_i clusters*, J. Am. Chem. Soc. **125**, 9494 (2003).

[262] M. Zhao, Y. Xia, Z. Tan, X. liu, and L. Mei, *Design and energetic characterization of ZnO clusters from first-principles calculations*, Phys. Lett. A **372**, 39 (2007).

[263] A. A. Al-Sunaidi, A. A. Sokol, C. R. A. Catlow, and S. M. Woodley, *Structures of zinc oxide nanoclusters: as found by revolutionaly algorithm techniques*, J. Phys. Chem. C **112**, 118860 (2008).

[264] A. V. Bulgakov, I. Ozerov, and W. Marine, *Laser ablation synthesis of zinc oxide clusters: a new family of fullerenes?*, arXiv:physics/0311117 (2003).

[265] S. Wu, N. Yuan, H. Yu, X. Wang, and Z. A. Schelly, *Synthesis and bandgap oscillation of uncapped, ZnO clusters by electroporation of vesicles*, Nanotechnology **17**, 4713 (2006).

[266] X. Cheng, F. Li, and Y. Zhao, *A DFT investigation on ZnO clusters and nanostructures*, J. Mol. Struct. **894**, 121 (2009).

[267] Q. Wang, Q. Sun, and P. Jena, *Ligand induced ferromagnetism in ZnO nanostructures*, J. Chem. Phys. **129**, 164714 (2008).

[268] J-H Song, T. Akiyamai, and A. J. Freeman *Stabilizing mechanism of the dipolar structure and its effects on formation of carriers in wurtzite 0001 films: InN and ZnO*, Phys. Rev. B **77**, 035332 (2008).

[269] O. Dulub, U. Diebold, and G. Kresse, *Novel Stabilization Mechanism on Polar Surfaces: ZnO(0001)-Zn*, Phys. Rev. Lett. **90**, 016102 (2003).

[270] G. Kresse, O. Dulub, and U. Diebold, *Competing stabilization mechanism for the polar ZnO(0001)-Zn surface*, Phys. Rev. B **68**, 245409 (2003).

[271] J. H. Lai, S. H. Su, H-H. Chen, J. C. A. Huang, and C-L Wu, *Stabilization of ZnO polar plane with charged surface nanodefects*, Phys. Rev. B **82**, 155406 (2010).

[272] Z. Yufei, G. Zhiyou, G. Xiaoqi, C. Dongxing, D. Yunxiao, and Z. Hongtao, *First-principles of wurtzite ZnO (0001) and (000$\bar{1}$) surface structures* , J. Semicond. **31**, 082001 (2010).

[273] P. Dev, H. Zeng and P. Zhang, *Defect-induced magnetism in nitride and oxide nanowires: Surface effects and quantum confinement* , Phys. Rev. B **82**, 165319 (2010).

[274] B. J. Nagare, S. Chacko, and D. G. Kanhere, *Ferromagnetism in Carbon-Doped Zinc Oxide Systems*, J. Phys. Chem. A **114**, 2689 (2010).

[275] H. Kwak and J. R. Chelikowsky, *Size-dependent induced magnetism in carbon-doped ZnO nanostructures*, Appl. Phys. Lett. **95**, 263108 (2009).

[276] C. Sudakar, J. S. Thakur, G. Lawes, R. Naik, and V. M. Naik, *Ferromagnetism induced by planar nanoscale CuO inclusions in Cu-doped ZnO thin films*, Phys. Rev. B **75**, 054423 (2007).

[277] X. Z. Li, J. Zhang, and D. J. Sellmyer, *Structural study of Mn-doped ZnO films by TEM*, Solid State Commun. **141**, 398 (2007).

[278] S. Zhou, K. Potzger, G. Zhang, F. Eichhorn, W. Skorupa, M. Helm, and J. Fassbender, *Crystalline Ni nanoparticles as the origin of ferromagnetism in Ni implanted ZnO crystals*, J. Appl. Phys. **100**, 114304 (2006).

[279] S. C. Wi, J.-S. Kang, J. H. Kim, S.-B. Cho, B. J. Kim, S. Yoon, B. J. Suh, S. W. Han, K. H. Kim, K. J. Kim, B. S. Kim, H. J. Song, H. J. Shin, J. H. Shim, and B. I. Min, *Electronic structure of $Zn_{1-x}Co_xO$ using photoemission and x-ray absorption spectroscopy*, Appl. Phys. Lett. **84**, 4233 (2004).

[280] M. Opel, K.-W. Nielsen, S. Bauer, S. T. B. Goennenwein, J. C. Cezar, D. Schmeisser, J. Simon, W. Mader, and R. Gross, *Nanosized superparamagnetic precipitates in cobalt-doped ZnO*, Eur. Phys. J. B **63**, 437 (2008).

[281] S. Ahlers, D. Bougeard, N. Sircar, G. Abstreiter, A. Trampert, M. Opel, and R. Gross, *Magnetic and structural properties of Ge_xMn_{1-x} films: Precipitation of intermetallic nanomagnets*, Phys. Rev. B **74**, 214411 (2006).

[282] C. Jaeger, C. Bihler, T. Vallaitis, S. T. B. Goennenwein, M. Opel, R. Gross, M. S. Brandt, *Spin-glass-like behavior of Ge:Mn*, Phys. Rev. B **74**, 045330 (2006).

[283] K. Shiraishi, *A New Slab Model Approach for Electronic Structure Calculation of Polar Semiconductor Surface*, J. Phys. Soc. Jpn. **59**, 3455 (1990).

[284] L.-W. Wang and J. Li, *First-principles thousand-atom quantum dot calculations*, Phys. Rev. B **69**, 153302 (2004).

[285] X. Huang, E. Lindgren, and J. R. Chelikowsky, *Surface passivation method for semiconductor nanostructures*, Phys. Rev. B **71**, 165328 (2005).

[286] K. Mohanta, S. K. Batabyal and A. J. Pal, *pn-junction rectifiers based on p-ZnO and nZnO nanoparticles*, Chem. Mater. **19**, 3662 (2007).

[287] K. Mohanta and A. J. Pal, *Diode junctions between two ZnO nanoparticles: Mechanism of rectification*, J. Appl. Phys. **105**, 024507 (2009).

[288] K. Mohanta and A. J. Pal, *Diode junctions between two ZnO nanoparticles: Current rectification and the role of particle size (and bandgap)*, Nanotechnology **20**, 185203 (2009).

[289] S. Mohammadi and C. R. Selvakumar, *Calculation of depletion layer thickness by including the mobile carriers*, IEEE Trans. Electron Devices **43**, 185 (1996).

[290] A. Ney, *Element specific versus integral structural and magnetic properties of Co:ZnO and Gd:GaN* Habiltation Thesis, University of Duisburg-Essen (2010)

[291] A. Ney, A. Kovács, V. Ney, S. Ye, K. Ollefs, T. Kammermeier, F. Wilhelm, A. Rogalev, and R. E. Dunin-Borkowski, *Structural, chemical and magnetic properties of secondary phases on Co-doped ZnO*, New J. Phys. **13**, 103001 (2011).

[292] M. Sawicki, W. Stefanowicz, and A. Ney, *Sensitive SQUID magnetometry for studying nanomagnetism*, Semicond. Sci. Technol. **26**, 064006 (2011).

[293] A. Ney, *Magnetic properties of semiconductors and substrates beyond diamagnetism studied by superconducting quantum interference device magnetometry*, Semicond. Sci. Technol. **26**, 064010 (2011).

[294] V. Ney, S. Ye, K. Ollefs, T. Kammermeier, F. Wilhelm, A. Rogalev, and A. Ney, *Co-doped ZnO epitaxial films: From a Brillouin-like paramagnet to a phase-separated superparamagnetic ensemble*, J. Nanosci. Nanotechnol. **10**, 5958 (2010).

[295] A. Ney, V. Ney, S. Ye, K. Ollefs, T. Kammermeier, T. C. Kaspar, S. A. Chambers, F. Wilhelm, and A. Rogalev, *Magnetism of Co doped ZnO with Al codoping: Carrier-induced mechanism versus extrinsic origins* Phys. Rev. B **82**, 041202 (2010).

[296] S. Ye, V. Ney, T. Kammermeier, K. Ollefs, S. Zhou, H. Schmidt, and A. Ney, *Influence of the developing magnetic order on the transport properties of epitaxial $Zn_{1-x}Co_xO$ films*, J. Phys. Conf. Ser. **200**, 052034 (2010).

[297] A. Ney, T. Kammermeier, K. Ollefs, V. Ney, T. C. Kaspar, S. A. Chambers, F. Wilhelm, and A. Rogalev, *Anisotropic paramagnetism of Co-doped ZnO epitaxial films*, Phys. Rev. B **81**, 054420 (2010).

[298] A. Ney, M. Opel, T. C. Kasper, V. Ney, S. Ye, K. Ollefs, T. Kammermeier, S. Bauer, K-W Nielsen, S. T. B. Goennenwein, M. H. Engelhard, S. Zhou, K. Potzger, J. Simon, W. Mader, S. M. Heald, J. C. Cezar, F. Wilhelm, A. Rogalev, R. Gross, and S. A. Chambers, *Advanced spectroscopic synchrotron techniques to unravel the intrinsic properties of diluted magnetic oxides: the case of Co:ZnO*, New J. Phys. **12**, 013020 (2010).

[299] V. Ney, S. Ye, T. Kammermeier, K. Ollefs, A. Ney, T. C. Kaspar, S. A. Chambers, F. Wilhelm, and A. Rogalev, *Tuning the magnetic properties of $Zn_{1-x}Co_xO$ films*, J. Magn. Magn. Mater. **322**, 1232 (2010).

[300] S. Ye, V. Ney, T. Kammermeier, K. Ollefs, A. Ney, F. Wilhelm and A. Rogalev, *Observation of the onset of magnetic clustering in superparamagnetic $Zn_{1-x}Co_xO$ films*, J. Appl. Phys. **104**, 083904 (2008).

[301] S. Ye, V. Ney, T. Kammermeier, K. Ollefs, S. Zhou, H. Schmidt, F. Wihelm, A. Rogalev, and A. Ney, *Absence of ferromagnetic-transport signatures in epitaxial paramagnetic and superparamagnetic $Zn_{0.95}Co_{0.05}O$ films*, Phys. Rev. B **80**, 245321 (2009).

[302] C. Knies, M. T. Elm, P. J. Klar, J. Stehr, D. M. Hofmann, N. Romanov,T. Kammermeier, and A. Ney, *Nonferromagnetic nanocrystalline ZnO:Co thin films doped with Zn interstitials*, J. Appl. Phys. **105**, 073918 (2009).

[303] V. Ney, S. Ye, T. Kammermeier, A. Ney, H. Zhou, J. Fallert, H. Kalt, F. -Y. Lo, A. Melnikov, and A. D. Weick, *Structural, magnetic, and optical properties of Co- and Gd-implanted ZnO(0001) substrates*, J. Appl. Phys. **104**, 083904 (2008).

[304] C. Meier, S. Lüttjohann, M. Offer, H. Wiggers and A. Lorke, *Silicon nanoparticles: Excitonic fine structure and oscillator strength,* Advances in Solid State Physics **48**, 79 (2009).

[305] C. Meier, A. Gondorf, S. Lüttjohann, A. Lorke and H. Wiggers, *Silicon nanoparticles: Absorption, emission, and the nature of electronic bandgap,* J. Appl. Phys. **101**, 103112 (2007).

[306] V. M. Fomin, V. N. Gladilin, J. T. Devreese, E. P. Pokatilov, S. N. Balaban and, S. N. Klimin, *Photoluminescence of spherical quantum dots,* Phys. Rev. B **57**, 2415 (1998).

[307] K. Hannewald, S. Glutsh and F. Bechstedt, *Theory of photoluminescence in semiconductors,* Phys. Rev. B **62**, 4519 (2000).

[308] K. Hannewald, S. Glutsh and F. Bechstedt, *Nonequilibrium theory pf photoluminescence excitation spectroscopy in semiconductors,* Phys. Stat. Sol. **238**, 517 (2003).

[309] V. A. Fonoberov, E. P. Pokatilov, V. A. Fomin and J. T. Devreese, *Photoluminescence of tetrahedral quantum-dot quantum wells,* Phys. Rev. Lett. **92**, 127402 (2004).

[310] V. A. Fonoberov, E. P. Pokatilov, V. M. Fomin and J. T. Devreese, *Photoluminescence of tetrahedral quantum-dot quantum wells,* Physica E **26**, 63 (2005).

[311] T. Feldtmann, L. Schneebeli, M. Kira and S. W. Koch, *Quantum theory of light emission from a semiconductor quantum dot,* Phys. Rev. B **73**, 155319 (2006).

[312] F. Trani, G. Cantele, D. Ninno, and G. Iadonisi, *Tight-binding calculation of the optical absorption cross section of spherical and ellipsoid silicon nanocrystals,* Phys. Rev. B **72**, 075423 (2005).

[313] V. M. Fomin, E. P. Pkatilov, J. T. Devreese, S. N. Klimin, G. D. Gladilin and S. N. Balaban, *Multiphonon photoluminescence and Raman scattering in semiconductor quantum dots,* Solid-State Electronics **42**, 1309 (1998).

[314] T. O. Cheche, M. C. Chang and S. H. Lin, *Electron-phonon interaction in absorption and photoluminescence spectra of quantum dots,* Chemical Physics **309**, 109 (2005).

[315] L. van Dijk, S. P. Kersten, P. Jonkheijm, P. van der Schoot and P. A. Bobbert, *Photoluminescence spectra od self/assembling helical supramolecular assemblies: A theoretical study,* Phys. Rev. B **57**, 2415 (1998).

[316] A. Gupta, *Study of surface modified silicon nanoparticles for printable optoelectronics,* Doctoral Thesis, University of Duisburg-Essen (2011).

[317] P. Vogl, H. P. Hjalmarson and J. D. Dow, *A Semi-empirical tight-binding theory of the electronic structure of semiconductors,* J. Phys. Chem. Solids **44**, 365 (1983).

[318] S. Y. Ren, X. Chen and J. D. Dow, *Tight-binding $sp3d^5$ Hamiltonian for Si*, J. Phys. Chem. Solids **59**, 403 (1998).

[319] C. Tserbak, H. M. Polatoglou, and G. Theodorou, *Unified approach to the electronic structure of strained Si/Ge superlattices*, Phys. Rev. B **47**, 7104 (1993).

[320] Y. M. Niquet, C. Delerue, G. Allan, and M. Lannoo, *Method for tight-binding parametrization: Application to silicon nanostructures*, Phys. Rev. B **62**, 5109 (2000).

[321] J. C. Slater and G. F. Koster, *Simplified LCAO Method for the Periodic Potential Problem*, Phys. Rev. **94**, 1498 (1954).

[322] I. Kwon, R. Biswas, C. Z. Wang, K. M. Ho and C. M. Soukoulis, *Transferable tight-binding models for silicon*, Phys. Rev. B **49**, 7242 (1994).

Acknowledgments

As the thesis is compiled, I pause to look back in time and try to acknowledge the invaluable cooperation I have received from many individuals which has eventually lead to the success of my thesis work.

My deepest appreciation goes to Prof. Dr. Peter Entel. He has exposed me to the beautiful subject of computational materials sciences and have given me a chance to carry on research work under his valuable supervision. I have been benefited from his kindness and generosity in many occasions. My thanks goes to him for his help for which I remain indebted.

Through out my work I have got active support from the enthusiastic group members like, Dr. Markus E. Gruner, Dr. Alfred Hucht, Dr. Ralf Meyer, Dr. Heike C. Herper, Dr. Georg Rollmann, Dr. Waheed A. Adeagbo, Dr. Alexey Zayak, Anna Grünebom, Mario Siewert, Dennis Commtese, and Antje Dannenberg, some of them are presently holding positions outside the group, either in industrial or in academic research. Many thanks to Prof. Jürgen König and his group members for their welcoming and approachable gestures. I specially thank Dr. Herper for going through the early version of my thesis and suggesting remarks for improvement. I thank Dr. Hucht for allowing me to use the Monte Carlo routine he has developed.

One of the important infrastructure in my work in the computational facility. I acknowledge the numerous computational time I have used from the university computational center where I have done most of my calculations. Some calculations are also done in the computational center from University of Dortmund (LiDO).

I thank Prof. Peter Kratzer and Dr. Sung Sakong with whom I often discussed. I got some valuable suggestions on hybrid-functional calculations from Dr. Sakong. Their views on the problems of ZnO gave me much understanding and confidence.

I thank Dr. Masako Ogura and Prof. Hisazumi Akai with whom I have collaborated for my studies on transition metal doped zinc oxide by the KKR Green's function method for electronic structure calculation, which has led to cooperative publications. I also thank Dr. Phivos Marvopolous for many discussions on KKR method. I appreciate his quick response to my email filled with questions.

I thank Dr. Shreekantha Sil, Viswa Bharati University, India, for his active participation with me for several studies like the carbon doped ZnO problem, modeling photoluminescence in tight-binding formalism and also in studies with the GW method. The tight-binding formalism for the photoluminescence is added as an appendix in the thesis.

My sincere thanks to Prof. Surjyo Narayan Behera (late) for his discussion on the d^0 magnetism in

carbon doped ZnO.
I have benefited from discussions with many experimental colleagues, notably, Dr. Andreas Ney, Dr. Anoop Gupta, Prof. Markus Winterer and Prof. Gerd Bacher.
Special thanks to Prof. Gouri Shankar Tripathi who has been a source of encouragement form the time of my masters studies at Berhampur University.
My association with physicists at Institute of Physics (IoP), Bhubaneswar, has been very cordial and beneficial. I thank Prof. S. N. Sahu for being very understanding and for his encouragement during my short-stay as doctoral student in his group. I thank Prof. B. N. Dev (currently at Indian Association of Cultivation of Sciences, Kolkata) for his generosity he has bestowed upon me.
There are many passive contributers to the thesis. First of all I thank my family for boosting the courage for moving forward in my career, even though that meant I stay away from home for so long. I thank all my friends. Finally, I thank Sanjubala for her patience and understanding and for her partnership in many causal events.

List of own publications

1. S. K. Nayak, M. E. Gruner, S. Sakong, S. Sil, P. Kratzer, S. N. Behera, and P. Entel, *Anisotropic ferromagnetism in carbon doped zinc oxide from first-principles studies*, Phys. Rev. B (communicated)

2. S. K. Nayak, A. Ney, M. E. Gruner, S. N. Behera, G. S. Tripathi, and P. Entel *Absence of ferromagnetic interaction in Co-Co nearest neighbor impurity pairs in ZnO: An analysis from GGA+U studies*, communicated as conference paper to International Workshop on Functional Materials (IWFM-2011), India

3. S. K. Nayak, H. C. Herper and P. Entel, *Magnetic phase Diagram of transition metal doped ZnO from density functional theory calculations and Monte Carlo simulations*, Mater. Res. Soc. Symp. Proc. **1260**, 1260-T10-22 (2010)

4. P. Entel, M. E. Gruner, A. Dannenberg, M. Siewert, S. K. Nayak, H. C. Herper and V. D. Buchelnikov, *Fundamental aspects of magnetic shape memory alloys: Insights from ab initio and Monte Carlo studies*, Materials Science Forum **635**, 3 (2010)

5. S. K. Nayak, M. Ogura, A. Hucht, H. Akai and P. Entel, *Monte Carlo simulations of diluted magnetic semiconductors using ab initio exchange parameters*, J. Phys. Condens. Matter **21**, 064238 (2009)

6. S. K. Nayak, M. Ogura, A. Hucht, S. Buschmann, H. Akai and P. Entel, *Ab initio simulations of diluted magnetic semiconductors: cobalt-doped zinc oxide*, Phys. Stat. Sol. (a) **205**, 1839 (2008)

7. V. D. Buchelnikov, P. Entel, S. V. Taskaev, V. V. Sokolovskiy, A. Hucht, M. Ogura, H. Akai, M. E. Gruner and S. K. Nayak, *Monte Carlo study of the influence of antiferromagnetic exchange interactions on the phase transitions of ferromagnetic Ni-Mn-X alloys (X=In,Sn,Sb)*, Phys. Rev. B **78**, 184427 (2008)

8. P. Entel, M. E. Gruner, A. Hucht, R. Meyer, G. Rollmann, S. Sahoo, and S. K. Nayak, *Simulating structure, magnetism and electronic properties of monoatomic, binary and ternary transition metal nanoclusters*, in: Mesoscopic, Nanoscopic and Macroscopic Materials: Proceedings of the International Workshop on Mesoscopic, Nanoscopic and Macroscopic Materials (IWMNMM-2008), AIP Conference Proceedings **1063**, 3 (2008)

9. P. Entel, V. D. Buchelnikov, M. E. Gruner, A. Hucht, V. V. Khovailo, S. K. Nayak, A. T. Zayak *Shape memory alloys: A summary of recent achievements*, Mater. Sci. Forum **583**, 21 (2008)

10. S. K. Nayak, M. E. Gruner and P. Entel, *Possible one-dimensional structures obtained from transition metal atom doped silicon nanoclusters*, Phase Transitions **79**, 709 (2006)

11. S. K. Nayak, M. E. Gruner and P. Entel, *Domain formation in hollow spherical Invar nanoparticles*, Phase Transitions **78**, 711 (2005)